UNIVERSITY OF CALIFORNIA

Los Angeles

Very High Energy Emission from the Galactic Center with VERITAS

A dissertation submitted in partial satisfaction

of the requirements for the degree

Doctor of Philosophy in Physics

by

Matthew Buchovecky

2019

ABSTRACT OF THE DISSERTATION

Very High Energy Emission from the Galactic Center with VERITAS

by

Matthew Buchovecky

Doctor of Philosophy in Physics

University of California, Los Angeles, 2019

Professor Rene Ong, Chair

The Galactic Center (GC) is an extremely energetic region, host to a variety of powerful astronomical sources and rare astrophysical processes that emit a large flux of non-thermal radiation. The inner $375 \times 600\,\mathrm{pc}$ region, called the Central Molecular Zone (CMZ), is home to the supermassive black hole Sgr A*, massive cloud complexes, supernova remnants, and likely the peak concentration of dark matter in the Galaxy. It has been studied across an extremely wide range of wavelengths by many instruments.

In this dissertation, I present the results of my analysis of the very high-energy (VHE) ($E > 100\,\mathrm{GeV}$) gamma-ray emission from the GC using data from about 155 hours of quality observations taken with the VERITAS imaging atmospheric Cherenkov telescope. This emission includes a strong central point source VER J1745–290, coincident with the position of Sgr A*, and diffuse emission that extends along the Galactic ridge. VER J1745–290 is detected at a significance of 38σ, and I reconstruct its spectrum and lightcurve. Its spectrum is best fit by a power law with an index of -2.16 ± 0.18, a flux normalization of $(11.76 \pm 2.03) \times 10^{-12}\,\mathrm{TeV}\,\mathrm{cm}^{-2}\,\mathrm{s}^{-1}$ at $1\,\mathrm{TeV}$, and an exponential cutoff at $10.8 \pm 3.0\,\mathrm{TeV}$. The exponential cutoff in its spectral shape, along with its apparent lack of variability in the very-high-energy gamma ray range favor electron models of its emission, such as the plerion model of emission from the pulsar wind nebula G359.95–0.04. I also present the results of my analysis on the morphology and, for the first time with VERITAS, the spectrum of diffuse emission in the GC. I find an approximately 52% correlation of the gamma signal to

molecular gas as traced by CS(1-0) line emission. I report an energy spectrum that is best fit by a pure power law with a hard index of -2.26 ± 0.13, showing no evidence of a cutoff over $40\,\mathrm{TeV}$. This strengthens the evidence of a potential accelerator of PeV cosmic rays being present in the GC. Using these results, I discuss the impact on the models of diffuse emission and possible connections to the central source. I also provide detections and spectra of other sources within the field of view of VERITAS.

The dissertation of Matthew Buchovecky is approved.

Qing Zhou

Matt Malkan

Rene Ong, Committee Chair

University of California, Los Angeles

2019

To my mom . . .

who always supported me

and helped me pursue all my goals

TABLE OF CONTENTS

LIST OF TABLES

LIST OF ACRONYMS

VERITAS Very Energetic Radiation Imaging Telescope Array System

FLWO Fred Lawrence Whipple Observatory

IACT imaging atmospheric Cherenkov telescope

VEGAS VERITAS Gamma-ray Analysis Suite

CORSIKA COsmic Ray SImulations for KAscade

GC Galactic Center

SMBH supermassive black hole

VHE very high-energy

HE high-energy

MC molecular cloud

CMZ Central Molecular Zone

CMB cosmic microwave background

AGN active galactic nucleus

ISM interstellar medium

SNR supernova remnant

NRF non-thermal radio filament

PWN pulsar wind nebula

MSP millisecond pulsar

EM electromagnetic

CR cosmic ray

VBF VERITAS bank format

IRF instrument response function

LT lookup table

EA effective area

BDT Boosted Decision Tree

PMT photomultiplier tube

DAQ data acquisition

CFD constant fraction discriminator

RFB rate feedback

FADC flash analog-to-digital converter

NSB night sky background

VPM Very Energetic Radiation Imaging Telescope Array System (VERITAS) pointing monitor

DQM data quality monitoring

MW Milky Way

IR infrared

FIR far infrared radiation

EM electromagnetic

IC inverse Compton

FoV field of view

LZA large zenith angle

SZA small zenith angle

PSF point spread function

RRM reflected region method

RBM ring background method

IC inverse Compton

EAS extensive air shower

MAGIC Major Atmospheric Gamma Imaging Cherenkov

H.E.S.S. High Energy Stereoscopic System

CTA Cherenkov Telescope Array

VLA Very Large Array

LAT Large Area Telescope

VLBI very-long-baseline interferometry

DM dark matter

CDM cold dark matter

WIMP weakly interacting massive particle

LSP lightest supersymmetric particle

MSL mean scaled length

MSW mean scaled width

ID impact distance

RMS root mean square

K-N Klein–Nishina

GZK Greisen–Zatsepin–Kuzmin

STP standard temperature and pressure

NASA National Aeronautics and Space Administration

TMVA Toolkit for Multivariate Data Analysis

PDG Particle Data Group

ACKNOWLEDGMENTS

"Measure what is measurable, and make measurable what is not so."

— Galileo Galilei

"I have never met a man so ignorant that I couldn't learn something from him."

— Galileo Galilei

"For a successful technology, reality must take precedence over public relations, for Nature cannot be fooled."

— Richard Feynman

June 2010	Graduated Carnegie Mellon University
	Bachelor of Science, Physics
	Philosophy Minor
September 2012	M.S. (Physics)
2012–2013	General Anti-Particle Spectrometer (GAPS) Experiment
2013–2019	VERITAS (Very Energetic Radiation Imaging Telescope Array System)

PUBLICATIONS AND PRESENTATIONS

Committee on Space Research (COSPAR) 2018 'Very High Energy Gamma Ray Emission from the Galactic Center with VERITAS'

Results of this dissertation to be published in 2019

CHAPTER 1

Introduction to the Galactic Center (GC)

The Milky Way is the barred spiral galaxy that is home to Earth and our Solar System. The center of the Milky Way Galaxy, or the Galactic Center (GC), is one of the most interesting astronomical regions we can observe. Galaxies form by the gravitational attraction of matter, so their central regions are extremely dense in mass and energy. This enormous amount of matter creates a wide range of physical processes we could not recreate on our planet, offering insight into the high-energy astrophysics and the dynamics of our Galaxy and galactic nuclei in general. Our GC is host to an extremely large number of astronomical sources, including supernova remnants (SNRs), pulsar wind nebulae (PWNe), large extended molecular clouds (MCs), as well as vast star-forming regions and is predicted to have the peak density of dark matter (DM) in the Galaxy. The most dense region is called the Central Molecular Zone (CMZ), and is generally considered to be the innermost 4° by 2° around the center. Coincident with the center of mass of the GC lies perhaps the most interesting source, the central supermassive black hole (SMBH) known as Sagittarius A* (Sgr A*). Because SMBHs are only known to exist at the centers of galaxies, Sgr A* is the closest one we can observe. An illustration of a SMBH at the center of a galaxy, surrounded by a disk of accreting matter, can be seen in Figure 1.1.

Between these various sources, there is a great amount of unique emission across nearly all wavelengths, from radio to gamma-ray energies. At almost all energies, there is strong emission from the center as well as vast diffuse emission from the molecular material along the Galactic plane. At lower energies, such as at radio wavelengths, the central emission is known to be associated with Sgr A*. At higher energies, the emission becomes more mysterious, as lower statistics and higher positional uncertainty make it difficult to definitively associate

emission with a specific astrophysical object. In the very high-energy gamma ray range, the central emitter is referred to as J1745–290. Its position is consistent with Sgr A*, but because of limited spatial resolution, other candidate sources cannot be ruled out.

The diffuse emission is also of great interest and may have a connection to the central point source of very high-energy (VHE) emission. The diffuse gamma-ray emission is thought to be caused by interactions of the molecular material with extremely energetic particles that pervade the Galaxy called cosmic rays (CRs). The origin of the CRs is not fully understood, but the VHE diffuse emission studied by VERITAS and the High Energy Stereoscopic System (H.E.S.S.) hint at the potential for a central accelerator of VHE cosmic rays. This accelerator could be J1745–290, or another source entirely.

In this chapter, I introduce the scientific research relevant to my thesis. In the next section, I introduce Sgr A* and other important objects in the inner GC region. Then I provide a summary of observations of the GC over all energy ranges. I discuss the questions being studied via gamma rays and the scientific motivation for answering those questions.

Figure 1.1: An artist conception of a supermassive black hole (NASA, 2013). The spiraling structure is called the accretion disk, and is formed by surrounding dust and matter flowing toward the center of gravity. The large column extending from the center is an outflowing jet of energetic particles. Jets are observed in many supermassive black hole systems although no jet has been definitively observed from Sgr A*.

1.1 Galactic Center Objects

1.1.1 Sgr A*

The existence of SMBHs in the center of galaxies, including our own Milky Way (MW) Galaxy, was first hypothesized in 1971 by Lynden-Bell & Rees. They proposed that the observed properties of quasars, such as their high luminosity, could be explained if the nuclei of galaxies are black holes. In their model, radiation pressure drives dust particles away from the accreting matter, creating nuclear winds at high temperature. Indeed, this model is consistent with the observation of infrared emission from the GC (Becklin & Neugebauer, 1968). Balick & Brown (1974) discovered a radio source of synchrotron radiation using the *Green Bank Interferometer* at the National Radio Astronomy Observatory. They gave it the official name Sagittarius A* (Sgr A*). While no jet like the one in Figure 1.1 has been definitely detected in Sgr A*, the *Chandra X-ray observatory* has seen X-ray evidence of a likely parsec-scale jet (Li et al., 2013; Zhu et al., 2018).

The position of an astronomical source can be given by several different astronomical coordinate systems. The equatorial coordinate system measures the position in right ascension and declination angles eastward along and perpendicular to the celestial plane. The J2000 epoch of this system is commonly used for naming objects, such as the central VHE source J1745–290. The Galactic coordinate system is useful for objects near the center of the Galaxy. Its coordinate axes are Galactic latitude and Galactic longitude. Lines of constant Galactic latitude lie approximately parallel to the Galactic plane. Its primary direction (0, 0) points toward the approximate center of the Milky Way. The most commonly quoted position of Sgr A* is the radio position found in Reid & Brunthaler, 2004, with J2000 coordinates of $\left(17^{\mathrm{h}}45^{\mathrm{m}}40.0409^{\mathrm{s}}, 29°0'28.118''\right)$ or equivalently $(359.944\,249°, -0.046\,165°)$ in Galactic coordinates. They used interferometry data from the *Very Large Baseline Array* (*VLBA*) to track the proper motion of Sgr A* and they concluded that the motion of Sgr A* relative to the Galaxy is less than about $20\,\mathrm{km/s}$. It has been shown that the radio emission from Sgr A* and the position of the central mass coincide within $\approx 10\,\mathrm{millarcsec}$ (Ghez et al., 2005).

While the exact distance to the center of the Galaxy is not precisely known, many estimates have been found by different methods. Eisenhauer et al. (2005) studied a star named S0-2 (S2), whose orbit is very close to Sgr A*, with near-infrared astrometric data from *NAOS/CONICA* and spectroscopic data from *SPIFFI*. By measuring its proper motion and the redshift from its line of sight velocity, they found a distance of (7.62 ± 0.32) kpc (kiloparsecs), which is on the lower end of estimates. Vanhollebeke et al. (2009) got a higher estimate of (8.7 ± 0.5) kpc by comparing simulations of the Galactic bulge's stellar population and metallicity to infrared data from *2MASS* and gravitational lensing data from *OGLE-II*. Boehle et al. (2016) have recently improved the mass and distance estimates with twenty years of speckle image data from the *Keck* telescope using deep adaptive optics to measure the stellar orbits of S2 and another nearby star S0-38. Their estimate of the mass was $M_{bh} = (4.02 \pm 0.16 \pm 0.04) \times 10^6 \, M_{\odot}$, and they determined a distance of $R_0 = 7.86 \pm 0.14 \pm 0.04$ kpc. This R_0 value is used for calculations performed in this dissertation involving the distance to the GC. At this distance, a parallax angle of $1 \, \mu as$ (microarcseconds) corresponds to a physical size of about $0.008 \, AU$ (3.8×10^{-11} kpc or 1.2×10^6 km).

To support the idea that Sgr A* is in fact a SMBH, many of its properties have been studied, and much of this work has been done by the Galactic Center Group at the University of California, Los Angeles (UCLA). By following the orbits of stars very close to Sgr A*, its mass can be inferred and its size constrained. Figure 1.2a shows the orbits of stars around Sgr A* as studied by the *Keck* telescope. For example, (Ghez et al., 2008) found that S2 had an orbit with a period of 15.2 years, a pericenter of 1.8×10^{10} km, and a center consistent with the radio / infrared (IR) position of Sgr A*. This led them to measure the enclosed mass to be roughly $M_{bh} = 4.1 \pm 0.6 \times 10^6 M_{\odot}$, where $M_{\odot}$ is the mass of the Sun, and the error gives the 68% confidence interval. There have been multiple measurements made by other collaborations that are consistent with this value. One such study that looked at a total of 6000 stars found a consistent central mass and an additional extended mass of $(1.0 \pm 0.5) \times 10^6 M_{\odot}$ within the central parsec (Schödel et al., 2009).

The mass of a black hole can be used to determine the radius of the event horizon, the region in which gravity is too strong for anything, including light, to escape. The

4

Schwarzschild radius R_s results from the spherically symmetric solution of the Einstein field equations for a non-rotating object:

$$R_s = \frac{2GM}{c^2} \tag{1.1}$$

where M is the mass of the black hole, G is the gravitational constant, and c is the speed of light. For the approximate mass of Sgr A*, this gives a value of $R_s \approx 1.2 \times 10^7 \, \text{km} \approx 3.9 \times 10^{-7} \, \text{pc}$.

The radius of Sgr A* must be less than the pericenter of orbit of any star to avoid a stellar disruption, so the radius can be constrained by measuring the smallest orbital distances for stars such as S2. By measuring their proper motion with *Keck*, Ghez et al. (2005) were able to simultaneously derive the orbits of seven central stars. They determined that the central 'dark' mass associated with Sgr A* must be contained within a radius of $1 \, \text{mas}$, or $1.2 \times 10^9 \, \text{km}$, at a position consistent with its radio source.

The intrinsic size of Sgr A* can also be examined by looking at high-resolution radio imaging. Using *very-long-baseline interferometry (VLBI)* at $1.3 \, \text{mm}$ wavelength, Doeleman et al. (2008) found an intrinsic diameter of $37^{+16}_{-10} \, \mu\text{as}$. Using estimated values for the mass of Sgr A* and the distance to the center of the Galaxy from Subsection 1.1.1, this corresponds to a physical diameter of $4.35 \times 10^7 \, \text{km}$, which is greater than the predicted Schwarzschild radius. Doeleman et al. (2008) claim that their data suggests that the radio emission may be coming from the accretion flow surrounding the central black hole.

1.1.2 Sagittarius A

The SMBH Sgr A* is one of three components in a larger complex called Sagittarius A. Figure 1.3a shows a labeled X-ray image of the complex, which also includes Sgr A East and Sgr A West.

Sgr A West Also called the 'mini-spiral', Sgr A West is a spiral-shaped superposition of gas streams that orbit Sgr A*. Streams of matter orbiting inwards from the surrounding gas cloud emit thermal radiation (Lo & Claussen, 1983). The spiral arms are surrounded by a circumnuclear disk (CMD) of high-density molecular material. A radio image of the Sgr A

(a)	(b)
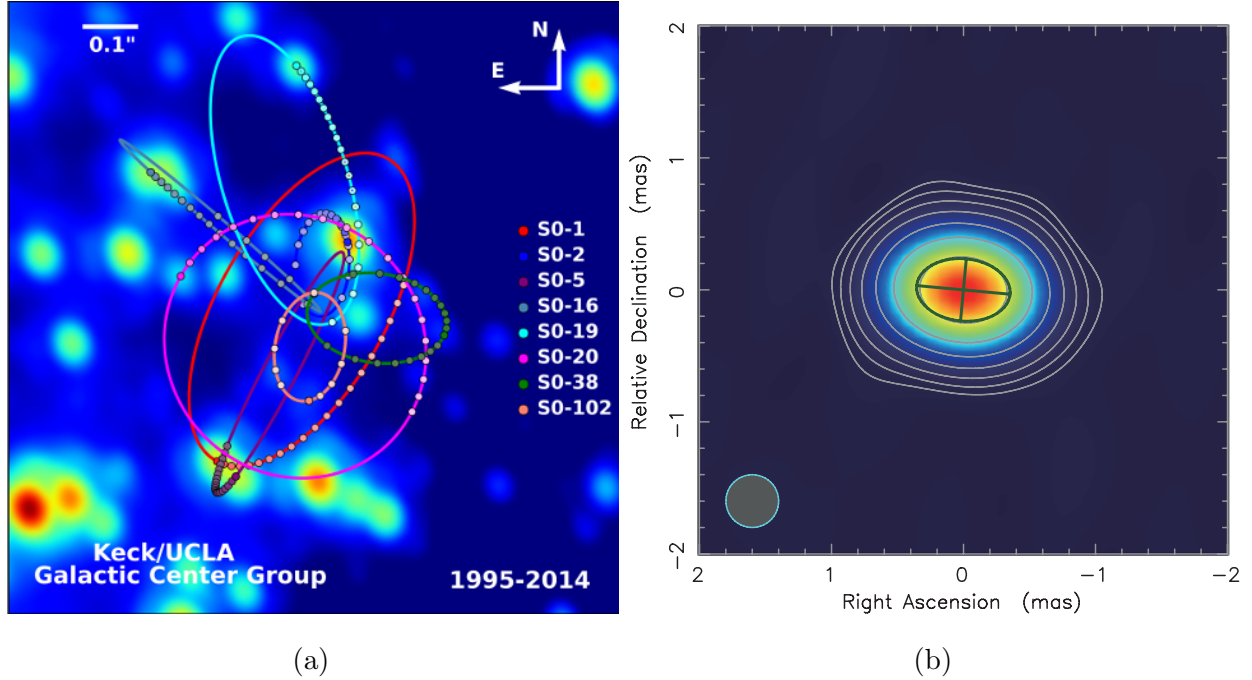
Figure 1.2: (a) Radio image of the inner square arcsecond of our Galaxy showing the orbits of nearby stars. (b) Image at 7 mm of Sgr A* at the milliarcsecond scale (Akiyama et al., 2013). The best-fit elliptical Gaussian model of the signal is drawn.

West region is pictured in Figure 1.3b.

Pedlar et al. (1989) observe absorption at 90 cm of the Sgr A East's non-thermal emission which follows the structure of Sgr A West, showing that it is behind Sgr A West. In Herrnstein & Ho, 2004, they determine that Sgr A West is in front of most of Sgr A East along our line of sight. A study of low-frequency radio emission shows that Sgr A West's spectral flux is decreased in the energy range affected by free-free absorption, while the corresponding flux of Sgr A* is not reduced (Roy & Rao, 2004). This suggests that Sgr A* lies between Earth and Sgr A West, as its emission would suffer the same decrease if it had to pass through Sgr A West.

Sgr A East   Sgr A East is an extended shell-like SNR surrounding Sgr A West in projection that emits strongly in radio and X-rays. SNRs are the structure remaining after a supernova event in which a star explodes, expelling its matter away from it. The supernova explosion

6

releases a great amount of energy and creates a shockwave of ejected matter, resulting in a luminous structure called a supernova remnant (SNR). The SNR shock picks up interstellar matter as it expands and is capable of accelerating particles to very high energies. Sgr A East was identified in Ekers et al., 1983 by its non-thermal radio emission, and also goes by the name G0.0+0.0. It is elliptical in shape, as seen in Figure 1.3a, with a major axis of about 10.5 pc and a minor axis of 8 pc. Both its morphology and spectral index in the radio waveband were consistent with that of SNRs, but its lifetime was longer than expected. Later, X-ray evidence from *Chandra* (Maeda et al., 2001) and the *XMM-NEWTON* satellite showed signatures of metallic ions. Their spectra both showed Kα lines that were emitted by iron (Fe), sulfur (S), argon (Ar), and calcium (Ca). The chemical abundances they observed were consistent with either a type-Ia or type-II supernova event, offering more definitive evidence Sgr A East is in fact an SNR. Lau et al. (2015) observed the infrared signal from warm dust near the center of Sgr A East. The presence of such dust in an SNR that is about 10,000 years old is evidence that supernovae are an important source of cosmic dust.

1.1.3   Central Molecular Zone

The CMZ is home to Sagittarius A as well as many other sources of emission, accounting for a large percentage of the Galaxy's luminosity. Overall, it is a massive, dense region that contains about 10 % of the MW's molecular gas (Morris & Serabyn, 1996). It is also characterized by its high temperature, large dispersion of velocities, and the apparent presence of very strong magnetic fields. VERITAS observations of the GC cover the full CMZ and the area immediately around it. While the majority of Galactic gas is mostly ionized interstellar medium (ISM), large regions of high density allow molecules (mostly H$_2$) to form. These regions, called molecular clouds (MCs), create strong peaks of CS, CO, and C line emission (Tsuboi et al., 1999), which can be used to trace their density. Sgr B2 is the largest of many MCs in the CMZ, with a mass of around a few million solar masses and an extent of about 20 pc. Its density averages about $10^3\,\mathrm{cm}^{-3}$ and reaches the order of $10^6\,\mathrm{cm}^{-3}$ in its core of 5 pc (Lis & Goldsmith, 1990).
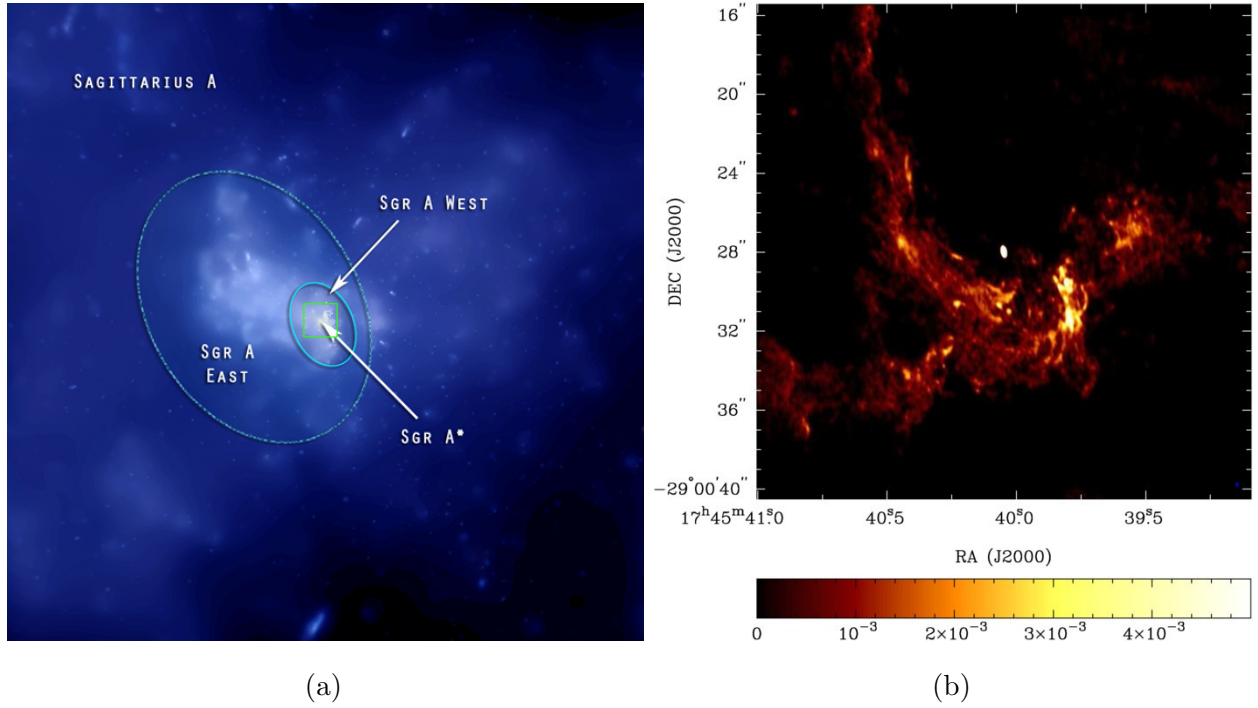
Figure 1.3: Close-up images of the Sagittarius A complex. Image (a) shows a *Chandra* X-ray image, 8.4 arcminutes per side, highlighting Sgr A East, Sgr A West, and Sgr A*. (Credit: NASA/CXC/MIT/F.K.Baganoff et al.) Image (b) shows a *Very Large Array (VLA)* image of 1.3 cm emission of the inner 25 arcseconds of Sgr A West (Zhao et al., 2009). The region in (b) is highlighted by the green square in (a).

Because of its great mass, the CMZ has a huge population of stars and star clusters. There are estimated to be over 100 million stars within the central parsec around Sgr A*. Within it are the two largest and most dense young ($< 5\,\mathrm{Myr}$) stellar clusters in the Galaxy, the Arches Cluster and the Quintuplet Cluster. These clusters produce large amounts of stellar winds, or charged particles that flow continuously from a star. There are also multiple HII regions, which are regions of ionized interstellar hydrogen left over where stars have formed. Aging stars with sufficient mass, greater than 5 solar masses, can explode into supernovae, creating SNRs and leaving behind either a black hole or a pulsar. Pulsars are magnetized rotating neutron stars that emit collimated beams of matter called jets. Their jets can create a cloud of gas or dust called a pulsar wind nebula (PWN) or plerion.

The SNR G0.9+0.1, located at Galactic coordinates ($0.87°$, $0.08°$), is a strong gamma-ray

point source located in the CMZ (Aharonian et al., 2005). It has a gamma-ray flux of 2 % of the Crab Nebula, and is a good target for studying the gamma ray spectrum of SNRs. The spectrum of a source quantifies the flux as a function of energy and is critical to understanding the processes occurring in an astrophysical source. A candidate PWN, named G359.95–0.04, also lies in the center of the Galaxy, less than ten arcseconds from Sgr A*. This is too close to resolve for current gamma ray telescopes, but is another possible source of the TeV emission from J1745–290.

1.2 The GC Region as Imaged in Multiple Wavelengths

The Galactic Center (GC) has been observed for nearly 100 years by many different experiments covering a wide range of wavebands. Each waveband of emission reveals a unique set of sources, features, and morphologies. Each different physical mechanism for emission produces electromagnetic (EM) radiation of different energies, and the amount of radiation produced by each mechanism depends on different physical parameters of the source, such as field strength or particle populations. By quantifying the energy spectrum, or the flux of emission as a function of energy, over a large energy range, we can maximize the empirical data for comparison to theoretical models. In this chapter, I give an overview of the history of GC observations and science leading into the VHE gamma-ray regime.

1.2.1 Radio

The GC was first discovered in radio waves in 1932 when Karl Jansky observed EM radiation coming from the rough direction of the center of the Galaxy (Jansky, 1933). Radio wavelengths typically range between millimeters and thousands of kilometers in length. In this low energy range of the spectrum, emission comes largely from synchrotron radiation, which occurs when electrons are accelerated by a magnetic field. This sort of acceleration requires a strong magnetic field, and thus the radio luminosity can indicate the strength and orientation of magnetic fields, as well as properties of the population of electrons. Emission lines from various molecules can be used to trace the presence of molecular gas and to estimate
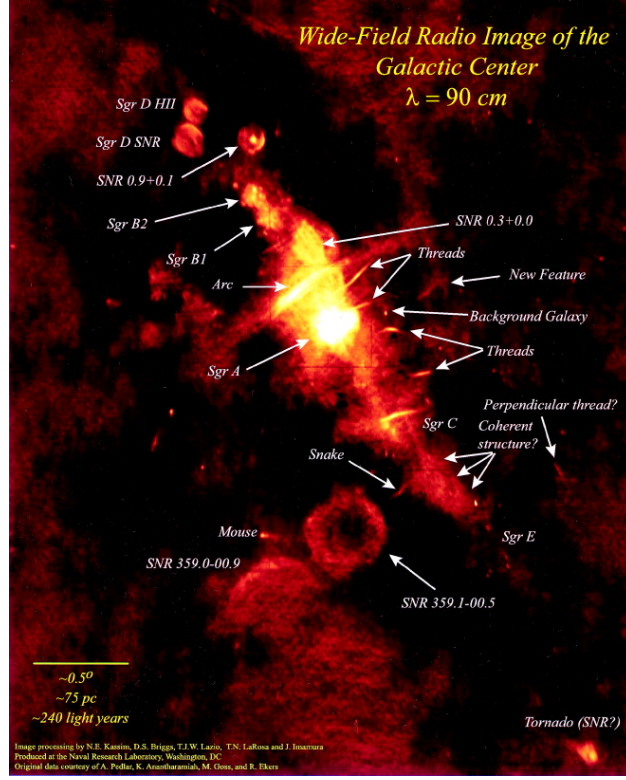
Figure 1.4: A high resolution image of the inner $2.5° \times 4°$ or roughly $375 \times 600\,\text{pc}$ of the GC region. The image is compiled from $90\,\text{cm}$ observations taken with *VLA* (LaRosa et al., 2000) and projected in equatorial coordinates, with the various structures labeled. Sgr B1, B2, C, and D are the major cloud complexes.

the density of gas in a region. A common line used to trace gas in MCs is the CS(1-0) line, which is emitted when carbon monosulfide transitions from its first excited rotational state to the ground state.

In 1983, the *VLA* telescope was able to image the GC in enough detail to reveal its radio structure (Ekers et al., 1983; Lo & Claussen, 1983). Figure 1.4 shows a detailed and labelled image from Yusef-Zadeh et al., 1984. The central bright SMBH Sgr A* can be clearly seen, as well as the large radio arc, non-thermal filaments, a collection of supernova remnants including G0.9+0.1, and the many cloud complexes Sgr B1, B2, C, and D. In addition to Sgr A* and the shape of the GC halo, these images also showed detail of a large arc extending from the GC halo (Yusef-Zadeh et al., 1984).

10

A close look at the Radio Arc shows that it is composed, though not exclusively, of several filamentary structures. These structures, referred to as non-thermal radio filaments (NRFs), are also found elsewhere in the inner GC region. They are long, thin structures, with lengths of about 40 pc and widths of less than 1 pc. Their characteristic spectral indices in the radio band fall in the range of $-0.5 < \alpha < 0.3$ (Linden, 2013a). In addition, the radio emission was measured to be polarized, leading Yusef-Zadeh et al. (1984) to conjecture that there may be a poloidal magnetic flux density of $\approx 100\,\mu\text{G}$ present around the GC (Tsuboi et al., 1986). This notion was strengthened by the original observations that the filaments had a preferred orientation with their lengths being perpendicular to the Galactic plane. Several faint filaments, an order-of-magnitude higher in number than the pronounced NRFs, were subsequently discovered by a more sensitive *VLA* survey (Yusef-Zadeh et al., 2004). While most filaments have a strong orientation preference, those fainter filaments do not universally have such a preference. This information can help constrain the possible presence of a large-scale poloidal magnetic field. These fainter filaments were also found to group into clusters in star-forming regions, as did the brighter NRFs. Star-forming clusters are home to stars, such as Wolf-Rayet stars and early-type B stars, whose combined winds can create a greater collective wind. Such a strong wind, when in the dense stellar environment of the GC, can produce shock waves capable of relativistic particle acceleration (Yusef-Zadeh, 2003). These filaments commonly terminate near compact or resolved shell-like thermal sources (Yusef-Zadeh et al., 2004).

More modern radio arrays have been able to create much more detailed images of the region. The most detailed, high-resolution image to date was created with the radio telescope *MeerKAT*, and is shown in Figure 1.5. It resolves a number of features too small to be resolved with previous instruments, as well as finer segments of the radio filaments. Star-forming regions and SNRs can be seen in much greater detail.
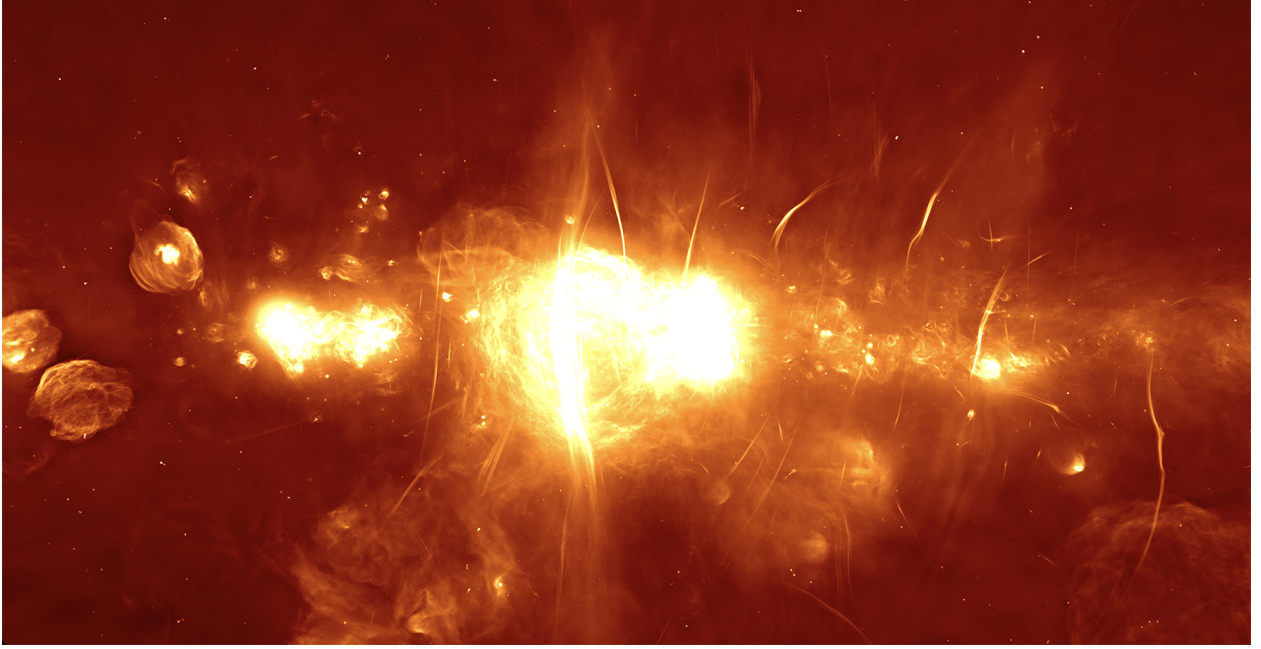
Figure 1.5: The highest resolution image of the inner 2° × 1° of the GC produced with observations by the radio telescope *MeerKAT*. The color scale represents the brightness of the radio signal, with red being faint and white being the brightest (Lorenzo, 2018).

1.2.2 Submillimeter / Infrared

Submillimeter (sub-mm) astronomy examines photons of light between microwave and infrared (IR), and is good for investigating MCs and dark nebulae. The CMZ has been imaged by experiments such as *Scuba* (Pierce-Price et al., 2000). The sub-mm observations revealed most of the same structures as in radio, and found spectral indices for many clouds. They also estimated the total mass of clouds in the inner 400 pc to be $(50 \pm 10) \times 10^6 \, \mathrm{M_\odot}$.

Far infrared (FIR) radiation ranges from $\approx 1.2 \, \mathrm{meV}$ to $83 \, \mathrm{meV}$, while near infrared (NIR) ranges from $\approx 886 \, \mathrm{meV}$ to $1653 \, \mathrm{meV}$. The CMZ constitutes 5–10% of the luminosity of IR and Lyman continuum photons in the Galaxy (Morris & Serabyn, 1996). FIR emission and Hα emission are believed to trace active star-forming regions (van Eldik, 2015). Star-forming regions are important because they contain strong particle winds capable of accelerating particles to high energies, and because they can be home to many supernovae and SNRs. O-type and B-type stars are early type stars with mass $> 2M_\odot$ that emit UV radiation. The

resulting ionization of gas creates $H\alpha$ emission, which is a red spectral line in the Balmer series, and the heating of interstellar dust creates FIR emission (Devereux & Young, 1990).

In 2003, the first IR flaring of Sgr A* was observed by the *Very Large Telescope* (Genzel et al., 2003) and the *Keck* telescope (Ghez et al., 2003). Unlike in X-rays (see Subsection 1.2.4), the non-flaring state in IR is neither steady nor periodic. Rather, the emission intensity seems to follow a red noise pattern (Do et al., 2009), which is also referred to as brown noise because its stochastic variability mimics Brownian motion. Witzel et al. (2018) present an extensive dataset of IR variability monitoring of Sgr A* by four different experiments. They found the characteristic timescale of stochastic variability to be $\tau_b = 243^{+82}_{-57}$ minutes, and a spectral index of $\alpha_s \approx 0.6$ for NIR emission when the flux density is $0.3\,\mathrm{mJy}$ or greater. They also confirmed that Sgr A* follows trend of negative correlation between luminosity and the rate of stochastic variability for active galactic nuclei (AGNs). Liu et al. (2006b) provide a reasonable production mechanism for emission in the sub-mm / IR range occurring within about 20 Schwarzschild radii of Sgr A*. In their model, electrons have resonant interactions with magnetohydrodynamic turbulence in the accretion torus around the black hole, undergoing stochastic acceleration. This model can also be used to explain IR and possibly X-ray flaring via thermal synchrotron and synchrotron self-Compton radiation (Liu et al., 2006a), although there are numerous more recent models.

1.2.3 Optical / Ultraviolet

Along our line-of-sight to the GC, there is a thick presence of interstellar dust that lies in the Galactic plane. Light waves whose wavelength is similar to the size of these dust particles are effectively blocked, obscuring the view of the GC in that waveband. In fact, the optical and ultraviolet ranges suffer an extinction on the order of 30 visual magnitudes (Morris & Serabyn, 1996). This makes the GC practically unobservable from the optical band up to soft (lower energy) X-rays, becoming visible only when photon energies exceed $\gtrsim 1\,\mathrm{keV}$ and the waves are small enough. O-type and B-type stars found in star-forming regions are thought to emit optical and UV radiation.

1.2.4 X-Ray

The GC has been studied by several experiments in the X-ray waveband, which ranges from ≈ 0.1–$100\,\mathrm{keV}$. The emission in this waveband is dominated by bremsstrahlung radiation which is emitted by an electron that is rapidly accelerated in the electric field of protons or other nuclei (see Subsection 2.3.2). The amount of bremsstrahlung is therefore a good way to determine the density of cosmic ray electrons and ambient protons in a region.

The first detection of an X-ray source coincident with Sgr A* was done by *Chandra* in 2001 (Baganoff et al., 2003), which produced the first arcsecond resolution X-ray image of the central square 17 arcminutes or $40\,\mathrm{pc} \times 40\,\mathrm{pc}$ of the GC in the energy range 0.5–$7\,\mathrm{keV}$. The central X-ray source was identified as CXOGC J174540.0–290027. Its position is coincident within $0.27'' \pm 0.18''$ of Sgr A*. They observed a quiescent flux of $F(2 - -10\,\mathrm{keV}) = 1.3 \times 10^{-13}\,\mathrm{ergs/cm^2/s}$, which, after corrections for absorption, gives a luminosity $L \approx 2.4 \times 10^{33}\,\mathrm{erg/s}$. This falls about ten orders of magnitude below the Eddington luminosity of the black hole, which is about $5.17 \times 10^{44}\,\mathrm{erg/s}$. The Eddington limit is the maximum luminosity for which the gravitational pressure of a body is able to balance the outward radiation pressure, and depends only on the mass M of the body.

$$L_{\mathrm{Edd}} = \frac{4\pi G M m_p c}{\sigma_T} \tag{1.2}$$

$$\cong 1.26 \times 10^{31} \left(\frac{M}{M_\odot} \right) \mathrm{W} \tag{1.3}$$

$$= 3.2 \times 10^4 \left(\frac{M}{M_\odot} \right) L_\odot \tag{1.4}$$

Here m_p is the mass of a proton, σ_T is the Thomson cross section (see Appendix A.1), and $L_\odot$ is the luminosity of the Sun. (For a list of relevant physical constants and values, see Section A.4.) This observation also revealed rapid flaring from the direction of Sgr A*, reaching 45 times the quiescent state in the peak of flaring (Baganoff et al., 2001). *Chandra* has also detected 17 X-ray features with filamentary structure (Johnson et al., 2009), similar to, but separate from, the radio filaments, called non thermal filaments (NTFs).

The *NuSTAR* satellite was able to create the first GC image with sub-arcminute detail for energies between $10\,\mathrm{keV}$ and $79\,\mathrm{keV}$, shown in Figure 1.6 (Mori et al., 2015). This allowed

them to resolve the *INTEGRAL* source IGR J17456-2901, which is the central emission from 15 keV to 10 MeV, into multiple point sources, MCs, and NTFs. The image also resolved a new component of emission called the central component of hard X-ray emission (CHXE) whose nature is unknown.
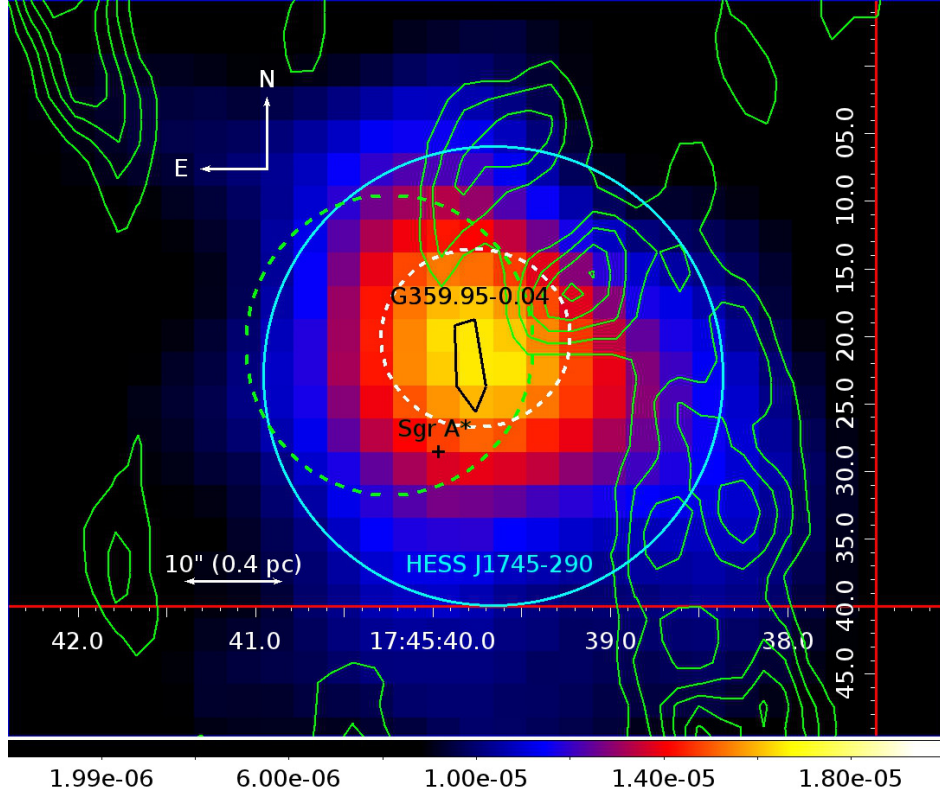
Figure 1.6: *NuSTAR* X-ray map of the central 3 arcminutes of the GC from Mori et al., 2015. The black polygon marks the PWN candidate G359.95-0.04, and the white dashed circle shows the 90 % confidence level (including statistical and systematic errors) for the position of the associated point source in the 20–40 keV band. The cyan dashed circle shows the centroid position of HESS J1745–290, and the green dashed circle shows the centroid position of the CHXE. The green solid lines are millimeter-waveband contours of HCN and HCO$^+$ line emission ($J = 1 - 0$) from the circumnuclear disk.

For more than 15 years of observing, Sgr A* has exhibited persistent and relatively frequent X-ray flaring of varying levels of intensity (Ponti et al., 2015). Flaring in the 2–10 keV range was seen by *Swift*, which observed Sgr A* quasi-daily in an observing campaign

that spanned from February 2006 to October 2011 (Degenaar et al., 2013). During this time, *Swift* observed six bright flares of $L \gtrsim 10^{35}$ erg/s , and constrained the occurrence of bright flares to be $\simeq 0.1$–0.2 flares/day. The timescales of flares were between 5 minutes and a few hours, and the total observation time was 0.8 Ms. Unfortunately, no gamma-ray observations were taken on the same night as any of these flares. Soon after, in 2012, *Chandra* conducted a campaign between February and October, observing the GC 38 times for a grand total of ≈ 3 Ms (Neilsen et al., 2013), also in the 2–10 keV band. In that time, 39 X-ray flares were detected, with luminosities ranging from 10^{34} to 2×10^{35} erg/s, exceeding the quiescent state by a factor of about 10. The brightest flare ever observed, which occurred during this campaign, had a luminosity of $L \approx 5 \times 10^{35}$ erg/s (Nowak et al., 2012). The durations ranged from $\mathcal{O}(100\,\mathrm{s})$ to $\mathcal{O}(8\,\mathrm{ks})$,[1] and they occurred with a frequency of about one per day. Of the nights with flaring, VERITAS had taken data for two of them, Modified Julian Date (MJD) 56047.7 and 56066.4. VERITAS did not detect any significant changes to its flux level for these observations (Archer et al., 2014). This is consistent with a previous simultaneous observation taken with *Chandra* and H.E.S.S. in 2005 (Aharonian et al., 2008), where an X-ray flare showed no increase in TeV flux. *NuSTAR* also conducted a campaign in the middle of 2012, detecting four medium-intensity flares lasting less than an hour (Barrière et al., 2014). Their spectrum was measured up to 79 keV, and is included in Figure 3.10. Time-varying X-ray emission has also been detected in the surrounding diffuse areas in the CMZ, particularly in Sgr B2 (Terrier et al., 2010; Clavel et al., 2012). IR flares are found to occur ~ 4 times as frequently as X-ray flares, and every X-ray flare coincided with an IR flare (Ponti et al., 2015).

The periapse passage of the mysterious gas cloud G2 sparked much scientific interest and motivated several campaigns with the hope that a great amount of variability or flaring would be seen, as many of the models for emission involve mass accretion. Although no clear increase in variability was seen, there were several strong flares detected shortly after the passage by *XMM-Newton* (Ponti et al., 2015). VERITAS attempted to observe during this time, but was unfortunately unable to operate due to bad weather.

---

[1] $\mathcal{O}$ denotes "on the order of".

Using high-resolution images from *VLA* and spectroscopic data from *Chandra*, Li et al. (2013) found potential evidence for a jet, or a collimated stream of relativistic particles that are often found flowing from quasars or from the active galactic nuclei (AGNs) of radio galaxies. They associate the X-ray feature G359.944-0.052 with a radio shock front in the eastern arm of Sgr A West. Their hypothesis is that the jet has a sharp momentum peak along the rotation axis of the Galaxy, and ultrarelativistic electrons are created by the shock and subsequently create synchrotron radiation that is seen as G359.944-0.052. Although this is an interesting possibility, no jet has yet been definitively distinguished from Sgr A*, and if it does exist, we do not know its orientation. It is believed that jets orient with the axis of accretion flow, but this is not guaranteed to be the case. While VERITAS does not have the ability to distinguish the structure of jets, variability in the emission near Sgr A* would support the idea of a semi-active black hole, which could indicate the presence of jets.

1.2.5   Gamma Rays

Gamma rays are defined as any photons having greater than $\approx 100\,\mathrm{keV}$ of energy. Early observations of the GC were performed by *Energetic Gamma Ray Experiment Telescope (EGRET)*, which was a space-based telescope equipped on NASA's *Compton Gamma Ray Observatory* satellite. It was designed to directly detect gamma rays in the energy range from $30\,\mathrm{MeV}$ to $30\,\mathrm{GeV}$. Bertsch et al. (1998) found strong emission above $500\,\mathrm{MeV}$ within a $0.2°$ circle around the GC. The emission profile was found to be consistent with a point source, and was given the name 3EG J1745–2851. The analysis of *EGRET* data showed a broken spectrum, with a hard index of ≈ -1.30 below, and a soft index ≈ -3.1 above the break energy of $1900\,\mathrm{MeV}$. Later analysis in Nolan et al., 2003 found that the position of 3EG J1745–2851 was actually not consistent with the center of the Galaxy, and found evidence that its flux may have a small variability. Pohl (2004) confirmed the offset, finding a best fit position of $l = 0.11°$ and $b = -0.04°$, but found no evidence of flux variability above a level of $30\,\%$. Its position was consistent with Sgr A East, however its luminosity in this energy range is almost two orders of magnitude greater than any other SNR detected by *EGRET* (Fatuzzo & Melia, 2003).

NASA's space-based gamma-ray instrument the *Fermi*-Large Area Telescope (LAT) has a detection range from 20 MeV to 300 GeV. Its field of view (FoV) is large enough to observe the entire GC region at once. The emission observed by *Fermi*-LAT is mostly due to nonthermal bremsstrahlung, which occurs when high-energy (GeV) electrons interact with gas particles. *Fermi* detected a strong point source associated with the GC. It is published as J1745.6–2859c in the third *Fermi*-LAT source catalog (3FGL) (Fermi-LAT Collaboration et al., 2015a). Because the angular resolution of the *Fermi*-LAT is about 0.15° above 10 GeV, this source cannot be distinguished from Sgr A East. In the first *Fermi*-LAT Inner Galaxy point source Catalog (1FIG) (Fermi-LAT Collaboration et al., 2015b), the central source is named 1FIG J1745.5-2859.

Fermi-LAT has detected two large "bubbles" that originate at the GC, creating a shape similar to a filled-in figure eight (Su et al., 2010). They extend 50° in latitude above and below the Galactic disk and have a maximum width of about 40° in longitude. They could be evidence of an extremely energetic event occurring on the order of 10^7 years ago. Examples could be nuclear starburst activity or a massive accretion event (Su et al., 2010). The spectrum they observed was hard, with an index of $\alpha \approx -2$, and was very consistent across the entire extent of both bubbles. They note that this is harder than the spectrum created by inverse Compton (IC) scattering. They also found a spatial correlation between the bubbles and the *Wilkinson Microwave Anisotropy Probe* (*WMAP*) haze, and between the edges of the bubbles and *ROSAT* X-ray emission in the 1.5–2 eV range. Yang et al. (2012) found evidence for jets in the Fermi bubbles that was supported by 3D magnetohydrodynamic simulations, however this is considered controversial by some. The Fermi bubbles are fascinating features that indicate past activity, but they are very large and difficult for VERITAS to study.

1.2.6   Very High Energy Gamma Rays

The Galactic Center was first detected at very high energies ($E > 100$ GeV) in 2004 with the CANGAROO-II imaging atmospheric Cherenkov telescope (IACT) (Tsuchiya et al., 2004). They observed gamma rays having energies above a threshold of 250 GeV up to
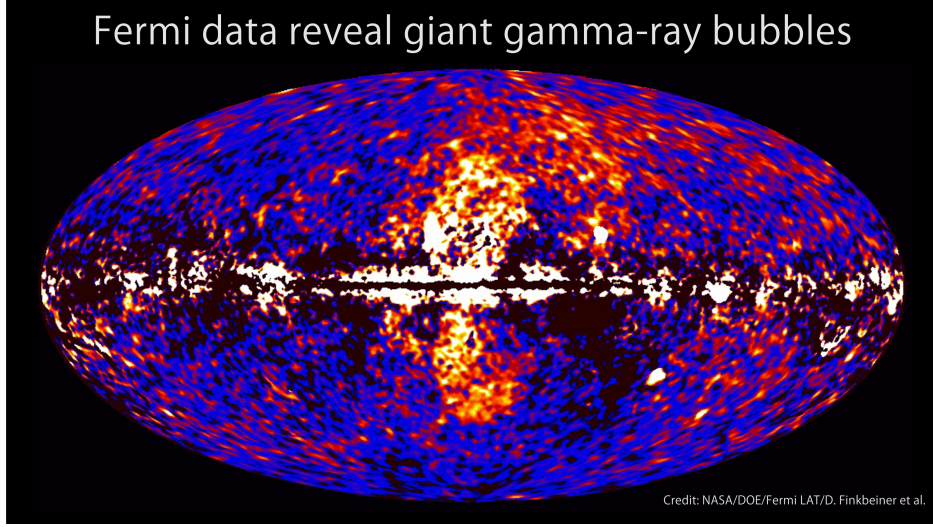
Figure 1.7: *Fermi*-LAT skymap of the Galactic plane at 1–10 GeV, showing the bubbles extending from the Galactic Center ridge. The *Fermi* bubbles extend over 50 degrees north and south in Galactic longitude.

2500 GeV. The detected GC spectrum was very soft, with a differential spectral flux of $\frac{dN}{dE} \propto E^{-4.6\pm0.5}$. The integral flux was about an order of magnitude lower than that of the Crab Nebula. The position was consistent with that of the *EGRET* source 3EG J1745–2851 to within CANGAROO's systematic uncertainty of 0.1°. Shortly thereafter, a signal of even higher energy, just above the CANGAROO energy of 2.5 TeV, was seen by the *Whipple* 10 m gamma-ray telescope at the Fred Lawrence Whipple Observatory (FLWO), which now hosts VERITAS. However, with only 26 hours of observing data, the statistical significance only reached 3.7 standard deviations or 3.7σ, not meeting the typical requirement of 5σ to be considered a firm detection (Kosack & VERITAS, 2004). In that same year, H.E.S.S. achieved the definitive detection in the TeV range of the GC, giving the source the name H.E.S.S. J1745–290 (Aharonian et al., 2004). The detected GC source had an energy range extending from 165 GeV to nearly 10 TeV, giving it the highest-energy spectral points at that time. However, H.E.S.S.'s spectrum differed greatly from that of CANGAROO, with a substantially harder index of 2.21 ± 0.09 in the same energy range. It was also much harder than the spectrum observed by *EGRET*. There was also a disagreement in flux, with CANGAROO and *EGRET* finding fluxes much higher than H.E.S.S. H.E.S.S. is considered to

be the more accurate measurement at very high energies. The H.E.S.S. result was supported by a subsequent detection by the Major Atmospheric Gamma Imaging Cherenkov (MAGIC) telescope system (Albert et al., 2006). Their spectrum of 2.2 ± 0.2 was almost identical to H.E.S.S. and had a statistical significance of $7.3\,\sigma$. The flux MAGIC observed was consistent with the H.E.S.S. flux within the uncertainties.

More recently, the GC has been detected and studied by VERITAS, with the first publication coming from data taken between 2010 and 2014. Archer et al. (2014) found the position of J1745–290 to be $\ell = -0.077° \pm 0.006°_{\text{stat}} \pm 0.013°_{\text{sys}}$ and $b = -0.049° \pm 0.003°_{\text{stat}} \pm 0.013°_{\text{sys}}$ in Galactic coordinates. The full skymap with the signal from J1745–290 subtracted out can be seen in Figure 1.8. Since then, H.E.S.S. (Aharonian et al., 2006a) and VERITAS have continued to study the GC region, improving results with hardware upgrades, more observational data, and advanced analysis techniques. There are several other known VHE sources within the field of view (FoV) of the GC for both VERITAS and H.E.S.S. G0.9+0.1 is a very strong and distinct composite SNR located just within a degree of the GC, detected first by H.E.S.S. (Aharonian et al., 2005), then also by VERITAS (Smith, 2015). H.E.S.S. also detected two sources farther in the west. One of these sources is HESS J1745–303, which is thought to be a SNR with an associated MC (Aharonian et al., 2006b). The other is a strong, extended source HESS J1741–302 (Tibolla et al., 2008), which is currently considered to be unidentified. These last two sources have not been detected by VERITAS, although there does seem to some signal near their H.E.S.S. locations. Perhaps the most intriguing and challenging is a source, or possibly sources, very near to Sgr A*. H.E.S.S. found a very strong, unidentified point source, HESS J1745–285, within 0.2° of Sgr A*, whose signal is only exceeded by Sgr A* (Lemiere et al., 2015). VERITAS reported seeing extended emission that peaked near the H.E.S.S. position of this source but offset by about 0.1° (Archer et al., 2016). The most recent results will be covered in Chapter 3.
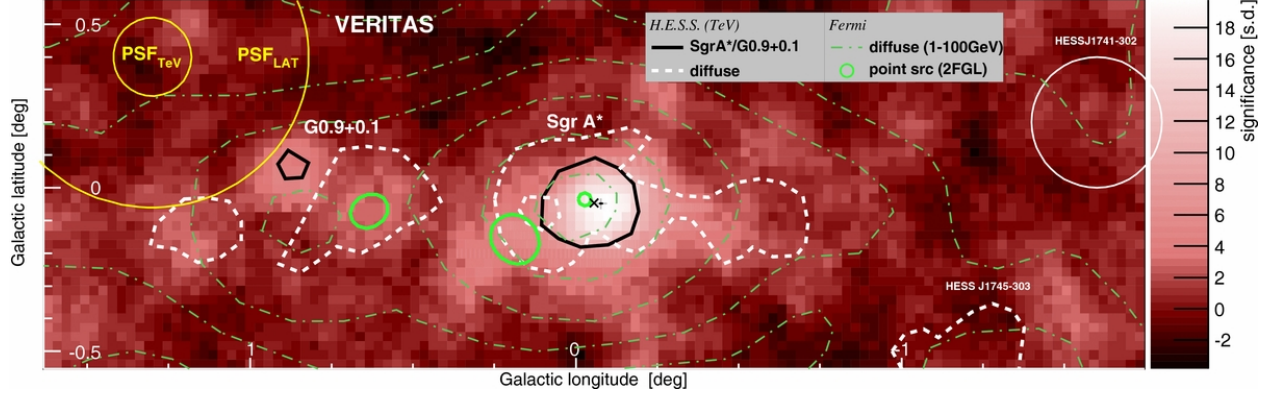
Figure 1.8: A significance skymap of emission above 2.5 TeV in the GC region using VERITAS data taken between 2010-2012 (Archer et al., 2014). The position of Sgr A* is noted by the black ′x′. The green contour lines indicate the 1–100 GeV diffuse emission from *Fermi*-LAT. The other sources, HESS J1741–302 and J1745–303, will be described later in the text (Subsection 7.5.3).

1.2.6.1 VHE Source Summary

As can be seen in Figure 1.8, the VERITAS skymap from Archer et al., 2014 with J1745–290 and G0.9+0.1 subtracted, there are a wealth of sources in the GC that emit in the VHE range in addition to the central point source consistent with the position of Sgr A*. Present throughout the CMZ are regions of diffuse emission that are very strong close to the Galactic center and along the Galactic disk. The strongest diffuse region is the extended emission from the direction of the MC Sgr B2. The morphology of extended diffuse emission is not fully understood, but is thought to be correlated to molecular gas (Aharonian et al., 2006a). This is because the emission may be caused by interactions between cosmic rays and molecular particles.

Both H.E.S.S. and VERITAS detected strong, unidentified sources very close to Sgr A*. HESS J1745–285 was detected above the CMZ at a level of 6σ by H.E.S.S., about $0.23°$ away from Sgr A* (Lemiere et al., 2015). This source has an X-ray counterpart and it lies between the NRFs of the Radio arc. VERITAS saw an excess coming from Galactic latitude $\ell = 0.055° \pm 0.01°_{\mathrm{stat}} \pm 0.013°_{\mathrm{sys}}$ and Galactic longitude $b = -0.148° \pm 0.01°_{\mathrm{stat}} \pm 0.013°_{\mathrm{sys}}$ about $0.1°$ from the position of HESS J1746–285, and named it VER J1746–289 (Archer

21

et al., 2016). These pointings are both close enough to the source that their signal cannot be fully distinguished from that of Sgr A* given the large systematic uncertainties of the VERITAS and H.E.S.S. positions. It is of great interest whether this emission is from an active source or a passive source like diffuse emission. This could possibly indicate that GC sources share a common cosmic ray source. The source G0.9+0.1, which is an SNR / PWN, has been strongly detected first by H.E.S.S. and later by VERITAS. Finally, in the direction of negative Galactic longitude are two extended H.E.S.S. sources J1741–302 and J1745–303.

1.3   Dissertation Outline

In this dissertation I present my research on the VHE emission from the GC with VERITAS data. My primary focus is on the strong central source and the diffuse emission along the GC ridge. I also investigate the possibility of a PeVatron accelerator of cosmic rays. In the next chapter, I explain the relevant astrophysics of CRs and the mechanisms by which they create gamma rays. Then I compare and contrast the most popular models of VHE emission from the unidentified central point source J1745–290 as well as the diffuse emission. I detail the VERITAS instrument as well as the technique it uses to detect and record gamma-ray events. I outline both the standard steps of data analysis and the advanced techniques I developed to deal with the difficulties of the region and its data. Finally, I present my results on the morphology, spectrum, and variability of the emission and discuss its implications on the potential emission models.

CHAPTER 2

Very High Energy (VHE) Astrophysics

In order to fully understand the information that emission at different energies tells us about sources, we must understand the processes that lead to and create that emission. Astrophysical objects and events are capable of accelerating cosmic ray particles to high energies, up to and exceeding 10^{21} eV in some cases. These CRs diffuse into their surrounding environment, where they interact with other particles and fields, creating electromagnetic radiation. These accelerated primary CRs are capable of creating VHE gamma rays through various interactions with the ISM and cosmic microwave background (CMB) photons in the Galaxy. There are a few primary physical mechanisms capable of creating gamma rays, and one or more of them can fit into a broader emission model for any source. In this chapter, I discuss the physics behind cosmic ray and gamma ray production.

2.1   Cosmic Rays

Cosmic rays are charged particles that are accelerated to the highest energies known in the universe and permeate the Galaxy. They were first discovered in 1912 by Victor Hess, for which he was awarded the Nobel Prize in Physics in 1936. Their origin is one of the greatest and most long-standing questions in astrophysics. The mechanism responsible for creating them must be capable of outputting an extremely large amount of energy, and must have the proper composition of particles to match observations. There are a number of physical mechanisms for particles to reach high energies in settings such as the GC. We can also better understand the diffuse emission around a potential source of CRs if we accurately model the diffusion process. In this section, I discuss the mechanisms that are understood to

be capable of accelerating charged particles to TeV energies, and the equation that dictates particle diffusion.

The composition of CRs is about $90\,\%$ protons, $9\,\%$ helium nuclei, and less than $1\,\%$ heavier atoms and electrons. Because of energy losses to the ISM, CR particles have a typical lifetime of about 10^7 years (Longair, 2011). The Galaxy, on the other hand, but is about 1.35×10^{10} years old (Carollo et al., 2016), so the current population of CRs could not have been created in a single burst event. The total luminosity of CRs in the Galaxy can be estimated by

$$L_{\mathrm{CR}} = \frac{V \rho_E}{\tau_{\mathrm{r}}} \tag{2.1}$$

where V is the volume of the Galactic disk, ρ_E is the average energy density, and τ_{r} is the characteristic residence time of a CR particle in the disk. Using estimates for each parameter, the total CR luminosity was found to be about 5×10^{40} erg/s (Berezinskii et al., 1990; Dogiel et al., 2002). Not many astrophysical sources are energetic enough to achieve such a high luminosity, but Galactic supernovae output 10^{41}–10^{42} erg/s, making them a potential source of CRs in the Galaxy.

2.1.1 Fermi Acceleration

Fermi acceleration is the acceleration of charged particles by repeated reflections against a magnetic mirror or a rapidly moving shock front. There are two types of Fermi acceleration, first order and second order, each of which occurs in a different physical context and results in a different energy spectrum of accelerated particles.

2.1.1.1 2nd order

The original mechanism, now called second order Fermi acceleration, was hypothesized by Enrico Fermi (1949) as the acceleration mechanism for cosmic rays. He pictured the fast, streaming motion of particles in low-density regions of interstellar media. With these streams of particles move strong magnetic fields through the highly conductive ISM. These magnetic field lines will exhibit jagged and randomized patterns, rather than aligned patterns which

24

would require a great increase in the magnetic energy. He referred to the large inhomogeneities (sharp changes) in the magnetic field as magnetic mirrors, because particles reflect upon collision with them. An illustration of this process is shown in Figure 2.1a. Upon each reflection, a particle with energy E changes its energy by

$$\Delta E = E \left[2\beta_{\text{cloud}} \beta_{\text{particle}} \cos \theta + 2\beta_{\text{cloud}}^2 \right] \tag{2.2}$$

where $\beta = \frac{v}{c}$ is the velocity expressed as a fraction of the speed of light, and θ is the angle between the particle velocity and the line of force from the mirror (Longair, 2011). This results in an energy gain for head-on collisions, as is the case for both Newtonian and relativistic kinematics. Conversely, the particle will lose energy in collisions in which the particle overtakes the magnetic mirror. However, the probability of a collision depends on the angle of approach θ and is proportional to

$$1 + \beta_{\text{cloud}} \cos \theta. \tag{2.3}$$

Hence, head-on collisions are more likely than overtaking collisions. Integrating the probability of a collision multiplied by the energy change over θ from 0 to π gives the expectation value of the energy change for a single collision of

$$\left\langle \frac{\Delta E}{E} \right\rangle = \frac{8}{3} \beta_{\text{cloud}}^2 \tag{2.4}$$

which is an overall energy gain proportional to the second order of β_{cloud}. To find the energy spectrum, this energy gain can be plugged into the steady-state diffusion-loss equation (2.15) with no source term and the lifetime set equal to the characteristic time of escape from the acceleration region τ_{esc}. The resulting energy spectrum is

$$\frac{dN(E)}{dE} = -\left(1 + \frac{1}{\alpha \tau_{\text{esc}}} \right) \frac{N(E)}{E} \tag{2.5}$$

where $\alpha = \frac{8}{3} \beta_{\text{cloud}}^2$ is the proportional energy gain. Integrating gives

$$N(E) \propto E^{-1 - (\alpha \tau_{\text{esc}})^{-1}}. \tag{2.6}$$

(a) 2nd order Fermi acceleration.

(b) 1st order Fermi acceleration.
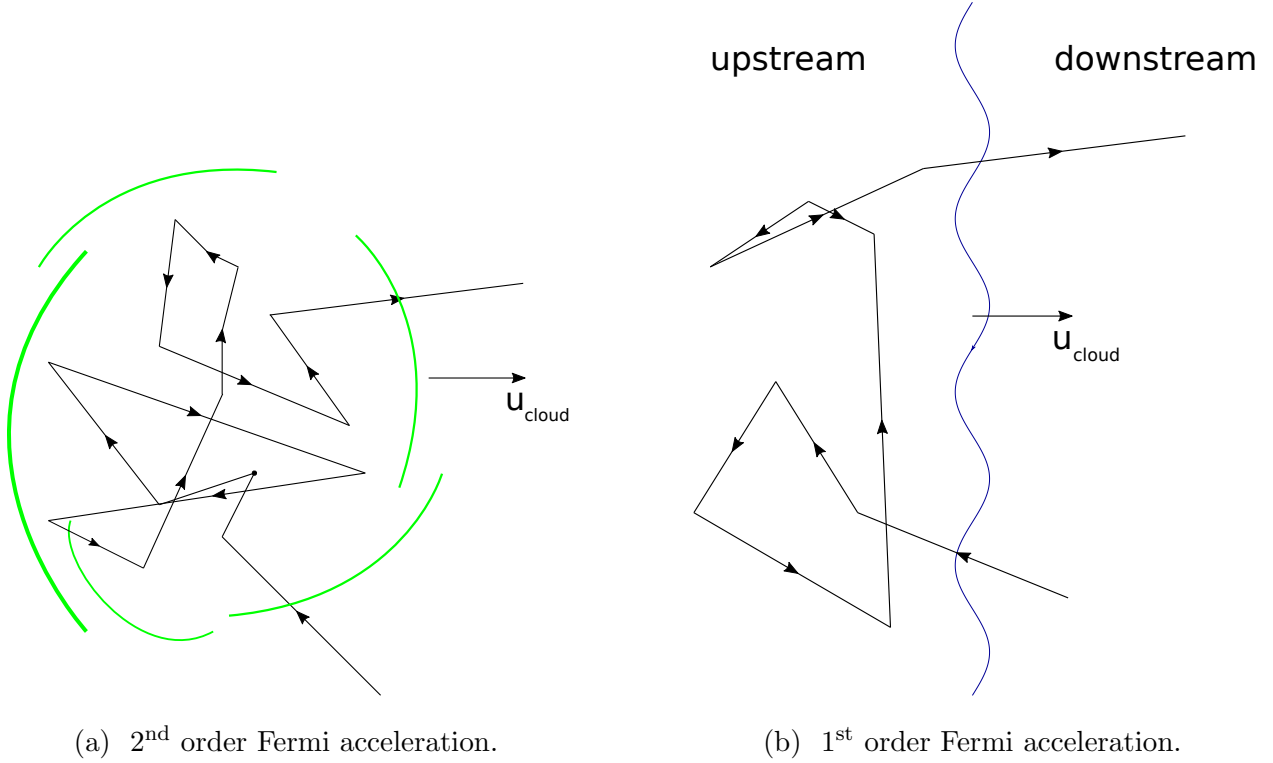
Figure 2.1: Illustrations of both mechanisms of Fermi acceleration. First order shock acceleration across a shock front is shown in (b). Second order Fermi acceleration in a moving cloud is shown in (a). The path of the accelerated particle is shown by arrows.

The injection problem It must be noted that because of ionization losses, particles can only experience a large net gain in energy if their initial energy is above a critical energy[1], so that the average gain in energy over time exceeds the rate of ionization loss (see Figure 2.2). Fermi (1949) addresses the issue of how protons and heavier nuclei are injected into the above-described accelerator with a critical energy. He proposes a scenario of regeneration where high-energy protons collide with low-energy protons, yielding a 'spray' of mesons and two nucleons; some fraction of those nucleons are protons above the so-called injection threshold. However, it is still not known how the first population of particles achieve high enough energy to begin this cycle (Balogh & Treumann, 2013).

---

[1]Fermi estimated this critical energy of acceleration for typical interstellar (medium) conditions is about 200 MeV.

2.1.1.2 1$^{\text{st}}$ order

A more recent and prominent version of Fermi acceleration occurs near the fronts of shock waves. It is called "diffusive shock acceleration," or first order Fermi acceleration, because the energy gain is proportional to the first power of the speed of the shock front, rather than the second order in magnetic clouds. Shock fronts emanating from supernovae, for example, contain magnetic fields with strong gradients similar to those involved in second order Fermi acceleration that move along with the rapid velocity speed of the shock. First order Fermi acceleration can occur when a charged particle experiences successive reflections upstream and downstream across a diffusive shock wavefront, as pictured in Figure 2.1b. They will experience head-on collisions that cause acceleration, and thus they gain in energy with every reflection.
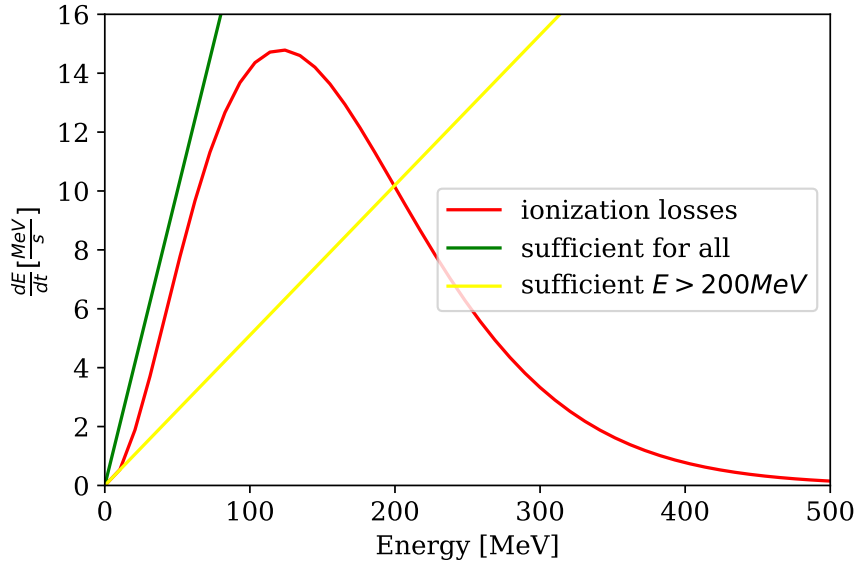
Figure 2.2: Plot of change in energy with respect to time versus energy for the cases of a particle gaining energy under Fermi acceleration, and for ionization loss. For particles to overcome ionization losses completely, they must either be accelerated by a sufficiently strong accelerator (green), or they must be injected with energies for which the energy gain exceeds the energy loss. For the yellow line, this means the particle would need to be injected above the intersection with the energy loss curve at 200 MeV.

The resulting energy spectrum of first order Fermi acceleration is derived in Longair, 2011. If, on average, the energy is multiplied by a factor $b > 1$, after k collisions the particle would have on average

$$E = E_0 b^k \tag{2.7}$$

We assume upon each reflection, the particle has a probability P of escaping and a complementary probability of remaining within the confines of the shock front. The number of particles remaining N, after an initial N_0 particles each go through k reflections is

$$N = N_0 P^k \tag{2.8}$$

Combining Equations 2.7 and 2.8 after substituting out k,

$$\frac{\ln(N/N_0)}{\ln(E/E_0)} = \frac{\ln P}{\ln b} \tag{2.9}$$

$$\frac{N}{N_0} = \left(\frac{E}{E_0}\right)^{\ln P/\ln b} \tag{2.10}$$

leads to

$$N(E)\, dE = C E^{-1+(\ln P/\ln b)} dE, \tag{2.11}$$

which in differential form is:

$$\frac{dN(E)}{dE} \propto E^{(\ln P/\ln b)-1} \tag{2.12}$$

where $N(E)$ is the number of particles with energy greater than or equal to E. This equation can be identified with Equation 2.5 if

$$\ln P/\ln b = -\left(\alpha \tau_{\mathrm{esc}}\right)^{-1} \tag{2.13}$$

where P and τ_{esc} are related, as are b and α. A population of particles undergoing this process will have a resultant energy spectrum described by

$$\frac{dN}{dE} = E^{-\alpha} \tag{2.14}$$

where the spectral index $\alpha \gtrsim 2$ depends on the shock's compression ratio.

Diffusive shock acceleration of electrons has been observed in the heliosphere (Baring, 1997) and in Earth's foreshock transients (Liu et al., 2017).

2.1.2 Cosmic Ray Diffusion

As we have discussed, cosmic rays are only accelerated to high energies under certain conditions, yet cosmic ray populations pervade the Galaxy. Diffusion is the process by which particles of different species, such as cosmic ray protons, spread out from their original source into the ISM or MCs. On the microscopic scale, the motion of an individual particle is randomized by scattering due to irregularities in the magnetic field, but the collective motion of particles of a particular species is determined by the properties of that species and the material through which the particles diffuse. The distribution of particles undergoing diffusion can be described by a standard differential equation, the diffusion-loss equation:

$$\frac{dN(E)}{dt} = \frac{\partial}{\partial E}\left[b(E)N(E)\right] + Q(E,t) + D\nabla^2 N(E) \tag{2.15}$$

where N is the particle number density per unit volume, $D\nabla^2 N(E)$ is the diffusion term, Q is the injection rate per unit volume, and $b(E) = -dE/dt$ is the energy loss term (Ginzburg & Syrovatski, 1964). When discussing high-energy cosmic ray protons, inelastic hadronic collisions will destroy some particles and create others (see Subsection 2.3.4), changing the particle species composition. Longair (2011) writes the diffusion-loss equation for a specific species, denoted by i, and adds terms to account for these effects:

$$\frac{\partial N_i}{\partial t} = D\nabla^2 N_i + \frac{\partial}{\partial E}\left[b(E)N_i(E)\right] - \frac{N_i}{\tau_i} + Q_i + \sum_{j>i}\frac{P_{ji}}{\tau_j}N_j \tag{2.16}$$

where N_i is number density of species i, τ_i is its characteristic lifetime, and P_{ij} the probability of species i being created in an inelastic collision that destroys a nucleus of species j.

To characterize diffusion at the GC, the H.E.S.S. collaboration (Abramowski et al., 2016) use a well-known steady-state solution from Atoyan et al. (1995). They begin the derivation with the spherically symmetric form of Equation 2.15, using the standard diffusion approximation of neglecting convection by setting $\vec{V} = 0$ (Ginzburg & Syrovatski, 1964),

$$\frac{\partial n}{\partial t} = \frac{D}{r^2}\frac{\partial}{\partial r}r^2\frac{\partial n}{\partial r} + \frac{\partial}{\partial E}\left(bn\right) + Q \tag{2.17}$$

where Q is the source term, r is the radial distance from the source, and D is the diffusion coefficient. In the steady state, the time derivative of the distribution function $\frac{\partial n}{\partial t} = 0$. The

homogeneous ($Q = 0$) solution is simple, but Equation 2.17 can be solved for an arbitrary energy spectrum of injection $Q = \Delta n (E)$. They start with an assumed initial uniform distribution of cosmic rays within a source of radius r_s, so n_0 is described by the density multiplied by the Heaviside step function $H (r_s - r)$. The equation is then put into a more readily solvable form by performing mathematically advantageous variable changes. Imposing initial conditions and taking the limit $r_s \to 0$, they attain the Green's function for the differential equation. The integral over the injection time leads to the stationary distribution function for an arbitrary injection spectrum $\Delta n (E)$. The energy loss term b can be broken into parts for ionization losses (b_0), bremsstrahlung losses ($b_1 \gamma$), and synchrotron and inverse Compton losses ($b_2 \gamma^2$), such that

$$b (\gamma) = b_0 + b_1 \gamma + b_2 \gamma^2$$

(see Section 2.3). In this instance, b is given in terms of the Lorentz factor $\gamma = \frac{1}{\sqrt{1-v^2/c^2}}$ rather than E to keep the units of all b terms consistent. For time scales of $t < 10^7$ yr, only synchrotron and Compton energy loss terms are non-negligible. These are accounted for in the $b_2 \gamma^2$ term. For a more specific solution, they assume the source follows a power law distribution of $\Delta n = \Delta n_0 E^{-\alpha}$ and the diffusion coefficient has a power-law dependence on energy $D \propto E^\delta$. For the case of burst-like injection with $t_{\text{injection}} \ll t_{\text{observation}}$, the electrons will be distributed as a power law distribution with an increased exponent

$$\alpha' = \alpha + \frac{3}{2}\delta.$$

Atoyan et al. (1995) also find a qualitatively different result for the case of continuous injection. Abramowski et al. (2016) use this result to find the radial distribution function w of cosmic rays in the CMZ assuming a central accelerator injects particles continuously at the rate $\dot{Q}_p (E)$. The cosmic ray density for protons as a function of r is

$$w_{\text{CR}} (E, r, t) = \frac{\dot{Q}_p (E)}{4 \pi D (E)} \text{erfc} \left(\frac{r}{r_{\text{diff}}} \right) \tag{2.18}$$

where $D (E)$ is the diffusion coefficient, and $r_{\text{diff}} \approx \sqrt{4Dt}$ is the diffusion radius, applicable when $t < t_{pp} \approx 5 \times 10^4 \left(\frac{n}{10^3} \right)^{-1}$ yr.

Understanding diffusion is important because cosmic rays can interact with diffuse clouds of molecular matter, creating secondary cosmic rays and gamma rays. These interactions are more likely in regions with high-density MCs, and diffuse gamma-ray sources can be seen if the population of primary cosmic rays and molecular material are dense enough. I discuss the occurrence of this in the GC ridge in Section 3.1. A more complete version of the diffusion equation with additional terms to increase accuracy of the model can be found in Strong et al., 2007. In applications where a solution cannot be found, software such as the GALPROP (Galactic propagation) code can be used to perform numerical computations for simulating the propagation of relativistic particles and the emissions produced therein (Strong & Moskalenko, 1998).

2.1.3 Cosmic Ray Flux

The flux of charged cosmic rays reaching Earth is, to our knowledge, mostly isotropic (Bird et al., 1993), due to the bending of their trajectories by intergalactic magnetic fields. Its isotropy, as well as its composition, are the main clues to its origin. The majority of the flux of cosmic rays reaching Earth are protons or heavier nuclei. Their mass to charge ratio is higher than that of electrons, allowing them to maintain a kinetic energy that is higher relative to their radiative losses, which are proportional to charge. The proportion of cosmic ray electrons reaching Earth is much smaller, peaking at around 1–2 % at a few GeV and decreasing with energy (Hillas, 2006). The presence of electrons can be inferred from synchrotron radiation in regions with large magnetic fields. In even smaller proportion are secondary gamma rays, which are created when the primary cosmic rays interact with molecular material. The proportion of the background gamma-ray flux to that of hadronic cosmic rays is estimated to be smaller than modern instruments' best sensitivities, about $\frac{I_\gamma}{I_h} = 10^{-5}$ in the 10–100 TeV range according to Halzen et al., 1990. In the energy range 200–500 TeV, Sasano (1999) placed an upper limit on this proportion of 3×10^{-3} at a confidence level of 90%. Upper limits for multiple experiments in different energy ranges can be found in Ong, 2006.

The origin of CR acceleration is mysterious and could come from a mix of Galactic and

extragalactic sources. The gamma-ray sources mentioned above (Subsection 2.2.1) could all be potential accelerators that contribute to the population of CRs. Another main clue to narrowing the putative sources of cosmic rays are the energy spectra of different cosmic ray particles. A set of cosmic ray spectra covering 1 to 10^{11} GeV reaching Earth is shown in Figure 2.3. The all-particle flux spectrum follows a power law with a consistent index across many experiments, which holds above 10 GeV until a point called the "knee" around 3 PeV. First order Fermi acceleration is adequate to explain the spectrum up to the knee. The differential flux intensity in this range is

$$\frac{dN}{dEd\Omega}(E) \approx 1.8 \times 10^4 \left(E/1\,\text{GeV}\right)^{-\alpha} \frac{\text{nucleons}}{m^2 \cdot s \cdot sr \cdot GeV} \tag{2.19}$$

where $\alpha \approx 2.7$ is the differential spectral index and $\alpha - 1$ is the index of the integral spectral flux J (Tanabashi et al., 2018). The spectrum softens after the knee, possibly because that energy is the maximum energy that many Galactic sources can achieve. This is either because of a physical acceleration limit or rigidity dependent escape from the Galaxy; higher energy CRs are likely to be created by extragalactic sources.

After the knee there appears to be a "second knee", after which the spectrum softens again, and then an "ankle", after which the spectrum hardens. There is a sharp cutoff after 10^{20} eV as particles approach the Greisen–Zatsepin–Kuzmin (GZK) limit (Greisen, 1966; Zatsepin & Kuz'min, 1966), which is due to proton-photon interactions between CRs and the CMB that result in pion production. The most energetic cosmic rays ever detected had energies of about 3×10^{20} eV (Bird et al., 1993; Yamamoto & for the Pierre Auger Collaboration, 2007), close to the energy of a baseball traveling over 50 km/hr. The scope of this dissertation is restricted to Galactic sources and energies up to the knee.

We can also determine if other parameters, such as magnetic field strengths, are adequately strong. The Hillas criterion (Hillas, 1984)

$$E_{\text{max}} = (\beta_{\text{shock}})qBR \tag{2.20}$$

puts an upper limit on the energy of a particle with charge q that can be achieved by a candidate accelerator of size R, with magnetic flux density B (Ptitsyna & Troitsky, 2008). A
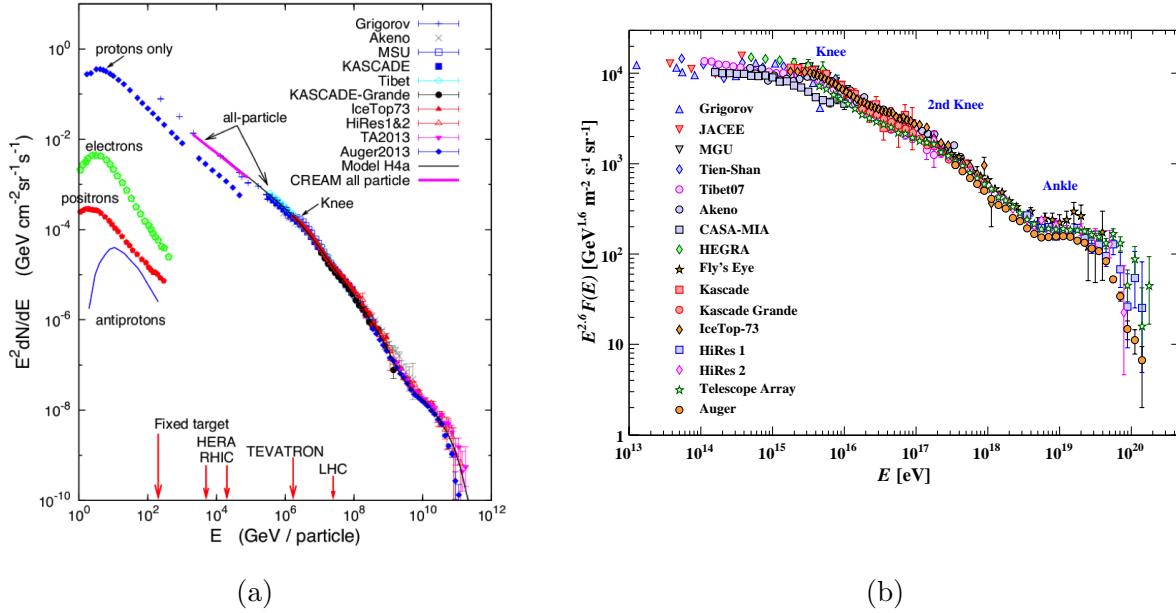
Figure 2.3: The cosmic ray flux spectrum of all particles as measured by multiple experiments on Earth. The full energy range is shown in (a) (Blasi, 2013). Figure (b) shows an expanded view of the flux around and above the knee (Tanabashi et al., 2018).

Hillas plot shows the line required to achieve a specified energy in relation to the limits for various sources. A recent Hillas plot for is shown in Figure 2.4, with the lower boundary of the Hillas criterion for 10^{20} eV protons drawn in blue. Galactic CRs are believed to originate in the shock waves of SNRs, but SNRs may only be able to explain acceleration up to the knee (Weekes, 2003). Candidates for ultra high-energy cosmic ray accelerators above the knees are typically extragalactic and include active galaxies.

The average energy density of CRs in the Galaxy is roughly $1\,\mathrm{eV/cm^3}$ (Blasi, 2013). A key consideration in determining the source of cosmic rays is whether the overall energetics of the proposed acceleration mechanisms output enough energy to create the populations we observe. As previously stated, SNRs are abundant in the Galaxy and their total luminosity is sufficient to provide the CR luminosity, requiring only a kinetic energy conversion efficiency of 1–10 %. According to Helder et al. (2009), only three SNRs would be required per century if their conversion efficiency is 10 %. Great progress has been made recently in establishing
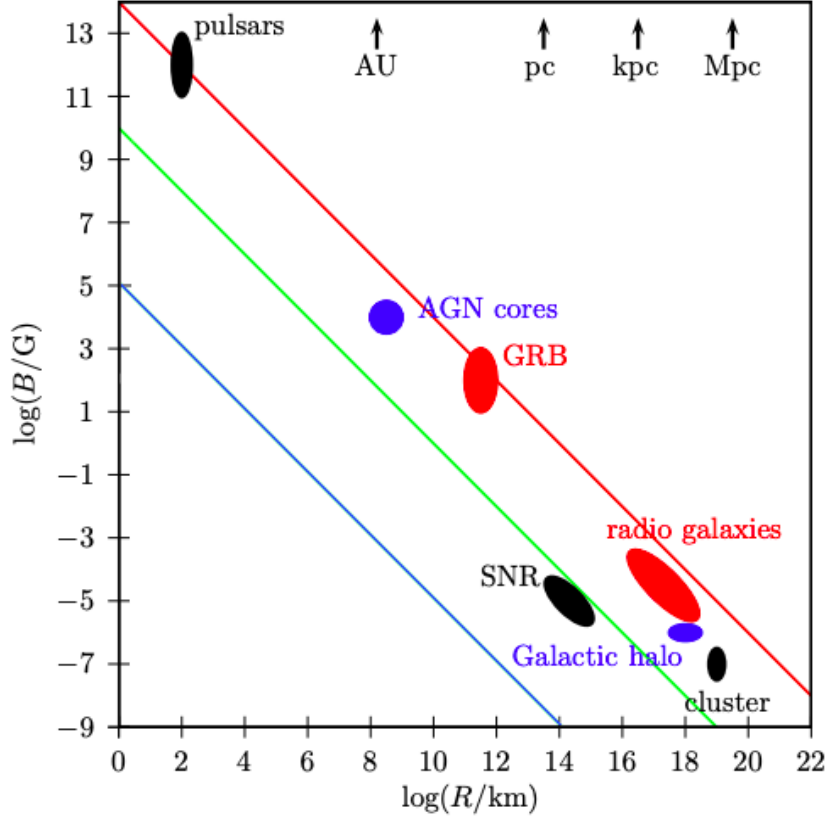
Figure 2.4: Hillas plot showing the magnetic field versus size for candidates of cosmic ray acceleration. The lines are the lower boundaries of the Hillas criterion for 10^{21} eV protons (red), 10^{20} eV iron nuclei (green), and 1 TeV protons (blue) (Bustamante et al., 2009). SNRs are the only Galactic source capable of accelerating TeV protons.

SNRs as the main theoretical source of Galactic cosmic rays. Evidence of hadron acceleration via diffusive shock acceleration has been seen by *Fermi*-LAT in Tycho's SNR G120.1+1.4 (Morlino & Caprioli, 2011), as well as W44 and IC 443 (Fermi-LAT Collaboration et al., 2013). The power-law index of diffuse shock acceleration is also consistent with SNRs. However, the expected index of 2 is harder than the observed cosmic-ray spectrum (see Figure 2.3). A softening of the index, which amounts to a reduction in the flux of higher energy particles, could be explained by magnetic feedback on propagation, or could occur as particles diffuse away from their original source (Blasi, 2013). Additionally, SNRs have an elemental composition that matches that of CRs (Tsujimoto et al., 1995).

Evidence of 10^{14} eV CRs has been detected at the forward shocks of SN 1006 Koyama et al., 1995 and also in reverse shocks (Rho et al., 2002). One major shortcoming of SNRs is that they are not known to produce particles with energies higher than 100 TeV. This makes an acute need to find a Galactic PeVatron, or producer of PeV cosmic rays, one of which may reside in the GC.

2.2   The Gamma Ray Sky

The observable sky in VHE gamma rays, as pictured in Figure 2.5, shows strong localized fluxes of gamma-ray radiation from individual astrophysical sources. Figure 2.6 shows the GeV *Fermi*-LAT skymap using its most recent (Pass 8) data. Because their charge causes their paths to be bent by magnetic fields, cosmic rays cannot be traced back to their origin based on their incoming direction. Gamma rays, which are high-energy photons, do not have charge and follow straight paths that can be traced back to their source, excepting any major gravitational lensing effects. They can come from a multitude of point and extended sources, including, but not limited to, blazars, SNRs, and AGNs. Gamma-ray sources can emit by multiple different mechanisms that depend on different properties of the source. Combining observations of flux over a wide range can be used to constrain physical parameters of sources, helping to select between theoretical models of emission. Both cosmic and gamma rays of very high energy create air showers upon entering Earth's atmosphere, and detecting them requires understanding the interactions involved.

2.2.1   Sources of Gamma Rays

Because of their effectively straight trajectories from their source, gamma rays and lower energy photons are the best way to study individual objects. There are a multitude of different gamma-ray observatories, covering energy ranges from tens of MeV to over 50 TeV. Gamma rays can be detected directly in space-borne experiments, such as *Fermi*-LAT. They can also be detected by ground-based IACTs, such as VERITAS, H.E.S.S., and MAGIC which collect the bursts of light they produce when interacting with the atmosphere. Each ground-
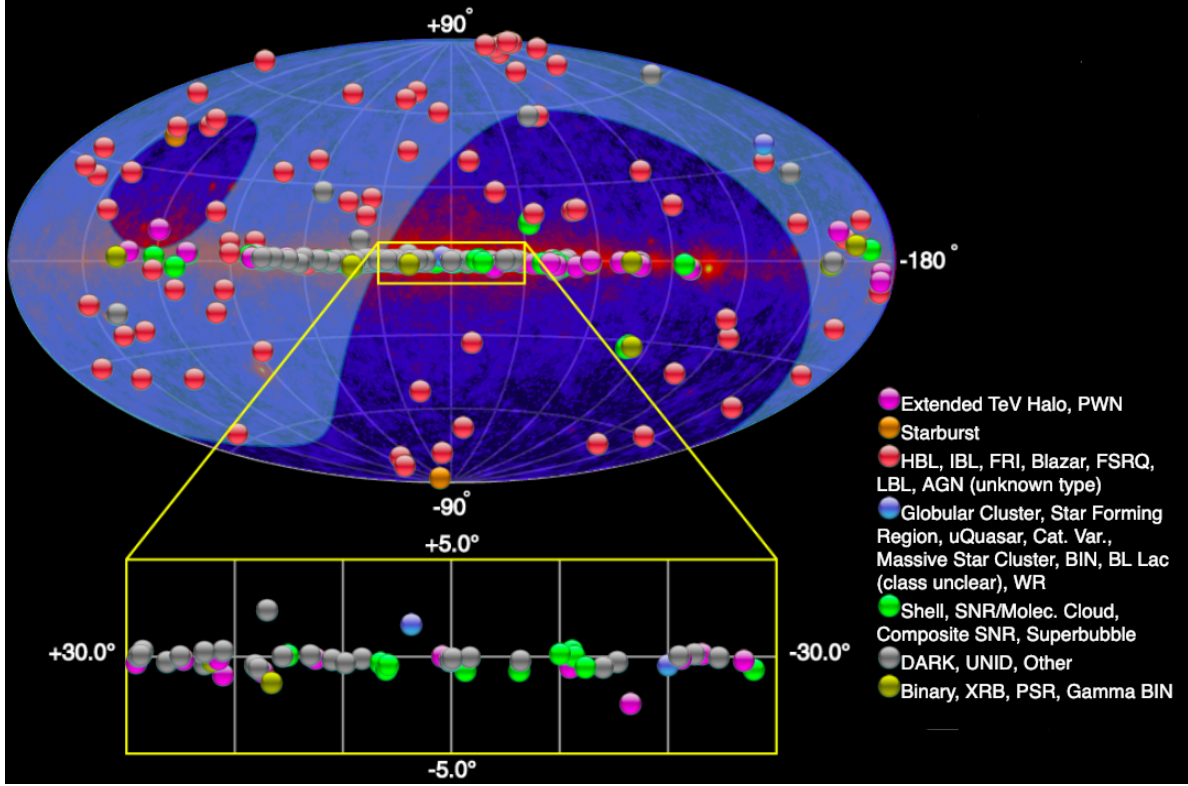
Figure 2.5: Map of the TeVCat catalog of VHE sources. The coordinates are Galactic longitude (horizontal) and latitude (vertical). The heat map represents the *Fermi*-LAT signal at GeV energies. Skymap and legend from `http://tevcat.uchicago.edu/`, January 2019.

based experiment has a different view of the sky depending on its geographic coordinates. Space-based experiments can observe a large FoV of π steradians. Figure 2.5 gives a view of the VHE gamma-ray sky from the online astronomical catalog TeVCat. The signal above $1\,\text{GeV}$ from the *Fermi*-LAT all-sky map is shown as the background heat map, and the half of the sky observable by VERITAS and MAGIC is shown lighter. The points represent VHE gamma-ray sources; they are given different colors according to which of the seven categories they belong. The categories are PWNe, binary systems, AGNs (including blazars), SNRs, starburst galaxies, star clusters or star-forming regions, and unidentified (UNID/DARK) sources. A zoomed-in view of the inner $60° \times 10°$ of the galaxy shows the large number of point sources around the Galactic plane.

SNRs, PWNe, and binary star systems are common Galactic sources of gamma rays.

36
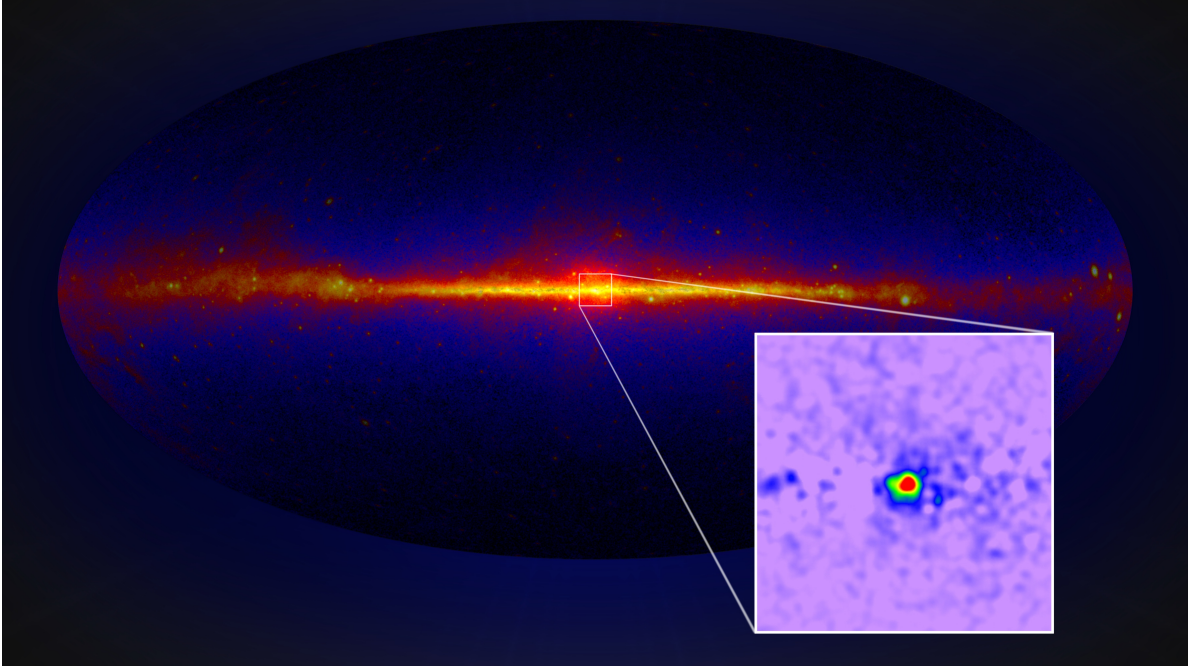
Figure 2.6: GeV skymap from *Fermi*-LAT. Credit: NASA/DOE/Fermi-LAT Collaboration and T. Linden (Univ. of Chicago).

After a supernova event, the ejected matter expands outward in a relativistic shock wave, the front of which is called its shell. A PWN, or plerion, is a nebula, or dust cloud, that surrounds and is powered by a central pulsar found inside an SNR shock. An example of a luminous SNR near the Galactic Center (GC) is G0.9+0.1. In the VHE regime, the spectra of most objects follow pure or modified power laws with negative indices. These spectra reflect the acceleration and emission mechanisms prevalent at high energies.

The total luminosity of emission can be inferred from the observed flux if the distance to the source is known. If the flux is F for a detector at a distance R, the luminosity L can be found by integrating the flux over the surface of a sphere of radius R, as this encompasses all of the energy output, and it assumes isotropic emission.

$$L = 4\pi R^2 F(R) \tag{2.21}$$

It is the luminosity, rather than the flux, that is important when determining the total energy output of a source.

2.3 High-Energy Gamma Radiation Mechanisms

In this section, I explain the mechanisms by which accelerated particles generate high-energy photons. The VHE gamma rays studied by VERITAS and other experiments far exceed the energy produced by thermal processes, and their overall energy distribution does not follow the Planck blackbody spectrum or that of thermal bremsstrahlung. The primary flux contributions of gamma-ray sources come from four non-thermal processes: synchrotron radiation, bremsstrahlung, inverse Compton scattering, and neutral pion decay. An approximate breakdown of their contributions to the non-thermal electromagnetic flux from the Crab Nebula is shown in Figure 2.7.
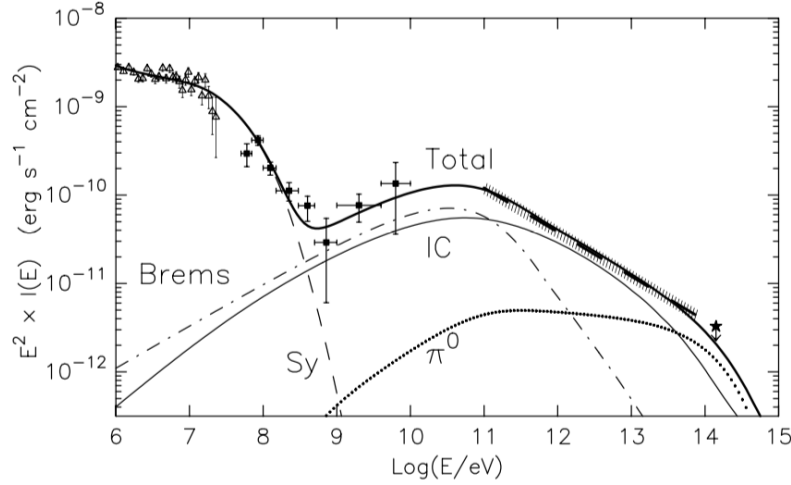
Figure 2.7: Emission spectrum of high-energy electromagnetic radiation from the Crab Nebula broken down by production mechanisms (Aharonian & Atoyan, 1998). The mechanisms are synchrotron (dashed line), bremsstrahlung (alternating dashes and dots), inverse Compton scattering (solid line), and neutral pion decay (dotted line). The bold solid line is the sum total of all of the models above, and the points are the observed flux points from different experiments.

2.3.1 Synchrotron Radiation

Synchrotron radiation, or magnetobremsstrahlung, is a form of radiation emitted from electrons when they are accelerated by a strong magnetic field. Heavier particles such as protons emit this radiation as well, but the flux of synchrotron is dominated by emission from electrons, which experience much greater acceleration. A particle moving with velocity components perpendicular to a strong magnetic field will be bent in a helical pattern whose axis is aligned in the direction of the magnetic field. The perpendicular component of velocity is $v_\perp = v\sin\alpha$, where α is the *pitch angle*, or the angle between the velocity and the magnetic field. The electron travels with a gyromagnetic radius $r_g = \frac{\gamma m v_\perp}{|q|B}$ and a gyromagnetic angular frequency of $\omega_r = \frac{eB}{\gamma m_e}$ (m_e is the rest mass of the electron). As it moves along this path, it experiences an acceleration of $a_\perp = evB\sin\alpha/\gamma m_e$ toward the axis of the helix.

Radiation of accelerated charged particles   When a charged particle is accelerated, a disturbance in its surrounding electromagnetic field emanates from the charge at the speed of light. An early classical examination by J. J. Thomson determined that this pulse of disturbance creates a nonzero Poynting vector $\vec{S} = \vec{E} \times \vec{H}$. By integrating the Poynting flux $\left|\vec{S}\right|$ over all solid angles, we get the Larmor formula for the radiation rate,

$$-\left(\frac{dE}{dt}\right) = \frac{q^2\,|\mathbf{a}|^2}{6\pi\epsilon_0 c^3} \tag{2.22}$$

where $\mathbf{a}$ is the acceleration of the charge q, and ϵ_0 is the permittivity of free space. This same formula can be derived classically from Maxwell's equations. The relativistically correct, time-retarded potentials arising from a moving point charge in the Lorenz gauge are called the Liénard–Wiechert potentials. The resulting scalar potential Φ and vector potential $\vec{A}$ are:

$$\Phi\left(\vec{r}, t\right) = \frac{1}{4\pi\epsilon_0 r}\left[\frac{q}{1 - \vec{\beta}\cdot\hat{n}_{\mathrm{obs}}}\right] \tag{2.23}$$

$$\vec{A}\left(\vec{r}, t\right) = \frac{\vec{\beta}}{c}\Phi\left(\vec{r}, t\right) \tag{2.24}$$

where $\vec{r} = r\hat{n}_{\mathrm{obs}}$ is the vector pointing from the source charge to the observer, r is its magnitude, and $\hat{n}$ is its corresponding unit vector. The radiation rate dE/dt is Lorentz-invariant, so the nonrelativistic Larmor formula (Equation 2.22) may be applied to the proper

acceleration in the instantaneous rest frame of the electron. The Fourier transform of the acceleration $\dot{v}$ is the frequency domain representation of $\dot{\mathbf{v}}(t)$. The intensity spectrum as a function of angular frequency $I(\omega)$ can be found by applying Parseval's theorem to the acceleration $\dot{\mathbf{v}}(\omega)$:

$$I(\omega) = \frac{q^2}{3\pi\epsilon_0 c^3} |\dot{\mathbf{v}}(\omega)|^2 \tag{2.25}$$

The relativistic intensity spectrum can be found by boosting from the electron frame into the laboratory frame via a Lorentz transformation. These expressions are the basis for both synchrotron and bremsstrahlung, which are explained in the next section.

The accelerated electron will emit synchrotron radiation in the shape of a cone whose axis is in the direction of the electron's instantaneous velocity. The cone will have an interior angle of $\theta = \arcsin 1/\gamma$, which is small enough for relativistic particles to use the small-angle approximation (Longair, 2011). See Figure 2.9a for an illustration of synchrotron radiation.

The power of emission for a single electron is

$$-\left(\frac{dE}{dt}\right) = 2c\sigma_T U_{\mathrm{mag}}\gamma^2 \sin^2\alpha \tag{2.26}$$

$$= \frac{c\sigma_T B^2 \gamma^2 \sin^2\alpha}{\mu_0} \tag{2.27}$$

where μ_0 is the permeability of free space, $U_{\mathrm{mag}} = \frac{B^2}{2\mu_0}$ is the magnetic energy density, and σ_T is the Thomson cross-section (Equation 2.40). Because the electron directions will be effectively random, the probability distribution of the pitch angle α will follow $p(\alpha)\, d\alpha = \frac{1}{2}\sin\alpha\, d\alpha$. The average power radiated by electrons with an isotropic distribution of pitch angles is found by integrating Equation 2.27 multiplied by that probability density over the full range of α. The α terms can be extracted and the integral left to evaluate is $\frac{1}{2}\int_0^\pi \sin^3\alpha\, d\alpha = \frac{2}{3}$. The angle-averaged radiation power is then

$$P = \frac{2c\sigma_T B^2 \gamma^2}{3\mu_0}. \tag{2.28}$$

Emissivity j is defined as the energy emission per unit time per unit volume. The single-electron emissivity of synchrotron radiation as a function of frequency ν is

$$j(\nu) = \frac{\sqrt{3}e^3 B \sin\alpha}{4\pi\epsilon_0 c m_e} F\left(\frac{\nu}{\nu_c}\right) \tag{2.29}$$

where $q = e$ is the electron charge and $nu_c = \frac{3\gamma^2 eB}{4\pi m_e} \sin \alpha$ is the relativistic critical frequency. We also define the function $F(x) = x \int_x^\infty K_{5/3}(z)\, dz$, where K_n represents the nth order modified bessel function of the second kind. In the high-energy limit, which is relevant to my analysis, this approaches

$$j(\nu) \propto \nu^{1/2} \exp(-\nu/\nu_c). \tag{2.30}$$

There is a critical angular frequency

$$\omega_{\text{c}} = \frac{3c\gamma^2 eB \sin \alpha}{2vm_e} \tag{2.31}$$

above which the emissivity cuts off exponentially.

The spectrum of synchrotron radiation observed from a source is related to its magnetic field strength and electron population. Longair (2011), following Rybicki & Lightman, 1979, derive the energy spectrum assuming a population of electrons with a power-law distribution. The number density $N(E)$ of electrons in the interval $[E, E + dE]$ is described by

$$N(E)\, dE = \kappa E^{-p} dE \tag{2.32}$$

where κ is the normalization constant and p is the exponential index. Multiplying the number density $N(E)$ by the energy loss-rate gives the emissivity of the population of electrons

$$j(\nu)\, d\nu = \left(-\frac{dE}{dt}\right) N(E)\, dE. \tag{2.33}$$

Solving the energy and differential in terms of the frequency and substituting into Equation 2.33:

$$j(\nu)\, d\nu = \frac{2\kappa \sigma_T m_e c^3}{3\mu_0} \left(\frac{e}{2\pi m_e}\right)^{\frac{p-3}{2}} B^{\frac{p+1}{2}} \nu^{-(p-1)/2}. \tag{2.34}$$

It is important to look at the proportionality of the emissivity to physical properties such as the magnetic field and the electron spectrum.

$$j(\nu) \propto \kappa B^{(p+1)/2} \nu^{-(p-1)/2}. \tag{2.35}$$

The emissivity as a function of frequency is described by a power law. The index of frequency is closely related to the index of the electron power law, and has a value of $(p-1)/2$. It is

41

related to the magnetic flux density by a power law with an index $(p+1)/2$, an increment of one. The magnitude of flux density is directly proportional to the electron density constant κ.

Synchrotron emission can come from a variety of sources that cover a wide range of these physical parameters. Consequently, it emits radiation over a broad spectrum spanning from radio waves to X-rays. For example, assuming the estimated average magnetic flux density in the Galaxy $B \approx 1\,\text{nT}$, electrons with energy $\mathcal{O}\left(10^{11}\,\text{eV}\right)$ will emit radio waves in the GHz range. In fact, synchrotron radiation is the dominant form of Galactic radio emission, with contributions that come primarily from SNRs. Although it does not create gamma rays detectable by VERITAS, Equation 2.35 can be used to constrain magnetic field and electron density. This information can be combined with data from other wavebands to constrain models for a given source region.

2.3.2 Bremsstrahlung

Bremsstrahlung is the radiation emitted from an electron that is decelerated by the electric field of another charged particle. It is another manifestation of radiation from an accelerated charge (Section 2.3.1), but with a fundamentally different acceleration from the circular motion that causes synchrotron radiation. It is also called *free-free* emission and braking radiation, because the electron will decelerate along its direction of motion, emitting its lost kinetic energy in the form of photons. Bremsstrahlung is a common source of gamma rays and also the dominant loss mechanism for charged particles moving through the atmosphere with high speed.

Longair's derivation begins with the Coulomb field of a stationary target nucleus transformed into the frame of the relativistic electron. The components of the acceleration experienced by the electron in the field of a nucleus with atomic number Z are:

$$\left.\begin{aligned} a_{\parallel} &= \frac{\gamma Z e^2 v t}{4\pi\epsilon_0 m_e \left[b^2 + (\gamma v t)^2\right]^{3/2}} \\ a_{\perp} &= \frac{\gamma Z e^2 b}{4\pi\epsilon_0 m_e \left[b^2 + (\gamma v t)^2\right]^{3/2}} \end{aligned}\right\} \tag{2.36}$$

42

if the electron approaches at an impact distance b. The magnitude of the acceleration $|\dot{\mathbf{v}}(\omega)|$ is related to the intensity by Equation 2.25. Boosting back from the rest frame of the electron to the rest frame of the nucleus and integrating over the valid range of impact distances yields the classical result for the energy loss rate of the electron (Longair, 2011),

$$-\frac{dE}{dt} = E\frac{Z^2 e^6 N}{12\pi\epsilon_0^3 m_e^2 c^4 \hbar}\ln\left(\frac{192}{Z^{1/3}}\right), \tag{2.37}$$

which is very close to the result obtained with a full quantum treatment by Bethe & Heitler (1934):

$$-\frac{dE}{dt} = \frac{Z(Z+1.3)e^6 N}{16\pi^3\epsilon_0^3 m_e^2 c^4 \hbar}E\left[\ln\left(\frac{183}{Z^{1/3}}\right)+\frac{1}{8}\right]. \tag{2.38}$$

$\hbar$ is the reduced Planck constant, equal to $h/2\pi$. It is important to note that the radiation rate is directly proportional to the electron's energy E. This means that a population of electrons that follows a power law will emit an energy spectrum with the same index. The emitted photons have about a third of the initial energy on average, but can have energies near the total energy of the electron.

The rate of interaction between two particles is quantified by its cross section, an effective area within which particles must meet for the interaction to occur. For a more detailed explanation of interaction cross section, see Appendix A.1. The high-frequency limit of the differential cross section with respect to energy for a bremsstrahlung interaction, derived by Fano using the Sauter approximation (Fano, 1959; Koch & Motz, 1959), is given in Strong et al., 2000:

$$\left(\frac{d\sigma}{dk}\right)_{\text{FS}} = 4\pi Z^3 \alpha_f^2 r_e^2 \frac{\gamma_0\beta_0}{k(\gamma_0-1)^2}\left\{\frac{3}{4}+\frac{\gamma_0(\gamma_0-2)}{\gamma_0+1}\left[1-\frac{1}{2\beta_0\gamma_0^2}\ln\left(\frac{1+\beta_0}{1-\beta_0}\right)\right]\right\} \tag{2.39}$$

where k represents the energy and momentum of the photon emitted, $r_e = \frac{e^2}{4\pi\epsilon_0 m_e c^2}$ is the classical electron radius, α_f is the fine structure constant, and the 0 (naught) subscript specifies properties of the electron prior to deflection.

Because bremsstrahlung only requires a population of high-energy electrons and target material, it is common in many sources throughout the universe that cover a wide range of energies. These sources fall into two categories, thermal and nonthermal, which describe the energy distribution of the electron population. Thermal bremsstrahlung is emitted

from plasmas with electrons who follow the Maxwell–Boltzmann probability distribution of temperature. Nonthermal bremsstrahlung originates from nonthermal populations such as the cosmic ray electrons accelerated in Fermi shocks. This type of emission dominates the X-rays detected by space-borne experiments such as the *Chandra X-ray Observatory*, *NuSTAR*, *ROSAT*, and *Suzaku*. Its spectrum extends up to low energy gamma rays observed by Fermi, but not to the VHE gamma rays observed by VERITAS. It is important to my analysis, still, because the flux of bremsstrahlung depends on both the density of high-energy electrons and the target nucleus density. Observations in the bremsstrahlung regime therefore provide useful information about these populations, which are involved in other gamma-ray production mechanisms. This information can be combined with other data, such as from synchrotron radiation, to further constrain the parameter space. Example spectra from leptonic mechanisms from SNRs are shown in Figure 2.8a.

2.3.3 Inverse Compton Scattering

Inverse Compton (IC) scattering is the process whereby an ultrarelativistic electron upscatters a low-energy photon, imparting a large fraction of its energy to that photon to create a VHE photon. It is the time reversal of Compton scattering, where a high-energy photon scatters an electron to higher energy. Because scattering is symmetric under time-reversal, the same interaction cross section applies to both Compton and inverse Compton scattering.

At the lowest energies, where the process is called Thomson scattering and there is little transfer of energy, the cross section is simply the Thomson cross section,

$$\sigma_T \equiv \frac{\langle P_{\text{scattered}} \rangle}{\langle \Phi_{\text{incident}} \rangle} \tag{2.40}$$

$$= \frac{2\mu_0 e^4}{12\pi m_e^2 \epsilon_0 c^2} \tag{2.41}$$

$$= \frac{8\pi}{3} r_e^2 \tag{2.42}$$

$$\approx 6.65 \times 10^{-29} \, \text{m}^2 \tag{2.43}$$

where Equation 2.42 is written in terms of the classical electron radius.

At higher energies, quantum effects become appreciable, and an accurate cross section calculation requires a quantum mechanical treatment. The differential cross section for Compton scattering is described by the Klein–Nishina Formula (Klein & Nishina, 1929):

$$\frac{d\sigma}{d\Omega} = \alpha_f^2 r_c^2 P(E_\gamma, \theta)^2 [P(E_\gamma, \theta) + P(E_\gamma, \theta)^{-1} - \sin^2(\theta)]/2 \tag{2.44}$$

with

$$P(E_\gamma, \theta) = \frac{1}{1 + (E_\gamma/m_e c^2)(1 - \cos\theta)}$$

$$= E'(E_\gamma, \theta)/E(E_\gamma, \theta)$$

as the ratio of the final energy of the photon to the initial energy of the photon, $r_c = \hbar/m_e c$ as the electron's reduced Compton wavelength and $d\Omega = \sin\theta\, d\theta\, d\phi$ as the solid angle differential. The total cross section, after integrating over all solid angles, is

$$\sigma_{K-N} = \pi r_e^2 \frac{1}{x} \left\{ \left[1 - \frac{2(x+1)}{x^2} \right] \ln(2x+1) + \frac{1}{2} + \frac{4}{x} - \frac{1}{2(2x+1)^2} \right\} \tag{2.45}$$

with x defined as $\hbar\omega/m_e c^2$. In the low-energy limit, or Thomson regime, only small corrections are made to the Thomson cross section:

$$\sigma_{\text{KN}} \sim \sigma_T \left(1 - 2x + \frac{26x^2}{5} \right). \tag{2.46}$$

The Klein-Nishina regime is the high-energy limit of this cross section, where the photon energy $E_\gamma \gg m_e c^2$:

$$\sigma_{\text{KN}} \sim \frac{3\sigma_T}{8x} \left[\ln(2x) + \frac{1}{2} \right] \tag{2.47}$$

This is the cross section relevant for interactions that can create VHE gamma rays up to the range detectable by VERITAS. The Lorentz-invariant total radiated power is

$$P = -\left(\frac{dE}{dt} \right)_{\text{IC}} = \frac{4}{3} \sigma_T c \beta^2 \gamma^2 u_{\text{rad}}, \tag{2.48}$$

where γ and β are the Lorentz factor and velocity of the electron, respectively. The energy density of radiation is

$$u_{\text{rad}}(\nu) = n(\nu) h\nu, \tag{2.49}$$

and n is the number density of photons in the lab frame. The total emission from a source depends directly upon the density of the photon field and the electron population in the source region.

The spectral shape of IC radiation will be tied to the electron spectrum of the source. In the case of an electron population with a power law spectrum as in Equation 2.32, the resulting flux of emitted photons will also be a power law with index

$$a_\gamma = (p+1)/2. \tag{2.50}$$

inverse Compton (IC) scattering is one of the most important mechanisms for gamma-ray production. This process can occur in concert with relativistic synchrotron electrons, which can scatter the lower energy photons emitted from synchroradiation to X-ray and gamma-ray energy.
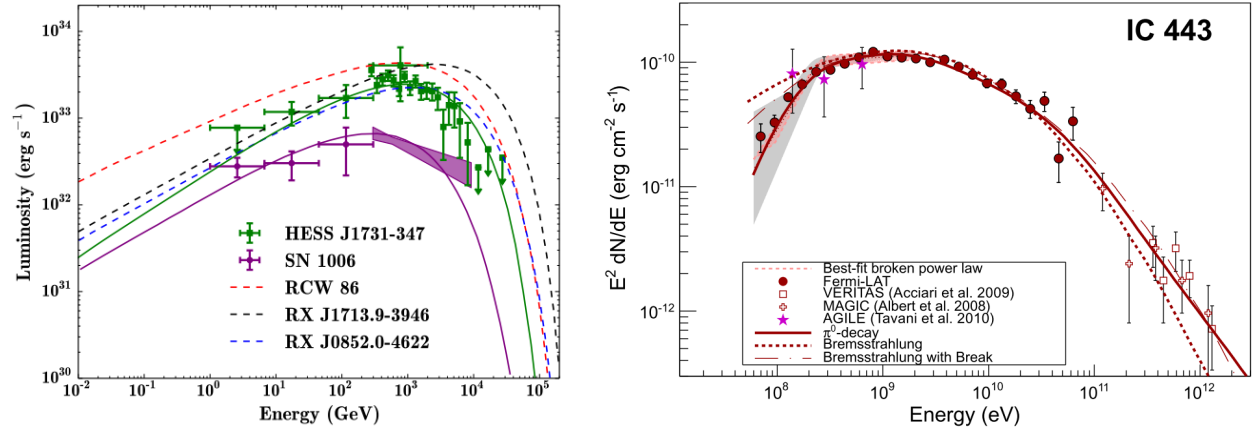
(a) Leptonic modeling of the gamma-ray emission for multiple shell-type SNRs. The emission is modeled by inverse Compton scattering (Condon et al., 2017). The TeV emission points are from H.E.S.S. measurements.

(b) Gamma-ray spectrum of IC 443 with points measured by *Fermi*-LAT at GeV energies and by VERITAS and MAGIC at TeV energies. The emission is best fit by a neutral pion decay model (Fermi-LAT Collaboration et al., 2013).

Figure 2.8

2.3.4 Inelastic Hadronic Collisions

Inelastic hadronic collisions occur when a high-energy hadron, such as a cosmic ray proton, collides directly with a target nucleus, breaking it into several parts. This process, called spallation, occurs readily in the ISM and Earth's atmosphere, creating air showers of many new particles (see subsubsection 4.1.1.2). These products include neutral pions, which decay into VHE gamma rays.

Breaking apart a nucleus requires more direct contact than scattering because the strong force that holds the nucleus together acts only at very short range. The relevant cross sections are then found for the target nucleus and high-energy cosmic ray proton based on their physical size. For a nucleus at rest, the cross section of a direct hit is estimated as the cross-sectional area of a sphere with radius

$$R = 1.2 \times 10^{-15} A^{1/3} \, \text{m}, \tag{2.51}$$

where A is the mass number of the nucleus. The effective size of a relativistic proton can be estimated as the uncertainty in position using Heisenberg's uncertainty principle,

$$\Delta x \approx {\hbar}/{p} \tag{2.52}$$

$$= \hbar/\gamma m_p v \tag{2.53}$$

The uncertainty in position Δx corresponds to the *de Broglie* wavelength of a matter wave, and is approximately $2 \times 10^{-19} \, \text{m}$ for a $1 \, \text{TeV}$ proton.

The products yielded by spallation are mainly pions, but also include kaons, baryons, strange particles,[2] and antinucleons given sufficient energy of the incident cosmic ray. Pions and kaons are not stable and decay into other particles by a few different decay modes. Kaons can produce either muons via $K^{+/-} \rightarrow \mu^{+/-} + \nu_\mu$, neutral pions via $K^{+/-} \rightarrow \pi^{+/-} + \pi^0$, and

---

[2]Strange particles are hadrons that contain strange quarks.

charged pions via $K^0 \rightarrow \pi^+ + \pi^-$. The decay modes for the three kinds of pions are:

$$\pi^0 \rightarrow \gamma\gamma \tag{2.54}$$

$$\pi^+ \rightarrow \mu^+ + \nu_\mu \tag{2.55}$$

$$\pi^- \rightarrow \mu^- + \bar{\nu}_\mu \tag{2.56}$$

About one third of the pions produced in this way are neutral pions, so neutral pion decay is the major pathway from hadronic collisions to gamma rays. Gamma rays are also produced in much smaller proportions by rarer particles such as the strange η-meson. Neutral pions have a mean lifetime τ of $(8.52 \pm 0.18) \times 10^{-17}$ s, a rest mass of $135.0 \, \text{MeV}/c^2$ (Tanabashi et al., 2018), and a quark composition of $\frac{u\bar{u}-d\bar{d}}{\sqrt{2}}$. A diagram of π^0 decay (2.54) is shown in Figure 2.9d. The two gamma rays produced must be the same angle above and below the neutral pion's initial velocity to satisfy conservation of momentum and energy. The angle θ must decrease as the energy of the π^0 increases. In addition, the gamma rays must have the same energy, so each gamma ray gets half of the incident energy upon decay.

Since the π^0 has a rest mass of $135 \, \text{MeV}/c^2$, the minimum energy of gamma rays emitted during neutral pion decay is $67.5 \, \text{MeV}$; hence, we see a broad maximum in the spectrum near the minimum energy called the pion bump. This bump is a signature of neutral pion decay, while neutrinos are a signature of charged pion decay. The overall flux of gamma rays from neutral pion decay depends on the density of cosmic rays and target molecular gas. The spectrum beyond the bump also depends on the spectrum of the cosmic ray population. An example spectrum of neutral pion decay from the SNR IC 443 is shown in Figure 2.8b.

2.4 Summary

Figure 2.9 contains diagrams for all of the gamma-ray emission mechanisms discussed in this section.
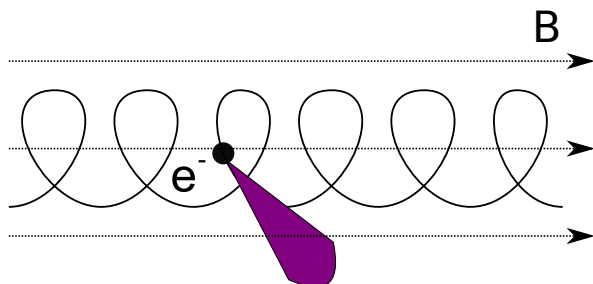
(a) Illustration of synchrotron radiation. A cone of light is emitted from the charged particle as it is bent by a magnetic field.
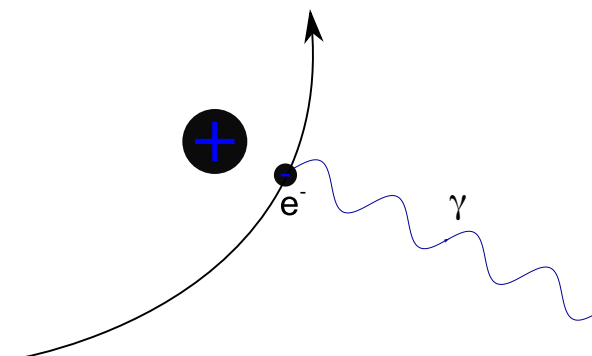
(b) Bremsstrahlung radiation resulting from an electron approaching a nucleus and being bent by its electric field.
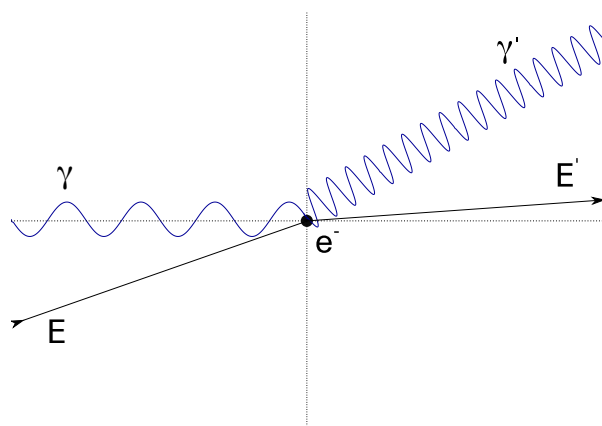
(c) Illustration of Inverse Compton scattering. A high-energy electron scatters a low-energy photon to higher energy.
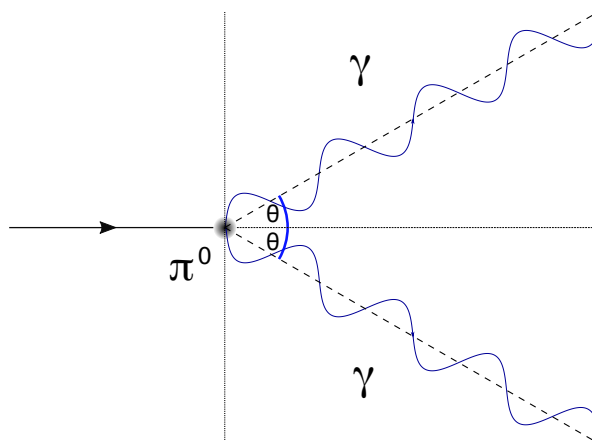
(d) Neutral pion decay into two gamma rays. The neutral pion typically originates from a hadronic cascade.

Figure 2.9: Diagrams of the major mechanisms for gamma-ray emission: synchrotron radiation (a), bremsstrahlung (b), inverse Compton scattering (c), neutral pion decay (d).

CHAPTER 3

VHE Emission from the Galactic Center

The central questions addressed in this dissertation are the emission mechanism of the unknown central gamma-ray source and the potential of an associated PeVatron accelerator of Galactic cosmic rays. The high energies involved are particularly unique and interesting compared to lower energy emission, which is more common, easier to study, and consequently better understood. Unfortunately, because of the low angular resolution of IACTs and low statistics of gamma-ray events resulting from a negative-indexed power law flux, the highest energies are the most difficult to study. This chapter covers the most prominent models proposed to explain the possible mechanisms for gamma ray emission and cosmic ray production in the GC, and how data from VERITAS, H.E.S.S., and Fermi can distinguish between those models.

3.1 Modern Gamma-ray Picture of the GC

Selecting valid models to explain the gamma-ray emission requires a close examination of VHE data in conjunction with our knowledge at lower energies. Modern gamma-ray experiments have advanced their techniques and equipment over the years, improving the accuracy and precision over older experiments. Currently, the gamma-ray experiments most relevant to my analysis are VERITAS, H.E.S.S., and *Fermi*-LAT. In this section, I enumerate the most crucial and modern results from gamma-ray observations in the GC region.

The energy ranges covered by GC observations for the current gamma-ray experiments are given in Table 3.1. H.E.S.S. and VERITAS cover a combined range from $100\,\mathrm{GeV}$ to $40\,\mathrm{TeV}$, and the two experiments overlap from $2\,\mathrm{TeV}$ to about $30\,\mathrm{TeV}$. The large zenith angle

at which VERITAS observes the GC is responsible for increasing the energy threshold and the effective area at the largest energies, extending its spectral points beyond the highest energies acquired in most analyses at standard zenith angles (see Section 4.3 for more detailed performance specifications of VERITAS).

Experiment	Energy threshold	Energy Max	Angular Resolution
Fermi-LAT	100 MeV	300 GeV	0.15° (> 10 GeV)
H.E.S.S.	200 GeV	30 TeV	0.08°
VERITAS	2 TeV	40 TeV	0.125°

Table 3.1: Table of energy ranges and angular resolution of modern gamma-ray instruments for GC observations.

The most recent H.E.S.S. significance skymaps (prior to this work), produced with 259 hours of data taken between 2004 and 2012, are shown in Figure 3.1. Top shows the full significance map for gamma rays over 100 GeV, and bottom shows the residual significance skymap after subtraction of two major point sources, G0.9+0.1 and HESS J1745–290. The cyan lines represent contours of the CS1-0 line emission, which traces the density of molecular gas. The brightness temperature is integrated over Local Standard of Rest velocity from -200 km/s to 200 km/s (Tsuboi et al., 1999). The signal is also smoothed by H.E.S.S.'s point spread function (PSF), which describes the distribution of reconstructed directions for events emanating from a point source (see Subsection 6.4.2). The 68 % containment radius of their PSF is 0.077°. HESS J1746–285, marked by the black cross, is coincident with the GC radio arc (Yusef-Zadeh et al., 1984).

VERITAS's most recent skymap, from Archer et al., 2016, is shown in Figure 3.2. It uses quality-selected observation data amounting to about 85 hours of livetime. The strongest point sources, J1745–290 (labelled Sagittarius A*) and G0.9+0.1, can be seen clearly. The color scale, representing statistical significance, is limited to 15σ so that the structure of gamma-ray signal outside of the central emission can be seen in more detail.
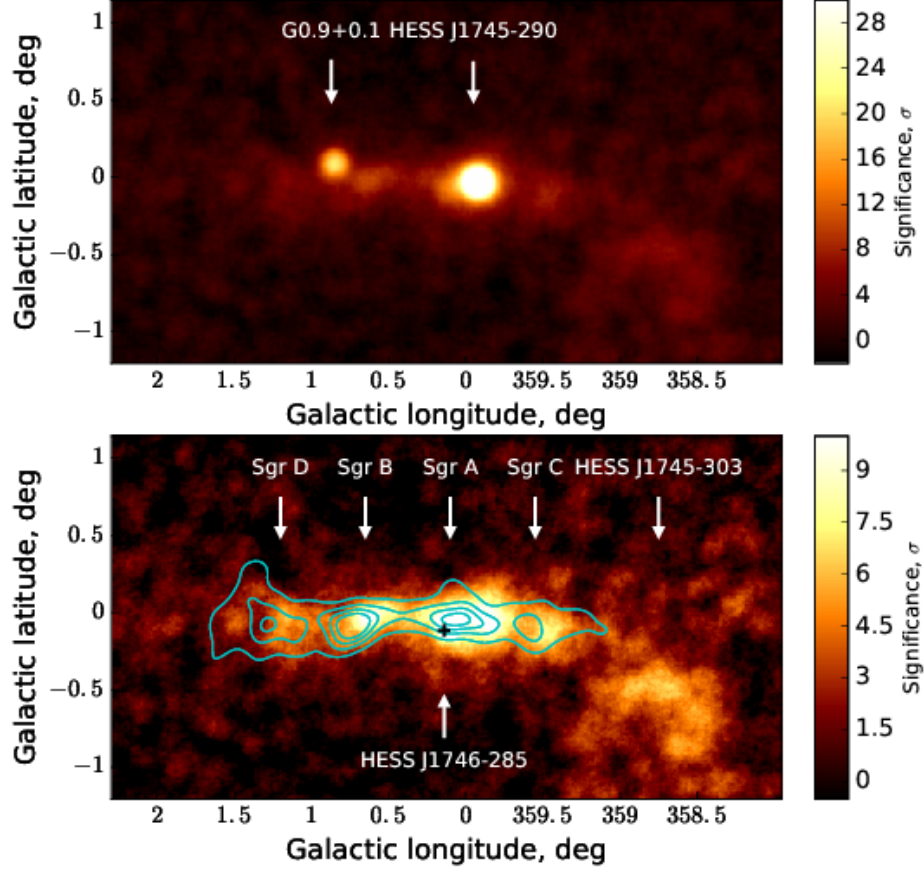
Figure 3.1: H.E.S.S. skymaps of the GC region (H.E.S.S. Collaboration et al., 2017). The significance map of events above $100\,\mathrm{GeV}$ is shown on top, while the bottom is the residual map after subtracting the point sources G0.9+0.1 and HESS J1745–290. The position of HESS J1745–285 is marked by the black cross. The cyan contours are the integrated signal of CS brightness temperature (Tsuboi et al., 1999) smoothed with H.E.S.S.'s PSF.

3.1.1 Central Point Source: J1745–290

The top image in Figure 3.3 shows the excess map corresponding to Figure 3.2 with no limit placed on the color scale. The central point source J1745–290 is strongly detected at a significance of $> 25\sigma$. The best-fit position VER J1745–290 in Galactic coordinates is $\ell = 359.94° \pm 0.002°_{\mathrm{stat}} \pm 0.013°_{\mathrm{sys}}$, $b = -0.053° \pm 0.002°_{\mathrm{stat}} \pm 0.013°_{\mathrm{sys}}$, which is consistent with both HESS J1745–290 and the radio position of Sgr A*. HESS J1745–290 was found to be point-like and have a best-fit position of $\ell = 359.944862$, $b = -0.043908$, with an error circle
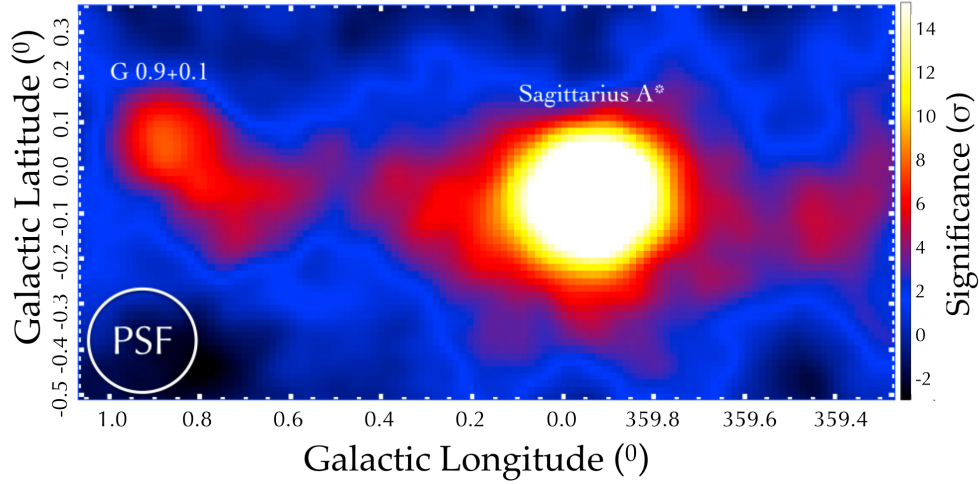
Figure 3.2: VERITAS skymap of gamma-ray emission above 2 TeV from the GC region (Archer et al., 2016). The color scale, which represents significance in each spatial bin, is limited to 15σ, leaving the central region saturated.

of radius 0.0036° (Acero et al., 2010) (the positional uncertainty of H.E.S.S. is considerably lower because of its advanced pointing calibration). This position is consistent with the positions of Sgr A* and G395.95-0.04, but inconsistent with the peak radio signal of Sgr A East. An upper limit of 1.2 arcminutes was placed on any intrinsic size J1745–290 may have, which corresponds to about 2.7 parsecs given our assumed distance to the GC. This is simply a constraint based on measurement limitations and not a suggestion of extension; J1745–290 is still considered to be a point source. The lack of positional certainty is the critical issue when it comes to determining the source of emission.

The most recent spectral points from VERITAS (Archer et al., 2016) prior to this work for the central source J1745–290 are plotted in Figure 3.3 with the H.E.S.S. spectral points published in Aharonian et al., 2009. The combined points from H.E.S.S. and VERITAS were fit by three different forms of power law. The first is a pure power law, with a differential flux given by:

$$\frac{dN}{dE} = N_0 \left(\frac{E}{E_0} \right)^{-\Gamma} \tag{3.1}$$

where the parameter Γ is called the differential spectral index, N_0 is the flux normalization, and $E_0 = 1\,\text{TeV}$ is the normalization energy. The next model is a modified power law with

an exponential cutoff:

$$\frac{dN}{dE} = N_0 \left(\frac{E}{1\,\text{TeV}}\right)^{-\Gamma} \times \exp\left(-\frac{E}{E_{\text{cut}}}\right) \tag{3.2}$$

where E_{cut} is the cutoff energy. The third model is a smoothly broken power law, given by the equation:

$$\frac{dN}{dE} = N_0 \left(\frac{E}{1\,\text{TeV}}\right)^{-\Gamma_1} \times \frac{1}{1 + \left(\frac{E}{E_{\text{break}}}\right)^{\Gamma_2 - \Gamma_1}} \tag{3.3}$$

where E_{break} is the break energy, and there are two index parameters Γ_1 and Γ_2. The best-fit parameters as well as the reduced chi squared (χ^2/ν) of the fit for each model are shown in Table 3.2. The reduced chi squared value is the value of χ^2 divided by the number of degrees of freedom (nu), which is the number of points minus the number of fit parameters. The modified power laws are preferred over the pure power law, with reduced chi squared values much closer to the ideal value of 1.

Model	N_0 (cm^{-2} s^{-1} TeV^{-1})	Γ_1	Γ_2	E_{break} or E_{cut} (TeV)	$\frac{\chi^2}{\nu}$
Power Law	2.36 ($\pm$ 0.05) $\times$ 10^{-12}	2.37 $\pm$ 0.02	N/A	N/A	148/32
Exp. Cutoff Power Law	2.82 ($\pm$ 0.08) $\times$ 10^{-12}	2.05 $\pm$ 0.04	N/A	12.1 $\pm$ 1.6	35/31
Smoothly Broken Power Law	2.55 ($\pm$ 0.07) $\times$ 10^{-12}	2.14 $\pm$ 0.04	4.39 $\pm$ 0.39	12.1 $\pm$ 1.7	32/30

Table 3.2: Best fit parameters for the spectrum of J1745–290 in Figure 3.3. The parameters are defined in the text.

The most recent H.E.S.S. spectral points are shown in Figure 3.8 (Abramowski et al., 2016). The spectral reconstruction uses a forward-folding method that is based on a two-dimensional maximum-likelihood procedure (Piron et al., 2001). Though the points change slightly from 2009, the spectrum is still best fit by a modified power law with a cutoff energy of about 10 TeV. The best-fit parameters can be found in Table 3.3, along with those for the most recent VERITAS and MAGIC results for comparison. The MAGIC spectrum, reconstructed with 67 hours of data, spans energies of $300\,\text{GeV} - 40\,\text{TeV}$ (Ahnen et al., 2016).

The results of all experiments are mostly consistent, with the parameters for flux normalization and exponential index falling within statistical and systematic errors of each other. The exponential cutoff value, however, is more consistent between VERITAS and
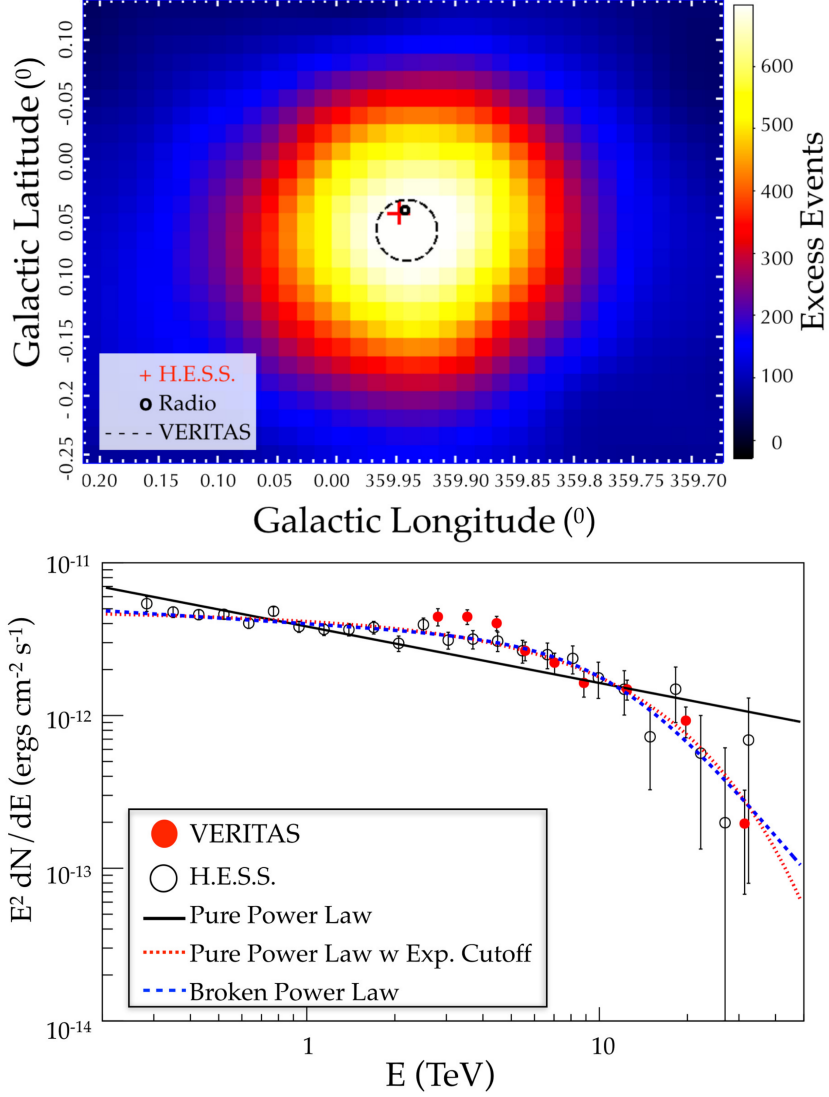
Figure 3.3: Top: The VERITAS excess map zoomed in on J1745–290 (Archer et al., 2016). Bottom: the spectrum of J1745–290 as reconstructed by VERITAS, including H.E.S.S. points from Aharonian et al., 2009. The joint data are fit with a pure power law (black line), a broken power law (blue dashed line), or a power law with an exponential cutoff (red dashed line). The latter two forms provide the best fits.

H.E.S.S., while MAGIC estimates it to be lower. The cutoff energy distinguishes the emission mechanism from that of the diffuse emission in the region, and it is also important for the comparison between theoretical models presented in Section 3.2.

An expanded view of the spectral energy distribution can be seen in Figure 3.4 (Parsons

et al., 2015). It is evident that the spectral flux matches from the GeV range to the TeV range. This could be suggestive of a common origin for the emission in both domains (van Eldik, 2015).

The integral VHE flux, based on the line of best fit of the H.E.S.S. data, is about $2 \times 10^{-12}\,\mathrm{cm}^{-2}\mathrm{s}^{-1}$ above $1\,\mathrm{TeV}$ (Aharonian et al., 2004). The implied TeV luminosity of 1–$10\,\mathrm{TeV}$ gamma rays from J1745–290 is on the order of 10^{35} ergs/s (Genzel et al., 2010). Any model of emission will need to be capable of producing this luminosity given the understood physical parameters of the GC.

Experiment	$N_0[10^{-12}\,\mathrm{TeV}^{-1}\mathrm{cm}^{-2}\mathrm{s}^{-1}]$	Index (Γ)	$E_{\mathrm{cut}}[\mathrm{TeV}]$
VERITAS	2.82 ± 0.08	2.05 ± 0.04	12.1 ± 1.6
H.E.S.S.	$2.55 \pm 0.04_{\mathrm{stat}} \pm 0.37_{\mathrm{sys}}$	$2.14 \pm 0.02_{\mathrm{stat}} \pm 0.10_{\mathrm{sys}}$	$10.7 \pm 2.0_{\mathrm{stat}} \pm 2.1_{\mathrm{sys}}$
MAGIC	2.62 ± 0.32	1.85 ± 0.13	7.57 ± 2.29

Table 3.3: Table summarizing spectral fits in by VHE gamma-ray instruments to an exponentially cutoff power law form for J1745–290. VERITAS: Archer et al., 2016, H.E.S.S.: Abramowski et al., 2016, MAGIC: Ahnen et al., 2016. The flux normalization constants, N_0, are given for normalization energies of $1\,\mathrm{TeV}$. The flux normalization constant for MAGIC is re-calculated for $E_{\mathrm{norm}} = 1\,\mathrm{TeV}$ to be consistent with the other instruments.

The GC has been observed in VHE for about 15 years by four experiments: Whipple, H.E.S.S., MAGIC, and VERITAS. So far, none have reported any significant variability of the VHE flux on any time scale. Figure 3.5 shows the lightcurve of J1745–290 prior to this work with points from VERITAS (Archer et al., 2014). The vertical blue dashed lines (from left to right) represent the time of a *SWIFT* flare (Degenaar et al., 2013) and simultaneous observations with *Chandra* (Neilsen et al., 2013). Even during the periapse passage of the massive gas cloud G2, during which MAGIC was observing, no significant variability was seen (Ward et al., 2015; Ahnen et al., 2016). The detection of flaring or any variability would have dramatic impact on the possible models of VHE emission from J1745–290. Because of the low photon statistics, the sensitivity of detection for a hypothetical flare would depend
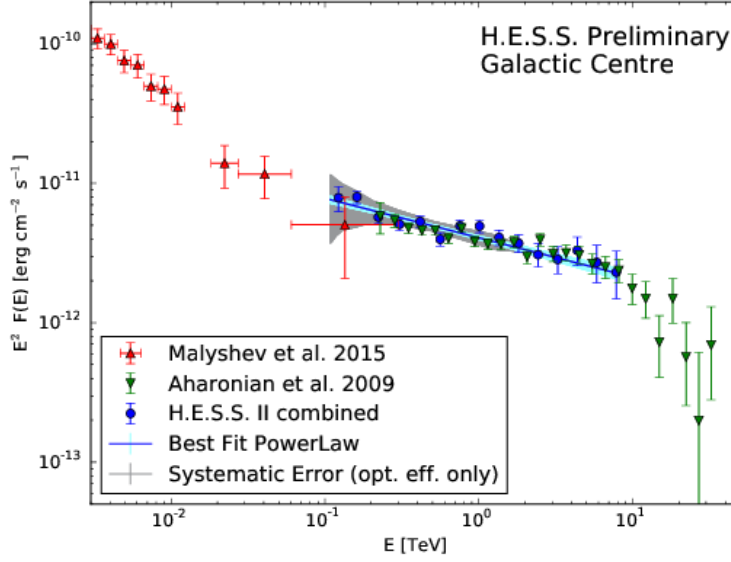
Figure 3.4: Spectral energy distribution of J1745–290 comparing results from *Fermi*-LAT (Malyshev et al., 2015), H.E.S.S. I (Aharonian et al., 2009), and H.E.S.S. II (Parsons et al., 2015).

heavily on its duration (van Eldik, 2015). According to estimates in Aharonian et al., 2009, a flare level (increase above the quiescent flux) of 200 % would be necessary for a detection to occur in a duration of a few hours, while a 90 day flare could be detected with as low as a 30 % increase in flux.

3.1.2 Diffuse Emission

One of the most important results in the last few years has come from H.E.S.S.'s improved analysis of the diffuse emission in the GC, resulting in evidence of PeV Galactic CRs (Abramowski et al., 2016). By reconstructing the energy spectrum of the diffuse emission along the Galactic plane, the H.E.S.S. collaboration demonstrates that it has no cutoff or spectral break up to almost 40 TeV. Since the gamma rays are secondary particles, the primaries are estimated to be consistent with 1 PeV energies. Proton primaries are heavily favored because of the unbroken power-law form of the spectrum. Abramowski et al. (2016) analyzed the signal within the annulus sector pictured in Figure 3.6 (right), which has an
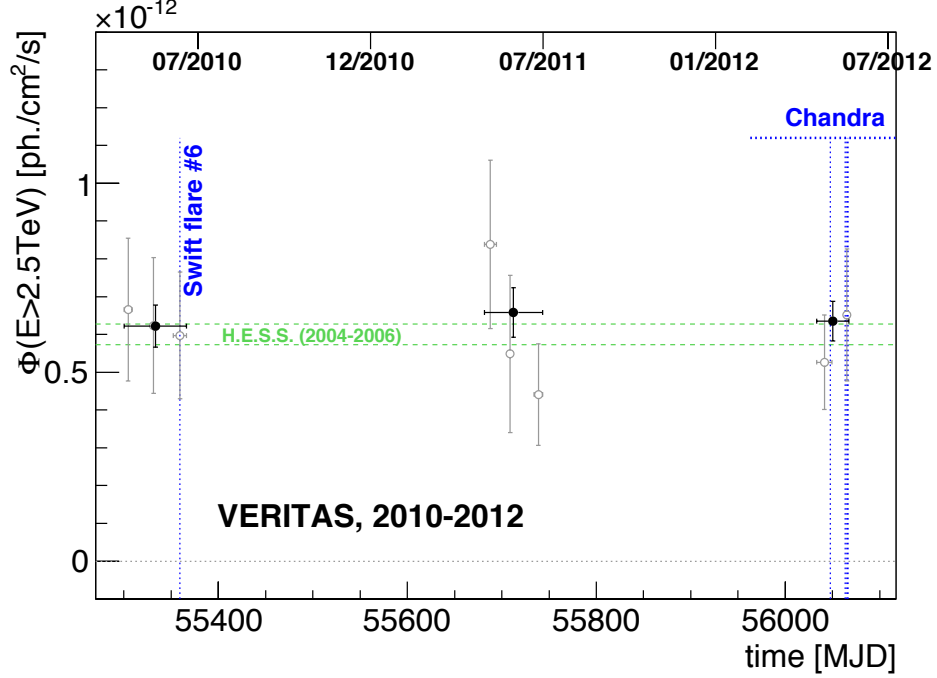
Figure 3.5: Lightcurve of the integral flux above 2.5 TeV (Archer et al., 2014). The open points are the VERITAS flux points in monthly bins, while the solid black points are the yearly averaged bins, with vertical error bars and horizontal bars representing the width of the time bin. The dashed horizontal green lines mark the range of the average flux measured by H.E.S.S. from 2004–2006. The horizontal dashed blue line denotes the period of *Chandra* observations, and the vertical dashed blue lines denote *Chandra* observations simultaneous with VERITAS.

inner radius large enough to avoid contamination from J1745–290 and excludes a 66° sector to prevent contamination from HESS J1746–285. The resulting spectrum, calculated with the forward-folding method from Piron et al., 2001, is pictured in the left of Figure 3.8 (the diffuse flux is multiplied by 10 for better visibility of the points). They found the diffuse spectrum is best fit by a pure power law (the solid red line) with an index $\Gamma \approx 2.3$ (Abramowski et al., 2016). For comparison, curves are drawn for the expected gamma-ray spectrum resulting from neutral pion decay for proton populations with an index of 2.4 ($\Gamma_p \approx \Gamma_\gamma + 0.1$) and exponential cutoffs of 2.9 PeV, 0.6 PeV, and 0.4 PeV (recall that the knee in the CR spectrum occurs at around 2 Pev). The preference of the pure power law indicates there is no cutoff in

the proton population for the case of hadronic emission.
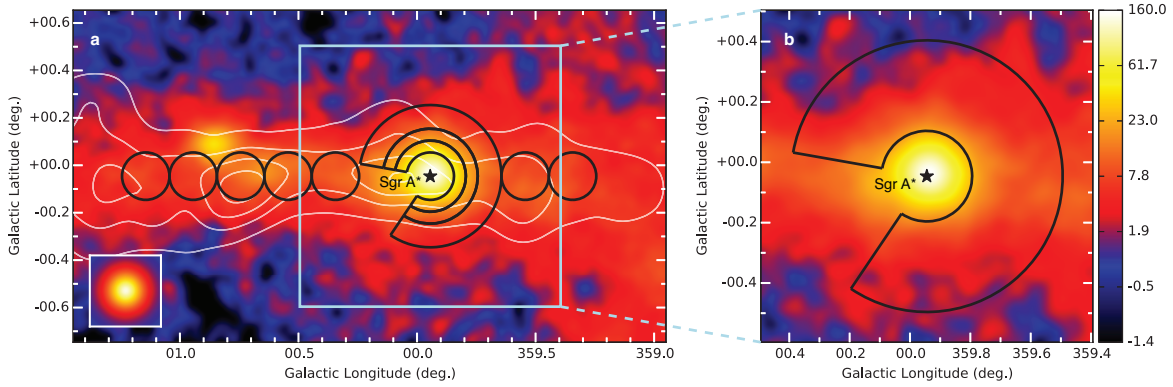
Figure 3.6: H.E.S.S. gamma-ray image of the GC region, with the color scale showing counts per 0.02° square bin (pixel) from Abramowski et al., 2016. The black regions on the left outline the regions of diffuse emission used for calculating the cosmic ray energy density. The white lines are contours of the CS line emission from Tsuboi et al., 1999. The simulated PSF is displayed in the bottom left inlay. The right shows a zoom of the blue-gray box on the left, with the region used for calculating the diffuse spectrum outlined in black. The black star represents Sgr A*.

The H.E.S.S. Collaboration et al. (2017) has further refined their results using a newly available 2D iterative maximum likelihood method to separate the ridge emission into four extended components in addition to the two point sources G0.9+0.1 (see subsubsection 3.1.3.1) and J1745–290. All components are significantly detected above 5σ. The most dominant one is called the dense gas component (DGC) and constitutes about half (52%) of the total flux. It is modeled by convolving the dense matter template as estimated by dense gas tracers with a 2D symmetric Gaussian centered at the origin in Galactic coordinates with a width of $1.11° \pm 0.17°_{\text{stat}} \pm 0.17°_{\text{sys}}$.

The next major component, called the large scale component (LSC), constitutes another 32% of the flux in the GC ridge, and does not correlate with the dense gas tracers. The LSC is modeled as an asymmetric 2D Gaussian centered at the position of Sgr A* with width parameters corresponding to extension in Galactic longitude and latitude. It is important to note that dense gas tracers, such as CS, are less effective at tracing gas if it is too diffuse or

too dense. It is possible that the LSC emission is due to interactions with low-density H_2 molecules. This is supported by data that show about 30% of the molecular gas in the CMZ is H_2 with a density of about $100\,\mathrm{cm}^{-3}$ (Dahmen et al., 1997).

Also centered on Sgr A* is a central component (CC) that is modeled as a symmetric Gaussian, which accounts for another 12% of the ridge flux. Its extent, $\sigma = 0.11°$, is about double the H.E.S.S. PSF, which separates this component from J1745–290 emission. The H.E.S.S. collaboration posits that the central component is from the increased energy density of CRs in the inner $20\,\mathrm{pc}$ of the CMZ, which is estimated to be about 10 times as high as that of the CMZ as a whole.

The final component, slightly offset from Sgr A*, is a small extended source named HESS J1746–285. For more information about this source, see subsubsection 3.1.3.2.

The results of the iterative model are shown in Table 3.4. The correlation between diffuse emission and molecular matter provide strong evidence for models of diffuse emission for which the majority of the emission is produced by the interaction of CRs with molecular matter.

Operating under the hypothesis that the diffuse emission is all caused by the same mechanism, H.E.S.S. Collaboration et al. (2017) averaged the spectrum over all diffuse regions using a stacking procedure that combines the statistics from those regions while adjusting their errors to account for double-counting of background statistics. The overall spectrum is best described by a power law with an index of $2.28 \pm 0.03_{\mathrm{stat}} \pm 0.2_{\mathrm{sys}}$ and a differential flux normalization of $(1.2 \pm 0.04_{\mathrm{stat}} \pm 0.2_{\mathrm{sys}}) \times 10^{-8}\,\mathrm{TeV}^{-1}\mathrm{cm}^{-2}\mathrm{s}^{-1}\mathrm{sr}^{-1}$ at $1\,\mathrm{TeV}$. This implies a total gamma-ray luminosity above $1\,\mathrm{TeV}$ of $2 \times 10^{35}\,\mathrm{erg\,s}^{-1}$ in the inner $2° \times 0.6°$.

The figure on the right in 3.8 shows the radial profile of the CR energy density of particles with energies $\geq 10\,\mathrm{TeV}$, integrated along the line of sight . The data are fit to constant, $1/r$, and $1/r^2$ curves. The best value of $\chi^2/\nu = 11.8/9$ results from the $1/r$ fit. Leaving the exponent of $1/r$ as a free parameter (fitting to $1/r^\alpha$) yields a best-fit value of $\alpha = 1.10 \pm 0.12$. This is consistent with the $1/r$ dependence, which is indicative of a steady source of CRs. This can be seen in Equation 2.18, which has a continuous injection rate $\dot{Q}(E)$ and follows a
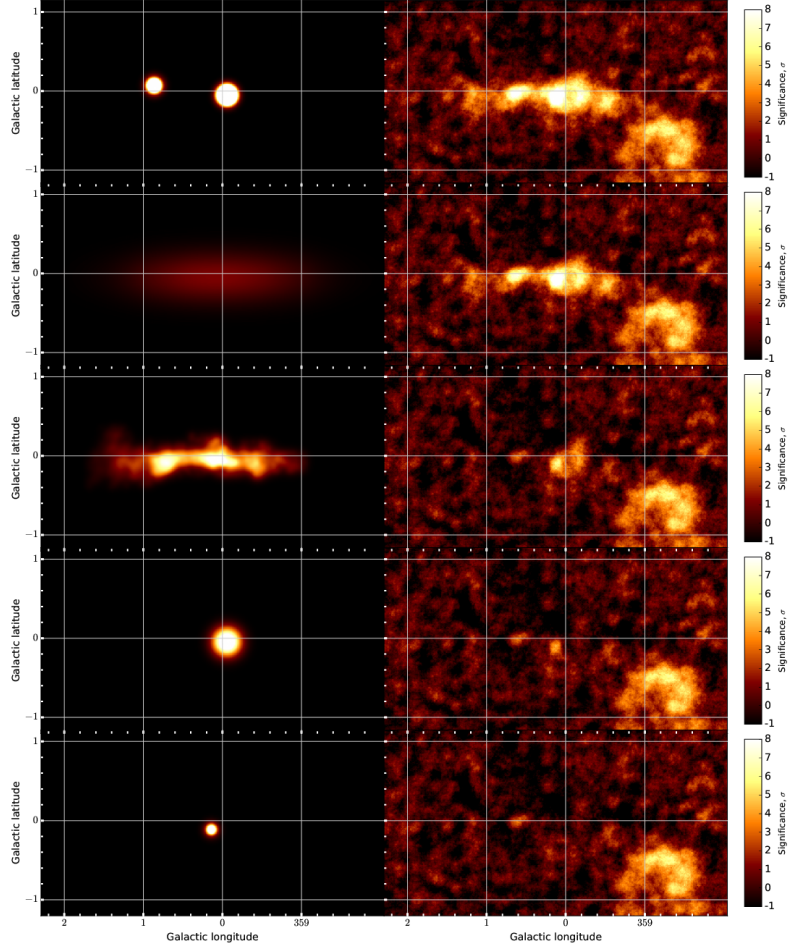
Figure 3.7: H.E.S.S. skymap showing the successive iterative stages breaking down the gamma-ray signal into components (H.E.S.S. Collaboration et al., 2017). The modeled components are shown on the left, and the residual skymap after subtraction of that component and those preceding it are shown on the right. The components from top to bottom are: the point sources J1745–290 and G0.9+0.1, the LSC, the DGC, the CC, and HESS J1746–285.

roughly $1/r$ dependence for $r < r_{\text{diff}}$.

3.1.3 Other Sources in the GC

VERITAS and H.E.S.S. also reconstructed the position and spectra of other sources, including SNR G0.9+0.1 and an unidentified source adjacent to the central source J1745–290. These sources are not central to my thesis but offer opportunities to study CR acceleration

Table 3.4: Fit parameters for the model components of the H.E.S.S. diffuse emission shown in Figure 3.7, including flux normalization at $1\,\mathrm{TeV}$ and extension of the source. If no extension is listed, the component is modeled as a point source. The components are the dense gas component (DGC), the large scale component (LSC), and the central component (CC) (H.E.S.S. Collaboration et al., 2017).

Model component	Extension (degrees)	Differential Flux (1 TeV) $[10^{-12}\mathrm{cm}^{-2}\mathrm{s}^{-1}\mathrm{TeV}^{-1}]$
Point Sources		
G0.9+0.1	–	$0.88 \pm 0.04_{stat} \pm 0.25_{sys}$
HESS J1745–290	–	$2.9 \pm 0.4_{stat} \pm 0.8_{sys}$
Extended Sources		
Dense Gas (DGC)	$\sigma = 1.11° \pm 0.17°_{stat} \pm 0.17°_{sys}$	$4.3 \pm 0.9_{stat} \pm 1.5_{sys}$
Central (CC)	$\sigma = 0.11° \pm 0.01°_{stat} \pm 0.02°_{sys}$	$1.03 \pm 0.05_{stat} \pm 0.25_{sys}$
Large Scale (LSC)	$\sigma_{\mathrm{x}} = 0.97°\,^{+0.04°}_{-0.02°}{}_{stat} \pm 0.13°_{sys}$ $\sigma_{\mathrm{y}} = 0.22° \pm 0.06°_{stat} \pm 0.07°_{sys}$	$2.68 \pm 0.6_{stat} \pm 1.3_{sys}$
HESS J1746−285	$\sigma_{\mathrm{x}} = 0.03° \pm 0.03°_{stat} \pm 0.03°_{sys}$ $\sigma_{\mathrm{y}} = 0.02° \pm 0.02°_{stat} \pm 0.03°_{sys}$	$0.24 \pm 0.03_{stat} \pm 0.07_{sys}$
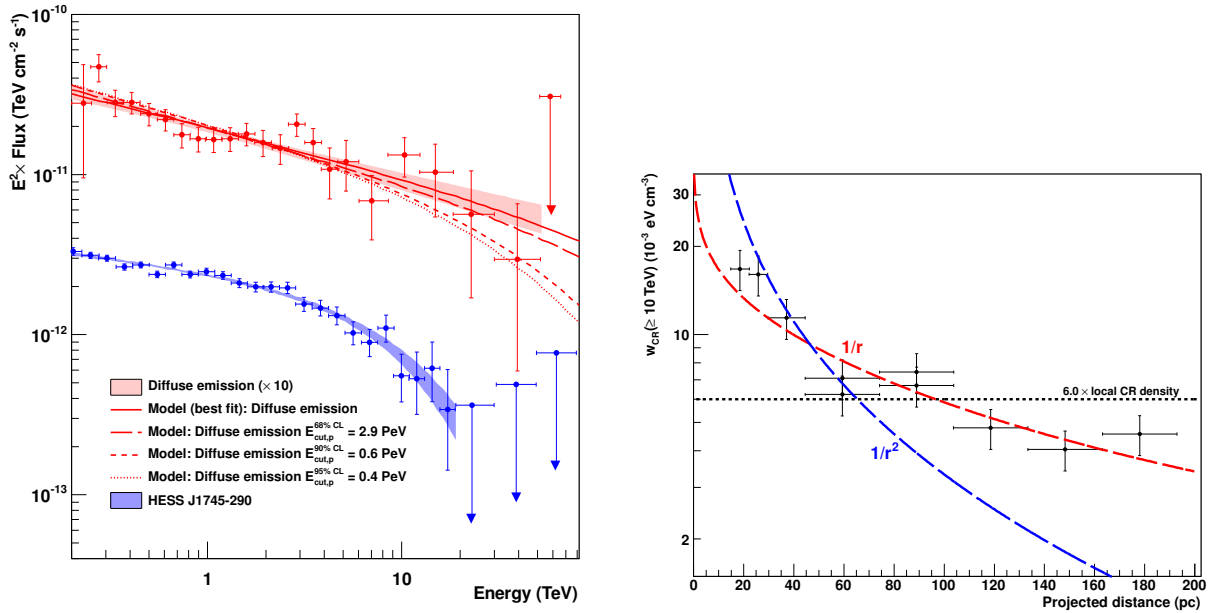
Figure 3.8: Left: spectra of diffuse emission (red) in the GC and the central source J1745–290 (blue) from Abramowski et al., 2016. Vertical and horizontal error bars represent the 1σ errors and bin sizes, respectively, and the shaded areas highlight the 1σ confidence bands for the best fit of each source. The diffuse spectrum is extracted from the annulus sector in the image on the right of Figure 3.6, and its scale is multiplied by 10 to separate it from J1745–290. The red curves show the best fit power law and computed models of neutral pion decay. Right: radial profile of the CR energy density versus the projected radial distance from Sgr A* (Abramowski et al., 2016). The curves are fits of the data to constant (black), $1/r$ (red), and $1/r^2$ (blue) forms.

and gamma-ray emission in the GC environment.

3.1.3.1   SNR G0.9+0.1

SNR G0.9+0.1 is a composite supernova remnant containing a bright, central, compact PWN and a surrounding external radio shell with a steep spectrum. It is the second strongest gamma-ray source in the CMZ and useful for studying the acceleration potential of SNRs in regions such as the GC.

The previous VERITAS result (Archer et al., 2016) gave a position of $l = 0.860° \pm 0.015°_{\text{stat}} \pm 0.013°_{\text{sys}}$, $b = 0.067° \pm 0.020°_{\text{stat}} \pm 0.013°_{\text{sys}}$ (Figure 3.9, left). The joint spectrum, including points from VERITAS and H.E.S.S., is shown in Figure 3.9, right. As is common for an SNR, the spectrum is best fit by a pure power law. The joint spectrum is best fit by a pure power law with an index of $2.51 \pm 0.07_{\text{stat}}$ which is in the normal range for SNRs. The flux normalization at $1\,\text{TeV}$ was also consistent with H.E.S.S., with a value of $N_0 = (0.707 \pm 0.066) \times 10^{-12}\,\text{cm}^{-2}\,\text{s}^{-1}\,\text{TeV}^{-1}$. This joint fit is consistent with the fit of the H.E.S.S. points from Aharonian et al., 2005, which had an index of 2.40 ± 0.11 and flux normalization of $(0.838 \pm 0.132) \times 10^{-12}\,\text{cm}^{-2}\,\text{s}^{-1}\,\text{TeV}^{-1}$ at $1\,\text{TeV}$.

The spectrum shows no sign of a cutoff over its entire range, which extends to almost $20\,\text{TeV}$. That contrasts with the clear cutoff seen in J1745–290, but $20\,\text{TeV}$ is still within the normal range of SNRs and PWNe, albeit on the higher end. This index is in the expected range for SNRs and is consistent with diffusive shock acceleration in general.
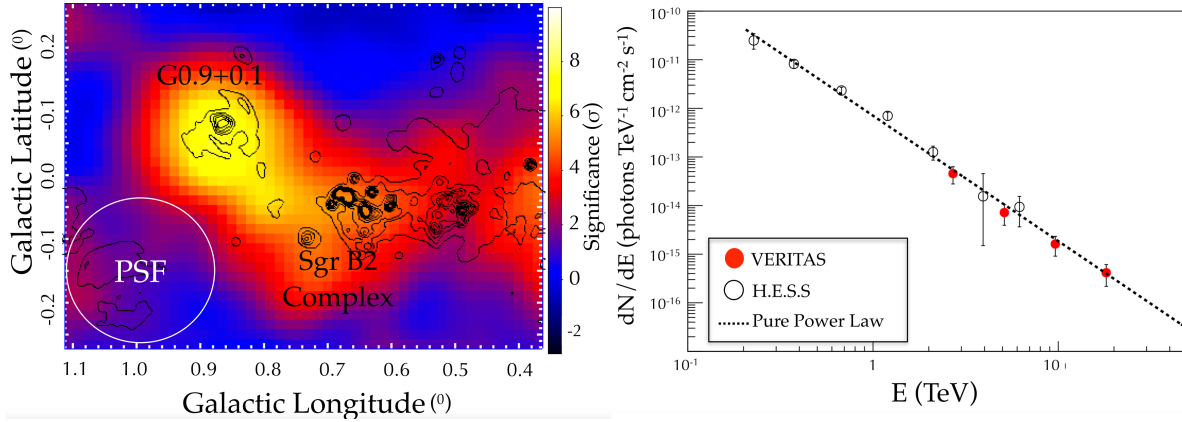
Figure 3.9: VERITAS skymap (left) and spectrum (right) of G0.9+0.1 from Archer et al., 2016. The spectrum includes H.E.S.S. points from Aharonian et al., 2005. The joint fit is best fit by a pure power law with an index of $2.51 \pm 0.07_{\text{stat}}$ and a flux normalization of $(7.07 \pm 0.66_{\text{stat}}) \times 10^{-11}\,\text{cm}^{-2}\,\text{s}^{-1}\,\text{TeV}^{-1}$ at $1\,\text{TeV}$.

3.1.3.2 Unidentified Source HESS J1746–285 / VER J1746–289

The final diffuse component mentioned in Subsection 3.1.2, HESS J1746–285, has not been identified with certainty, but is associated with a few known objects. The emission is likely to be from either a PWN or giant MC, and in either case can be compared with different possible emission mechanisms I am studying.

Its position in H.E.S.S.'s diffuse analysis is $\ell = 0.14° \pm 0.01$, $b = -0.11° \pm 0.02°$ in Galactic coordinates (H.E.S.S. Collaboration et al., 2017). Its spectrum above $0.35\,\mathrm{TeV}$ is best fit by a pure power law with an index of 2.2 ± 0.2 and a flux normalization of $F(1\,\mathrm{TeV}) = (1.8 \pm 0.5) \times 10^{-13}\,\mathrm{cm}^{-2}\,\mathrm{s}^{-1}\mathrm{T}, \mathrm{eV}^{-1}$. Its position falls near the center of the IR structure called the Radio Arc Bubble, which has a diameter of about 10 arcseconds (Butterfield et al., 2017; Rodriguez-Fernandez et al., 2001). It is also coincident with the PWN candidate G0.13-0.11 (Wang et al., 2002), with which the *Fermi*-LAT source 3FGL J1746.3-2851c is also associated. G0.13-0.11 is thought to be the most likely source of the VHE emission (Lemiere et al., 2015; H.E.S.S. Collaboration et al., 2017). While HESS J1746–285 appears to have a small extension (see Table 3.4), the Radio Arc Bubble's extension is markedly larger ($> 0.08°$). Its VHE spectral index is on the hard end of the typical range for a PWN.

At a similar location, VERITAS found an enhanced excess named VER J1746–289 at a position of $\ell = 0.055° \pm 0.01°_{\mathrm{stat}} \pm 0.013°_{\mathrm{sys}}$, $b = -0.148° \pm 0.01°_{\mathrm{stat}} \pm 0.013°_{\mathrm{sys}}$ (Archer et al., 2016). Its position was found by fitting an asymmetric 2D Gaussian with widths of $\sigma_\ell = 0.08°$ and $\sigma_b = 0.03°$ and a rotation angle with respect to Galactic latitude of $-15.4°$. Its statistical significance is 7.6σ and 6.7σ before and after applying trials factors, respectively. It is possible that differences between the VERITAS and H.E.S.S. measurements of the position and morphology of HESS J1746–285 have to do with the increased energy threshold of VERITAS (Archer et al., 2016).

MAGIC also found a corresponding source at Galactic coordinates of $(0.137°, -0.121°)$ with an uncertainty of $0.03°$. It was given the name MAGIC J1746.4-2853 (Ahnen et al., 2016). This source is closer in position to HESS J1746–285 than VER J1746–289. Because of

the proximity and consistent morphology of all three sources, they have the same associations and are likely to be the same source. Ahnen et al. (2016) also propose that the giant molecular cloud G0.11-0.11 may create VHE emission via its interactions with high-energy particles. It is important to note that the VERITAS source contains more of the diffuse emission that was separated in the H.E.S.S. analysis. In my analysis, I will investigate the VERITAS position of VER J1746–289 more closely.

3.2 Models of VHE Emission from J1745–290

The more information we learn about the characterization of VHE emission from the GC, the better we will be able to determine its production mechanism. Unlike lower-energy experiments, VERITAS, H.E.S.S., MAGIC, or *Fermi*-LAT do not have pointing accuracy sufficient to distinguish the exact location of emission, so there are several potential candidates for the high energy emission. The most popular candidate is the SMBH itself, for which numerous emission models have been proposed with hadronic, leptonic, and hybrid mechanisms. With Sgr A East ruled out by high precision measurements of the centroid (Acero et al., 2010), the primary alternative candidate is the PWN G359.95-0.04, discovered by *Chandra* by Baganoff et al. (2003) and originally hypothesized to be a PWN by (Wang et al., 2006). Due to its relatively low overall bolometric luminosity compared to other SMBHs ($10^{-8}L_{\mathrm{Edd}}$), the radiation fields surrounding the GC are mostly transparent to photons up to and exceeding $10\,\mathrm{TeV}$ (Aharonian & Neronov, 2005a). This is because there are less dense IR radiation fields in which pair production can occur.

The primary foci of investigation include localization of the source, the spectrum and total flux of emission, signs of variability and past activity, and understanding the relationship to diffuse emission. Figure 3.10 shows the spectral energy distribution of the GC point source with points from multiple experiments and predicted curves from various hadronic and leptonic models of gamma-ray emission. In this section I will discuss the physics and predictions of these and other models of emission from J1745–290 that do not conflict with observations.
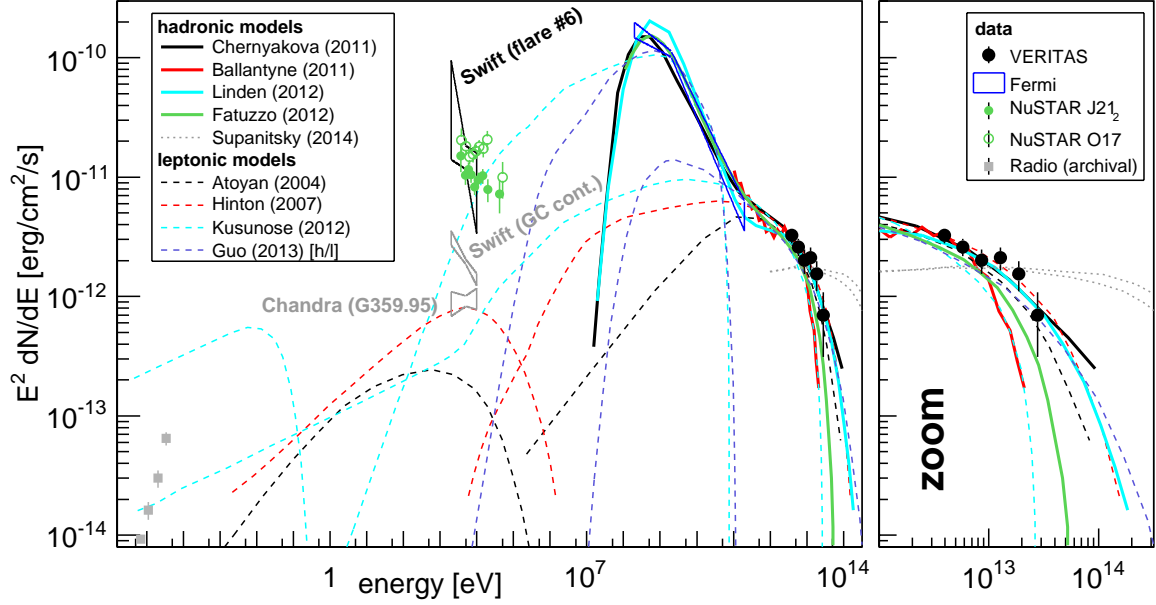
Figure 3.10: An overview of the spectrum of Sgr A* over a large range of wavelengths, including the observed spectra from various X-ray instruments, along with gamma-ray data from *Fermi*-LAT and VERITAS, compared with various models mentioned in this section (Archer et al., 2014).

3.2.1 Hadronic Models

There are numerous models that describe potential hadronic mechanisms of high-energy gamma ray emission, the majority of which predict the gamma-ray production to happen either very close to the event horizon of the SMBH, or in the ambient medium in the $\approx 10\,\mathrm{pc} \, \hat{=} \, 0.073°$ zone surrounding the SMBH (van Eldik, 2015).

Examples of the former case are the models proposed by Aharonian & Neronov (2005a) in which protons are accelerated within 10 Schwarzschild radii (R_s, Equation 1.1) of Sgr A*. The maximum energy achievable by protons in their model of electromagnetic acceleration is, by Equation 2.20,

$$E_p \sim eBR \tag{3.4}$$

$$\simeq 10^{18} \left(\frac{B}{10^4\,\mathrm{G}} \right) \left(\frac{M}{3 \times 10^6\,\mathrm{M_\odot}} \right) \, \mathrm{eV} \tag{3.5}$$

where M is the mass of Sgr A*, which has a current estimate of Sgr A* of about $4 \times 10^6\,\mathrm{M_\odot}$

(see Subsection 1.1.1). A common estimate of the value of the magnetic field strength near Sgr A* is only about $100\,\mathrm{G}$, however it is hard to measure and there may be regions that are much stronger.

Given this acceleration scenario, there are a few possible mechanisms proposed for protons to create gamma-ray emission. If the magnetic fields are strong, protons could emit gamma rays via synchrotron and curvature radiation. However, if the protons undergo synchrotron radiation in the same field that is causing their acceleration, the energy of synchrotron will be limited to $\epsilon_{\mathrm{max}} = \frac{9}{4\alpha_f} m_p c^2 \simeq 0.3\,\mathrm{TeV}$ with ideal parameters because of energy loss by synchrotron cooling (Aharonian & Neronov, 2005a). This picture is thus unable to explain the gamma-ray flux we observe unless the source of acceleration and emission moves toward Earth with a Lorentz factor of at least 10. An alternate scenario exists in which protons are accelerated along regular magnetic field lines and are injected into a separate region of chaotic fields. Curvature radiation in the regular magnetic fields could potentially create gamma rays with energies of $10\,\mathrm{TeV}$ for field strengths of $B \simeq 10^6\,\mathrm{G}$. However, with magnetic fields this strong, the mean free path for magnetic pair production would be too small for gamma rays exceeding $1\,\mathrm{TeV}$ to escape Sgr A*.

Another emission mechanism involves photo-meson interactions. Protons with energies on the order of $10^{18}\,\mathrm{eV}$ will interact with a high cross section with photons in the IR–mm range, which are very abundant. These interactions produce gamma rays, neutrons, and neutrinos. The gamma rays cover a wide range of energies, but only those up to $10^{12}\,\mathrm{eV}$ and above $10^{18}\,\mathrm{eV}$ will escape the approximately $10^{11}\,\mathrm{m}$ radius IR radiation field around the black hole. Detection of fluxes of $10^{18}\,\mathrm{TeV}$ gamma rays, neutrons, and neutrinos would offer support for this model. X-rays are created by electron cooling by magnetic fields of strength $B \geq 10\,\mathrm{G}$.

If the magnetic fields near Sgr A* are not stronger than $10^4\,\mathrm{G}$, as required by the above scenario, the protons will retain the energy not being lost by photo-meson interactions. They will then be free to interact with the ambient molecular gas where proton-proton interactions will occur, resulting in gamma rays via the mechanisms explained in Subsection 2.3.4. In this case, the protons must be accelerated by something other than magnetic fields, and could gain energy from strong shocks caused by accretion flow in the accretion disk. Secondary

gamma rays and electrons will be produced with a small efficiency on the order of 10^{-4}, which is determined by the ratio of accretion time to the proton-proton cooling time t_{pp}. The efficiency of this model for converting energy of the primary proton into secondary gamma rays is very small, on the order of 10^{-4}, for any moderate estimate of physical parameters in the acceleration regime. Therefore, to match the TeV luminosity of $10^{35}\,\mathrm{erg\,s^{-1}}$, a luminosity of $10^{39}\,\mathrm{erg\,s^{-1}}$ would need to be available for accelerating protons. This model predicts that X-ray flares should have accompanying TeV flares, though they may be of different magnitudes. It does not predict an associated neutrino flux.

All of the models in which the emission happens very close to the event horizon of Sgr A* (Aharonian & Neronov, 2005a) predict correlation between variability in X-rays and gamma rays, which has not been observed to this date. These models may be able to accommodate the spectrum of TeV emission, but underpredict the flux of 2FGL J1745.6-2858 compared to measurements (van Eldik, 2015).

There are also many models in which protons that are accelerated close to Sgr A* diffuse away and produce gamma rays farther out, in the inner $\approx 10\,\mathrm{pc}$ of the Galaxy (Aharonian & Neronov, 2005b; Liu et al., 2006b; Wang et al., 2009; Chernyakova et al., 2011; Ballantyne et al., 2011; Linden et al., 2012). In these models, protons are accelerated near the central SMBH, reaching very high energies as they orbit. Liu et al., 2006b introduce the idea that proton acceleration occurs in the same accretion torus that stochastically accelerates electrons which emit millimeter and shorter-wavelength photons. The high energy protons can then diffuse into the interstellar medium and interact with it, being injected either steadily or during times of impulsive accretion rates (resulting, for example, from tidal disruption of a star). This diffusion can take a long time compared to the duration of flares, making these models compatible with the lack of gamma-ray flares associated with known X-ray flares. Neutral pion decay is the primary channel for gamma-ray production following the hadronic interactions. If this is indeed the dominant mechanism, then the flux level we observe should tell us about the densities of the cosmic ray population and of molecular gas, which serves as the target for $p - p$ interactions.

In the case of steady-state hadronic emission, Linden et al. (2012) expect the gamma-ray

morphology to primarily reflect the distribution of target gas, rather than the patterns of cosmic ray injection and propagation. Therefore, comparisons of TeV morphology to dense gas tracers such as CS line emission are very important.

An important aspect of these different models is their ability to explain the spectral breaks and inflection points between different energy regimes. According to Chernyakova et al., 2011, the secondary electrons created in the hadronic interactions emit X-rays by synchrotron radiation and bremsstrahlung. Additionally, the MeV/GeV spectral break could be explained by energy dependence of the diffusion coefficient.

Fatuzzo & Melia (2012) claim that that the bimodal inflection in the GeV/TeV spectrum indicates a stochastic acceleration that does not lead to variability in the gamma-ray emission from Sgr A*. In this model, there is a molecular torus at the center of the Galaxy, with an inner radius about $1.2\,\mathrm{pc}$ (millions of Schwarzschild radii) in diameter with a thickness of about $1\,\mathrm{pc}$. This is surrounded by a uniform wind zone, where stellar winds from surrounding young stars interact with each other. Proton-proton scattering leads to π^0 decays or $\pi^{\pm}$ cascades which produce gamma rays. Such scattering in the inner torus produces gamma rays with a spectrum that is strong in the GeV range observed by *Fermi*-LAT. Scattering occurring in the wind zone is said to be responsible for the TeV emission.

The various models of hadronic emission fall into two distinct classes. In both, the acceleration of CRs happens very close to Sgr A*. In one class, the emission also occurs very close to Sgr A*, within tens of Schwarzschild radii, and in the other class, it happens after the CRs diffuse outward tens of parsecs. In the former case, abrupt changes in accretion rates would cause measurable flaring. One effective way to test between these two classes of models would be to put limits on the spectral variability above $10\,\mathrm{TeV}$ (Archer et al., 2016) The class of nearby emission would predict variability on hour timescales, while the class of emission occurring farther out only predicts variability on timescales of years or greater. A viable emission mechanism must be able to explain the TeV and explain, or be consistent with, nonthermal X-ray and GeV emission. According to Chernyshov et al., 2017, purely hadronic models underpredict the X-ray flux by an order of magnitude given parameters that reproduce the correct gamma-ray intensity. This is the case whether particles are injected

continuously or in a past transient event. There could, however, be a separate mechanism that causes the lower-energy emission.

3.2.1.1 VHE Neutrinos

Observations of high-energy neutrinos, including recent data from the IceCube experiment, may provide additional help in discriminating between mechanisms of gamma-ray emission that also emit neutrinos. Neutrinos are only produced in hadronic interactions, so observation of neutrinos coincident with gamma rays would provide very strong support for hadronic models of emission from J1745–290.

Fujita et al. (2015) predict that the accretion flows of low-luminosity AGNs, such as Sgr A*, will be radiatively inefficient if their accretion rate $\dot{M}$ is less than 10% of the Eddington accretion rate, $\dot{M}_{\mathrm{Edd}} = L_{\mathrm{Edd}}/c^2$. Protons accelerated stochastically in the radiatively inefficient accretion flow interact with nucleons and photons in the plasma of the accretion flow, generating gamma rays and neutrinos. The authors state that the gamma rays and neutrinos should thus have a similar spectra. Their model fits the data between 0.2 and $10\,\mathrm{TeV}$ if the accretion rate was greater by at least 3 orders of magnitude 100 or more years ago. This time frame is acceptable because the lifetime of the CRs exceeds 100 years. This circumstance is supported by studies such as Ryu et al., 2013, which finds evidence of previous strong flaring through X-ray echos off of the Sgr C complex.

Supanitsky (2014) discusses the same mechanism for neutrino production, beginning when cosmic ray protons interact with ambient protons. They examine the resulting spectra for gamma rays and neutrinos for different mechanisms of proton acceleration and compare them. They propose an observable, non-variable modification to spectral shape that is caused by gamma rays interacting with the radiation field in the ISM. Because the amount of interaction depends on the distance of the source, this information can be used to identify sources. The hypothesis that these neutrino events came from charged pion decays could be tested by VERITAS and other experiments, because we should see a similar spectrum of TeV gamma rays from neutral pion decays. Recently, *IceCube* detected several neutrinos with energy

greater than 30 TeV (Aartsen et al., 2013), seven of which came from near the direction of the GC. One of these occurred about three hours after a *Chandra*-observed X-ray flare of Sgr A*. They performed a time clustering analysis and found a *p*-value of only 0.009 that this neutrino event would be coincident with the flare within a 12 hour window purely by random chance. Another two were detected within a time period of one day, which by their calculation could only occur with a probability of 1.6 % if their distribution in time were random. Bai et al. (2014) believe this is evidence that Sgr A* is a point source emitter of VHE neutrinos.

3.2.2   Leptonic Models

There are also models that propose leptonic origins of the gamma-ray emission from the GC. The leptonic mechanism with the potential for creation of the highest energy gamma rays is inverse Compton (IC) scattering, where a high-energy electron scatters off a low energy photon, imparting much energy to the photon. The other mechanisms, synchrotron radiation and bremsstrahlung, do not create photons of high enough energy to dominate the VHE range. The cross-section for IC scattering is given by the Klein-Nishina formula, Equation 2.44. This means higher energy emission should be highly K-N suppressed when the radiation fields have higher temperatures. For example, if the temperature of the photon field exceeds 100 K, emission above 10 TeV will be highly suppressed. The flux of IC emission provides us with information different from hadronic models. The rate of IC processes depends on the population of high energy electrons and the density of ambient light near the GC. This ambient light could come from stars, cosmic microwave background, or other sources.

Soon after the first detection of the GC by H.E.S.S., a plerion, or wind nebula model of leptonic emission was proposed (Atoyan & Dermer, 2004). This model utilizes an advection-dominated accretion flow (ADAF). Electrons are accelerated to approximately 100 MeV in the inner $20R_s$ of the black hole by second-order Fermi processes. These processes are driven by the magnetohydrodynamics of the turbulent magnetized corona, which is a sea of plasma similar to what surrounds the Sun. These electrons emit synchrotron radiation in the radio /

sub-mm range. Closer to the center of the black hole, the orbit is said to be more stable, and instabilities and shocks will result in higher energies due to first-order Fermi acceleration. The synchrotron radiation from these higher energy electrons is responsible for the X-ray flares, such as those observed by *Chandra*, *XMM-Newton*, and *INTEGRAL*. The ADAF also drives a sub-relativistic magnetohydrodynamic wind, whose termination shock accelerates electrons much in the same way as a pulsar wind nebula, about $10^{14.5}$ m from the SMBH. These electrons, after injection, create steady-state X-ray emission and interact with the FIR dust radiation through IC scattering, bumping these photons to TeV energies.

In another leptonic model proposed by Kusunose & Takahara (2012), nonthermal electrons are accelerated by NIR and X-ray flares. These electrons accumulate in a region with a size of about 10^{16} m and magnetic fields weaker than 1×10^{-4} G, then IC scatter off of soft photons emitted by stars and dust.

One shortcoming of the various leptonic models is that most of them cannot explain the MeV/GeV emission and the TeV emission simultaneously. This could mean that there are just different regions of emission with different properties; there is too much positional uncertainty in *Fermi*-LAT, H.E.S.S., and VERITAS to say that the emission is coming from a single location. Models such as the curvature radiation-inverse Compton model (Aharonian & Neronov, 2005a) also require ordering of the electric and magnetic fields in the inner few R_s near the central SMBH. Purely leptonic models are able to explain both the X-ray and gamma-ray emission, and are theoretically better at explaining *Fermi*-LAT emission than any hadronic models (Malyshev et al., 2015).

Perhaps the most likely alternative to Sgr A* for an astrophysical source of TeV emission from J1745–290 is the energetic PWN G359.95-0.04. This source is too close to Sgr A* to be eliminated as a candidate based on its location, with its tail being a mere 4 arcseconds from the SMBH and its extent less than 5 arcseconds away. Furthermore, its quiescent state flux of X-ray emission is quadruple that of Sgr A*. The PWN could be a source of high energy electrons and positrons that are ejected in the wind powered by the spin down energy of the pulsar. These high-energy electrons inverse-Compton scatter off of ambient photons. Wang et al. (2006) claim that far infrared radiation (FIR) photons, such as stellar

photons reprocessed by dust, are better targets than the ultraviolet (UV) photons, which are suppressed by the Klein-Nishina effect. PWNe are not known to exhibit variable behavior, so observation of variability would disfavor G359.95-0.04 as the central emitter.

Hinton & Aharonian (2007) also discuss a relationship between G359.95-0.04 and the TeV emission from HESS J1745–290. They found that the X-ray spectrum softened as the distance increased from the pulsar's head. This could mean that the electrons are cooled by synchrotron radiation or Thomson scattering, rather than by IC scattering in the Klein–Nishina (K-N) regime. Based on the flux of the H.E.S.S. emission for $E \gtrsim 1\,\mathrm{TeV}$, they estimate the PWN to have a magnetic field strength of $\gtrsim 100\,\mu\mathrm{G}$ and an average FIR density of about $5000\,\mathrm{eV/cm^3}$. They predict an electron injection spectrum that follows $\frac{dN}{dE} \propto E^{-\alpha} e^{-E/E_0}$ with a spectral index of 2 and cutoff energy of $100\,\mathrm{TeV}$. The injection source should have a total power of $6.7 \times 10^{35}\,\mathrm{erg/s}$ and an age of 10,000 years according to this model.

They also discuss the possible relationship of J1745–290 to the *INTEGRAL* source IGR J1745.6-2901.

Another alternative model that could explain both the *Fermi*-LAT and TeV central excesses is a population of millisecond pulsars (MSPs) postulated by Bednarek & Sobczak, 2013. This MSP population at the GC could be the result of a past merger of globular clusters in the central parsec of the Galaxy. The *Fermi*-LAT and VHE emission would be due to the MSPs themselves and inverse-Compton scattered electrons accelerated in the wind regions of the MSPs, respectively. Given $10\,\%$ energy efficiency for HE lepton creation, thousands of MSPs would be required to exist within the central $10\,\mathrm{pc}$ region of the GC. In Bartels et al., 2016, this hypothesis is supported, and it is claimed it can explain all of the *Fermi*-LAT excess. In Bartels et al., 2018, they further this claim, adding that the binaries born from MSPs could create the $511\,\mathrm{keV}$ line emission.

All of the leptonic models discussed in this section are able to match the TeV spectrum observed (Archer et al., 2014). One weakness of the models proposed in Atoyan & Dermer, 2004 and Hinton & Aharonian, 2007 is that they do not match *Fermi*-LAT (Chernyakova et al., 2011) spectral points. It is possible, though, that the *Fermi*-LAT spectrum contains

signal from other sources because of its relatively poor angular resolution. Mori et al. (2015) analyze the spectral energy distribution of X-rays in the 20–40 keV range using *Chandra* data of IGR J17456–2901. They find it is consistent with a model that includes emission from G359.95–0.04 and the central hard X-ray emission (CHXE). Because the CHXE is not expected to emit gamma rays, they conclude G359.95–0.04 is the most likely X-ray counterpart of J1745–290.

3.2.3   Hybrid Models

There is no known reason that the emission must come from a single mechanism. (Guo et al., 2013) suggest a hybrid model that involves both hadronic and leptonic emission to explain the GeV/TeV shape. They assert that the occurrence of flares, such as those in the X-ray and NIR bands, imply there have been, and are, activities occurring in the GC that could accelerate protons and electrons. They suggest accretion of stars and gas as one such possibility for this activity. While this activity is thought to be continuous, it could explain the current gamma-ray flux as as originating from one large flare of $\gtrsim 10^{48}$ergs that occurred in the GC on the order of 100 years ago. This flare accelerated protons and electrons to very high energies, as well as a sea of soft thermal photons, which all diffused outward. In their model, TeV gamma rays are produced when the high energy protons collide with the ISM. The *Fermi*-LAT GeV emission is caused by IC scattering off the electrons, which also emit lower energy synchrotron radiation. The MeV–GeV portion of the spectrum is mostly due to the fast cooling electrons. They emit via IC scattering off of the soft photons in the radiation field near the inner parsec, which predicts the same physical location as Fatuzzo & Melia, 2012 for this part of the spectrum, albeit through a different mechanism. The hadrons that diffuse out farther (>3 pc) interact with the interstellar gas and create gamma rays via the familiar π^0 decay channel.

Hybrid models provide an alternative when purely hadronic or leptonic models have shortcomings. Chernyshov et al. (2017) suggest that hybrid models involving protons and electrons can explain emission from both the GeV and TeV central sources, but require a low

ratio of protons to electrons.

3.3   Models of Diffuse Emission

The mechanism behind the diffuse gamma-ray emission in the CMZ is one of the most important parts of painting a full picture of the GC. Of particular importance therein are its relationship to the concentrations of molecular matter and its large role in determining the total energetics of the region. For example, diffuse emission accounts for about 80% of the GC flux around the $80\,\mathrm{GeV}$ range (De Angelis & Mallamaci, 2018). Because of the strong correlation of the diffuse components with dense gas (see Figure 3.7), the most likely mechanisms of gamma-ray emission involve interactions between VHE cosmic ray particles and molecular particles and interstellar photons. The most relevant channels for TeV gamma rays are neutral pion decay for CR protons and IC scattering for CR electrons.

Observations such as those in Abramowski et al., 2016 show that the accelerator of these CRs appears to be at or near the GC. The accelerator could be the same source as J1745–290, such as Sgr A* or G359.95-0.04. If there is a common source of cosmic rays for Sgr A* and diffuse emission, its power will have to be extremely high.

Various models have been proposed to describe the diffusion of CR particles from the accelerator into the surrounding medium (this was covered in Subsection 2.1.2). Gaggero et al. (2017) present a CR transport model in which the diffusion coefficient depends on the position. This model is able to reproduce *Fermi*-LAT findings of a radially-dependent spectral index of the CR population.

The model proposed in Ballantyne et al., 2011 predicts that protons are accelerated by accretion flow to the SMBH, before diffusing outward to interact with the surrounding molecular gas. They examine two possible cases involving different diffusion coefficients that fit the H.E.S.S. data. One is a more sustained accelerator, lasting over 10,000 years, with a hard diffusion coefficient of $\alpha \approx 0.75$. The alternative model involves a softer diffusion coefficient of $\alpha \approx 2.7$, and a short burst that occurred ~ 10 years ago. The latter case predicts noticeable variability for shorter timescales of $\lesssim 5$ years, but for higher energies of

$E \gtrsim 10 \, \text{TeV}$.

One important distinction to make is that CR protons can diffuse farther because of their slower energy loss to synchrotron radiation. In general, models of hadronic emission from the central source will also show less variability. Leptonic models do not diffuse as far and favor the PWN source.

3.3.1 The GC as an Accelerator of PeV Cosmic Rays

Recent results from H.E.S.S. have shown evidence that the central point source J1745–290 could be host to an accelerator of PeV cosmic rays, or a PeVatron (Abramowski et al., 2016). This conjecture arises primarily because of the lack of a cutoff seen in the reconstructed spectrum in Figure 3.8, implying the presence of PeV or potentially higher CRs. By Equation 3.5, protons could reach PeV energies near Sgr A* if the magnetic field strength is only a few Gauss.

While the power-law index is consistent between the central point source and the diffuse emission, one point of discrepancy is the cutoff present in J1745–290 that is not seen up to 40 TeV in the diffuse spectrum. The cutoff could be explained by enhanced absorption caused by a small volume filling factor of the structure near the center of the Galaxy (Guo et al., 2016). This factor increases farther away from the GC, making negligible the enhancement in absorption. From more accurate modeling of interstellar radiation fields and the pair-absorption effects that occur within them, it has been shown that the expected high-energy cutoffs of diffuse gamma-ray emission could be understimated by a factor of approximately two (Porter et al., 2018).

Another potential PeVatron source of cosmic rays could be population of millisecond pulsars (MSPs) that are spatially distributed around a $10^3 \, \text{pc}$ bulge around the GC (Guépin et al., 2018). This is a much more sparse population of MSPs than the concentrated cluster postulated by Bednarek & Sobczak, 2013 to explain the emission from J1745–290. They were able to match the H.E.S.S. diffuse emission with a population of about 10^4 MSPs with moderate acceleration efficiencies of $\eta_{\text{acc}} \sim 0.03$.

Determining the accelerator, or accelerators, of PeV cosmic rays could explain the "knee" feature in the CR spectrum (Figure 2.3). A more detailed discussion will be included with my results in Section 7.4.

3.4 Dark Matter Annihilation in the Galactic Halo

Another potential source of gamma rays emanating from the GC is the annihilation of DM particles. The scientific background for the weakly interacting massive particle (WIMP) model of particle DM is summarized in Appendix A.2. Modern experiments could theoretically detect gamma rays resulting from annihilation of the lightest supersymmetric partner, the sneutralino. The primary channels examined by VERITAS are:

$$\chi\chi \to b\bar{b} \tag{3.6}$$

$$\chi\chi \to \tau^+\tau^- \tag{3.7}$$

where χ is the sneutralino. The GC is an excellent region to study because of its high J-factor (defined in Equation A.5), which is quoted in van Eldik, 2015 as $J\Delta\Omega \approx 2 \times 10^{21}$ GeV^{2}sr/cm^5.

VHE gamma-ray experiments such as VERITAS and H.E.S.S. have been able to constrain the annihilation cross-section of the above interactions to the maximum allowable values according to many supersymmetric models (Abramowski et al., 2015). As reported by Livio & Silk (2014), multi-TeV mass WIMPs are gaining popularity, and an annihilation signal could be detected at these masses by VERITAS or H.E.S.S. (Archer et al., 2014). At super-TeV masses, the annihilation cross-section of the DM particle could be increased further by Sommerfeld enhancements. Because the central region of the GC has too much emission from other sources to reliably pick out DM signals, gamma-ray instruments typically look in an annulus region excluding the central region. Since no excess has been seen in the annulus region, it is not possible to explain the GC excess by DM at TeV.
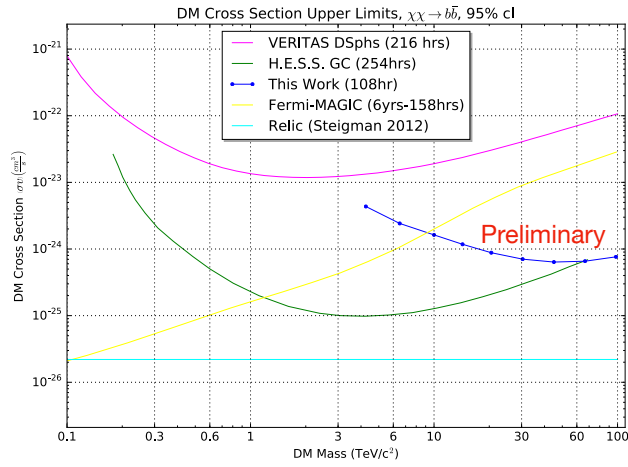
Figure 3.11: DM cross-section upper limits for the $\chi\chi \to b\bar{b}$ channel. At the upper end of DM mass, VERITAS can outperform H.E.S.S. Courtesy Nathan Kelly-Hoskins.

CHAPTER 4

VERITAS

My research has been conducted with the Very Energetic Radiation Imaging Telescope Array System (VERITAS) project. VERITAS is a ground-based imaging atmospheric Cherenkov telescope (IACT) designed to detect gamma rays in the very high-energy (VHE) regime. It is the successor of the Whipple 10m telescope and thus in the second generation of IACT instruments, among two others that are currently operating: MAGIC and H.E.S.S. The next generation of IACTs is underway with the construction of the much more powerful Cherenkov Telescope Array (CTA), however it will likely be a number of years before any data are taken. VERITAS is part of the Fred Lawrence Whipple Observatory (FLWO), located in Amado, Arizona at coordinates 31°40′30″N, 110°57′7″W and an altitude of 1268 m above sea level. For optimal gamma-ray detection, IACTs such as VERITAS are built in areas with low humidity and low levels of light pollution to reduce the amount of background light reflecting into the cameras. Higher altitude locations are preferable because gamma showers have to travel through less atmosphere, experiencing less dimming prior to detection, leading to a lower

Figure 4.1: The VERITAS site at FLWO in Arizona. The telescopes pictured from left to right are T2, T4, T1, and T3.

energy threshold for the instrument.

4.1 Imaging Atmospheric Cherenkov Technique

VERITAS detects gamma rays in the energy range of 80 GeV up to 50 TeV. In this very high energy range, particles entering Earth's atmosphere will create extensive air showers (EAS) as explained in Subsection 4.1.1. Thus, these gamma rays cannot be detected directly as with space-based telescopes such as the Fermi Large Area Telescope (Fermi-LAT). Ground-based VHE gamma-ray instruments such as VERITAS must employ a special technique to detect high energy gamma rays, referred to as the imaging atmospheric Cherenkov technique. The telescopes in an IACT focus Cherenkov light from the extensive air shower (EAS) onto their cameras and an image of the shower is recorded. The schematic of a typical IACT system can be seen in Figure 4.2.
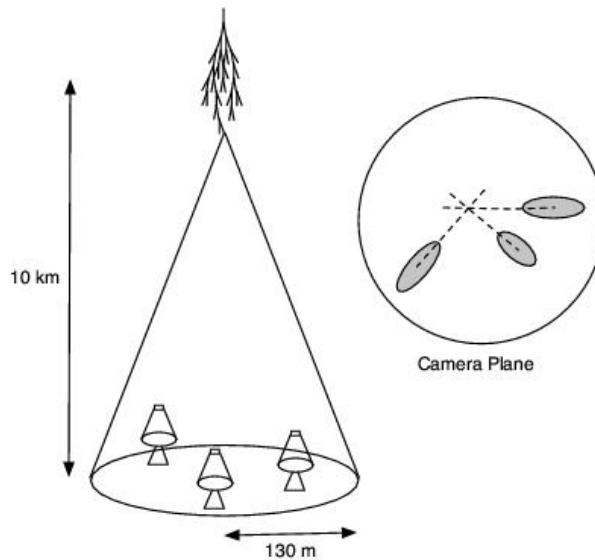
Figure 4.2: A diagram of a typical IACT collecting light from an extensive air shower, illustrating how the spread-out light from the shower is collected by the telescopes. 20 km is a typical height at which the shower is initiated (Holder, 2012).

The raw data from air shower images is processed through a multiple-stage analysis which is detailed in Chapter 5. The images are first parameterized, and those parameters are

used in combination to reconstruct the original energy and direction of the incident gamma ray. Having multiple telescopes provides multiple images, giving more information to help reconstruct the direction of the incoming particle. This also creates a larger collection area and takes advantage of the large spread of the Cherenkov air showers.

Another important step of the analysis is to determine if the air shower was initiated by a gamma ray or a hadronic cosmic ray. While astronomical sources will emit both kinds of particle, gamma rays are much more useful to study because they are uncharged and their trajectories are unaffected by magnetic fields. Their incoming direction is the same as their direction of origin, so with proper direction reconstruction a gamma ray can be properly attributed to a specific source in the sky. Both kinds of high-energy particles will create air showers of particles after entering the atmosphere, but the general shape of a shower depends on the particle that initiates it. VERITAS and other ground-based IACTs use this information to select which shower events are initiated by gamma rays.

4.1.1 Extensive Air Showers

The properties of air showers can be well-understood in terms of fundamental high-energy particle interactions. In Section 2.3, we discussed a number of interactions that energetic particles undergo in the presence of other particles. As the density of matter increases, so does the likelihood of those interactions. When a high-energy particle enters the relatively high density of Earth's atmosphere, it will interact with particles in the atmosphere, emitting radiation as it travels through the atmosphere. If the energy of the incident particle is great enough, it can collide with air molecules to produce new products. Because momentum in the reaction is necessarily conserved, the products will continue with momenta largely in the same direction as the incident particle. If these products are very energetic, they can repeat the same process, which results in a cascade of many particles and photons called an extensive air shower (EAS). Almost any primary particle with high enough energy can initiate an EAS, but the resulting cascades fall into two main categories that have distinctive characteristics. Hadronic air showers are initiated by a high energy proton, nucleus, or other hadronic particle.

Electromagnetic air showers are initiated by a gamma ray, electron, or π^0 which will decay into two gamma rays. Simulations of two such cascades is shown in Figure 4.3. These air showers can be detected by IACTs, so an understanding of their development is necessary.

4.1.1.1 Electromagnetic Cascades

If the primary particle is a high-energy photon, it will interact with the atmosphere to produce an electron-positron pair. That electron / positron pair will diverge and emit high-energy photons via bremsstrahlung. Those photons can themselves pair produce, and those particles will radiate bremsstrahlung of their own, and so on, creating a cascade of photons, electrons, and positrons. If the primary particle is instead an electron or positron, the same repeating cycle will begin with bremsstrahlung. A simulation of an electromagnetic cascade is shown in the left of Figure 4.3.

The development of the air shower can be described by the characteristic behavior of charged particles and high energy photons moving in the atmosphere. The radiation length (ξ) is defined as the mean expected length that an electron travels through a medium before its energy is reduced to $1/e$ of its original energy from bremsstrahlung. ξ happens to be very close to $7/9$ of the mean free path of pair production for a photon. The most recent value quoted for ξ by the Particle Data Group (PDG) is $36.62\,\mathrm{g/cm^2}$ (Tanabashi et al., 2018). Dividing this quantity by the density of the medium gives it in units of length. Utilizing this information, the total number of shower particles n and the average energy per particle can be estimated by the depth y the shower has traveled, $N = 2^{y/\xi}$, when using $\mathrm{g\,cm^{-2}}$.

This cascade cycle cannot continue indefinitely, however, because of the limited energy available from the primary particle. The bremsstrahlung loss rate is directly proportional to energy, while the rate of ionization loss increases logarithmically with energy (Tanabashi et al., 2018). Therefore, at high energies, bremsstrahlung is the dominant energy loss mechanism, and new photons will readily be made. At lower energies, ionization losses dominate, and there is a critical energy below which secondary particles will cease to produce any new secondaries. Though the critical energy can be defined in different ways, the definition that

is most descriptive of the development of the shower is from Rossi (1952), who chooses the energy at which the ionization loss in one radiation length is equal to the energy of the electron. The critical energy for air is on the order of 81 MeV. When secondaries have typical energies below the critical energy, the shower is said to have reached its maximum development, and the height at which this occurs is called the shower maximum height.

Most secondary shower particles at the shower maximum will have energy just below the critical energy, giving them a $\beta = \frac{v}{c}$ value of about 0.99998. The index of refraction n of air near sea level is about 1.000289, so the speed of light in that medium is about $0.999710c$. These electrons thus exceed the speed of light in the atmosphere and will emit a rather narrow cone of Cherenkov radiation, with an opening angle of about 1.33° according to Equation 4.1. At higher altitudes, the index gets closer to unity as density decreases, and the angle of the cone gets smaller. The Cherenkov spectrum is very bright in the blue–violet range for high-energy electrons in the atmosphere. What reaches the ground is a short ≈ 4 ns pulse of Cherenkov radiation in a compact ellipse shape. For showers initiated by 1 TeV gamma rays, there are no long-lived secondary particles that reach the surface of Earth, because particles below the critical energy will quickly be stopped by ionization losses. For EeV gamma rays, electrons, positrons, and secondary gamma rays will reach the surface.

4.1.1.2 Hadronic Cascades

When an air shower is initiated by a proton or nucleus, the result is a hadronic air shower. In this case, there is a wider array of less symmetric hadronic interactions when compared to EM showers. The primary proton first crashes into a target nucleus in the atmosphere. The nucleus undergoes spallation and breaks into many parts as described in Subsection 2.3.4. About half of the particles created are high-energy pions, kaons, protons, and neutrons, with momentum mostly in the forward (longitudinal) direction and a small amount of transverse (lateral) momentum (Longair, 2011). These secondaries can go on to create their own cascades. Unstable particles, such as pions, kaons, and radioactive nuclei will eventually decay. Neutral pions produced in this collision will undergo neutral pion decay

(see Subsection 2.3.4), yielding two gamma rays. Each of those gamma rays can create its own electromagnetic cascade. The spallation process repeats with any protons or nuclei with enough remaining energy, creating a hadronic air shower.

The maximum longitudinal development of the shower is reached when particles fall below $1\,\text{GeV}$, approximately the energy required for pion production. Protons below this energy will be brought to rest by ionization losses. The longitudinal development of the nucleonic cascade is characterized by the nuclear interaction length, just as the radiation length characterized the longitudinal development of electromagnetic showers. The nuclear interaction length is the mean distance a hadronic particle will travel before it participates in an inelastic collision. The nuclear interaction length in air at standard temperature and pressure (STP) is $\lambda_I = 90.1\,\text{g/cm}^2$ according to Tanabashi et al., 2018. Note that this is considerably longer than the typical radiation length, so hadronic air showers take longer to develop than EM air showers. Note that the lateral development of hadronic showers does not scale with the interaction length. The end result in hadronic showers that is a pulse of Cherenkov light like those resulting from EM cascades, but with generally differing properties.

4.1.1.3   Comparison of Hadronic and EM Showers

Hadronic showers take longer to develop compared to electromagnetic showers, as the nuclear interaction length is longer than the radiation length. Hadronic showers also have comparatively more variation in the depth of their first interaction with the atmosphere than electromagnetic air showers. The Cherenkov pulse that results from a hadronic cascade is much less regular than the pulse from electromagnetic air showers, which are more compact on average. When compared to hadronic showers, electromagnetic showers are distinguishable because they tend to be more uniform and compact and have less transverse momentum. You can see the comparison of simulations of an electromagnetic cascade and a hadronic shower in Figure 4.3.
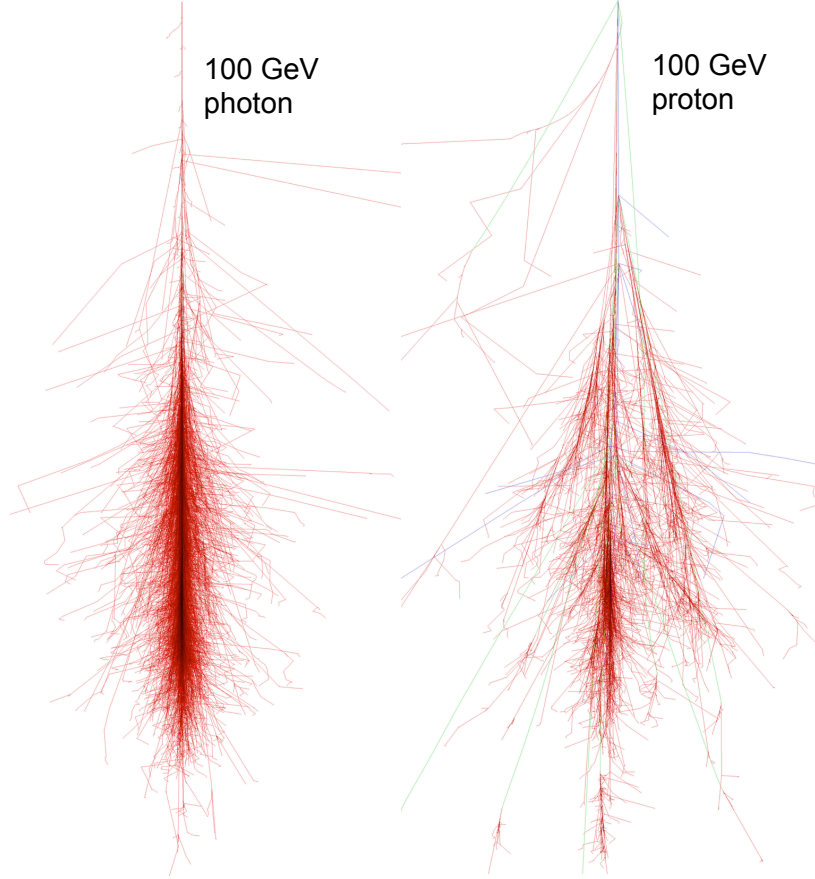
Figure 4.3: Images of simulations of air showers in Earth's atmosphere initiated by $100\,\text{GeV}$ gamma and hadron particles, respectively. The gamma showers (left) are notably more regular and compact than hadronic showers (right). Holder, 2015.

These EASs are detected by the imaging atmospheric Cherenkov technique, which is fully detailed in Chapter 4.

4.1.2 Cherenkov Radiation

The speed of light in a dielectric medium is reduced by a factor called the refractive index n, the value of which is a property of that medium. The reduced phase velocity of light in a medium is

$$v_p\left(n\right) = c/n$$

where $c = 299\,792\,458\,\text{m/s}$ is the speed of light in a vacuum. If the medium is nonmagnetic, $n = \sqrt{\kappa}$ where κ is the dielectric constant. While it is impossible for anything to move faster than c, it is possible for a massive particle to move through a dielectric medium at a speed greater than v_p. If that superluminal particle is charged, it will emit a cone of radiation called Cherenkov radiation. Cherenkov (1934) first detected this phenomenon experimentally, and after its theory was developed by Frank & Tamm (1937). In 1958, these three Russian physicists were awarded a joint Nobel prize in physics for the discovery and theory of the Cherenkov effect (Cherenkov et al., 1958).

As a charged particle passes through insulating material, it partially polarizes the atoms it passes, inducing dipole moments in them. As they return to their ground states, disturbances in the electromagnetic field propagate from those atoms. For a particle moving at low velocities, the radiation will interfere destructively because the disturbance is symmetric in front of and behind the particle. However, if the charged particle exceeds c/n, no disturbance propagates ahead of the superluminal particle, leaving a net electric dipole moment. Constructive interference occurs along a cone-shaped wavefront of angle θ, as illustrated in Figure 4.4. According to Huygens–Fresnel principle, this wavefront acts as a source of spherical wavelets, leading to coherent radiation. This emission is conceptually analogous to a sonic boom from the shock wave following a supersonic object.

The angle θ of the light cone relative to the axis of the motion of the charged particle depends only on the index of refraction n and the velocity of the charged particle expressed as β:

$$\cos(\theta) = \frac{1}{n\beta}. \tag{4.1}$$

Keep in mind, there is dispersion because the refractive index for EM radiation varies with its frequency. The rate of Cherenkov radiation emitted as a function of frequency can be derived from Maxwell's equations. The result is a continuous spectrum described by the Frank–Tamm formula: Frank & Tamm, 1937; Jackson, 1999.

$$\frac{dE}{dx} = \frac{q^2}{4\pi} \int_{v > \frac{c}{n(\omega)}} \mu(\omega)\,\omega \left(1 - \frac{c^2}{v^2 n^2(\omega)} \right) d\omega \tag{4.2}$$

A rough sketch of this spectral distribution is shown in Figure 4.5. The observed light is

$100\,\%$ polarized in the plane that contains both $\vec{v}$ and $\hat{n}$.
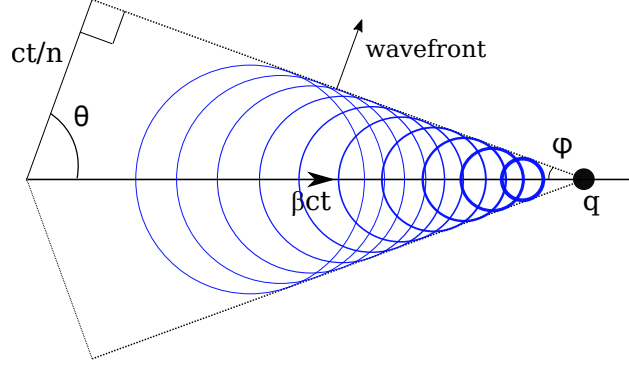
Figure 4.4: Diagram illustrating the wavefront emanating from a particle of charge q moving with a speed exceeding c/n. A right triangle is constructed, with the distance βct traveled by the particle in time t as the hypotenuse. The leg with length $\frac{c}{n}t$ represents the path of light emitted at $t = 0$. and the remaining side lies along the wavefront at an angle ϕ. The angle of the cone with respect to the direction of propagation is θ. Spherical waves are drawn, showing the wavefront at which they coherently interfere.

While it does not produce high-energy photons, Cherenkov radiation is a signature of the air showers created by cosmic rays, and is the signal detected by IACTs such as VERITAS.

4.2 The Very Energetic Radiation Imaging Telescope Array System (VERITAS)

In this section, I detail the composition of VERITAS telescopes and the array hardware and electronics used to detect Cherenkov showers and record data. The VERITAS array is composed of four telescopes in a roughly square arrangement, with an approximate separation of $120\,\mathrm{m}$ between telescopes. Each telescope has a large $12\,\mathrm{m}$ optical reflector composed of highly reflective independently adjustable mirrors of an f/1 Davies-Cotton design (Davies & Cotton, 1957). These mirrors concentrate light toward a central camera consisting of 499 Photonis XP 2970/02 photomultiplier tubes (PMTs) that are maximally sensitive to light in the wavelength range of Cherenkov radiation (Holder et al., 2008) (recall Figure 4.5).
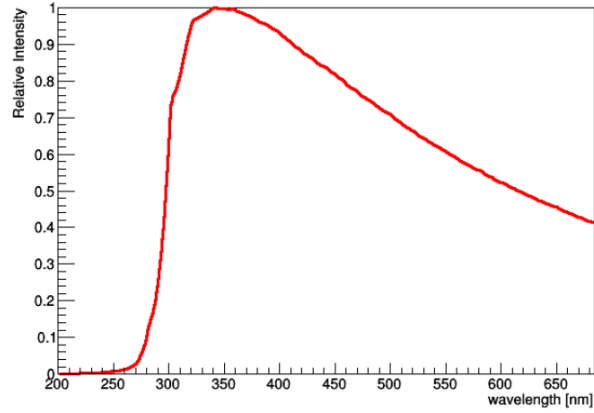
Figure 4.5: The expected intensity vs. wavelength of Cherenkov light for an EAS initiated by a 500 GeV gamma ray entering Earth's atmosphere. The vertical scale is the intensity relative to the peak intensity around 340 nm. Plot courtesy of Ralph Bird.

4.2.1 Telescopes and Cameras

4.2.1.1 Telescopes

Each telescope consists of a large multi-faceted reflector supported by an optical support structure (OSS). The reflector is composed of 350 independently adjustable mirror facets, each with an area of $0.322\,\mathrm{m}^2$ and a radius of curvature of 24 m. The glass mirror facets are made highly reflective by a process called aluminization, and their coating is protected by anodization. Their reflectivity can be maintained by recoating if reflectivity measurements show degradation. The facets have a combined total area of approximately $110\,\mathrm{m}^2$; their hexagonal shape allows for maximal use of their area. Each mirror facet focuses greater than 90 % of the incident life to within the diameter of a PMT (Nellen et al., 2008). EASs are very faint and extend over a very large area, so the large mirror area of the VERITAS reflectors efficiently collect photons from very faint showers from energies as low as 80 GeV which yield roughly $5\,\mathrm{photon/m}^2$. The mirrors are aligned individually so as to minimize the point spread function (PSF), which helps to minimize the positional uncertainty of sources. [1]

The camera on each telescope is mounted 12 m from the telescope on a quadrapod-stage

---

[1]The PSF of an imaging system describes how that system will image a point source.

which puts it at the focal plane of the mirrors, and is balanced by a counterweight. An altitude-over-azimuth positioner controls the pointing of the telescope (Gibbs et al., 2003). The position coordinates refer to the horizontal (or topocentric) coordinate system, where elevation (or altitude) refers to the angle above the horizon and azimuth refers to the angle measured clockwise, or eastward, from north. Tracking of the telescopes is more finely tuned by the VERITAS pointing monitors (VPMs), which use the bright stars in the field of view to precisely calculate the pointing direction of each telescope. Often we refer to the zenith angle, which is the complementary angle to elevation. A position encoder measures the pointing direction at a rate of 4 Hz and with an error generally less than 0.01°, then writes it to a database.

4.2.1.2   Cameras

Light collected by each telescope is reflected and focused onto the camera. That light is efficiently guided into the PMTs by Winston light cones (Winston, 1970), as pictured in Figure 4.6b. These light cones reduce the effective gap between pixels and the amount of lateral light not coming from the direction of the mirror reflection, which increases the amount of light collected by about 60 %.

The PMTs used by VERITAS are maximally sensitive in the blue–UV range, approximately the wavelength range of Cherenkov light, and have a high quantum efficiency, $\approx 20\,\%$ at 320 nm. They are powered to high voltages of 800–900 V giving them a gain on the order of 10^5. The voltage of each pixel can be set individually to tweak the gain; this is often done to keep the gain uniform between pixels despite changes that occur over time. After the light signal enters the PMT, it is converted to a heavily amplified analog current signal. The current then travels through an integrated preamplifier of high-bandwidth, providing an additional gain. Every PMT is AC coupled at the preamplifier, which filters out any DC signal. This effectively removes any offset introduced by the night sky background (NSB), so the digitized signal fluctuates around zero voltage.
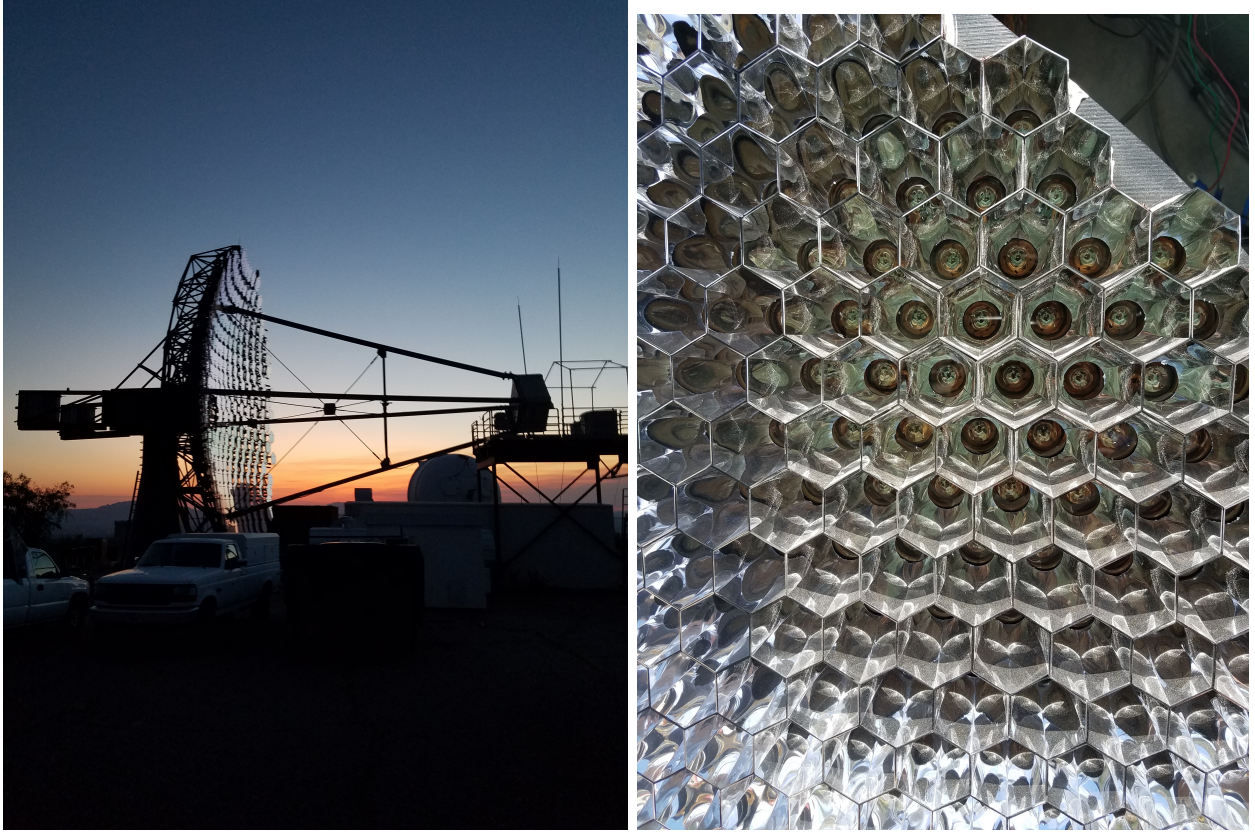
(a) Profile of a VERITAS telescope (T4) & camera   (b) Close up of Winston light cones.

Figure 4.6: Images of VERITAS telescope 4. A profile view of the telescope and camera is shown in (a) and a close-up view of the Winston light cones is shown in (b).

4.2.2 Trigger and Data Acquisition Systems

In this section I outline how VERITAS converts the light signal from the PMTs into a digital signal and records it for analysis. Even though observing is done during dark, moonless nights, there will always be a considerable level of background light entering the PMTs from nearby man-made sources and stars. VERITAS uses a three-level triggering system to suppress the recording of images of background light.

The signal from the PMT travels through a coaxial cable to a trailer that houses telescope electronics, where the signal is split three ways, each containing an identical copy of the signal from the PMT. One of the copies of the signal is amplified by a factor of 6 through the high gain circuit, digitized by an flash analog-to-digital converter (FADC), and streamed into a
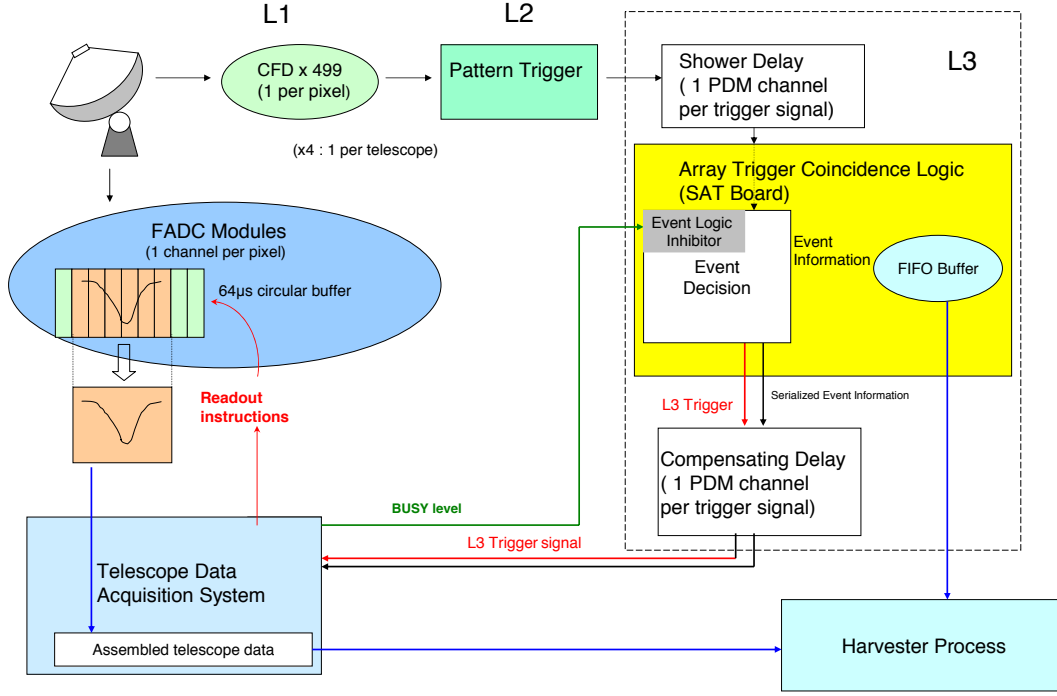
Figure 4.7: Schematic diagram of the VERITAS trigger system (Weinstein, 2007).

16,000 sample circular RAM buffer. The FADC integrates the voltage in each 2 ns sample window, converting the integrated signal into digital counts (dc), a unit proportional to the number of photoelectrons entering the PMT in that time window. The nominal conversional gain is 0.128 dc/mV for this circuit. The FADCs, however, are only able to measure analog signals of negative polarity. To make all readings artificially negative, an offset of nominal value 117 mV is subtracted from the signal prior to digitization. The sample rate of the VERITAS FADCs is 500 megasamples/s (Buckley et al., 2003), so the buffer holds 32 μ sec of data at a time.

A second identical copy of the signal is attenuated and sent through a time delay circuit. This is referred to as the low gain channel. The attenuated signal gets written to the buffer if the original signal exceeds $\gtrsim 120$ photoelectrons and saturates the FADC. The nominal

conversional gain for this circuit is 0.128 dc/mV.

The third copy of the signal is sent to the first level of the trigger system, or the pixel level (L1) trigger. The L1 trigger for each pixel is composed of a constant fraction discriminator (CFD), a block diagram of which is pictured in Figure 4.7. An individual pixel will only trigger if its PMT pulse exceeds a certain threshold voltage, which can be adjusted depending on conditions of the night sky. The CFDs employ a constant fraction threshold rather than a fixed threshold to determine the trigger time to reduce the jitter in that timing resulting from different pulse amplitudes. An additional circuit called the rate feedback (RFB) is incorporated into the CFD to stabilize the trigger rate under changing noise levels. It achieves this by increasing (decreasing) the trigger threshold under increasing
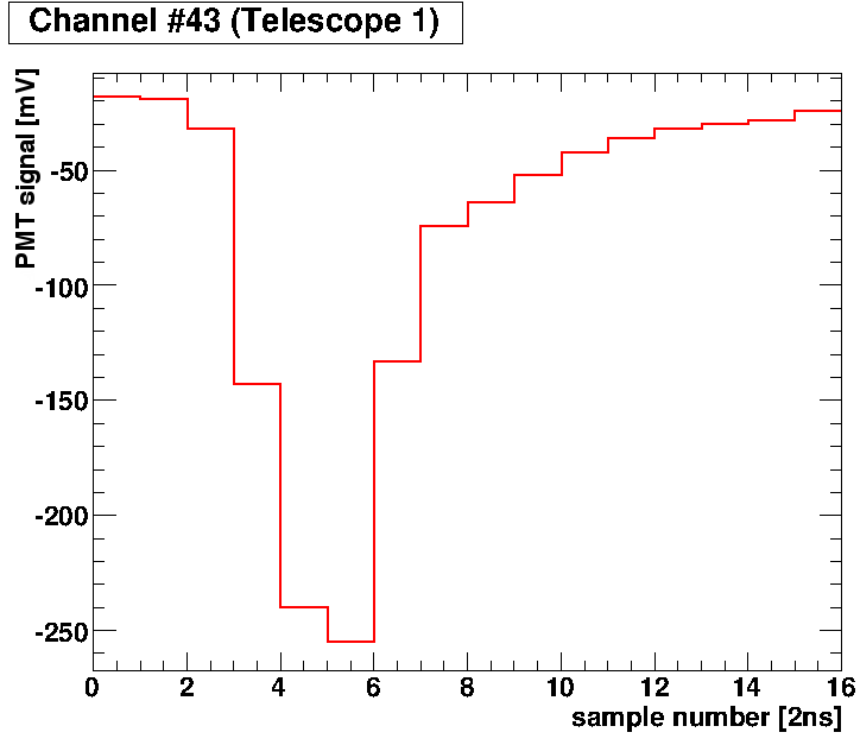
Figure 4.8: An example FADC trace of an air shower observed by VERITAS. Plotted is the integral of all pixel charges in a single telescope sampled in 2 ns windows. The fast rise time can be seen at the fourth sample. The telescope level (L3) trigger signal is sent back to the data acquisition (DAQ) system, which reads from the FADCs and the data are written to harvester.

(decreasing) noise levels. A schematic diagram of the CFD including the RFB circuit is shown in Figure 4.9.
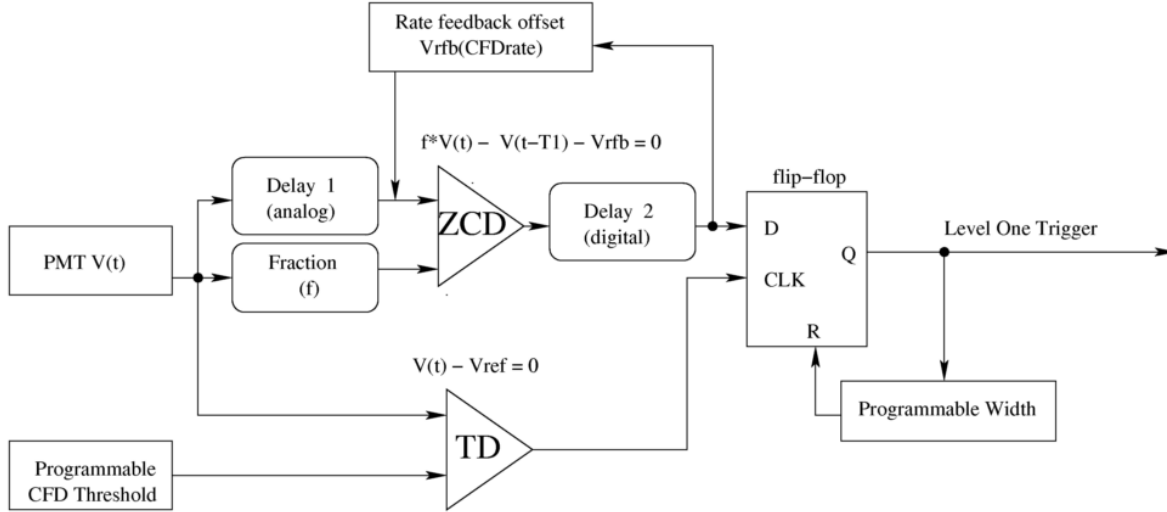
Figure 4.9: Schematic diagram of the CFD, including the RFB circuit (Hall et al., 2003).

The camera level (L2) trigger system recognizes when three or more adjacent pixels occur within a time coincidence window, which gives preference to compact Cherenkov showers radiated by gamma rays and prevents the recording of isolated pixel fluctuations. The typical rise time of Cherenkov pulses is 3–5 ns, so the width of this time coincidence window is typically 5–6 ns.

The final level of trigger is the L3 trigger, which occurs when two or more telescopes trigger within a certain coincidence time window. The actual arrival time of the L2 signals must be corrected for the differing cable lengths transmitting the signals. There is also a correction to account for the different times that the Cherenkov light front reaches each telescope; this correction depends on the telescope pointing direction. Despite these corrections, there is still a residual spread in arrival times of the L2 signal depending on multiple factors. These factors include the width and curvature of the developing Cherenkov wavefront, the L2 timing jitter for different image sizes, and variations in timing of various electronic components. To allow for this spread, the L3 system coincidence time window is currently set to a nominal value of 50 ns. The L3 trigger is then sent back to the telescopes through modules that delay

the logic signal so that it is received a fixed time relative to the L2 trigger in each telescope. Upon receiving this signal, the telescope initiates the data acquisition (DAQ) system.

The DAQ system reads data from the FADC's ring buffer, looking back 1500 samples corresponding to approximately $3\,\mu s$, depending on the telescope. The ring buffer cannot be read and written to simultaneously, so after every event trigger there is a period of dead-time during which no events can be triggered. This dead-time reduces the effective time of observation by roughly 10%, and is subtracted from the exposure in the analysis. The L3 trigger also tags array-level information such as the event number, a GPS timestamp, and other information on a FIFO (first in, first out) basis. A software process called the Harvester collects the L2 and L3 information, along with the FADC data, and compiles it into a single event. These events are also displayed by live analysis software called Quicklook used to monitor the run in real time. Once the run has completed, the events are compiled into a raw data file, and information about the run is stored in a mySQL database. The data file is formatted in the VERITAS bank format (VBF), which is a binary data file format designed by our group. The raw data includes the digitized signal traces in the PMTs recorded by the FADCs, tracking of the telescope pointing direction, and GPS time stamps for each event, as well as a header containing the run information.

4.2.3 Array Epochs

VERITAS has gone through two major changes to its array configuration, splitting its observing timeline into three epochs. In its original configuration, referred to as V4, telescope 1 (T1) was located only $35\,m$ from telescope 4 (T4). The first major change to the array was the move of T1 to a more symmetric location, which occurred in September, 2009. This move increased the effective area and reduced the background triggers from muon rings, improving sensitivity by approximately 30% (Perkins et al., 2009). The locations of the telescopes before and after this move are pictured in Figure 4.10. The second major change was an upgrade in the summer of 2012 of the PMTs along with an upgrade in the trigger electronics (Otte & VERITAS, 2011). The new PMTs have a higher quantum efficiency, which increased light

collection, and a narrower pulse width, which helped to further improve trigger timing. The epoch before this second upgrade but after the telescope move is referred to as V5, and the current epoch is referred to as V6.

(a) Original arrangement of telescopes in the V4 epoch.

(b) Satellite image of telescopes after T1 was moved to a more symmetric position.

Figure 4.10: The arrangement of telescopes for epochs before and after the relocation of telescope 1. Figure (a) shows the positions of the telescopes in the V4 epoch, while (b) shows the positions of the telescopes in the epochs V5 and V6. Images captured from Google Earth™.

4.3 Performance Specifications

The main motivation to build indirect gamma-ray detectors despite their more difficult analysis is their ability to detect particle showers over a larger area, compensating for the low flux of high energy particles. Ground-based instruments have a higher area of light collection than space-borne telescopes in part because they can be built much larger. Additionally, air showers spread over a very large area, which means the primary gamma ray or cosmic ray does not have to be directly incident on a telescope for it to be detected. These factors both contribute to what is called the effective area (A_{eff}), or the size of the area over which an incident particle can enter and be successfully reconstructed. For a comparison, *Fermi-LAT* has an $A_{\text{eff}} \approx 1\,\text{m}$ compared to a typical IACT with $A_{\text{eff}} \approx 1 \times 10^5\,\text{m}$. With its very large A_{eff}

VERITAS is also very sensitive, and can detect a source with 1 % of the Crab Nebula flux in under 25 hours at a statistical significance of 5σ for observations taken at high elevation. This large detecting area becomes crucial because gamma-ray events for VHE sources have fluxes that get lower and lower as energy increases. Particles that approach Earth at large zenith angles (low elevation) travel through more atmosphere before reaching the surface of Earth, which makes their air showers even more extensive, increasing A_{eff} for those energies. In Figure 4.11, A_{eff} is plotted as a function of energy for 70° and 25° elevation. The showers at large zenith angle (LZA) are also much fainter, which increases the minimum detectable energy, or energy threshold. The energy resolution, or uncertainty in energy divided by energy, is nominally $\approx 17\,\%$ at 1 TeV. The angular resolution is $r_{68} = 0.08°$ (68% containment radius) for energies of 1 TeV. See sections 6.1.1 and 6.4.2 for a more detailed analysis of energy bias and angular resolution for the GC observations at LZA.
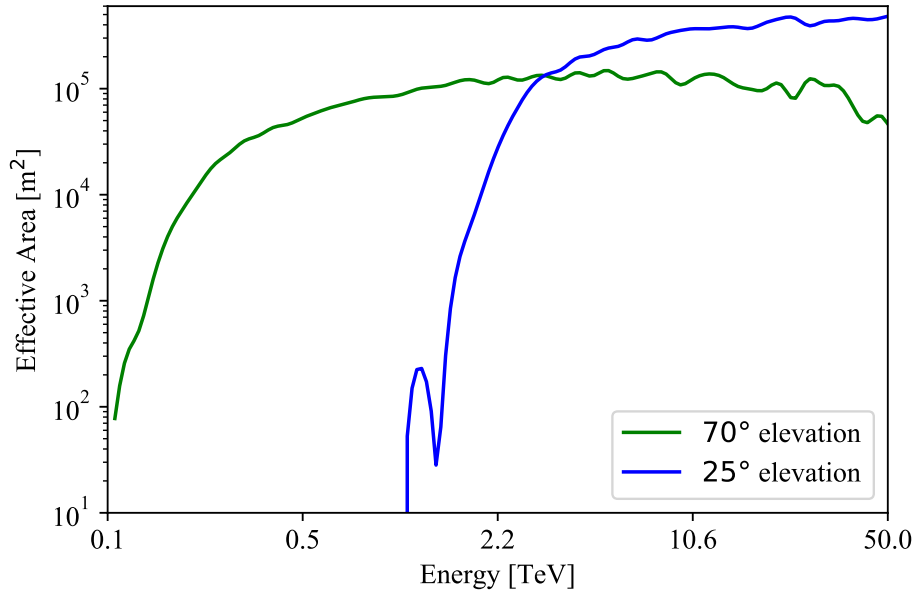
Figure 4.11: A plot of effective area vs. energy at 70° (green) and 25° (blue) elevation. The effective area (EA) for low elevation exceeds that of high elevation above 2.5 TeV.

4.4 Observations with VERITAS

Cherenkov pulses from air showers are very faint and can only be detected by PMTs that are too sensitive to run when there is sunlight. VERITAS only observes during dark time when there is minimal sunlight, and the moon must be avoided when it is too bright. Observations can be prevented by weather conditions such as excessive clouds, precipitation, excessive humidity, or high winds. Clouds are of particular concern because they can block light from showers or reflect light from nearby sources toward the telescopes. This is one of the disadvantages of ground-based telescopes, as the average duty cycle in a given observing year is about 11%. Even when weather conditions appear clear to the naked eye, small distant clouds or a light haze can be enough to decrease the quality of data taken. During observations, weather conditions from local weather stations are closely monitored by the observers. VERITAS also has a set of different monitoring instruments, including cameras on the telescopes that give live visual images of the sky conditions. Multiple FIR pyrometers measure the sky temperature at the zenith and along the optical axis of two telescopes. The pyrometers detect the presence of clouds, as they are substantially warmer than clear sky. A LIDAR (light imaging, detecting, and ranging) ceilometer measures the altitude and thickness of any clouds or haze that may be directly above the telescope array. The monitoring measurements are recorded and saved to a database so the proper data can be associated with an observing run. Observers also closely monitor the L3 rates of each telescope, which should maintain steady rates on the order of hundreds of Hz. Large fluctuations in the L3 rate can indicate cloud movement or flashes from light sources such as headlights.

During each run, the observers assign a weather rating based on the current conditions, and may leave comments about any potential problems with the observing conditions or equipment. They can also suggest time cuts, which are portions of time that are to be excluded from data analysis. All of this information is written to the database and associated with its date and run number for future reference. Observers also monitor output from the Quicklook software, which analyzes every event to select the gamma-ray shower events and reconstruct their directions. This is referred to as the "Online" analysis, and is a

simplified, faster version of the full, "Offline" analysis (see Chapter 5). Quicklook frequently calculates the gamma-ray rate and statistical significance of the targeted source, and updates a significance skymap. While approximate calculations, Quicklook results can be used to determine if a source requires additional time or follow up observations, such as the case of a source flaring. Such observing opportunities are referred to as Targets of Opportunity, or ToO triggers.

At the end of an observing run, the raw data along with the file header are written to a VBF file, and those data files are copied to a data archive at UCLA. After the data is transferred, each run is ready for a next-day analysis. In this process, the data are analyzed with default settings, and various diagnostic plots of the hardware are produced. In a process called data quality monitoring (DQM), these results are examined by a person who determines and reports the quality level of the data. This helps the collaboration to evaluate how much quality data has been taken and make any necessary adjustments to an observing campaign. The person performing the DQM can also suggest their own set of time cuts. The data file and the database are available to members of the group for further, more proper offline analysis as detailed in the next chapter.

4.4.1   Calibrations

Every experiment in practice will degrade over time in many ways that affect the efficacy of the instrument. To get consistently good results over the timescale of days to many years, calibrations must be performed regularly. One of the changing performance parameters is the relative gain of the PMTs. Approximately once a month, a process called flat-fielding is performed, and the actual voltage applied to each PMT is adjusted to make the make the PMT gains as close to each other as possible. The flat-fielding process keeps the PMT gains from diverging from each other, but the gains can drift a non-negligible amount from night to night. Flat-fielding every night would decrease the amount of observation time substantially, so at least once per night, short runs called flasher runs are performed to measure any such drift (Hanna et al., 2009). In a flasher run, the telescopes are illuminated by flashes or pulses

of LED light that peak in the Cherenkov wavelength band. The pulses are delivered at the rate of 300 Hz. The raw data are recorded, and the response to this uniform light can be analyzed to apply corrections via software to account for differences in gain. See Section 5.3.

4.5   GC Observations and Data

At the location of VERITAS the GC culminates between 24° and 31° elevation. While this complicates the analysis and reconstruction, it also allows VERITAS to see the highest energy gamma rays from the GC of any experiment, up to 50 TeV. LZA observations produce an energy threshold of approximately 2 TeV at LZA, compared to 85 GeV at small zenith angles.

Since 2010, VERITAS has taken about 170 hours of data while pointing to Sgr A*. All of these data fall into the V5 and V6 epochs and were taken in wobble mode, where the pointing is slightly offset from the source position to allow for better accounting of the background.

There have also been about 47 hours observed in an OFF region about 5° from the pointing of Sgr A*, in a region where there are no known gamma-ray sources. These data can be used to model the instrument response functions, such as acceptance, at the elevation angle of GC observations. From the available data, I have looked at all of the diagnostic plots and carefully selected the high quality data appropriate for analysis. My dataset is larger than that of any past VERITAS work, and new data will be taken over the next couple of years. Through our long-term plan, the GC is allocated at least 30 hours of observation each year, so the statistics of our analysis will improve with every year of observation.

CHAPTER 5

Data Analysis

Ground-based IACTs require a sophisticated analysis to reconstruct gamma-ray events from their resulting shower images and extract information about a source. In this section I explain how a typical offline analysis is performed to compile raw observation data from multiple runs and create high-statistics skymaps and energy spectra for an observed FoV. The offline analysis can be tailored to suit the specific source and observing conditions in a way that reconstructs the gamma-ray energies and directions as accurately as possible.

5.1   Selecting Quality Data

Before data are analyzed, it is important to assess the quality of data and compile a list of high quality runs. All of the information outlined in Section 4.4 is included in the DQM report for each run, and all such reports are hosted on a website and accessible by their associated run number or observing date. The analyzer may decide to review runs more closely and overwrite parts of the report. A web tool called the log-sheet generator, or loggen, enables the user to automatically generate run lists for a particular source or region. This tool can be set to compile only runs that meet certain parameters, such as a minimum weather rating or a requirement that all four telescopes participate in the array. Individual observing runs can be excluded for many other reasons, including electronic failures, inaccurate tracking, and weather-related issues. There may also be problems with one or more telescopes, and problem telescopes can be excluded from the analysis. Sometimes only a portion of a run is problematic, and time cuts can be applied to ignore those specific portions in analysis. The analyzer can choose to use the time cuts suggested by the observer, DQM, or may use his or

her own. Because accurate energy reconstruction requires images of higher quality, a separate higher-quality runlist may be used for spectral analyses.

5.2   Software Packages for Offline Analysis

The VERITAS collaboration has developed two primary software packages: EventDisplay (Maier & Holder, 2017) and VERITAS Gamma-ray Analysis Suite (VEGAS) (Cogan & VERITAS, 2007; Daniel & VERITAS, 2007). Both software packages read data from the same archived VBF files and perform the same basic analysis, but the algorithms are coded and tested independently. Both packages are written in C++ and utilize the ROOT data framework libraries made available by CERN (Brun & Rademakers, 1997). For any published results, a secondary analysis crosscheck with the alternate package is required to verify their consistency. My primary analysis was performed with VEGAS, so I detail the steps as performed by this package exclusively. VEGAS was developed by a team of developers at VERITAS over five years, and it is continually updated and improved upon by current members, myself included.

VEGAS has six primary stages:

1. calculation of pixel calibration,

2. application of pixel calibration and image cleaning,

3. image parameterization,

4. shower reconstruction,

5. gamma / hadron selection, and

6. skymap / spectral fit.

The first five stages are executed on a run-by-run basis, with data organized into trees and saved to a ROOT binary file along with run information for each run. The sixth and

final stage combines results from a list of files that have been processed through gamma / hadron selection.

5.3   Pixel Calibration

The first stage of analysis calculates hardware-dependent quantities of the data for both observing and flasher runs. These quantities are then used in the second stage to generate a collection of calibrated events that reflect the true signals and timing as accurately as possible.

5.3.1   Calibration Calculation

The very first stage of analysis is the only stage executed on both source observing runs and flasher calibration runs, as mentioned in Subsection 4.4.1. The status and timing offset data for every pixel are read from the database, as are the pointing data from the VPM database. Raw event-by-event charge signal data are read from the VBF file, and charge statistics are calculated. The motivation for finding the charge statistics is as follows:

In the absence of Cherenkov light, there will be a small fluctuating signal that varies on nanosecond timescales under the NSB. This signal, called the pedestal, can be used as a baseline to determine which pixels should be included in the image of a triggered event. During observation, pedestal events are force triggered by the L3 system and recorded at a rate of $1\,\mathrm{Hz}$.

For every data run, the mean value of the pedestal, $\bar{p}$, is calculated for each pixel i:

$$\bar{p}_i = \frac{1}{N} \sum_j^N p_{ij} \tag{5.1}$$

where j corresponds to the pedestal event number and N is the total number of pedestals recorded during the run. The noisiness of a pixel is measured by the root mean square of the pedestal values calculated around that pixel's mean pedestal value, and is referred to as its pedvar. The pedvars are used to select which pixels participate, by looking at how many

103

standard deviations a pixel's pedvar value is from the mean of all pixels in the telescope.

$$z_i = \frac{\sigma_i - \bar{\sigma}}{\sigma_{\mathrm{rms}}} \tag{5.2}$$

where $\bar{\sigma}$ is the mean pedvar and σ_{rms} is the root mean square (RMS) of the pedvar distributions. Pixels with exceptionally small pedvars of 2.5 standard deviations below the mean are considered dead pixels. Pixels with exceptionally large pedvars of 4 or more standard deviations above the mean are considered noisy pixels. Both dead pixels and noisy pixels are excluded from the analysis entirely.
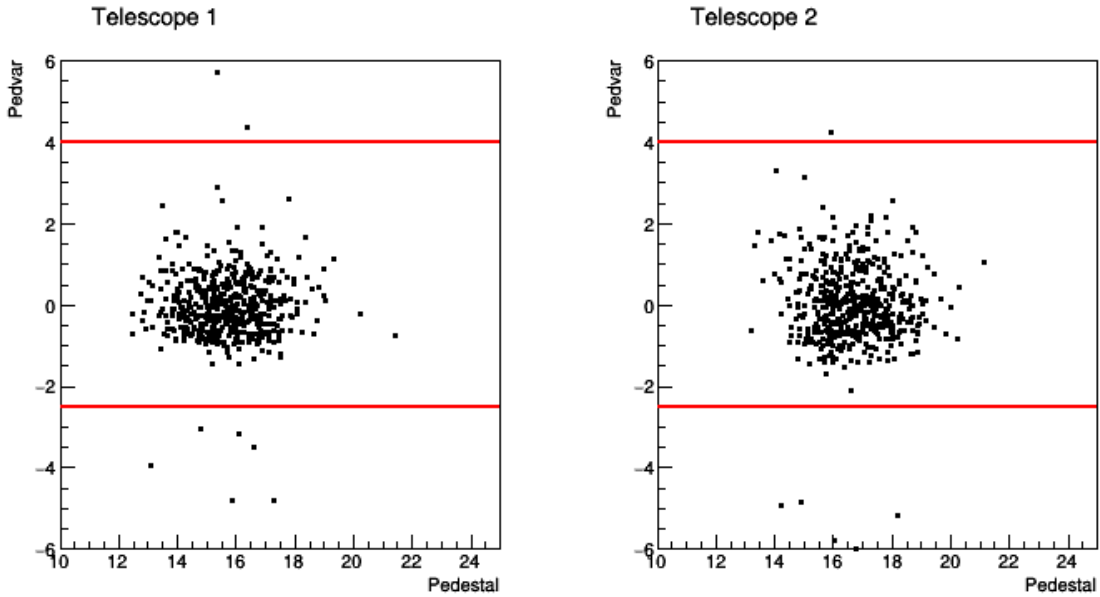
Figure 5.1: Two-dimensional histogram of the mean pedestal and pedvar values for telescope 1. The pedvar values for one GC run are given in units of z from Equation 5.2. Red lines are drawn at the minimum and maximum noise values.

The charge statistics are organized into a tree and saved to a ROOT file.

5.3.2 Calibration Application

The mean pedestal can be used to account for a nonuniform PMT response to light as mentioned in the previous chapter, and is applied to correct the source observing data, to ensure that the amount of Cherenkov light entering a PMT is accurately found from the

signal sent to the FADC. The pedestal is subtracted from the signal of each sample, and that difference is averaged over all events, resulting in the relative gain:

$$G_{\mathrm{rel},i} = \frac{\frac{1}{N} \sum_j^N s_{ij} - \bar{p}_i}{\bar{g}} \tag{5.3}$$

where $\bar{g}$ is the camera-averaged gain. Signal can be divided by the relative gain to normalize it and better reflect the true signal. This correction is applied to each pixel during this second stage of analysis, prior to image parameterization.

5.3.2.1   Image Cleaning

Noise fluctuations in pixels can be substantial, so it is necessary to select and analyze only pixels that are more evidently dominated by signal. This process, referred to as image cleaning, is also performed in the second stage of VEGAS. On an event-by-event basis, pedvar values are used as a basis for the process of image cleaning, whereby shower-image pixels are separated from pixels merely activated by the NSB. Pixels are selected based on their signal-to-noise ratio, (S/N), which is the value of the integrated charge divided by the pedvar. The signal in the FADC trace is integrated over the 7-sample window that maximizes the integral value, which will minimize the proportion of noise. Pixels with $S/N \geq 5$ are unlikely to be just fluctuations of NSB and are selected as shower-image pixels. Any pixel adjacent to a shower-image pixel that has a $S/N \geq 2.5$ is selected as a boundary pixel, which are simply the edge pixels of the shower image. The cleaned image consists of the shower-image and boundary pixels only; all other pixels are excluded from the subsequent image parameterization. The default cleaning algorithm I used also removes any isolated pixels, not adjacent to the cluster of image pixels, from the image. An example image in multiple stages of cleaning is shown in Figure 5.2.

5.4   Image Parameterization

In the third stage of analysis, the cleaned image is analyzed and parameterized into useful parameters called Hillas parameters (Hillas, 1985) that can be used for the subsequent
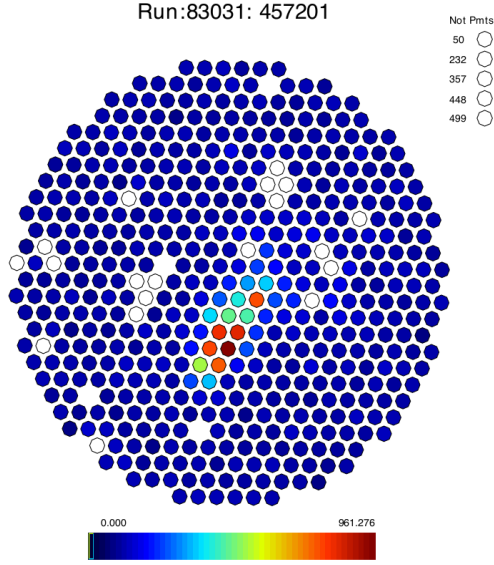
(a) Only gains applied.
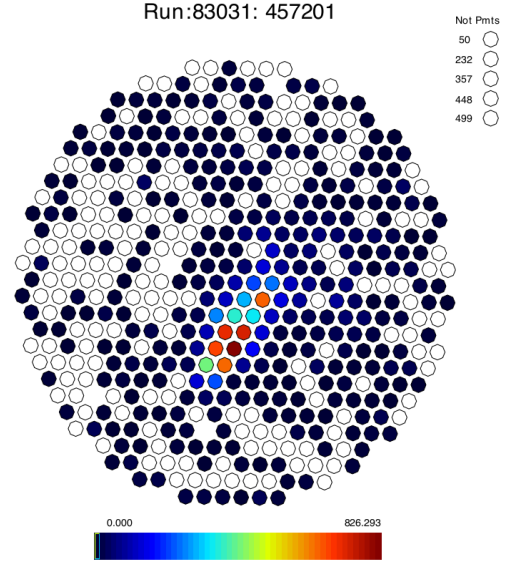
(b) Pedestals removed.
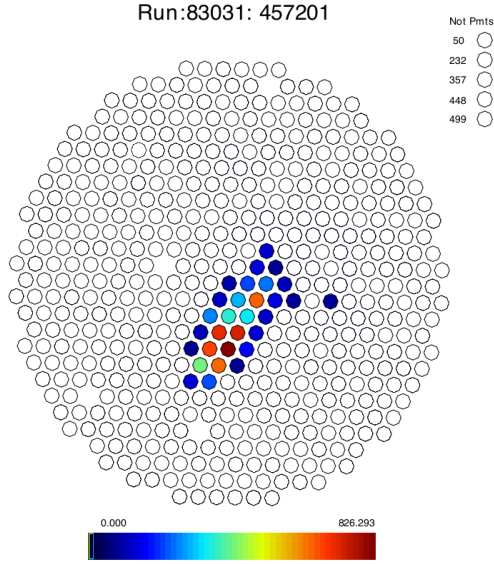
(c) Boundary and image pixels selected.
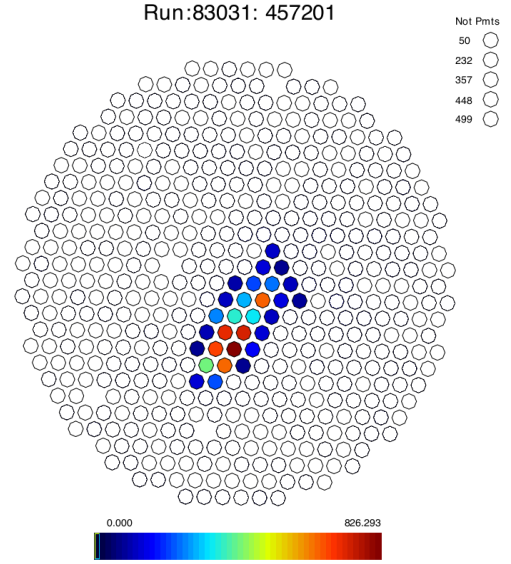
(d) Isolated pixels removed.

Figure 5.2: An example of the stages of pixel cleaning for a camera event eventually selected as a gamma ray. Figure (a) shows the mostly raw image with gain corrections applied. (b) shows the same image with pedestals removed. (c) shows that image with only the chosen image and boundary pixels. (d) shows that image after all default cleaning has been applied, removing all isolated pixels. The color scale represents the magnitude of the integrated signal in each PMT, and the holes represent L2 channels.

106

steps of shower reconstruction and gamma / hadron separation. Images from gamma rays are typically elliptical in nature, so a moment analysis of the image is performed, with the integrated signal in a pixel as its weight in the moment analysis. The main Hillas parameters and descriptions of how they are calculated from the moments of the image can be found in Table 5.1. An illustration of a parameterized shower ellipse with various dimensions marked is shown in Figure 5.3.

Parameter	Equation	Description
Size	$s = \sum_i s_i$	Sum of the traces s of all shower image and boundary pixels i, measured in digital counts (dc) (see Subsection 4.2.2). 0th moment of image.
Distance	$d = \sqrt{\langle x \rangle^2 + \langle y \rangle^2}$	Distance in degrees of the image centroid, or 1st moment, from the camera center.
Length	$l = \left(\frac{\sigma_x^2 + \sigma_y^2 + \lambda}{2} \right)^{1/2}$	The RMS spread (in degrees) of the signal counts along the image's major axis, which measures the lateral development of the shower. The major axis is the eigenvector of the 2nd central moment of the image.
Width	$w = \left(\frac{\sigma_x^2 + \sigma_y^2 - \lambda}{2} \right)^{1/2}$	The RMS spread (in degrees) of digital counts along the minor axis, which measures the vertical development of the shower.
Alpha	$\alpha = \arcsin \frac{b_{\text{miss}}}{d}$	Angle between the major axis and the line connecting the source position and image centroid.

Table 5.1: List of shower image Hillas parameters. The camera coordinates are x and y express the horizontal and vertical distance (in degrees) from the center of the camera, respectively. Their standard deviations are expressed as σ_x and σ_y. We define a parameter $\lambda = \sqrt{\left(\sigma_x^2 - \sigma_y^2 \right)^2 + 4\sigma_{xy}^2}$ where σ_{xy} is the covariance between x and y. The parameter b_{miss} is the minimum distance between major axis and the camera center.

The Hillas parameters of the camera images are not scientifically meaningful on their own,
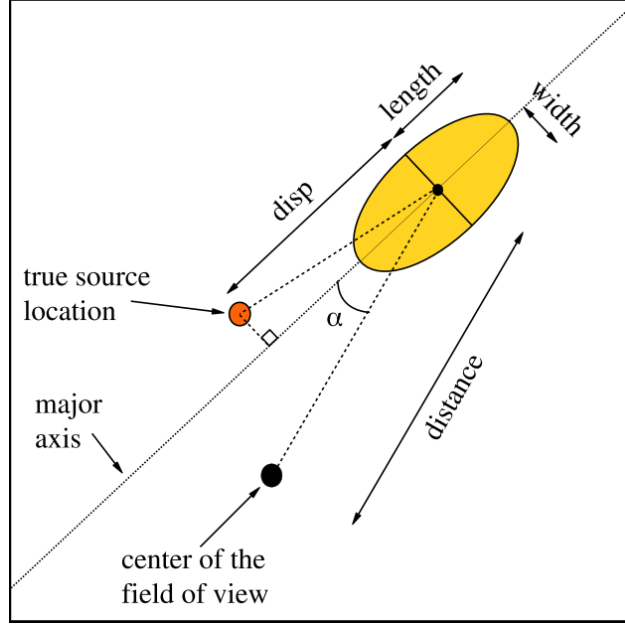
Figure 5.3: Illustration of a shower image parameterized in the camera plane. All parameters from Table 5.1 are shown, as well as the displacement parameter (see subsubsection 5.5.2.2) (Sentürk, 2013).

but can be used to classify and estimate important physical properties of the shower that created the images.

5.5 Shower Reconstruction

Once parameterized, all of the images of an event can be analyzed in combination to reconstruct properties of the shower that triggered the event. The most crucial physical properties are the primary direction, which is necessary for all analyses, and the energy, which is necessary for any spectral analysis. Other properties are also calculated to help find the physical quantities and to determine if an event is likely to have resulted from a gamma ray shower. In this section I describe how simulations and geometry are used to reconstruct the shower event and its properties.

5.5.1 Quality Cuts

Before analyzing the telescope images, we need to determine which images to include in the analysis. A number of minimum parameter requirements called quality cuts are imposed to ensure an image is detailed enough to not only reconstruct the primary particle direction, but to do so accurately. These cuts remove the majority of spurious events that are triggered by fluctuations in the NSB alone. There are standard values for these quality cuts, however I used values that were optimized for an LZA analysis. For more information on how optimal cuts were found for LZA analysis, see Subsection 6.3.2. Below I list the minimum parameter requirements that I cut in my analysis and the reason for imposing each requirement:

Size ≥ 500 (V5), $\geq 650\,\mathrm{dc}$ (V6)

> The size of an image is indicative of the amount of light that created the image, thus is a measure of the amount of information available for parameterization and reconstruction. The stronger the signal there is in digital counts, the less sensitive it is to noise, and more information typically means a more elliptical shape and less error in the determination of the major axis. Note this cut value is different for the two VERITAS epochs.

Number of pixels in image ≥ 5

> The reasoning for requiring a minimum number of pixels in the image after cleaning is similar to the size requirement, as having too few pixels makes it difficult to fit an elliptical shape.

Distance $\leq 1.38°$

> This requirement helps to insure that all or at least the majority of the ellipse of Cherenkov light was captured by the camera. Truncated images result in incorrect parameterization and poor reconstruction.

Number of telescopes ≥ 3

> The number of telescopes that pass image cuts is a measure of the quality of the direction reconstruction. The requirement is more strict for LZA analysis because direction reconstruction is more difficult.
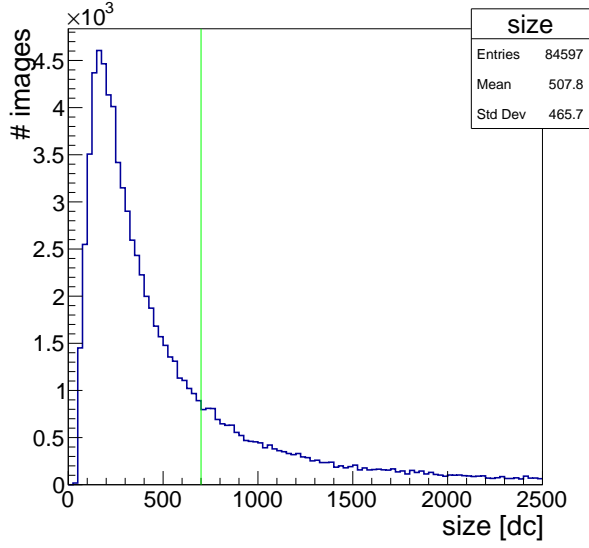
(a) Total image size after cleaning.
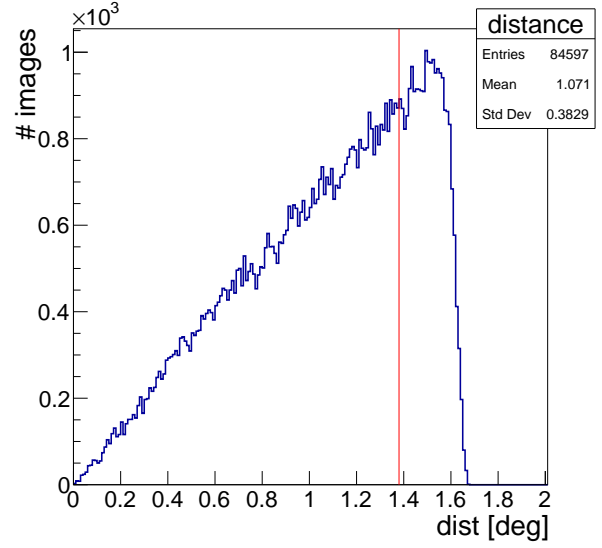
(b) Distance of image centroid from camera center.
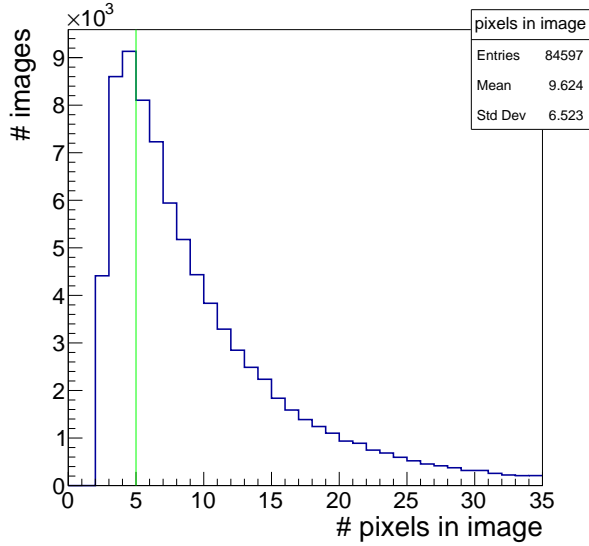
(c) Histogram of the number of pixels that pass cleaning in an image.
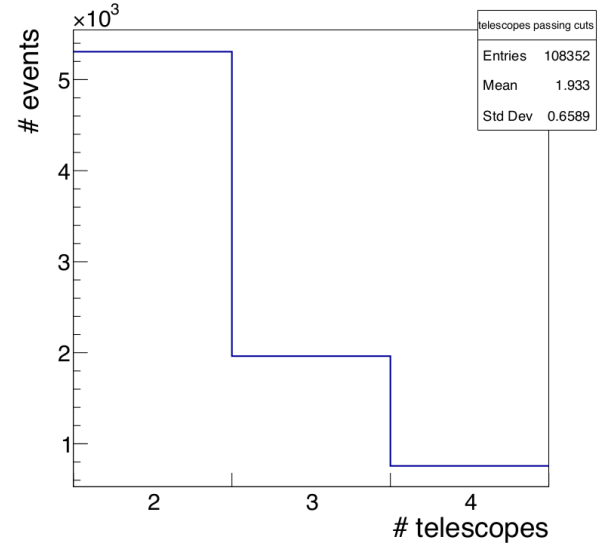
(d) Number of telescope images passing quality cuts in an event.

Figure 5.4: Parameter distributions for stage 4 quality cuts from a typical GC run taken in the V6 epoch. Minimum cut values are marked by green lines, and maximum cut values are marked by red lines.

The two values of the size cut correspond to the V5 and V6 epochs; the increase in light collection efficiency from the PMT upgrade allows for a higher threshold in image size. The optimal size cut also depends on the energy spectrum of the source being analyzed. Higher energy events will create larger size images than low-energy events on average. Sources with a harder spectra will have more high-energy events, so a stricter size constraint can be placed on image size. This also applies if the source is strong and has many gamma-ray events, because you can afford to throw out more events. On the other hand, weaker sources will have less total events and require less restrictive size cuts. For the GC analysis, we require events have at least three images that pass quality cuts because direction reconstruction is more difficult at LZA. Runs that only had only three telescopes participate in the array are excluded from GC runlists, because they contribute few events that meet the requirement of three telescopes passing quality cuts. The distance cut is also more strict at LZA because images tend to be more spread out.

5.5.2   Direction and Core Impact Location

The axis of the shower will develop along the direction of the primary gamma ray, and the major axis of the image ellipse is the projection of this axis onto the camera plane, which represents the focal field of view (FoV) of the observed region in the sky. Therefore, the direction of origin represented by a point in the camera plane would ideally lie along the major axis of the shower ellipse. If multiple images are available, this point would be at the common intersection point of all major axes. In practice, the major axes are not determined perfectly, and there is no single intersection point. Still, there are multiple methods for reconstructing the original direction of the shower.

5.5.2.1   Standard Geometric Method

To estimate the point of origin, the major axes of all shower images are projected onto the camera plane, as shown in Figure 5.5. If there are only two images, the point of origin is estimated to be the intersection point of the two major axes. If more than two images meet

the quality cuts in a given event, the point can be chosen through a simple minimization. The quantity that is minimized is the sum of squares of the perpendicular distances from each axis weighted by $\log_{10}(\text{size})$.

The core impact position is found by the same minimization procedure, however with the axes first projected into the ground plane. An example of the core impact position reconstruction is shown in Figure 5.6. The distance from the center of VERITAS to the impact position is called the impact distance. This parameter is useful in determining the intrinsic brightness of the shower; the farther away a shower develops, the more light spreads into the atmosphere making the image dimmer. For this reason it has a central role in estimating the energy of an event. The geometry of the images is also used to estimate the shower maximum height in this stage. This property can be used to help distinguish between gamma rays and hadronic rays, which take longer to reach maximum development.
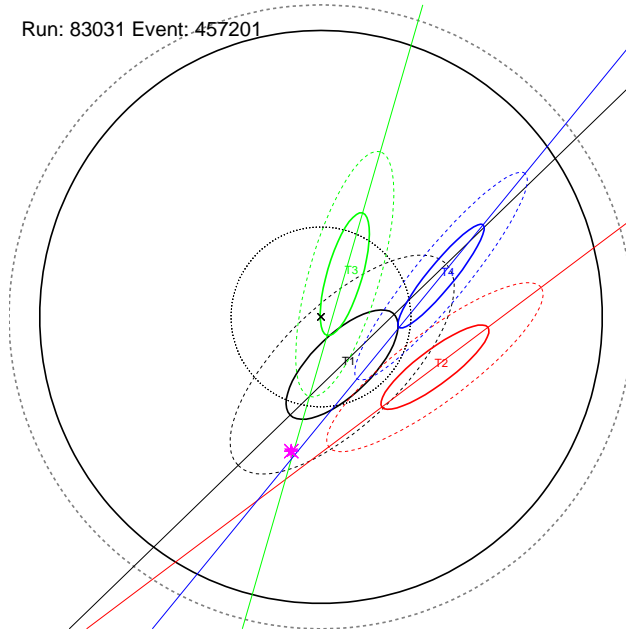
Figure 5.5: A projection of all four telescope images from a single shower event onto the camera plane. Their Hillas ellipses and major axes for each telescope are drawn in different colors. The reconstructed shower direction is marked with a pink star.

112
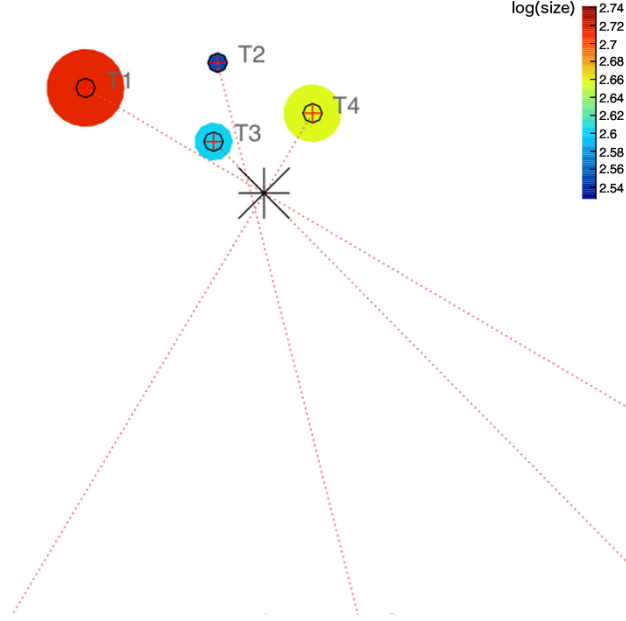
Figure 5.6: Projection of the same images from Figure 5.5 projected instead onto the ground plane. The reconstructed impact location is marked by the black star shape. The color and radii of the circles represent the size of the corresponding image.

5.5.2.2 Displacement Method

The larger the zenith angle (or the lower the elevation) of observation, the more parallel the major axes of the images from a particular shower will tend to be. This introduces a lot more bias in the above method for direction reconstruction, which starts to become substantial around 45° zenith. The very large zenith angle (LZA) of GC observations, which are always at zenith angles greater than 55°, presents a challenge for direction reconstruction. The near parallelism of the major axes of the images introduces a large uncertainty in their intersection point. To deal with this, VERITAS uses a modified algorithm called the displacement method (Sentürk & the VERITAS Collaboration, 2011). This method incorporates an estimate of the disp, or angular distance between the center of gravity of the image and the event direction (shown in Figure 5.3). This method exploits the relationship between size, displacement, and flatness of the image which is quantified by its relative width and length. The standard method for estimating the disp parameter is to produce an additional lookup table with simulations that records tables for the disp parameter. This parameter can be used in the

calculation of the shower direction to achieve a much better estimate. This method also requires a more strict proximity of the image to the center of the camera, or distance, for an image to pass quality requirements. Fortunately, this method has proven to work very well for LZA observations with VERITAS, improving angular resolution by more than a factor of two for 65° zenith (25° elevation), as shown in Figure 5.7. My analysis uses an improved implementation of the displacement algorithm, detailed in Subsection 5.7.1, that will enhance my results over previous GC analyses.
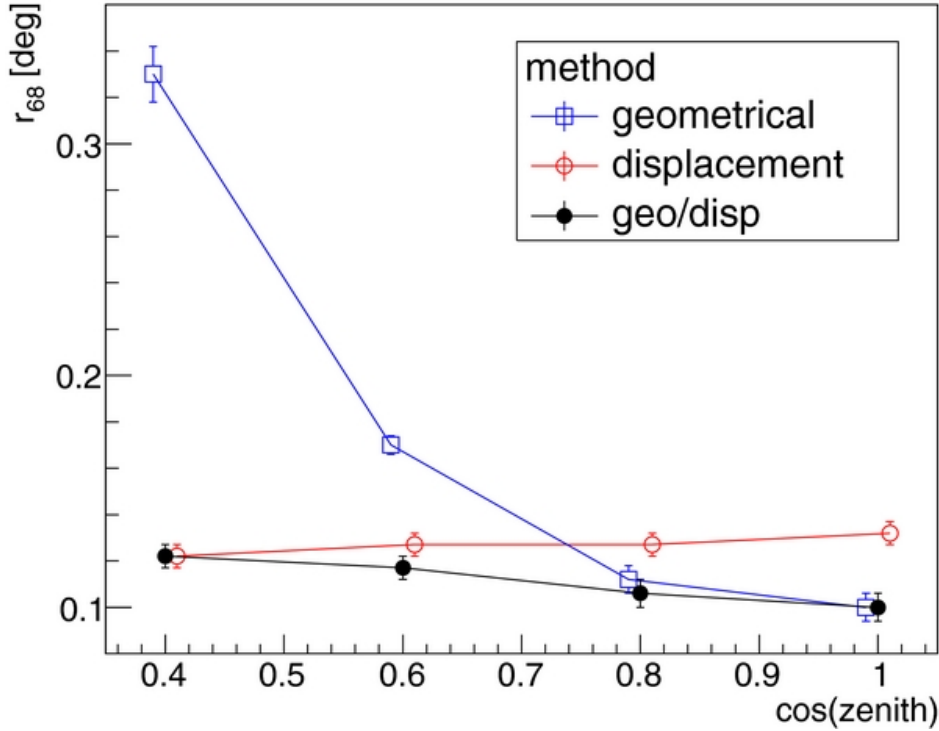
Figure 5.7: The angular resolution of VERITAS plotted as a function of the cosine of zenith angle for the standard geometric algorithm, the displacement method, and a weighted combination of both algorithms. The results are derived from Monte Carlo simulations which reconstructed showers from at least three telescope images. The displacement method outperforms the geometrical algorithm for zenith angles > 40°. Image credit: Archer et al., 2014.

5.5.3 Energy Reconstruction

The energy distribution of gamma-ray events from a source is the basis for the spectral analysis of that source. It is difficult to find an analytical function from which the energy of incoming gamma rays can be found given the Hillas parameters of the resulting images. A simple but effective, and computationally efficient, strategy for reconstructing the incident particle's energy is to generate a large number of detailed Monte Carlo events and use those to decide the most likely energy of the incoming photon given the size and impact distance of its shower image. The first step in generating these tables is producing realistic simulations of particles with known energies.

5.5.3.1 Simulations

The Monte Carlo simulations made for VERITAS have two major components that are created by two completely separate software packages. The first component is the shower simulation, whereby simulated primary events are generated and propagated through a simulated atmosphere. The particle trajectory and interactions with the atmosphere are simulated, resulting in a shower of Cherenkov light. For the purposes of the sources studied in my analysis, the primary particles thrown are gamma rays. Millions of gamma rays are thrown to achieve high statistics, and the energies vary in a randomized manner, covering a range from $50\,\mathrm{GeV}$ to $250\,\mathrm{TeV}$. The number of gamma rays thrown at each energy is proportional to the power law E^{-2}, which roughly reflects the inverse power law spectrum of most VHE sources. The events are thrown at random locations within an area $750\,\mathrm{m}$ in radius from the center of the array, with uniform numerical density by area. To simulate the different observing conditions, events are thrown at various zenith angles and azimuth angles to simulate observing at different positions in the sky, and at different angular offsets from the pointing direction to simulate the different observing modes. The shower and atmospheric simulations are done using a package called COsmic Ray SImulations for KAscade (CORSIKA) (Heck et al., 1998), which is developed by the Karlsruhe Institute of Technology group and used by a wide range of projects outside of VERITAS. VERITAS uses a simulation package

called Groptics to handle the ray tracing of photons. Groptics traces the reflections of the photons on the telescope mirrors and generates a set of hit times and positions in the camera plane.

I used a software package called GrISUDet for simulation of the VERITAS detector optics and electronics. Different light levels of the NSB can be simulated by artificially changing the pedvar levels in the detector simulations. For a given set of shower simulations, the detector simulations can be run and processed with multiple different pedvar values, and those noise levels are used as another parameter in the lookup tables described below. The end result is a set of VBF files in the same format as the real data that can be analyzed using the software packages described previously in this section.

5.5.3.2 Lookup Tables

With the simulation data available, another program is run to populate a large multi-dimensional arrays of lookup tables (LTs) with information about the showers. Each LT is a wrapper class around a weighted two-dimensional histogram that stores information. The z-axis of the histogram stores the weighed mean and standard deviation for one of three lookup parameters: width, length, and energy. The independent axes of all table histograms are $\log_{10}(size[dc])$ (range 1.5–5.5) and impact distance (0–800 m). Note that because simulations are being used, the impact location is known and the impact distance is calculated exactly. The tables in a file are organized into bins of a parameter space that describes the observing conditions of an event. The dimensions of that space are zenith angle, azimuth angle, wobble offset, noise level, and the telescope ID for the image. Each set of observing conditions has three separate tables, each of which contains information for a particular lookup parameter. To populate the LTs, first the standard analysis is run on the raw data files through the image parameterization stage. The LT manager loops through each image and checks if it passes quality cuts. Note that the size cut is excluded because the histograms are binned in the log of size. Each event that passes cuts is appended to a vector of values for that size / impact distance bin. After all events have been processed, the mean and standard deviation

116

of each lookup parameter are calculated for each bin. The histogram's bin content is set to the mean value, and its error is set to the standard deviation of values. Once fully populated, the tables are combined into a single ROOT file for use with real data. LTs corresponding to different atmospheric conditions, such as for summer and winter, or for different array epochs, are stored in separate files.

During shower reconstruction (stage 4), an LT can be used to look up expected values and standard deviations of its three parameters. These are used for calculating stereo parameters (explained in the next section) and for the standard method of energy reconstruction. For every image, the appropriate histograms are examined in order to find the parameter value based on the size and the core impact distance. The program performs a multi-dimensional interpolation between tables and bins to return a mean value and error. In the standard method of energy reconstruction, the energy used for an event is the average of the energies found for each telescope image. The uncertainty is found by taking the RMS of the energy values about the average.

5.5.4   Stereo Parameters

For a given event, it is useful to compare the width and length to their expected values under the relevant observing conditions, size, and impact distance. In the same way the median values of energy were found from the appropriate LT, given size and impact distance, the expected values for width and length are extrapolated from their corresponding tables. The ratio of the value to the expected value is a more useful quantity and is referred to as the scaled length (width), whose value indicates clearly if a shower is longer (wider) or shorter (thinner) than an average gamma ray.

The normalization of these quantities allows their values to be arithmetically averaged, despite different telescopes expecting different scales due to asymmetry resulting from the direction of the incoming gamma ray. The distribution of these values for gamma rays will peak at 1, and serves as a powerful parameter for separating gamma showers from hadronic showers and other background events. This is because of the tendency of hadronic showers

117

to spread light much more unevenly, meaning values of scaled width or scaled length will exceed unity more frequently.

Parameters such as scaled width and scaled length of all telescopes participating in an event can be combined into stereo parameters referred to as mean scaled parameters. The equations for mean scaled width (MSW) and mean scaled length (MSL), are given in Equations 5.4 and 5.5.

$$l_{\text{ms}} = \frac{1}{N_{\text{tel}}} \sum_{i=1}^{N_{\text{tel}}} \frac{l_i}{l_{\text{sim}}(S_i, z_i, d_i, n_i)} \tag{5.4}$$

$$w_{\text{ms}} = \frac{1}{N_{\text{tel}}} \sum_{i=1}^{N_{\text{tel}}} \frac{w_i}{w_{\text{sim}}(S_i, z_i, d_i, n_i)} \tag{5.5}$$

These parameters are useful in describing the overall shape of the reconstructed shower so it can be classified in the next stage.

5.6   Signal / Background Separation

Not every event triggered by the L3 system is guaranteed to be caused by a gamma-ray event. In fact, less than 1% of recorded events are caused by gamma ray showers. The fifth stage of VEGAS selects the most likely gamma rays from the set to be analyzed in the final stage. It also excludes all events that fall within the supplied time cuts.

To properly identify a gamma ray event, we employ the stereo parameters of the reconstructed shower. Example distributions of several different stereo parameters are shown in Figure 5.8, and it is evident these parameters follow very different distributions for gamma rays when compared to background hadronic rays. There are two common methods by which these parameters are used to decide if a shower is electromagnetic or hadronic in nature: box cuts and Boosted Decision Trees (BDTs) (see Subsection 5.7.2).
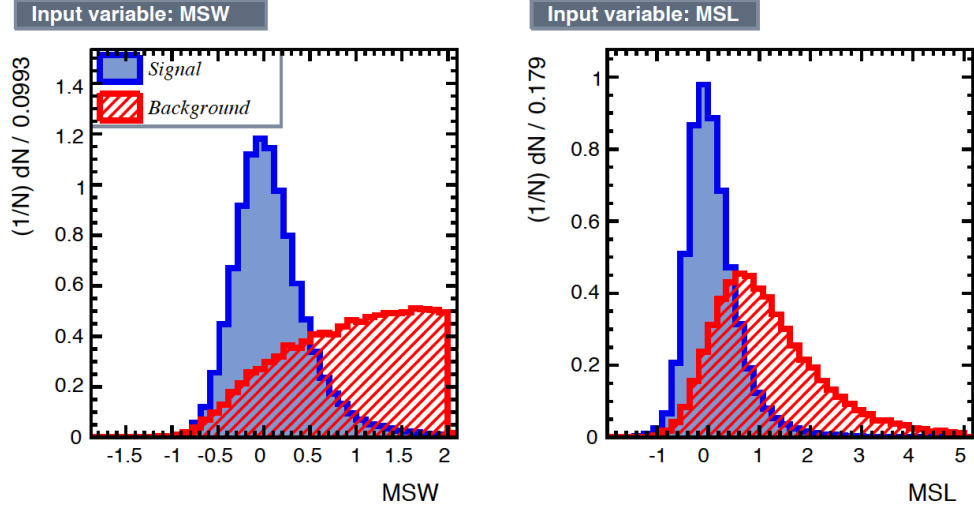
Figure 5.8: Stereo parameter distributions for mean scaled width (left) and mean scaled length (right). Separate curves are overlaid for the distributions of signal events and background events. The signal is composed of simulated gamma-ray events, and the background is composed of data events that do not come from a source region. It can be seen that within a certain range of each parameter, the shower events are almost purely hadronic in origin. Events in this plot are in the V6 epoch, have energies between 1 and 50 TeV, and have zenith angles between 42.5° and 75°.

5.6.1 Box Cuts

The simplest, most standard method for for gamma / hadron separation is imposing box cuts on stereo parameters. The procedure for box cuts begins by comparing the parameter values of an event to predetermined maximum and minimum values. If the value does not fall between the maximum and minimum values, that event is classified as a hadronic event and cut from the analysis. The cuts on each parameter are performed independently, forming a hypercube or "box" in n-dimensional space, where n is the number of parameters by which events are selected. The most powerful separators in order are MSW and MSL, followed by the estimated shower maximum height which is used in certain analyses. The optimal cut values for each parameter are found through an optimization procedure described in Subsection 6.3.2. If the value for any parameter falls outside of that range, it is assumed to be a hadronic shower and is cut or excluded from the analysis. This method is effective, but

there is a non-negligible area of overlap between signal and background for each parameter. This means that box cuts will cut out some signal and include some background.

5.7   Boosted Decision Tree (BDT) Methods

Many of the problems in this chapter rely on simple approximation methods, such as LTs and box cuts. Machine learning algorithms are a modern and rapidly advancing method of multivariate data analysis that have been shown to be extremely powerful for solving complex problems that do not have deterministic solutions. These algorithms recognize patterns in large amounts of training data and build models for making predictions about new data. In the context of gamma-ray astronomy, a model, once trained, could take as input select parameters of an image or reconstructed shower event and make predictions about other properties of that event. These predictions can be made using one of two types of supervised learning: regression or classification.

The technique of Boosted Decision Trees (BDTs) has found many applications in astronomy over recent years, and has been used by other IACTs such as MAGIC (Albert et al., 2008) and H.E.S.S. (Ohm et al., 2009). Common applications include classifying gamma-ray events and hadronic events, and performing regressions for estimating key parameters such as energy. C++ libraries for implementations of various machine learning algorithms are available in the ROOT Toolkit for Multivariate Data Analysis (TMVA) (Hoecker et al., 2007). Of the many TMVA algorithms, BDTs empirically work the best for gamma-ray astronomy, require little tweaking, and are faster than other effective algorithms such as neural nets. This was the only algorithm employed in my analysis, so it is the only one I will detail.

A decision tree is a graph structure that represents a series of branching tests that eventually lead to a decision. Decision trees can be boosted by training new trees to help in the decision process. Each non-terminal node represents a test, and each branch represents a different outcome of that test. A branch can lead to either another test node, or a terminal node which contains a decision. For the instances used in my analysis, the tests were all comparisons of a particular parameter to a specific value, and terminal nodes represent either

a classification or a predicted value of the target variable. Figure 5.9 shows an example of what a tree could look like in my analysis.
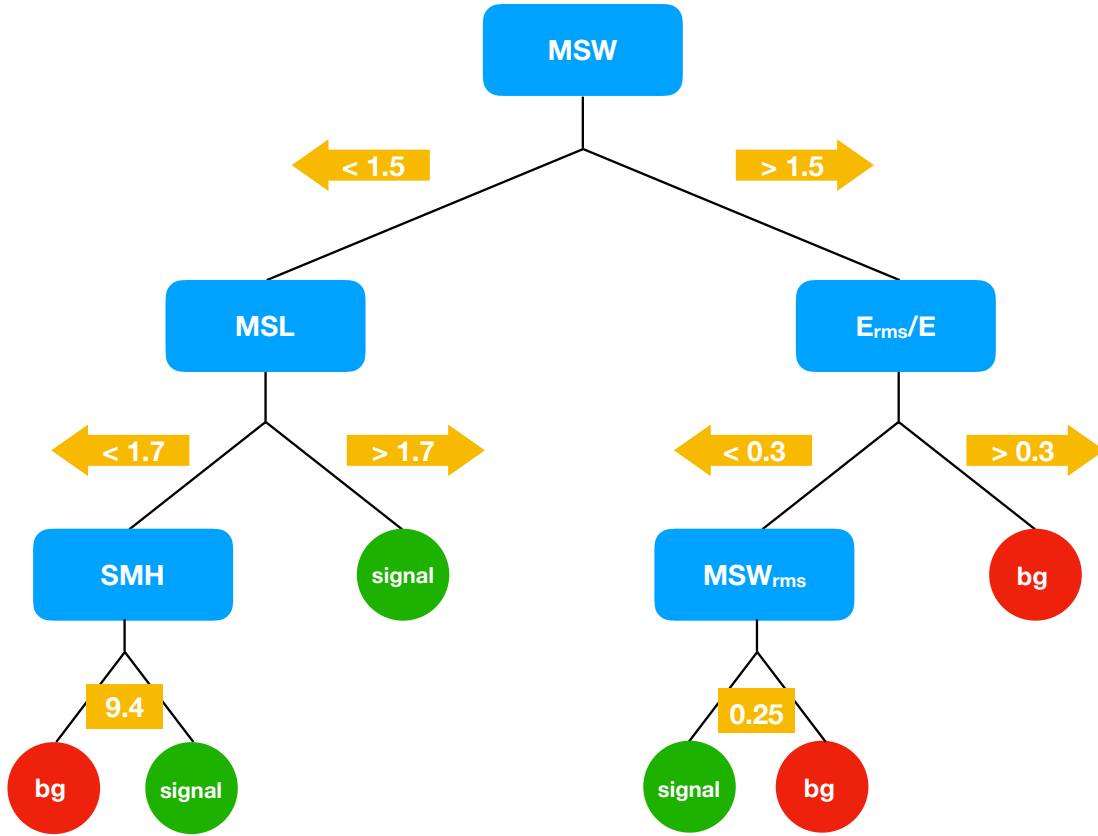
Figure 5.9: An illustration of the graph structure of an example decision tree. At each level, a test is performed on the value of a parameter, and the next node visited depends on the result of that test. The tree is traversed until a terminal node is reached, at which point a decision is chosen.

5.7.1 Improved Disp Method with BDTs

The disp method introduced in subsubsection 5.5.2.2 provides a crucial improvement to direction reconstruction at LZA. An improved version of the disp method (called disp 5t) had been recently developed for VEGAS, but was not used on the most recently published GC analysis. Rather than using the standard LT method, this method performs a multivariate

regression with BDTs to estimate the value and uncertainty of the disp parameter.

Training for the disp estimator proceeds as outlined in Appendix A.3 for a regression, but it is important to note that events in this context refer to images rather than detected shower events. Appropriate simulations are processed through image parameterization, and new ROOT trees are created with the images that pass basic quality cuts. The true disp is calculated for the simulated images and written to the tree along with the training parameters. The training variables used for the disp estimator are: size, width, length, timing gradient, and loss. The timing gradient of an image measures the difference in photon arrival times along the major axis of the image, measured in nanoseconds per degree. Loss is the sum of the signals in all edge pixels, indicating how much of the Cherenkov signal is likely to fall outside of the camera.

Once the image events are split into training and testing subsets, a custom training macro is run that calls the TMVA classes for BDT regression, and the trees are built and added to the ensemble one by one. The disp training worked best using gradient boosting for the iterative process. At each iteration after the first tree, the squared residuals of the dataset are calculated for the current ensemble via the loss function

$$\sum_i [y_i - F(x_i)]^2 \tag{5.6}$$

where x_i are the input events, y_i is the true value of the target variable, and $F(x)$ is the predicted value for the target variable. The subsequent tree is then trained on those residuals, working toward minimizing the loss function.

Most of the options used were the TMVA standard for gradient-boosted BDTs. Also worth noting is that a large number (2000) of shallow trees with a max depth of three were used to build the ensemble.

Additional estimators are trained to estimate the error on both the disp parameter and the direction of the major axis. The error on the disp parameter requires first training the disp estimator, then creating a new variable $\delta_{\mathrm{disp}} = d_{\mathrm{est}} - d_{\mathrm{true}}$, and training on that variable. Both estimators are trained in the same way with the same training variables, except the disp error also uses the disp estimate as a training variable. These error estimates quantify

122

the reliability of the images. The best estimate for the disp parameter of an event is found by taking the mean of the estimates for each image, weighted by their reliability according to the error estimates. This gives preference to images with comparatively lower uncertainty. The weighted disp estimate provided by the BDT is used in direction reconstruction just as it was in the original disp method. This method further improved the angular resolution of direction reconstruction at both large and small zenith angles.

5.7.2 Event Classification with BDTs

As shown in Figure 5.8, the signal and background distributions for the box cut parameters overlap. Thus, BDTs have great potential for event selection because multivariate analysis can look at the combination of multiple variables rather than performing separate cuts (Ohm et al., 2009). A BDT classification was implemented into VEGAS using TMVA as an alternative method for event selection (Krause et al., 2017).

Event selection requires training on only two classifications: signal and background. The signal was composed of simulated gamma-ray events, so there was no background contamination. The background was trained with real data in regions with no known gamma-ray emission, such as dwarf galaxies. The training variables used were the logarithm of the following stereo parameters: MSL, MSW, the RMS of MSL, RMS of MSW, and shower max height, as well as the RMS of energy divided by energy.

The distributions of these parameters, however, have a strong dependence on the energy – even after mean scaling. The shape of signal and background showers are also distorted when passing through more atmosphere, so the distributions of MSW and MSL have a dependence on zenith angle as well. To avoid biasing the training toward any particular energy or inadvertently selecting events based on their zeniths, weights tables must be binned in energy and zenith angle. This means that separate classifiers are trained and tested with events only falling within the corresponding energy and zenith bins.

The method of box cuts can then be replaced with BDTs in the event selection stage. For each reconstructed event, the appropriate classifier is chosen based on its energy and

123

zenith angle. The event then traverses each tree in the forest in the same way described in Appendix A.3 for testing events. The weighted average of outcomes of all trees in the ensemble is assigned to the event as a classification score, which describes how signal-like the event is. Gamma-ray events are selected if they exceed a certain value of that score.

The classification score, while describing discrete classes, is a continuous variable, and can be optimized in the same way as box cuts (see Subsection 6.3.2). An optimization process is run on the classification score to optimize the sensitivity of the Crab, a strong source, for each energy/zenith bin. This method, if properly trained and optimized, has been shown to improve analysis sensitivity by up to $10\,\%$ over box cuts.

5.8 Source Detection and Spectral Analysis

Once all runs in the runlist have been processed, the collection of selected gamma-ray events can be examined to determine how statistically significant the source signal is above the background. In the sixth stage of the VEGAS analysis (item 6 in the previous list), said significance can be found for many locations in the observed FoV, generating a significance skymap. If a source location is detected significantly enough, its energy spectrum can also be constructed.

5.8.1 Signal Region

For all point source analyses, an appropriately sized ON region is chosen – typically a circle centered around the chosen test position. The angular size of the ON region should be large enough to account for the PSF and any extension of the source, but should be small enough to limit background contamination. Because the PSF increases as the event energy decreases, soft spectra are given a larger search window. For a given run, we define N_{on} to be the number of events that have reconstructed directions within the bounds of the ON region.

5.8.2 Background Estimation

While advanced techniques for gamma / hadron separation can reduce the number of hadronic showers, every analysis will have a background that cannot be removed. This background comes from hadronic showers misclassified as gamma ray showers. The rate of these background events across the sky is assumed to depend only on zenith angle. Thus, they enter the atmosphere nearly isotropically across the FoV of an observation. It is necessary, then, to measure the background rate for your observing conditions, including zenith angle and NSB level. Sources are analyzed in terms of the signal excess, or the signal counts after subtracting the background. There are multiple methods commonly used to estimate the background rate that have various advantages and disadvantages.

Camera acceptance An important consideration when it comes to designing methods of background estimation is the concept of camera acceptance. The detection rate across the camera is not uniform, and we define acceptance to be the relative detection rate at a location in the camera, with 1.0 being the value at the location of highest efficiency. The dominant factor that influences the acceptance is that images are better reconstructed closer to the center of the camera. Most acceptances are assumed to be radially symmetric or at least have a strong radial component. Other factors are discussed in the advanced analysis section.

5.8.2.1 ON / OFF Analysis

The original and most basic method for estimating background is by taking observations pointed directly at the source, called ON runs, immediately preceding or following observations pointed at a region appropriate for estimating the background, called OFF runs. The OFF region is chosen to mimic the conditions of the ON region as closely as possible, but must contain no known sources of gamma-ray emission. Typically, these regions are located within a few degrees of their corresponding ON region at the same declination (so the zenith angles will be consistent) and have similar NSB levels to the ON region. The simplifying assumption

made with this method is that the acceptance of the ON region matches that of the OFF region. We define N_{off} to be the number of selected events that are reconstructed within the designated OFF region. The number of counts in a given time interval are assumed to follow a Poisson distribution, and the best estimate for the rate is simply the number of counts divided by the time. The rate of background events in the ON region is also assumed to be the same as the rate in the OFF region, so

$$\frac{N_{\text{bg}}}{t_{\text{on}}} = \frac{N_{\text{off}}}{t_{\text{off}}}. \tag{5.7}$$

Equation 5.7 can be solved for the estimated number of background counts that occur in the ON region, $N_{\text{bg}} = \frac{N_{\text{off}}}{t_{\text{off}}} t_{\text{on}}$. In general, we define a value α as the ratio of background counts in the ON region to counts in the OFF region, such that

$$N_{\text{bg}} = \alpha N_{\text{off}}. \tag{5.8}$$

In the case of an ON/OFF analysis, this is just the ratio of observing times $\alpha = \frac{t_{\text{on}}}{t_{\text{off}}}$, and is kept close to 1. The excess signal above the background N_s is then expressed as

$$N_s = N_{\text{on}} - \alpha N_{\text{off}}. \tag{5.9}$$

The major disadvantage of this method is that the actual observing time on the source is halved. For this reason, it is much more common to point the telescopes at a point offset from the putative source position and then estimate the background from the same run using one of a few methods (Berge et al., 2006). Figure 5.10 illustrates this technique and two such methods for background estimation, described below. This mode of observation is often called "wobble" mode because subsequent runs are usually given the same offset amount but alternate through different orientations, wobbling around the source.

5.8.2.2   Reflected Region Method

The reflected region method (RRM) is the default method that is always run for wobble data, and is useful for both calculating the significance of the signal from a source and the energy spectrum of that signal. As with all other wobble methods, the RRM utilizes

background regions in the FoV of observation that are not within the source region. More specifically, the RRM picks several circular regions that have the same area as the source (ON) region, as shown in Figure 5.10a. The value of α in this case is then $\alpha_{\mathrm{RRM}} = {}^{1}\!/{}_{n_{\mathrm{regions}}}$, and N_{off} is the sum of counts in all OFF regions. These regions have centers equidistant from the center of the camera, offset by the same amount as the wobble offset from the source, but at different rotations around the center. The algorithm uses as many of these regions as it can fit around the center, provided the regions do not overlap each other or any exclusion regions. Exclusion regions are regions in the sky that are used to exclude known gamma-ray sources or bright stars. Typically a circular exclusion region of 0.3° is drawn around the putative source so the background regions are not contaminated by any signal events. For extended sources, the size of the source exclusion can be larger. A major strength of this method is that, by assuming a radially symmetric acceptance function, all regions used will have the same acceptance, therefore no correction is needed to account for differing acceptance. This method is weak for small wobble offsets or when there are too many exclusion regions because the amount of background area will be too small to get adequate statistics.

5.8.2.3 Ring Background Method

The ring background method (RBM) (Berge et al., 2006) is applicable to any point in the FoV. In this background method, the background region is an annulus centered around the ON region, as shown in Figure 5.10b. This makes it possible to find a suitable background region for any point in the FoV. The alpha parameter in this case is the ratio of the area (solid angle) of the test source region to the area of the background annulus, corrected for differences in acceptance. The default thickness of the annulus is the same as the diameter of the source region.

The major disadvantage of this method compared to the RRM is the lack of radial symmetry in the background region – meaning there will be asymmetric acceptances. This asymmetry is corrected by weighting every event by its acceptance according to its position on the camera. However, because acceptance also depends on energy, this method is inadequate

127

for spectral reconstruction.

(a) Reflected regions   (b) Ring background
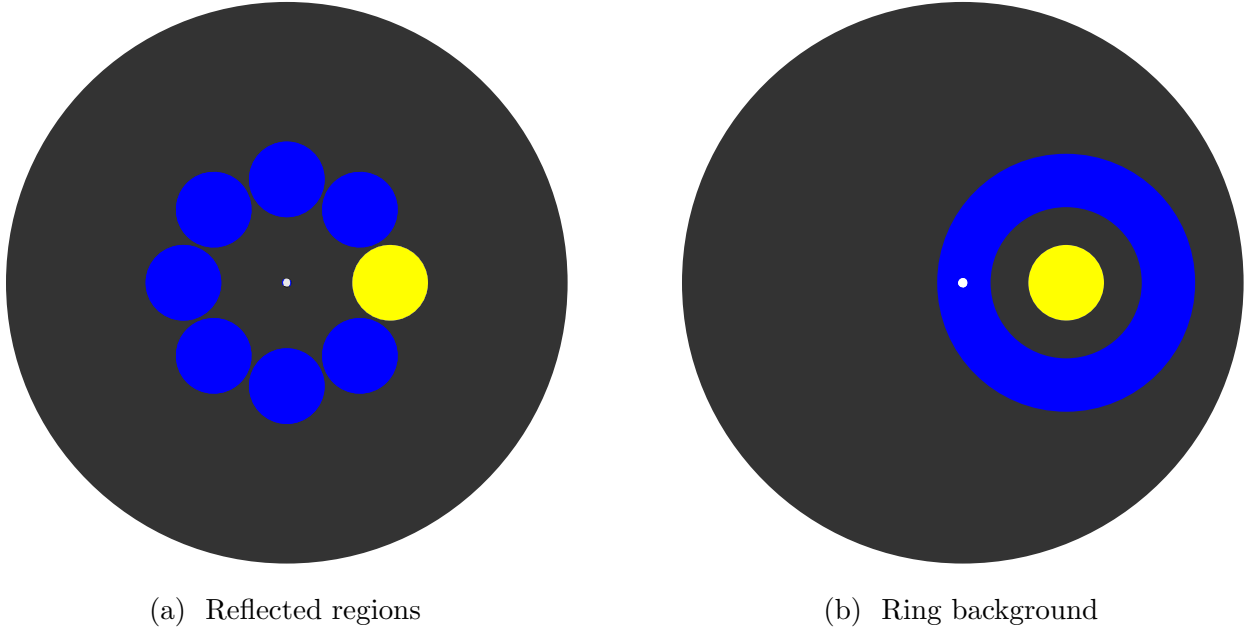
Figure 5.10: The signal (yellow) and background (blue) regions drawn in the camera plane for the RRM (a) and RBM (b) analyses. The white dot at the center represents the observation pointing direction.

5.8.3 Signal Extraction

Once the number of background events, N_{off}, and the α parameter have been estimated, the excess N_{excess} can be calculated:

$$N_{\text{excess}} = N_{\text{on}} - \alpha N_{\text{off}}. \tag{5.10}$$

If the excess is positive, this means the ON counts exceed the expected number of background counts in the ON region. A statistical analysis is performed to determine the probability that an excess comes from a true gamma-ray source, rather than a mere upward fluctuation in the background events. There are many schools of thought in statistics that have led to numerous different ways of estimating the significance of observed counts from a putative source.

Li & Ma (1983) performed an extensive study using Monte Carlo simulations to test variant methods by which astronomers were reporting positive detections of gamma-ray

sources. They found these methods frequently overestimated the significance of the source signal. They present two formulae of their own for estimating the statistical significance of a purported gamma-ray signal. The first is a formula that gives the significance S as the number of standard deviations that the counts in the signal region are above the background counts, $S = \frac{N_s}{\hat{\sigma}(N_s)}$ They are careful when evaluating the standard deviation to work in the assumption that there is no source, meaning the counts in the signal region are also due to background. From this, they arrive at Equation 5.11.

$$S = \frac{N_{\mathrm{on}} - \alpha N_{\mathrm{off}}}{\sqrt{\alpha \left(N_{\mathrm{on}} + N_{\mathrm{off}} \right)}} \tag{5.11}$$

In the case that the number of counts $N \gtrsim 10$, the distribution of counts N_s about 0 will approximate a normal distribution. The confidence level then corresponds to the Gaussian probability of being within S standard deviations of the mean.

They also developed a more careful formula for significance using hypothesis testing; this is the formula we use in our VEGAS analysis, see Equation 5.15. In this case, the null hypothesis is that no gamma-ray source exists in the ON region and the expectation of source counts

$$\langle N_{\mathrm{s}} \rangle = 0. \tag{5.12}$$

The observed events in both regions are then purely background and have the same expectation values,

$$\langle N_{\mathrm{on}} \rangle = \langle N_{\mathrm{off}} \rangle = \langle N_{\mathrm{bg}} \rangle . \tag{5.13}$$

The maximum likelihood estimate (MLE) for the background rate is

$$< N_{\mathrm{bg}} >= \frac{\alpha}{1 + \alpha}(N_{\mathrm{on}} + N_{\mathrm{off}}). \tag{5.14}$$

The alternative hypothesis is simply the case that the null hypothesis is not true, so $\langle N_s \rangle \neq 0$. The MLE of N_{s} is the excess as defined in Equation 5.10, and the MLE of N_{bg} is given by Equation 5.8. The maximum likelihood ratio λ is defined as the ratio of the likelihood function of the null hypothesis given the data to the likelihood function of the alternative hypothesis given the same data. The likelihood function is the probability of observed values N_{on} and N_{off} given the MLEs from above.

If the null hypothesis is true, the quantity $-2\ln\lambda$ approximately follows a χ^2 distribution with 1 degree of freedom, if counts are sufficiently high, because it is the square of a random normal variable. The $\sqrt{-2\ln\lambda}$ is the absolute value of a normally distributed variable, representing the significance S:

$$S = \pm\sqrt{2} \left\{ N_{\text{on}} \ln \left[\frac{1+\alpha}{\alpha} \left(\frac{N_{\text{on}}}{N_{\text{on}} + N_{\text{off}}} \right) \right] + N_{\text{off}} \ln \left[(1+\alpha) \left(\frac{N_{\text{off}}}{N_{\text{on}} + N_{\text{off}}} \right) \right] \right\}^{1/2} \quad (5.15)$$

where the sign is the same as the sign of the excess. The probability p of a significance calculation being S or above with no actual source is the Gaussian probability N of S with a mean value of 0 and a standard deviation of 1.

$$p = N(S; 0, 1) \quad (5.16)$$

In VEGAS, the significance is calculated with Equation 5.15 for each spatial bin in the skymap, generating a significance skymap, an example of which is shown in Figure 5.11.

5.8.4 Effective Area

In studying astrophysical sources, the best way to compare the data to theoretical models of emission is to accurately and precisely reconstruct the spectrum, which measures the flux as a function of photon energy. Spectral reconstruction is done in the final stage of the VEGAS analysis, along with skymap generation.

The position used to calculate the spectrum defaults to the location of the source, in this case Sgr A*, but can be changed to any coordinate that has data. Proper spectral reconstruction requires a lookup table of effective area, which uses simulations to translate a detected count rate into a flux, binned by incident photon energy. I have generated numerous custom effective area files that are tailored for LZA analyses for my own use, and have made these available to the collaboration as well.

For a simple direct detector with detection area A and perfect detection efficiency, the flux of N particles detected in a livetime t would be

$$F = \frac{N}{At}. \quad (5.17)$$
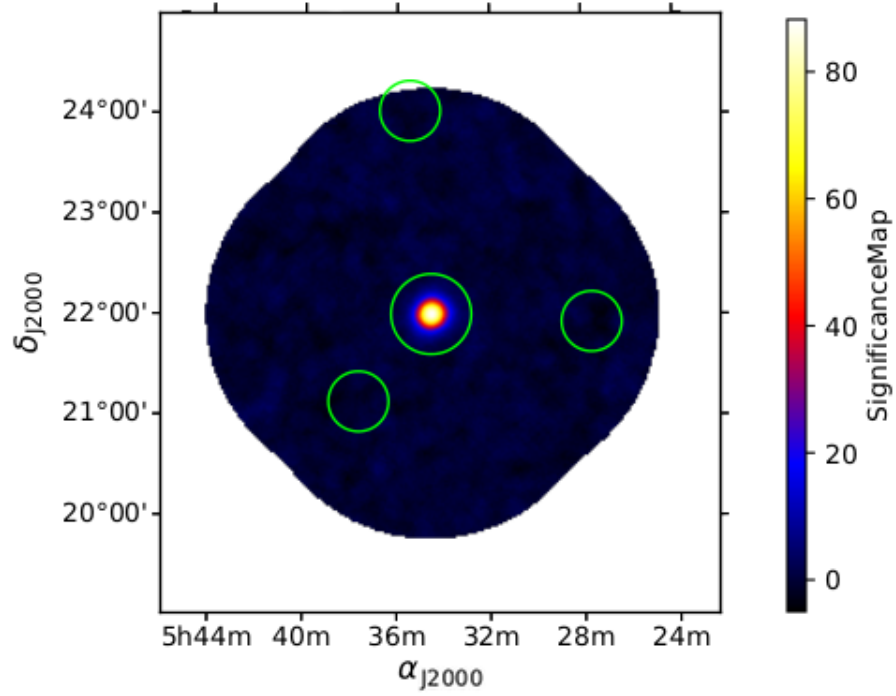
Figure 5.11: Skymap of gamma rays with $E > 85\,\mathrm{GeV}$ generated with 30 hours of observations taken with VERITAS during the V6 epoch. The color map represents the significance as defined in Equation 5.15. The coordinates are right ascension and declination. Exclusion regions not suitable for background estimation are drawn in green.

For an indirect detector such as VERITAS or any IACT, an instrument response function (IRF) named the effective area (EA) is found to measure the area over which an arriving particle will be successfully reconstructed. Essentially, it is a way to determine how many particles actually passed through a particular area in a specific time interval given the number of particles that were detected in that interval. The EA, while generally a property of the telescope array configuration, also depends strongly on the observing conditions and energy of an event. The zenith angle dependence is especially strong, because particles that approach the detector at low elevations must pass through more atmosphere before reaching the ground level. The EA tables in a file are organized by the same dimensions as LTs excepting telescope ID which is not applicable to an entire event. Both EA tables and LTs are organized into separate files by epoch and season. Each table contains a 1D histogram with a vertical axis

131

of effective area and is binned by $\log_{10}(E)$.

The method for filling EA tables uses the same set of simulations that were used to build the LT. Both the parameterised events tree and the tree containing all of the original simulated gamma-ray events and their properties are retained. The large number of simulated gamma-ray primaries are thrown uniformly over a large area A_{in}. This area is centered around the array and large enough to encompass all reconstructable incident particles. The parameterized events are then run through the shower reconstruction stage of VEGAS using the same cuts and configuration used in the analysis of real data. For each simulated event, its appropriate table is located and a counts histogram is filled, and if that event is successfully reconstructed, a separate counts histogram is filled. All three histograms have the same energy binning, and the bin is determined by the true energy, rather than reconstructed energy, by default. The total number of events that fall within that energy bin, according to their true energy, is N_{rec}.

The effective area in an energy bin is then the incident area A_{sim} multiplied by the fraction of simulated events that are reconstructed:

$$A_{\text{eff}}(E) = \frac{N_{\text{rec}}(E)}{N_{\text{sim}}(E)} A_{\text{sim}} \tag{5.18}$$

where N_{sim} and N_{rec} are the number of simulated and reconstructed events falling in that bin. A_{eff} can then be used with Equation 5.17 to find the flux.

Energy bias and resolution   For every EA, the energy bias and resolution are stored for each energy bin. The energy bias measures the systematic offset in reconstructed energy compared to the known simulated energy of the primary particle. The energy bias for a given simulated event is

$$bias = \frac{E_{\text{rec}} - E_{\text{sim}}}{E_{\text{sim}}}, \tag{5.19}$$

where E_{rec} is the reconstructed energy and E_{sim} is the true simulated energy of the event's primary particle. When producing EA tables, a histogram of this quantity, binned in $\log E$, is filled for each reconstructed simulation event. The energy bias quoted for a given energy is the mean value of this histogram in the proper energy bin. Energy resolution measures the

standard error in a bin as a percentage of the energy of that bin, and is quantified as the standard deviation of this histogram. If the bias in the energy estimate is too large for an event, the event can be excluded from the analysis entirely. The "safe energy range" is the range in which the bias is $\leq 10\,\%$, by default.

5.8.5 Flux Calculation

A spectral analysis is performed on a runlist with individual runs organized into run groups according to their corresponding EA files. When running a spectral analysis, all of the events in the runlist are looped through as in the skymap analysis. A large number of histograms made with the same energy binning record the statistics of ON and OFF counts. A histogram is filled with one count for each ON event, weighted by the inverse of the effective area for that event. A separate histogram is filled for OFF events with the same weighting factor. Once complete, the bin content and error of the weighted OFF histogram is scaled by alpha. A histogram containing the signal excess is found by subtracting the scaled OFF histogram from the ON histogram. The differential flux $\frac{dN}{dE}$ in each bin is calculated as the excess divided by the effective area A_{eff}, livetime t, and width ΔE of that bin (Equation 5.20).

$$\frac{dN}{dE} = \frac{\Delta N_{\text{exc}}}{A_{\text{eff}}t\Delta E} \tag{5.20}$$

Note the spectral analysis is only valid for a source that is significantly detected ($> 5\sigma$), assuring that the majority of events are signal events and that the energy spectrum is not biased toward that of the background.

Once the spectral points have been calculated, the spectrum is fit to a function of energy that describes the shape of the emission, typically a pure or modified power law. Reasonable parameter ranges are set for the index and normalization of the power law function. The fitting is done with a minimization routine called Minuit (James & Roos, 1975), and the parameters are reported along with goodness of fit. The decorrelation energy, where the uncertainty of the fit flux is minimal, is also printed. The spectral fit can be re-run with the normalization energy set to the decorrelation energy, which will reduce the uncertainty of the fit, narrowing the confidence band. This cycle can be repeated until the decorrelation energy

converges to the normalization energy, minimizing the confidence band butterfly.

The optimal cuts found, as well as the standard values for comparison, are listed in Table 6.2:

CHAPTER 6

Specialized Analysis for the Galactic Center

My GC analysis is non-standard in many ways. The low angle of elevation at which VERITAS observes the GC (about 25–30°, see top of Figure 6.1) introduces additional difficulties in analyzing shower events. This complication occurs because incident showers have to pass through a greater distance of atmosphere as the zenith angle increases. The GC region also has a very complex morphology, with multiple point sources and extended diffuse emission, making its signal much more complicated to analyze than a single point source. To improve upon previous analyses, I utilized and developed advanced techniques that were more optimal for LZA data and bright fields. I also developed a method to combine spectral statistics from multiple regions to extract a spectrum of the diffuse emission along the GC ridge. In this section, I describe the advanced analysis techniques I implemented for the GC work.

6.1 Energy Reconstruction

Energy reconstruction is of particular importance to this dissertation, as the energy spectra are central in discriminating between the models reviewed in Chapter 3. We are particularly interested in the highest energy spectral points where VERITAS has a uniquely high effective area (see Figure 4.11). The energy spectrum of both J1745–290 and the diffuse emission are of extreme importance in determining the mechanism of the central emission and the potential of a PeVatron at the center. However, energy reconstruction is no exception to the difficulties inherent in the analysis of LZA data, and our collaboration lacked software capable of extracting spectra from regions as spatially extensive in nature as the diffuse
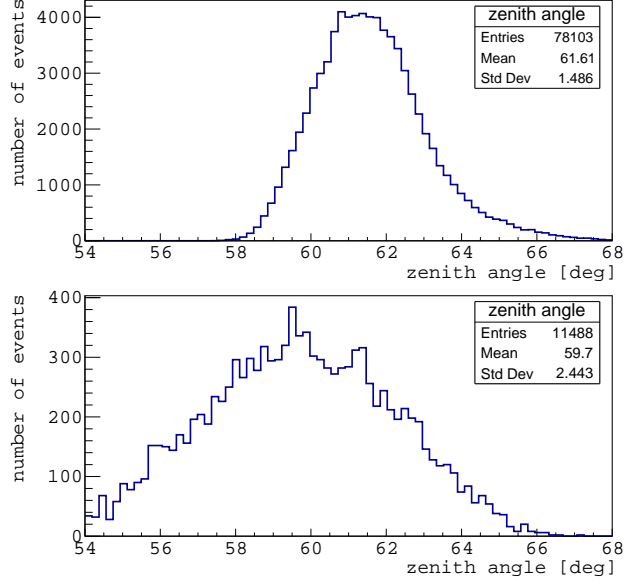
Figure 6.1: Zenith angle distributions of events in both my GC analysis (top) and Crab validation study (bottom).

emission. In this section, I detail the problems I found with previous GC analyses and the solutions I used to address them.

6.1.1 Energy Bias

A plot of the energy bias for a standard VEGAS analysis at small zenith angle (SZA) is shown in Figure 6.2 (see Section 5.8.4 for calculation of energy bias and resolution). For most energies, the bias is consistent with zero, with any deviation being much smaller than the energy resolution. The large positive bias at energies near or below the energy threshold is normal because low-energy events that pass the size cut will have sizes greater than the average for that energy, as the images lesser in size are not reconstructed. This bias at energies below the threshold can be ignored because such events are not included in the real analysis.

An investigation of the energy reconstruction for LZA simulations revealed a concerning negative bias that worsened as zenith angle increased. Figure 6.3 shows the energy bias and resolution for a zenith angle of 60 degrees. The parameterized LZA simulations used

136
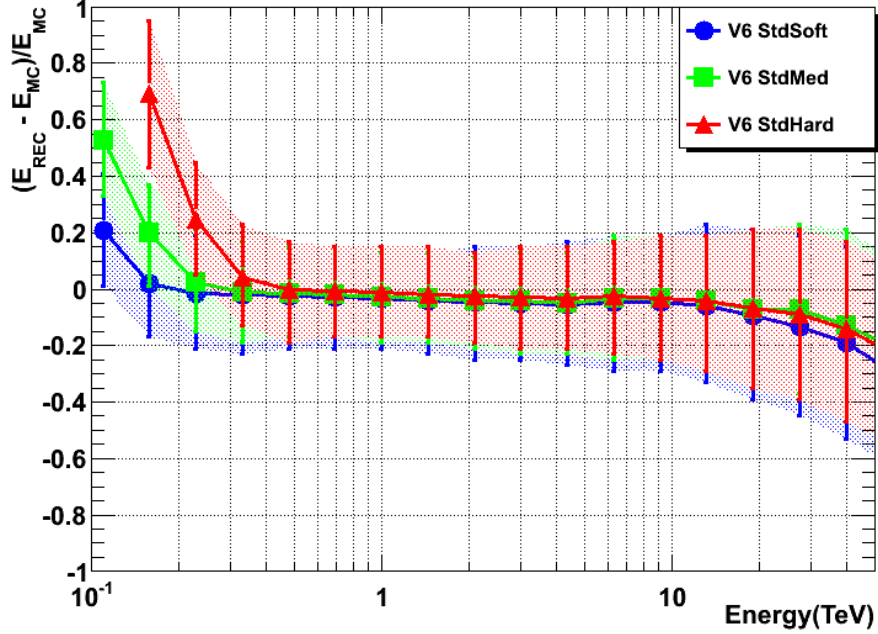
Figure 6.2: Energy bias curve for an analysis with VEGAS using data from epoch V6. The curves are shown for the three standard sets of cuts: soft (blue), medium (green), and hard (red). The error bars represent the energy resolution. The data are for small zenith angles.

for the GC analysis were processed with the BDT disp method (Subsection 5.7.1) of shower reconstruction, and the energy bias was found as per the calculation in Section 5.8.4. The simulations used to generate the plot were thrown at zenith angles of 60 and 65 degrees, with the standard wobble offset of 0.5 degrees, and used high noise levels and atmospheric simulations typical of GC data. For comparison, I also processed the same simulations with the standard geometric direction reconstruction to investigate any effects of the *disp* method itself.

In order to separate the effects of the disp method from the direct effect of zenith angle on the energy reconstruction, the standard method was tested at various zenith angles as a control. I also tested the disp method at the two zenith ranges relevant to the GC observations. I found that most of the bias was a result of large zenith angles alone, but was worsened slightly by the disp method. The bias curve produced at 60° zenith with the standard method had a strong bias of about negative 20 percent, and the resolution increased to about 25 percent. By comparison, the BDT disp method at the same angle brought the energy bias

137
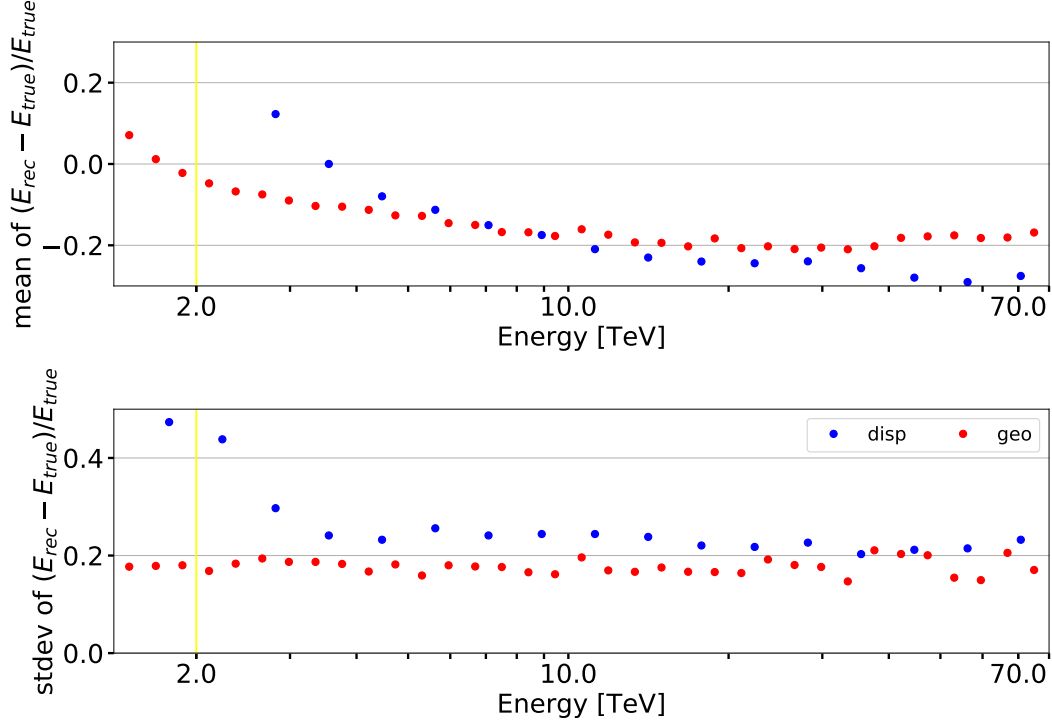
Figure 6.3: Comparison plot of energy bias and resolution produced with the standard geometric and disp methods of direction reconstruction. The plots used data from V6 simulations thrown at 60 and 65 degrees with noise typical of the GC. The energy bias (top) and resolution (bottom) are plotted as a percentage of the energy. The energy threshold is marked by the vertical yellow bar.

to about negative 26 percent and further increased the resolution to about 27 percent. At 65 degrees, the bias intensified more, approaching negative 30 percent, and the resolution reached higher levels of about 30 percent. These results are displayed in Figure 6.3. Table 6.1 summarizes the results of all energy bias tests. Note that the effects were similar for the LT disp method, but a few percentage points less severe.

It is important to note that impact distance, which is used as an LT parameter (see subsubsection 5.5.3.2), uses the same geometric method for direction reconstruction and suffers the same problems for LZA data. The direct relationship between impact distance and energy as estimated by the LT prompted the investigation of any bias in the impact distance when using the disp method for direction reconstruction.

Dir. Recon.	Energy Recon.	Zenith Angle	Energy Bias	Uncertainty
Standard	Standard	20°	≈ 0	18 %
Standard	Standard	60°	$-20\,\%$	25%
Disp 5t	Standard	60°	$-26\,\%$	27%
Disp 5t	Standard	65°	$-30\,\%$	30%
Disp 5t	BDT	60°	≈ 0	19%

Table 6.1: Summary of energy bias and uncertainty of simulations at small and large zenith angles. The energy bias and uncertainty are given as percentages of true energy. Because these quantities vary, average values are given for the important energy range.

The impact distance showed no bias for standard reconstruction (at all energies any bias was less than the uncertainty in the mean) for small zenith angles. The uncertainty slightly increased as zenith increased, and at 65 degrees there appeared to be a very small negative bias of less than 5 %. For small zenith angles, there was no strong trend in the impact distance bias of the disp method. However, use of the BDT disp method (5t) introduced a large negative ID bias of about 20% at 65 degrees (see Figure 6.4). The mean bias was similar for the LT disp method but with much higher variance.
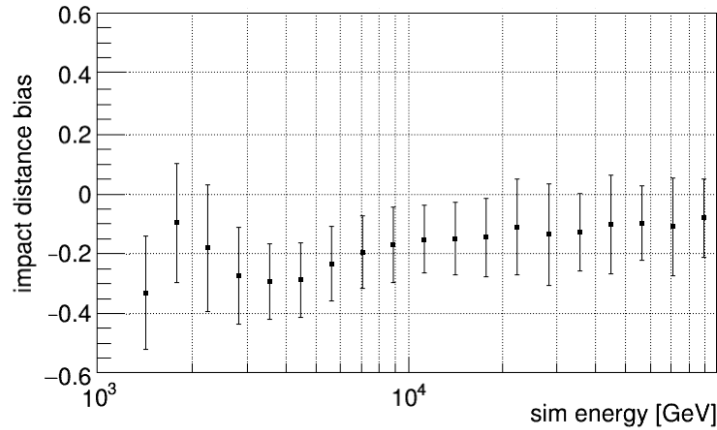
Figure 6.4: Bias curve for impact distance using disp reconstruction for V6 simulations at 65 degrees zenith angle. The points represent the mean bias in an energy bin and the error bars represent the average uncertainty.

Recall that the impact distance reconstruction follows the same geometric calculation as the default method of direction reconstruction, except it is performed in a different plane. There will always be a number of events that are able to pass the disp method but unable to pass the geometric method of direction reconstruction. It is possible that the unfavorable geometry of these events is causing the bias due to the inaccurate estimation of the major axis. Because the LT is filled according to the true impact location from the simulation, a bias in the reconstructed impact distance will cause the energy to be retrieved from a bin with a lower impact distance than it should. For a given size, this means the energy will be lower than if it were retrieved from the correct impact distance in most cases, causing a bias in the LT method of energy reconstruction. The introduction of a negative impact distance bias when using the disp method is thus consistent with the energy bias becoming more negative.

The mean energy stored in the LTs changes very quickly at large zenith angles; bins with zenith angles of 65° generally have a mean value that is 20–30 % higher than 60° bins, holding other dimensions constant. As with other aspects of simulations (lookup parameters, EA tables, BDT event selection), the energy reconstruction would benefit greatly from more fine variation in zenith.

6.1.2 Energy Regression with BDTs

The energy spectrum is central to my analysis, so improving the energy reconstruction was important. One possible strategy for doing this would be to use a method analogous to disp for the core location reconstruction with the aim of correcting the impact distance bias. A few people in the VERITAS collaboration had made such an attempt and found that estimating this parameter is much more difficult. Other IACTs have used decision trees for energy reconstruction, such as MAGIC (Albert et al., 2008), and the performance improvement of the new disp method showed the power of estimating parameters with BDT regression in a VERITAS analysis. I decided to experiment with machine learning on a small set of LZA simulations to see if there was potential for improving either the energy bias,

uncertainty, or both.

The first step was to organize the training data into ROOT trees compatible with the methods available in TMVA. Simulation data must be used because the true energy of the primary must be known. I used the same calibrated stage 2 simulation files that were previously processed for LT production. Each entry in the training tree represents a simulated shower event that triggered the array, and the entry is written with the Hillas parameters of all four telescopes for a shower event as well as the properties of the primary gamma ray. I wrote a ROOT macro that was used to automate the creation of trees for all desired parameters. The same quality cuts applied in LT production are applied to the events, including the minimum pixel requirement, three or more telescopes, and the distance cut. The size cut is excepted and used as a training variable, just as it is used as a lookup variable in the standard method.

The TMVA factory allows the automated training using different multivariate methods, so I began training and testing with a small subset of the parameter space of my analysis to determine the most effective method. To determine the most effective TMVA method, I tested various algorithms with their default settings and compared their resulting bias curves. I began with the same set of variables used for the disp estimator, as they had proven to be a strong set of predictors. BDTs were the most effective method, with adaptive boosting having a slight edge over gradient boosting. The k-Nearest-Neighbor method was almost as effective but much less efficient (slower by an order of magnitude).

After selecting BDTs with adaptive boosting as the best method, I ran the training with a superset of the training variables used previously. TMVA automatically ranks all of the input variables by their correlation with the target variable. Using this ranking as a guide, I iterated through each promising variable and trained a set of trees. A separate macro evaluated each new weights file on a given set of simulations and created a bias curve for comparison. No new variables were found to be helpful, but excluding the azimuth was found to help marginally. I decided to exclude this variable, reducing the number of input variables.

The true and predicted energies for each evaluated event were written to a ROOT tree.

141

This tree was subsequently used as the target for a new estimator, the predicted uncertainty of the energy. The training options and variables were held constant with the addition of the estimated energy as a training variable.

I tested the method on a more expansive parameter space, covering the full noise and zenith angle range that appear in the GC data. Training simulations included all observing offsets so that the trained weights were applicable to the spectrum of the diffuse region, which covers the full range of offsets. The number of events added at each offset was scaled according to the LZA acceptance curve to weight the offsets properly.

The next step was to tweak the training options of the adaptively boosted decision tree. These options included the number of trees in the ensemble, the maximum depth of trees, the minimum number of events required for a new node, and the number of cut values tested to achieve optimal node splitting. I iterated through the parameter space, first doing a coarse search for the best set of options, then refining the values with a fine search.

The best configuration for energy regression used adaptive boosting and ended up being more optimal for a small number of deep trees, as opposed to the large number of shallow trees that worked best for the disp method. No maximum depth was specified, and nodes terminated when they either had too few events or no longer added separation power. It is possible that directional biases correlated with training variables could be averaged out when tested on the full parameter set. To ensure the weights would perform consistently, they were tested on a subsets of the parameter space. For example, I tested weights trained on all offsets on a few singular values of offset and checked the bias curves for any offset-dependent bias. I found no such biases for the variables I used.

The energy bias and uncertainty of the optimized BDT weights for V6 simulations at 65° zenith angle is plotted with the LT method in Figure 6.5. As can be seen, the bias converges to zero quickly above the energy threshold and remains consistent up to the highest energies detectable by VERITAS. The energy uncertainty for the BDT method is lower than for the standard method over the full energy range and is more comparable to the standard method at SZA. The optimal training parameters were then used to train V5 simulations in the same

way, with the results showing the same improvement.
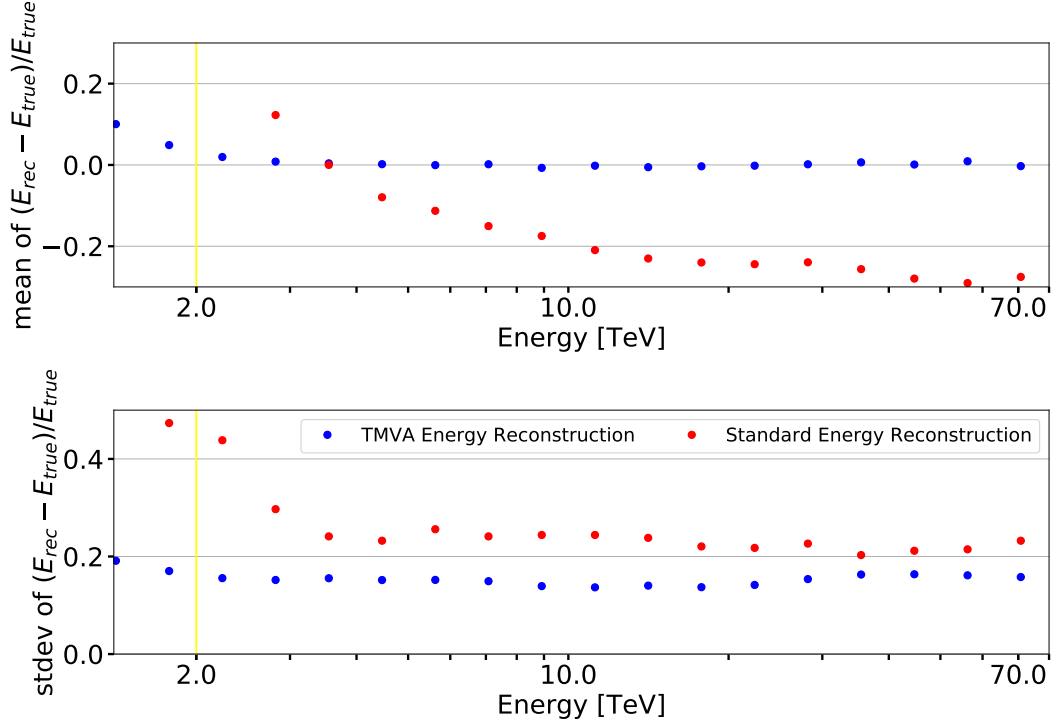
Figure 6.5: Histograms of the energy bias (top) and energy resolution (bottom) binned in energy for two different methods of energy reconstruction. The standard method for energy reconstruction is shown as red points, and the TMVA (BDT) method is shown in blue. The vertical yellow line marks the energy threshold. The simulations were thrown from a zenith angle of 65°, where the bias is most severe, and the detector simulations modeled the V6 array for the plot pictured.

Once I was confident in the trained weights files, I validated the new energy reconstruction with a full analysis of real data. The customary target on which to validate new methods is the Crab pulsar, a strong and steady source for which VERITAS takes a great deal of data covering a broad range of zenith angles. Starting in 2017, I requested a larger set of Crab data be taken between 25° and 30° elevation. Since that time, the total amount of observation data in that range has increased from five to ten hours. Because the gamma-ray rate of the Crab is very high, ten hours of data provide enough signal events to yield a statistical significance above 60σ, well above the rough requirement of 10σ for spectral reconstruction.

The distribution of zenith angles of Crab events from the data set I used is shown on the bottom of Figure 6.1.

A spectral analysis using this new energy reconstruction method required generating new EAs, as the EA energy bins are filled using the reconstructed energy rather than the true energy of the simulation by default (see Subsection 5.8.4). The event selection box cuts were optimized for LZA (see Subsection 6.3.2). Both the simulation and Crab data were processed through the shower reconstruction using the same options as previously used for the disp method, changing only the energy reconstruction method and the size cut. Each file was provided the proper energy reconstruction BDT weights file according to its epoch, atmosphere, and zenith angle. The event selection stage and EA production used the new optimized values for MSL and MSW.

The results of the Crab spectrum are shown in Figure 6.6, along with spectral points for the standard analysis at SZA and a BDT disp method at LZA with the standard method of energy reconstruction. The standard analysis points (purple) are consistent with the accepted spectrum of the Crab in this energy domain. The spectral points are fitted with a pure power law (Equation 3.1) from 2–10 TeV, which is the range common to SZA and LZA. The best fit parameters, shown below, show improved agreement between the standard method and the BDT method for energy regression. The spectral fits of LZA data processed with the standard method of energy reconstruction were not consistent with the standard SZA results. Both parameters, the flux normalization and power-law index, deviate from the accepted values by more than their respective errors.

6.2 Spectral Analysis

6.2.1 Diffuse Spectrum

The spectrum of the diffuse emission is of great interest, but VEGAS does not come with machinery to analyze diffuse regions; the default point source analysis can only look at circular ON regions. This precludes finding the spectrum in the Pacman-shaped sector,

144
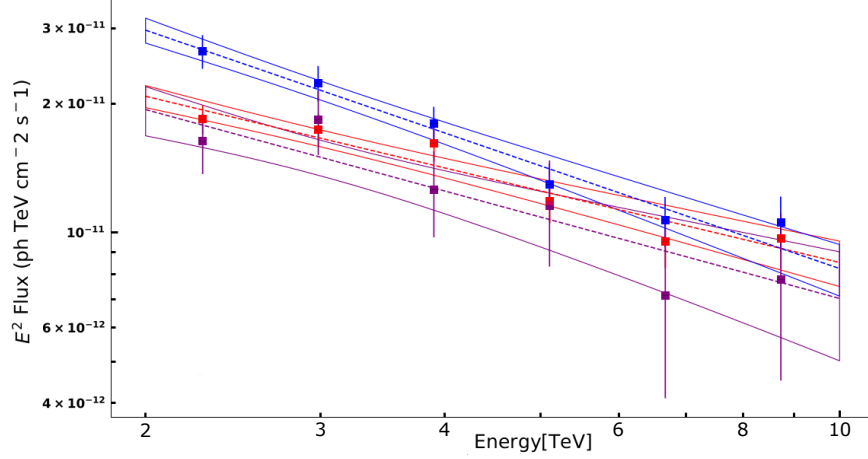
Figure 6.6:

Recon Method	N_0 (10^{-12}TeV^{-1}m^{-2}s^{-1})	Γ	E_0
Standard SZA (purple)	1.67 ± 0.16	-2.63 ± 0.22	3.0 TeV
Disp 5t (blue)	2.39 ± 0.12	-2.80 ± 0.11	3.0 TeV
Disp5t + ER3 (red)	1.85 ± 0.08	-2.55 ± 0.09	3.0 TeV

Comparison of the Crab spectrum for three methods of shower reconstruction. The purple points were produced using the standard methods for both direction and energy reconstruction on an SZA runlist. The blue points used the BDT disp method and standard energy reconstruction on an LZA runlist. The red points used the BDT disp method and BDT energy regression on same LZA runlist. The fit is performed over the spectral domain common to SZA and LZA analyses. The table gives the parameters N_0, Γ, and E_0 as defined in Equation 3.1.

pictured on the right in Figure 3.6, from which H.E.S.S. extracted the diffuse spectrum. While there were multiple regions along the ridge, there were not sufficient statistics to get a full spectrum with points of reasonable uncertainty from any single region.

To extract the spectrum from these circles along the ridge, I coded a macro that stacks the spectral regions and combines the statistics to create a single spectrum. The macro reads in all of the relevant histograms, including those for ON counts, OFF counts, livetime, effective area, and alphas, binned in energy. The histograms are combined by simply taking the bin-by-bin sum of every loaded histogram. A copy of the spectrum analysis class object
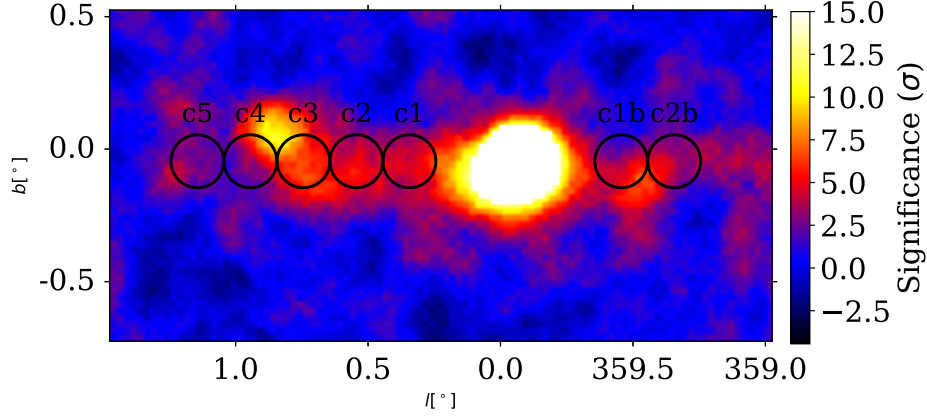
Figure 6.7: VERITAS skymap highlighting the GC regions from which the diffuse spectra are extracted. The black circles show the H.E.S.S. spatial regions from Figure 3.6. The VERITAS spectrum is extracted from the circular regions.

is reassigned with the combined histograms. Flux histograms are derived from the summed recorded histograms. Finally, the spectral analysis code is run as normal, calculating the spectral points and fitting them to the selected function.

The algorithm can be validated on any source by simply splitting a longer runlist into multiple subsets. One can recreate the total spectrum by running the spectral analysis on each sub-runlist and finding the combined spectrum of the results from each. The combined result can be compared to the result obtained by simply running the VEGAS spectral analysis on the runlist with the full set of runs. Indeed, both results are be consistent to within the limitations imposed by float precision carried over many operations.

Additional consideration needs to be taken when stacking multiple regions that come from the same runs, rather than combining separate non-overlapping runs on a singular region. The arc of background regions used in a RRM analysis depends on the location of the ON region and the telescope pointing specified by wobble offset and direction. For a given pointing, the background regions corresponding to one region may overlap with one or more background regions associated with other ON regions. Any events that occur in such overlaps are double-counted, artificially increasing the background statistics and underestimating the uncertainty in background flux. To prevent this effect, exclusion regions are strategically

146

added to prevent certain background regions from being drawn. Because the background regions are determined by the camera pointing, each of the eight pointing directions has its own set of exclusion regions. An example of the regions before and after the addition of exclusion regions can be seen in Figure 6.8.
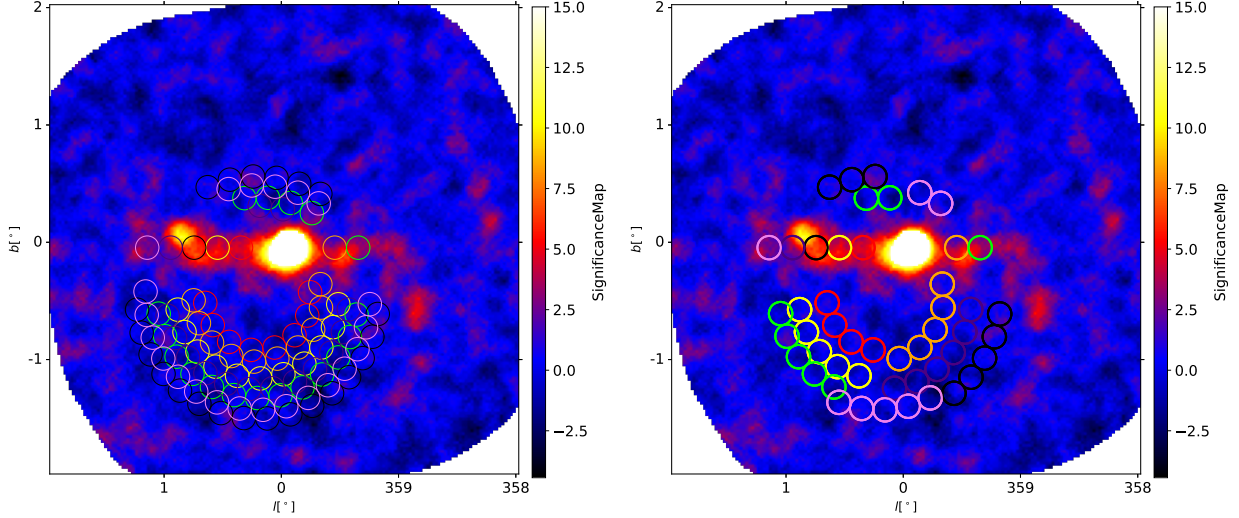
Figure 6.8: Skymap of the GC showing the background regions for the 0.5° East wobble pointing. The default regions shown on the left have significant overlap. On the right, the exclusion regions prevent overlapping regions from being used. The background regions are color-coded to match their corresponding ON region.

Small overlaps of less than 5 % were acceptable compared to the loss of excluding entire regions. For example, removing one background region from C2 (yellow) reduces the number of background events by 20 %. It was also found that the relative uncertainty in EA $\left(\frac{\sigma_{E_{\text{eff}}}}{E_{\text{eff}}}\right)$ more than doubled for a camera distance greater than 1.5°, so pointings at a distance larger than this were excluded when re-combining the histograms of the spectral analysis.

6.2.2 Lightcurve / Variability

Another key consideration in narrowing the possible emission models of J1745–290 is variability in its VHE flux. Variability can be inspected by looking at the lightcurve of a source, which plots the flux in bins of time, such as in Figure 3.5.

147

Lightcurves can be produced readily in VEGAS using a separate analysis class. The lightcurve points are calculated by a similar procedure to that in Subsection 5.8.5, but the histograms are binned in time rather than energy. The flux calculation still follows Equation 5.20. These flux points can be examined statistically to determine if there is flux variability. If no strong variability is detected, an upper limit can be placed on the frequency and magnitude of VHE flares.

To characterize the variability, or lack thereof, I employ a statistical method called the sliding window method. This involves choosing one or more time periods to be the size of the "window". This window is iteratively shifted, one time bin per iteration, and the flux inside the window is compared to the average flux outside of the window. The z-score distribution is plotted and compared to a normal distribution.

Because VERITAS does not observe the GC at all times, flares or variability may occur on short time scales and were simply not observed by VERITAS. If no statistically significant flaring is detected, upper limits can still be placed on the frequency of flaring that may have occurred when VERITAS was not observing using Monte Carlo simulations. For a given time period, flares of a specified frequency can be simulated to occur at randomized times within that period, and any flares that occur during active observations are treated as detected. By simulating many such periods, the probability of a flare being detected can be found for a specified flaring frequency. See Rolke, 2005 for how to find 99% confidence level on the frequency of flares.

6.3 Event Selection at Large Zenith Angle (LZA)

The shapes of shower images for electromagnetic and hadronic showers change with the observed zenith angle. The gradient of parameters such as MSW and MSL steepens increasingly as the zenith angle approaches 90°, changing the parameter distributions. Therefore, the classifiers and box cuts used for SZA will not be nearly as effective for a GC analysis, which results in decreased sensitivity. The two options for improving event selection in the GC analysis are to train BDTs or to optimize box cuts for LZA.

6.3.1 BDT Event Selection at Large Zenith Angle (LZA)

Because of the gains in sensitivity they offered for SZA analyses with VEGAS, I trained and tested a BDT classification for the event selection of the LZA analysis. I followed the same procedure detailed in Subsection 5.7.2, using training data appropriate for the GC. The simulations used for signal were the same as those used for the BDT energy regression described in Subsection 6.1.2, but with zenith bins of 55°, 60°, and 65°. Events from LZA observations of dark matter targets were used as background. Classification scores were optimized on LZA Crab observations, and an independent set of LZA Crab runs was used to validate the optimized set of BDTs.

Unfortunately, at the time of training, there were less than 15 hours of appropriate background observations. While VERITAS takes an abundance of Crab observations, less than 10 hours were taken below 30° elevation. Because of the steepness of the parameter gradient at GC elevations, data taken as high as 30° elevation is not ideal for optimization or validation. While the number of events provided by simulations was sufficient at SZA, the higher energy threshold at LZA reduces the number of useful events drastically (recall the differential energy distribution is proportional to E^{-2}). The highest energy bin, which covered the range 10–50 TeV, contained only $\mathcal{O}(1000)$ events. This number was inadequate even for a single energy bin, and could not be split into smaller energy ranges. In the case of GC spectra, the highest energy events are the rarest and most interesting, so classifying them correctly is extremely important.

The results of the validation did not show an increase in sensitivity, so this method was not used in my analysis. However, the method shows the potential for improvement if given more LZA observation data and more suitable simulation data. The additional LZA Crab data taken between 2017–2018 alone could have been sufficient, and more data will continue to be taken while VERITAS continues to operate. More LZA observations of DM targets were also taken in that time frame. Observations of the Sgr A Off position, which increased from 20 to 38 hours since I performed this training, could provide additional background events. The number of useful events could be increased by producing simulations with an altered

energy distribution, and they could be separated into finer energy bins. The large parameter gradient with respect to zenith could be addressed by producing simulations with primaries thrown at continuous, rather than discrete, zenith angles. With a continuous distribution of simulated zenith angles, it may even be possible to use zenith angle as a training parameter, avoiding the need for binning in zenith angle.

6.3.2 Box Cut Optimization

Box cut optimization is a simple procedure for finding the cuts that maximize the sensitivity for an analysis. The primary step is to process Crab data through all of the VEGAS stages and perform an RBM analysis for a large number of combinations of variable box cuts. A coarse search with large variations in the variables is done first, to reduce the computation time. Once a coarse maximum is found, a finer search is performed to find the optimal cut values more precisely. A dataframe was created with the Python module, Pandas (McKinney, 2010), to navigate through the large number of results. The module also helped me to ensure the maximum found was indeed a smooth maximum. The quality and event selection cuts varied were MSW, MSL, size, distance, and shower maximum height.

Cuts are best optimized on the Crab, a consistently strong source, because nearly all of the events within the ON region will be signal events rather than background events. Real events are preferable to simulated events (which are 100% gammas) because they are more accurate in this context because the showers are real and provide more accurate parameter distributions. I put together two runlists of high quality Crab data runs for the V5 and V6 epochs. The runs were chosen so that the zenith distribution roughly matched that of the full GC dataset. The Crab also has a similar spectral index to the GC source of about -2.5, which is considered medium hardness. The training runlist contained about 20 hours of LZA Crab observations, and the testing runlist contained about 25 hours of non-overlapping data. The sensitivity for each analysis must be calculated with the ON accounts scaled by its fraction f of the Crab flux where $f = \frac{F_{\text{source}}}{F_{\text{Crab}}}$. Background counts are not scaled, as the background rate
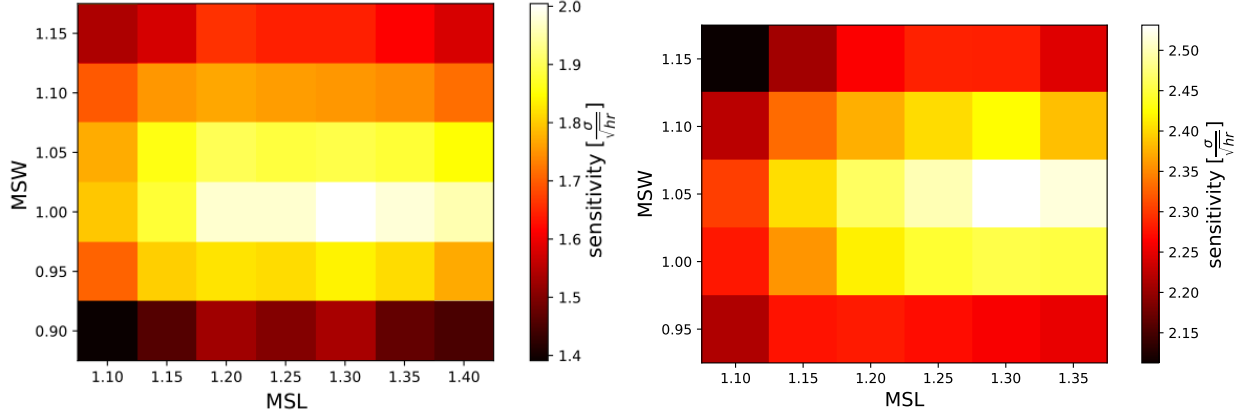
Figure 6.9: Heatmap grid of sensitivity for the mean scaled parameters produced during optimization. Pictured left is the grid for the V5 array, with the optimal size cut of 500. Pictured right is the V6 array with the optimal size cut of 650. The color scale is in units of standard deviations per square root of time.

does not depend on the source strength. Accordingly, the ON counts N_{on} are reduced to

$$N_{\text{on,reduced}} = (N_{\text{on}} - N_{\text{off}}) \cdot f. \tag{6.1}$$

while the OFF counts N_{off} are unchanged, and the significance is subsequently calculated.

A heatmap of re-scaled sensitivity in a grid of MSL and MSW is shown in Figure 6.9. The shower size is held constant at the optimal value for V5 (left) and V6 (right). As clearly shown, the maximum sensitivity occurs at an extremum rather than a saddle point. Similar tests showed that the parameters at the maximum sensitivity in the data frame reached their maxima smoothly. The GC has a value f between 5–10 % of the Crab rate, and my optimization was stable whether I used 5, 7, or 10 percent for the fraction f.

The optimal cuts found, as well as the standard values for comparison, are listed in Table 6.2. The optimized cuts increased the LZA sensitivity by about 10 %. The shower maximum height parameter proved to be ineffective for event selection at LZA, most likely because the showers that travel a greater distance will develop to their maximum length before they reach the surface of the Earth. Updating the cuts necessitated both custom effective areas and lookup tables.

151

Parameter	Optimized V5	Optimized V6	Legacy V5	Legacy V6
MSL	1.3	1.3	1.3	1.3
MSW	1.0	1.05	1.0	1.0
Size	500	650	400	700
Distance	1.38	1.38	1.38	1.38
Shower Max Height	7	7	7	7

Table 6.2: Table of optimized event selection cuts (left two columns) for the two data sets, V5 and V6, compared to standard values (right two columns).

6.4 RBM Analysis for the Skymap

In this section I discuss the special considerations in the LZA analysis for producing the overall skymap.

6.4.1 LZA Camera Acceptance

As the zenith of an event increases, the detection efficiency decreases. The default method of generating the camera acceptance with the wobble data being analyzed (see Section 5.8.2) is not trustworthy in this case, because there is too much extended emission to measure a uniform background. For the purpose of estimating the acceptance, the Sgr A Off region provides a better background estimation because it contains no known gamma-ray sources. Observations of the Sgr A Off region cover almost exactly the same zenith range as the Sgr A* ON region.

I developed code to create an acceptance map externally by compiling the count statistics of multiple data runs for a separate source. Pseudocode for the program is given in Algorithm 1. The output is a two-dimensional map spatially binned in camera coordinates.

The acceptance generated by this program is shown in Figure 6.10. This map was smoothed by a two dimensional Gaussian kernel for a better appearance. The width of the Gaussian is roughly the 68% containment radius of the point spread function (see Subsection 6.4.2).

Algorithm 1 Creates acceptance map from a list of runs
___
  1: **procedure** Generate Acceptance Map

  2:      **for all** runs in runlist **do**

  3:          **for all** bins in skymap **do**   ▷ covers full fov

  4:              **if** bin not within any exclusion region **then**

  5:                  bin livetime $+=$ run livetime

  6:      **for all** selected events (in all runs) **do**

  7:          **if** reconstructed event direction does not fall in exclusion region for that run **then**

  8:              increment bin in counts skymap (same fov)

  9:      **for all** bins in skymap **do** ▷ simultaneous iteration through livetime and counts maps

 10:          scale bin counts and uncertainty (of counts) by (total livetime / bin livetime)   ▷ this accounts for the different exposures of bins without artificially decreasing the relative uncertainty

 11:      Normalize the skymap so the maximum acceptance is 1.0
___

VEGAS does not use the two-dimensional camera acceptance map directly because, without impractically high statistics, the map will contain statistical fluctuations. Rather, it builds a radial histogram of acceptance and fits this distribution to a function in order to smooth the distribution. The events are placed into bins of r^2, where r is the radial distance of a spatial bin from the camera center in degrees, so that each bin covers the same area in two dimensions.

At very large zenith angles such as in GC observations, the difference in acceptance is measurable between the top and bottom of the camera. In Figure 6.10, this zenith gradient can clearly be seen. An zenith correction is available in the RBM analysis that is appropriate for LZA. The correlation is found between zenith angle and the ratio of the acceptance from the 2D map to the acceptance fitted by radial distance from the camera center. This correlation is fitted by a fourth order polynomial, and that function is used to apply corrections to the final acceptance that is used in the RBM analysis.
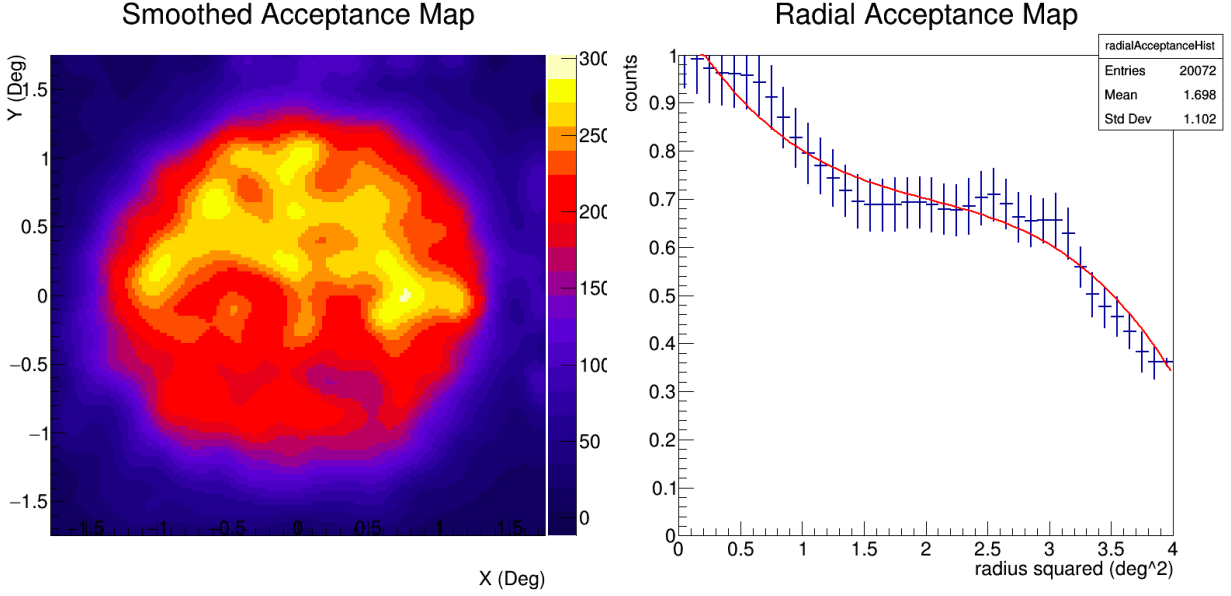
Figure 6.10: Two-dimensional acceptance map generated with Sgr A Off data (left). The coordinates represent the horizontal (X) and vertical (Y) camera coordinates, given in degrees. The color scale represents the acceptance. On the right is the radial projection of the acceptance map. The bins are the square of radial distance from the camera center.

6.4.2 Measuring the Point Spread Function at LZA

The point spread function (PSF) models the angular spread of reconstructed events coming from a single point source. The proper PSF model is needed in estimating the source position, which is found by fitting the excess signal around the point source to the point spread function. The PSF is also useful for quantifying the potential cross-contamination from nearby sources.

The PSF is most precisely modeled if the signal from the source is isolated from other signals. Simulation data were used so there would be no background, which cannot be removed from real data. To model the PSF, a histogram of event counts binned in the square of the angular distance between the true and reconstructed directions of the primary gamma ray, using the simulations processed for this analysis.

At SZA, the PSF can be well-modeled by a two-dimensional Gaussian function, however this fit is less optimal for an LZA analysis using disp reconstruction. The best fit, with

154

	sim correlated ON counts, king V5, 60deg, disp5t	sim correlated ON counts, king V6, 60deg, disp5t

(a) V5   (b) V6
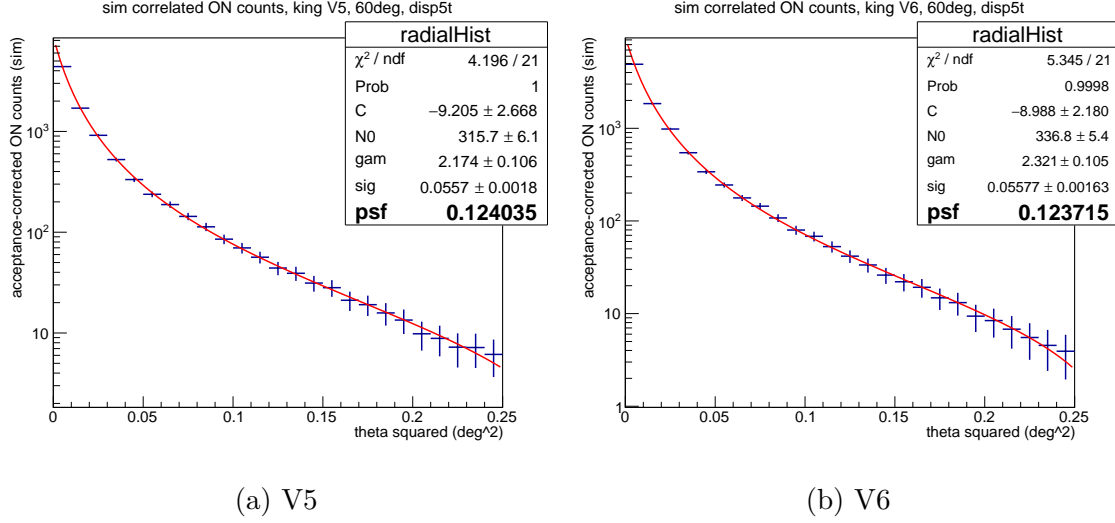
Figure 6.11: Plot of the PSF for V5 data (left) and V6 data (right). The histogram fit to a King function is shown on top and, beneath it, the residuals of the fit are shown. Events are binned in R^2 where R is the distance of the reconstruction from the source location.

the smallest value of reduced chi squared, was achieved with the radial King function from the Fermi website: (`https://fermi.gsfc.nasa.gov/ssc/data/analysis/documentation/Cicerone/Cicerone_LAT_IRFs/IRF_PSF.html`)

$$K(r, \sigma, \gamma) = \frac{1}{2\pi\sigma^2} \left(1 - \frac{1}{\gamma}\right) \left[1 + \frac{1}{2\gamma} \cdot \frac{r^2}{\sigma^2}\right]^{-\gamma} \tag{6.2}$$

where K is the probability density of reconstructed direction, $r^2 = (x - x_0)^2 + (y - y_0)^2$ is the radial parallax distance from the source, and σ and γ are free parameters. The variables x and y represent point coordinates and x_0 and y_0 are the source coordinate parameters.

The distribution of events, binned in the square of radial distance, is shown in Figure 6.11. The red curve is the best-fit King function, and its parameters are provided in the legend. The value of θ within which 68 % of events fall is the estimate of the angular resolution. The 68 % containment radius is about 0.124° for both epochs.

Using the PSF to estimate source position The position of a source is estimated using the PSF model. The acceptance-corrected excess skymap is fit to the function in two dimensions, yielding best fit parameters that include x_0 and y_0. Those parameters give the

best estimate of the source's coordinates. Positional estimation can be made much smaller than the angular resolution by having a statistically high number of events, but the positional accuracy is ultimately limited by the systematic pointing uncertainty.

6.4.3 Point Source Subtraction

While point sources tend to be heavily studied and emphasized in skymaps, we are also interested in the morphology of the surrounding diffuse emission. Two of the point sources in the VERITAS GC skymap, J1745–290 and G0.9+0.1, are very strong and they obscure large regions of the diffuse emission. The diffuse structure can be better revealed if the signal from these strong point sources is removed.

The same fit used above to find the position of the source can be subtracted from the excess map before the significance map is determined. The excess in each bin is reduced by the best-fit value of the source excess for that bin. The significance calculation then proceeds as normal, generating a point-source-subtracted significance skymap.

6.4.4 Systematic Error

Before reporting my results, it is wise to enumerate any systematic errors that cannot be reduced by statistics. The systematic uncertainty of the spectral flux normalization has been determined by the collaboration. Factors such as properties of the detector, atmosphere, and analysis. The accepted value is about 23%. Systematic errors of pointing uncertainty as well as limitations in the analysis contribute to uncertainties in position reconstruction.

CHAPTER 7

Results and Discussion

For my dissertation research, I carried out an analysis of VERITAS observations of the Galactic Center using VEGAS and my own specialized techniques. The primary focus of my results are analyses of the central VHE point source J1745–290 and the diffuse gamma-ray emission above 2 TeV in the Central Molecular Zone. I compare my results to the most recent VHE results presented in Section 3.1. Alongside my results, I discuss their relationship to the various models of emission from the Galactic Center (see Section 3.2) and of diffuse emission (Section 3.3), as well as their relationship to a potential PeVatron accelerator of cosmic rays in the Galactic Center (Subsection 3.3.1).

In this chapter, I present an overview of my analysis of the Galactic Center and show the skymap of the region. I look closely at the position, spectrum, and lightcurve of the central source, VER J1745–290. I analyze the diffuse emission, including its spectrum, morphology, and correlation to molecular matter. I also present my results for other point sources within the region, although these are less central to my thesis. I end with a summary and prospects for the future of Galactic Center analyses at very high energies.

7.1 Overview of my GC Analysis

Between 2010 and 2018, VERITAS observed a total of 155 hours of good-weather Galactic Center data. I performed an extensive data quality monitoring check of every Galactic Center run, reviewing every plot with an emphasis on the crucial plots of the L3 rates and FIR sky temperatures. I added time cuts to the database for portions of data with large spikes in the L3 rates (see Figure 7.1) or in the FIR values. I assigned them a score from 1 to 5 to rank

their quality: 3 being an average quality run with an A or B weather rating and 5 being a run with clear weather and no issues in its plots. Runs with a score of 3 or higher were put into a runlist for the ring background method (RBM) analysis. The runlist for the spectral analysis had runs with a score of 4 or higher, because good weather is more important for the spectral reconstruction. Runs were not included in the spectrum runlist unless all four telescopes participated in the array, because alternate array configurations require their own effective area tables and provide little additional data. Three telescope runs also contribute less than half of the events a four telescope run would, due to the requirement that three telescopes must pass quality cuts. The total exposure of the analysis after runlist selection, time cuts, and dead-time correction was 124.5 hours.
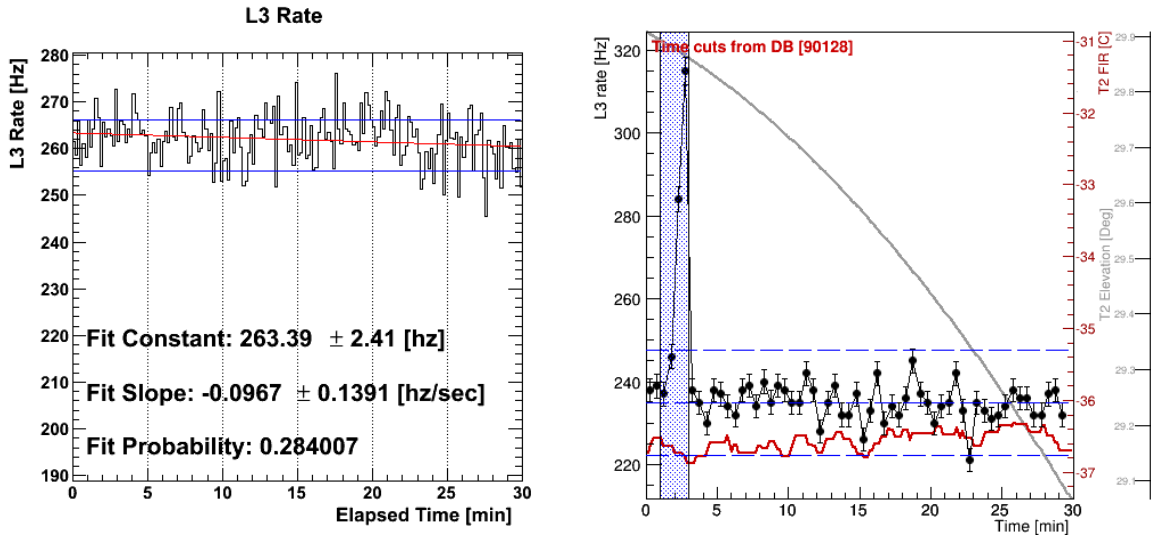
Figure 7.1: Data quality monitoring plots of the L3 rates versus time for two runs. The run on the left has a steady L3 rate and requires no time cuts. The run pictured on the right has a spike in the rates that is removed by a time cut which is marked by blue shading. The red lines plot the FIR temperature, and the gray curve on the right plots the tracking elevation. The blue dashed lines delineate the mean and 1 standard deviation interval of the L3 rate.

The main part of my analysis used a validated version of VEGAS (version 2.5.6), built with version 6.12/07 of the ROOT libraries. I branched code from this version, as detailed in Chapter 6. I also wrote additional external programs using ROOT and Python. The first two stages of VEGAS were performed with default settings for both flasher and observing

runs. I processed stage 2 simulations from raw VBF files, using archived simulations for noise levels and pedestals. I used these simulations to produce lookup tables covering zenith angles from 55–65°, offsets from 0–2°, and all simulated noise levels. The settings were customized to match the shower reconstruction stage for large zenith angle, with a maximum distance of 1.38° and a three telescope requirement for reconstruction. Direction reconstruction was performed by the *disp* BDT method described in Subsection 5.7.1.

Energy reconstruction was performed using the BDT regression method I developed in Subsection 6.1.2. I used the weights I trained with version 4.2.1 of the TMVA by the method described in that section. The simulations used for effective area production were processed with the same weights and settings as the data. The optimized large zenith angle (LZA) cuts I found in Subsection 6.3.2 were used in both effective area production and the event selection stage for the Galactic Center (GC) data.

The skymap and spectrum were produced separately, each with its own corresponding runlist. Circular exclusion regions of 0.3° radius were used for every known gamma-ray source except for Sgr A*, whose exclusion region was given a radius of 0.4°. The skymap and significance were calculated with the RBM analysis using the acceptance map generated from Sgr A Off data (see Subsection 6.4.1). The spectral analysis was run on the more strict runlist, with effective area groups organized by epoch.

7.2 Significance Skymap of the Galactic Center

The significance skymap above 1.9 TeV of the inner 4° × 2° of the GC region produced by my analysis is shown in Figure 7.2. The color scale represents significance, and in this map significance is limited in scale to 15 standard deviations (15σ) because the peak significance is over 39σ and condenses the remaining scale, obscuring the structure outside of the center. The peak significance occurs at Galactic coordinates (359.932°, −0.058°), about 0.018° from the nominal location of J1745–290.

The point sources and extended regions discussed in this chapter are labeled in green. This includes point sources VER J1745–290 and G0.9+0.1 (J1747–281), and extended sources

HESS J1745–303 and HESS J1741–302. The confused and potentially related sources, HESS J1746–285 and VER J1746–289, can be seen near the center. The circular regions outline the 68% confidence level (CL) of the best-fit positions for point sources, including statistical and systematic uncertainties. Elliptical regions outline the best estimate of the source extension for extended sources. The emission is brightest near the central source, VER J1745–290, coincident in position with Sgr A*. Strong diffuse emission is visible along the Galactic ridge, extending about 1.25° in each direction from the center. The diffuse emission has an apparent correlation to dense matter, which will be quantified in Section 7.4.
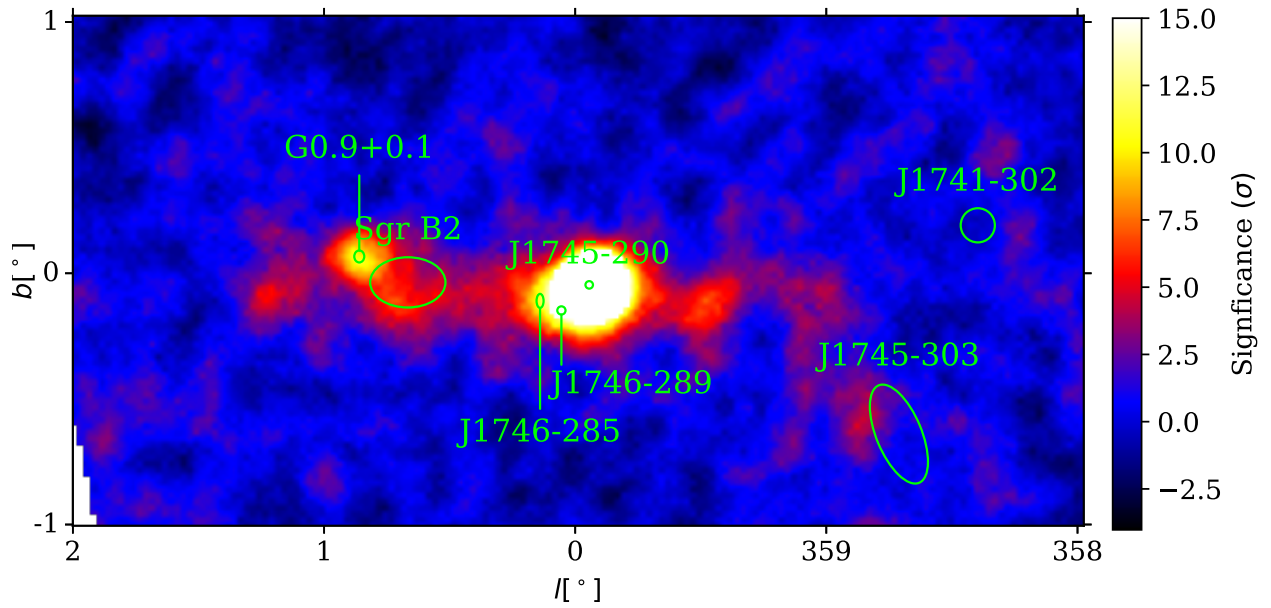
Figure 7.2: Significance skymap of gamma-ray emission above 2 TeV for my analysis covering the full FoV of the GC region. All known TeV sources and their positional uncertainty or extension are shown in green. The significance scale is limited to 15.0σ so the structure of the region outside of the strong central emission can be seen in more detail.

The distributions of the significance values for the spatial bins in the skymap (Figure 7.2) are given as histograms in Figure 7.3. In the absence of any gamma-ray sources, the variations in bins should be purely statistical in nature, and the significances should have a mean centered around 0.0 and a standard deviation of approximately 1.0. The distribution should be well-fit by a standard Gaussian. The top left plot, which includes all spatial bins, has a mean shifted to 0.71 by the sources in the map. With all exclusions, the mean is 0.002 ± 0.007, which is

consistent with 0.0 as would be expected with no sources, showing that the exclusion regions I used were effective. The width is 1.053 ± 0.007, which is not quite unity but is closer to 1.0 than previous analyses. This indicates that most systematic biases have been removed.
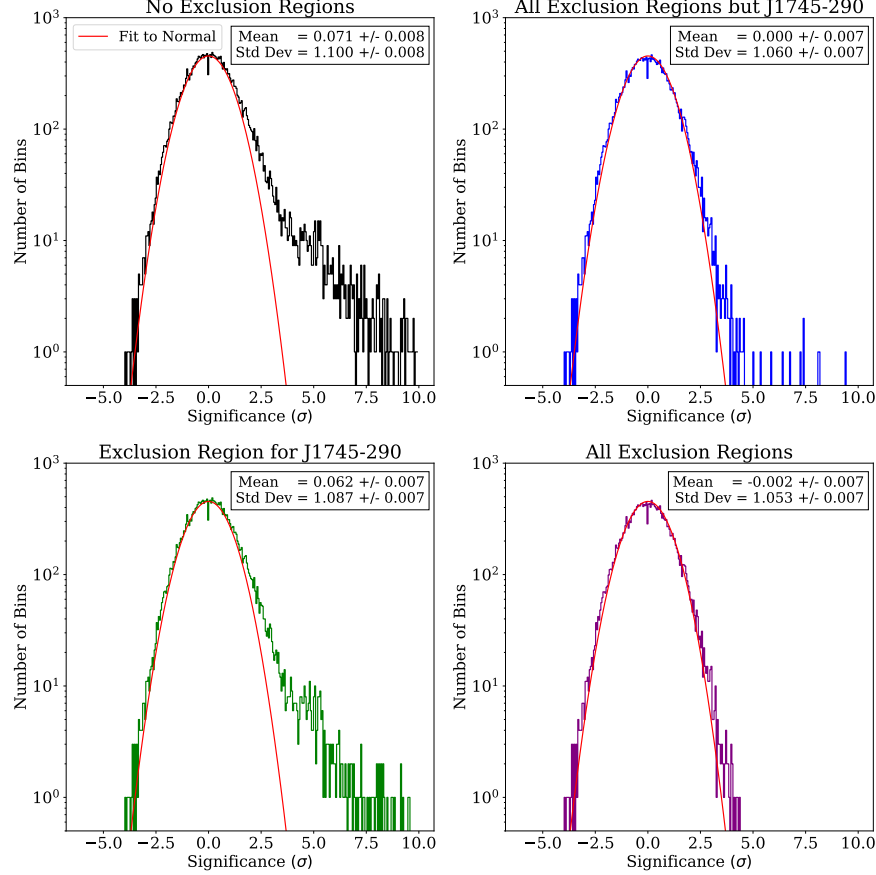
Figure 7.3: Significance distributions for the GC skymap in Figure 7.2. Each red curve is the best-fit Gaussian for that histogram. Pictured on the top left is a histogram showing the distribution of statistical significance for all spatial bins in the analysis FoV. The bottom left histogram excludes bins within the Sgr A* exclusion region, and the top right applies all exclusion regions except for the source region around Sgr A*. The bottom right histogram excludes bins within any exclusion region, and should represent only background bins.

The skymaps for events above 5 and $10\,\mathrm{TeV}$ are shown in Figure 7.4 on the top and bottom, respectively.
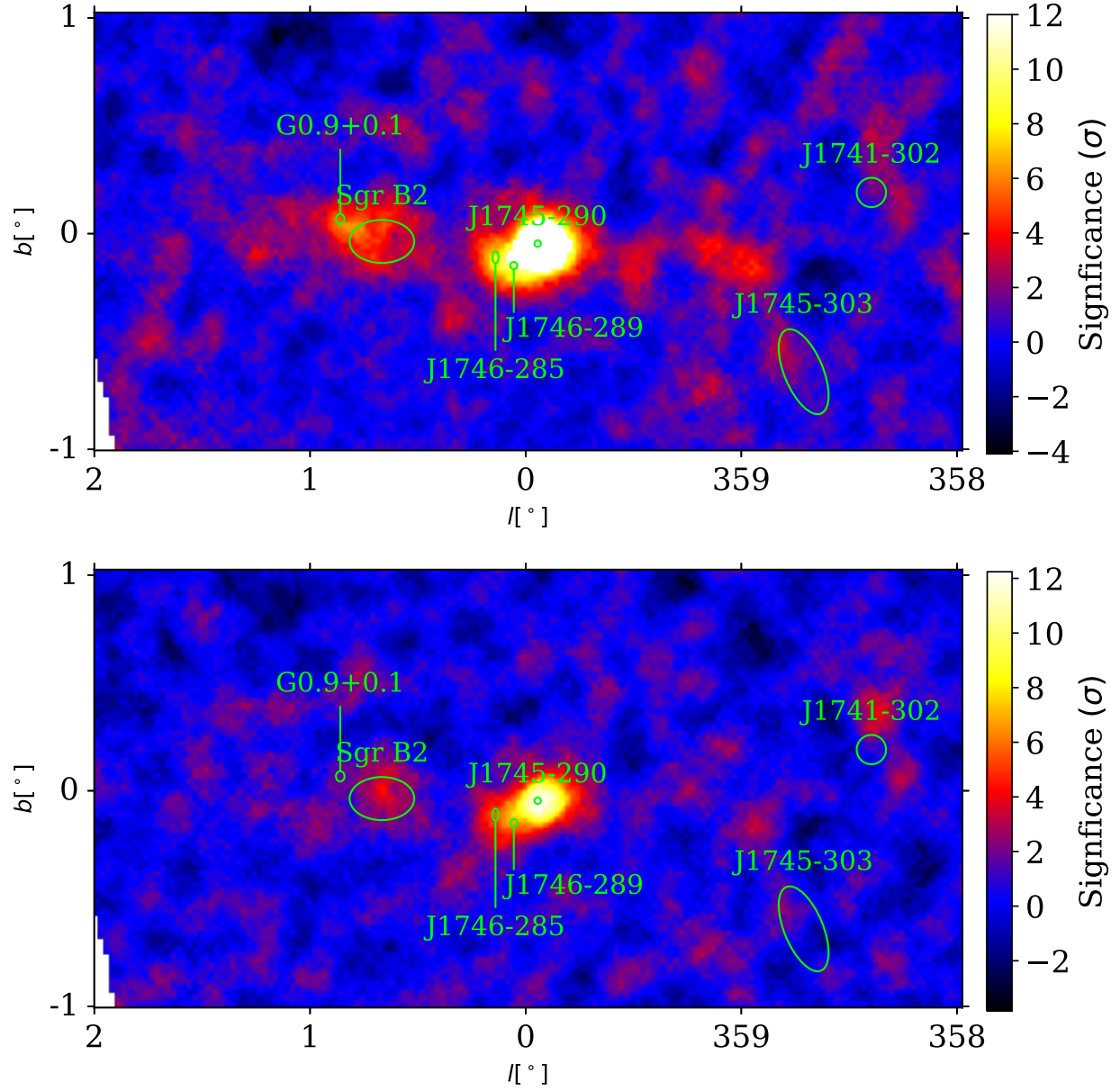
Figure 7.4: Significance skymaps for events over 5 TeV (top) and above 10 TeV (bottom). The scale maximum is decreased to 12.0σ because of the decrease in the overall signal.

7.3   VER J1745–290

The RBM analysis of the central gamma-ray source was performed with a circular ON region of size $0.1°$ centered on the nominal position of Sgr A* ($359.944°$, $-0.0462°$). The statistical significance found in the region was $37.5\,\sigma$, an increase from the previous result

162

of 25σ found in Archer et al., 2016. A total of 1106 events were detected in the ON region. The total number of background (OFF) events was 4609, with an α value of 0.055. The calculated excess was 426 counts, which gives a gamma-ray rate of about 3.4 gamma rays per hour (above $2\,\mathrm{TeV}$).

The position of a source is estimated by fitting the uncorrelated excess map to a two-dimensional function that models the shape of the reconstructed emission in the skymap. A point source should follow the shape of the PSF, which was found to be most consistent with the King function (Equation 6.2) at large zenith angles. The position is determined by the best-fit values of the parameters x_0 and y_0, which specify the center of the function. The best-fit position of VER J1745–290 in my analysis is $(359.930°, -0.047°)$ in Galactic coordinates, with an uncertainty of $0.018°$ (68% confidence interval). The uncertainty is dominated by a systematic uncertainty of $0.013°$, which is larger than a standard VERITAS analysis because of LZA effects.

Figure 7.5 shows the significance skymap with no scale suppression, zoomed in on the central emission. Circles are drawn showing the position and uncertainty for my VERITAS analysis (teal), the most recently published VERITAS result from Archer et al., 2016 (blue), and the H.E.S.S. result (magenta) from Acero et al., 2010; Abdalla et al., 2018. The VERITAS circles show 68% containment confidence contours of the best-fit positions. The dashed line shows the 68% containment radius of the VERITAS PSF centered on my best-fit position. The radio position of Sgr A* (Yusef-Zadeh et al., 1984) is shown as the black cross.

My position is consistent with the previous position of VER J1745–290, although it is shifted somewhat. It is also consistent with the position of HESS J1745–290, and the radio position of Sgr A*. While the pointing accuracy can be made much smaller than the PSF by having a statistically high number of events, it is ultimately limited by the systematic pointing uncertainty. The pointing uncertainty of H.E.S.S., about $13''$, is much smaller than that of VERITAS ($45''$) because of advanced telescope pointing control (Acero et al., 2010) and because H.E.S.S. observes at high elevation angles. H.E.S.S.'s result was able to exclude Sgr A East as a counterpart to HESS J1745−290. However, VERITAS, is unlikely to be able to do so with its current limitations.
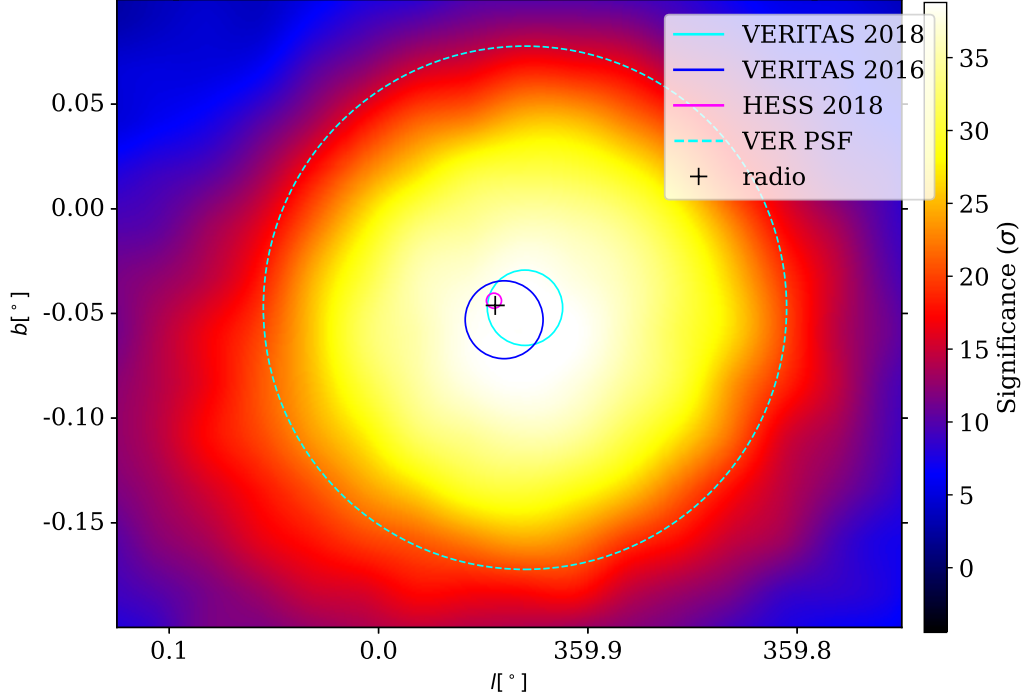
Figure 7.5: Significance skymap zoomed in on the central source J1745–290 with no scale suppression. The position of the central source J1745–290 is given for both VERITAS and H.E.S.S. The PSF is shown by the dashed line.

Exclusion of either Sgr A* or G359.95–0.04 would require an angular uncertainty below $4''$, which is the approximate distance of G359.95–0.04's tail from Sgr A* (Wang et al., 2006). This may be possible in the future with CTA, which will have a systematic pointing uncertainty as small as $5''$. The mean position of G359.95–0.04 is slightly farther away, as its head is about $8.7''$ away from Sgr A*.

7.3.1 Spectrum

The spectrum of VER J1745–290 from my analysis is shown in Figures 7.6 and 7.7. They plot the differential energy spectrum, $\frac{dN}{dE}$, times E^2 versus energy (TeV) in log-log scale. The spectrum was extracted from the same ON region used in the RBM analysis. It is important to note that the spectral analysis includes events from the diffuse emission and emission associated with HESS J1746–285 or VER J1746–289.

164
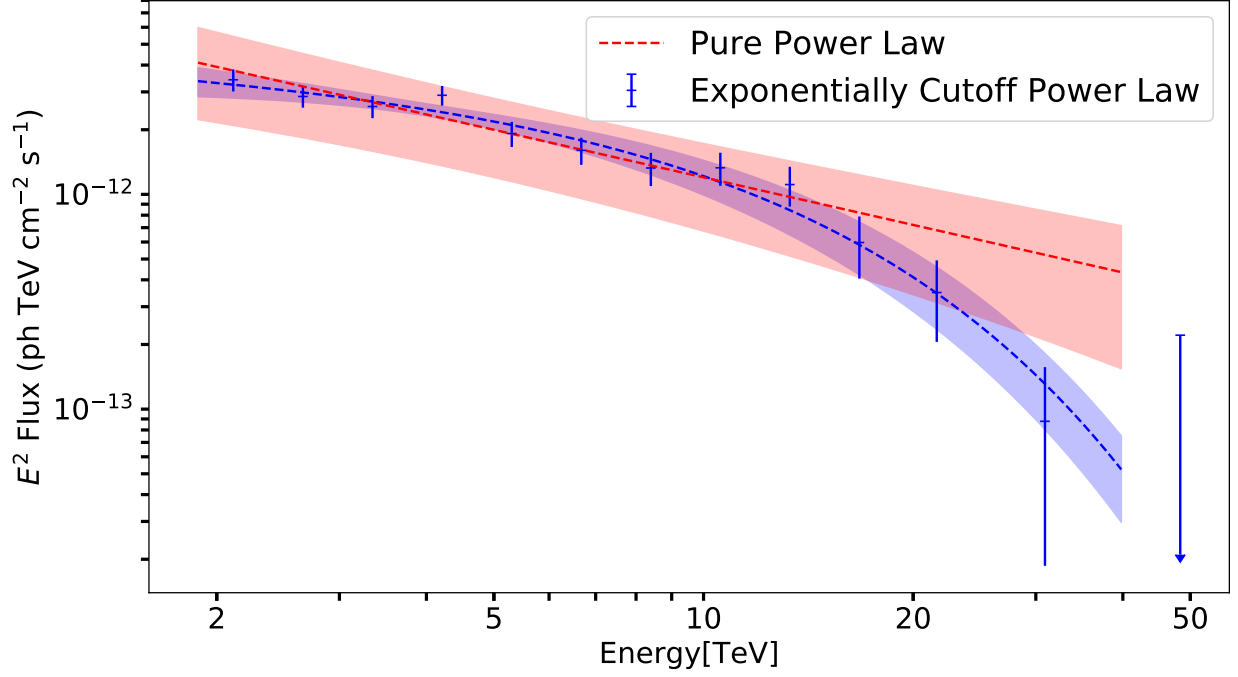
Figure 7.6: Spectrum of the central source J1745–290 from my analysis. The differential energy spectrum $\frac{dN}{dE}$ times E^2 is plotted versus energy. The down arrow represents an upper limit of flux in that bin. The red curve and blue curve represent the best-fit power law and power law with exponential cutoff, respectively. The corresponding shaded regions represent the 1σ confidence band.

The energy threshold for the VERITAS spectral analysis was $1.9\,\mathrm{TeV}$, and the highest energy bin has an upper edge of $39.8\,\mathrm{TeV}$. Figure 7.6 shows fitting of the VERITAS spectral points from my analysis alone. The points are best-fit by a power law with exponential cutoff (Equation 3.2). The best-fit curve is drawn as the dashed blue line, and the shaded region represents the 1σ confidence band of the fit.

Fits were performed to all three functions enumerated in Subsection 3.1.1, including a pure power law (Equation 3.1) and a smoothly broken power law (Equation 3.3). The results of all three fits are shown in Table 7.1, which includes the parameters and reduced chi squared value of each fit. The errors shown are statistical; systematic errors will be discussed later. The pure power law is strongly disfavored, with a reduced χ^2 value of $^{16.36}/_{10}$. Unlike previous results (Archer et al., 2016), my analysis shows some preference for an exponentially cutoff

Model	N_0 (TeV^{-1} m^{-2} s^{-1})	Γ_1	Γ_2	$E_{\text{cut,break}}$ (TeV)	$\frac{\chi^2}{\nu}$
Power Law	$(6.80 \pm 0.31) \times 10^{-10}$	2.69 ± 0.06	N/A	N/A	$\frac{16.36}{10}$
Cutoff PL	$(11.76 \pm 2.03) \times 10^{-10}$	2.16 ± 0.18	N/A	10.82 ± 2.97	$\frac{6.78}{9}$
Broken PL	$(7.41 \pm 0.45) \times 10^{-10}$	2.11 ± 0.11	4.20 ± 0.47	12.16 ± 2.63	$\frac{52.31}{34}$

Table 7.1: Best-fit parameters and their 1σ errors for the spectrum of J1745–290. The fit functions shown are a pure power law (PL, Equation 3.1), PL with exponential cutoff (Equation 3.2), and a smoothly broken PL (Equation 3.3). The normalization energy for all three fits is $E_0 = 5.3$ TeV. A power law with exponential cut off is the preferred fit to these data.

power law over a smoothly broken power law. Note that the smoothly broken power-law fit was only successful for the joint spectrum, thus the higher number of degrees of freedom compared to the other two fits. The cutoff energy from the former, (10.82 ± 2.97) TeV, is consistent with the break energy of the latter, (12.16 ± 2.63) TeV. The power law indices of the two preferred functions are also consistent, with values of -2.16 ± 0.18 and -2.11 ± 0.11 for the exponentially cutoff and smoothly broken power laws, respectively. The power law with exponential cutoff has a flux normalization constant of $(6.80 \pm 0.31) \times 10^{-10}$ TeV^{-1} m^{-2} s^{-1} at a normalization energy of 5.3 TeV. A conservative estimate of the systematic error for the flux normalization and power law index is about 40%.

Figure 7.7 adds the H.E.S.S. spectral points from Aharonian et al., 2009 to extend the spectrum down to 0.2 TeV. The fit is not performed with the more recent H.E.S.S. II data points from Abramowski et al., 2016, which have a lower normalization and do not produce a strong fit. A joint fit is performed on all points using the preferred spectral function, the power law with exponential cutoff. The best-fit flux normalization is $(2.85 \pm 0.12) \times 10^{-12}$ cm^{-2} s^{-1} TeV^{-1} at a normalization energy of 1 TeV. The index is 2.04 ± 0.03, and the cutoff energy E_{cut} is 13.47 ± 2.27 TeV.

Figure 7.8 shows a spectrum expanded down to GeV energies with *Fermi*-LAT points (Malyshev et al., 2015). The spectrum of the *Fermi*-LAT points for 3FGL J1746.3-2851c

is best-fit by a broken power law with a break energy at around $2\,\text{GeV}$. The index after the break energy is 2.68 ± 0.05, which is steeper than the VHE spectrum. The spectrum is, within errors, still continuous at the inflection point just above $100\,\text{GeV}$. This is suggestive of a difference between the GeV and TeV emission mechanisms. It also shows points from the MAGIC spectrum (Ahnen et al., 2016).
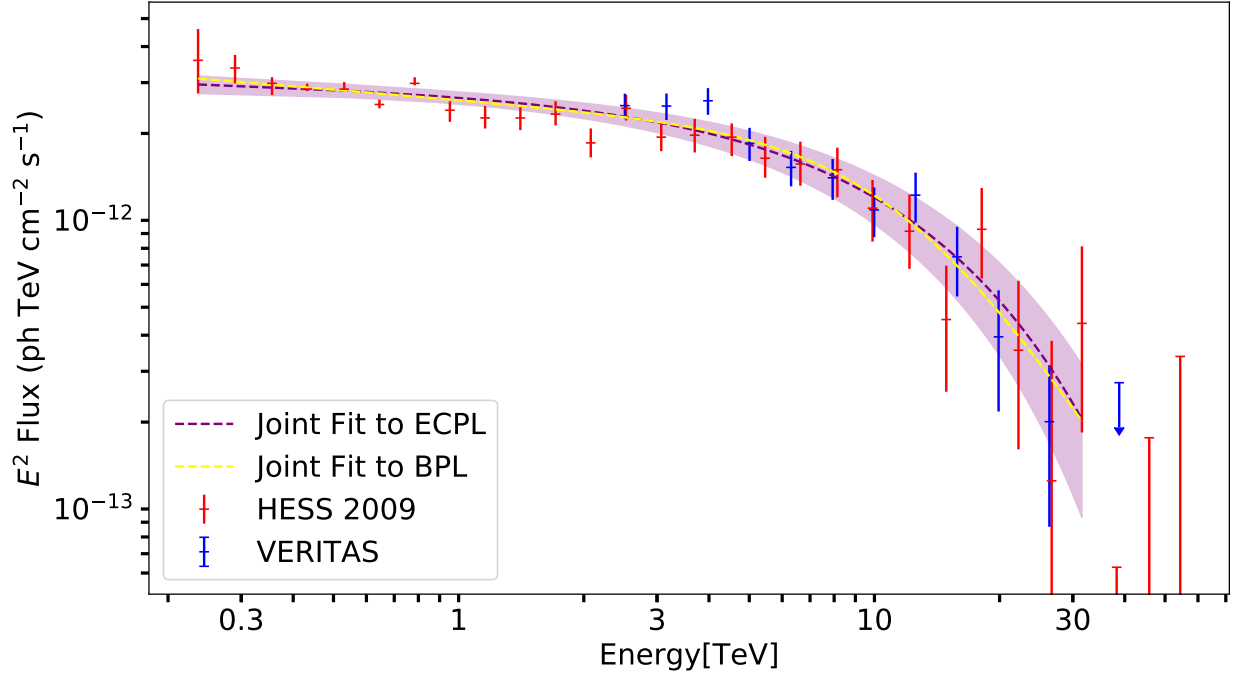
Figure 7.7: Joint spectrum of J1745–290 with points from my analysis (blue) and H.E.S.S. (red, Aharonian et al., 2009). The best-fit exponentially cutoff power law for the joint spectrum and its 1σ confidence band are shown in purple, and the best-fit smoothly broken power law is yellow.

The implied integral flux above $1\,\text{TeV}$ is found by integrating $\frac{dN}{dE}$ and evaluating it from $1\,\text{TeV}$ to infinity. For the best-fit exponentially cutoff power law of my spectrum, this evaluates to roughly $2.9 \times 10^{-12}\,\text{ph}\,\text{cm}^{-2}\,\text{s}^{-1}$. This is roughly $10\,\%$ of the Crab flux in the same energy range. However, in the Galactic Center at $\approx 8\,\text{kpc}$ from Earth is approximately four times farther from than the Crab, meaning that the effective VHE luminosity of the GC makes it one of the strongest sources in our Galaxy at TeV energy.

The total energy intensity is found by integrating $E\frac{dN}{dE}$ and has units of TeV/cm^2/s. This
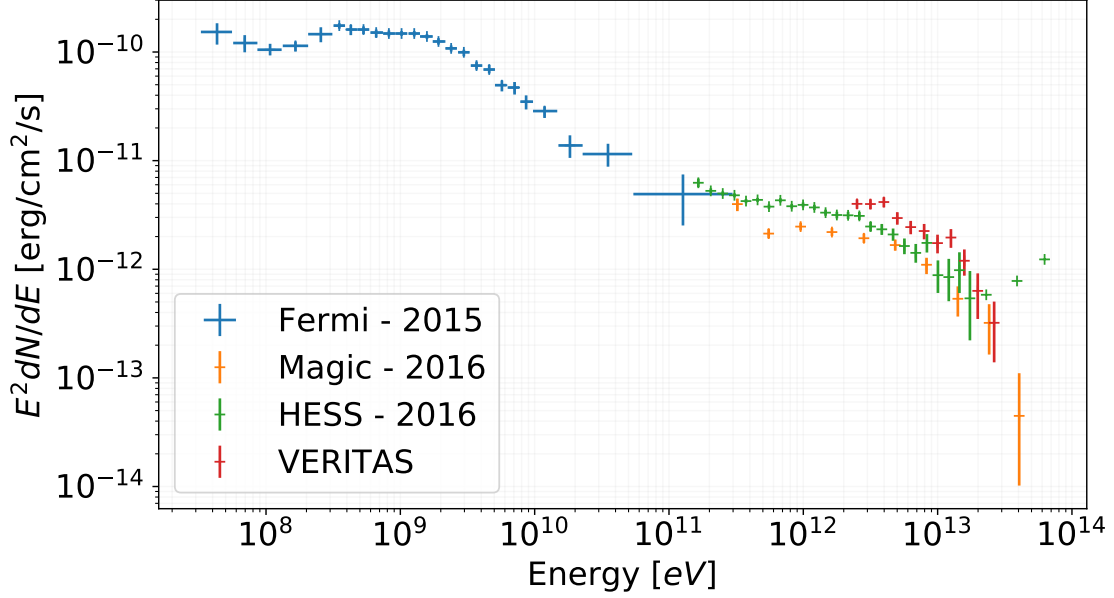
Figure 7.8: Expanded gamma-ray spectrum of J1745–290 including points from my analysis (Figure 7.6), H.E.S.S. (Abramowski et al., 2016), MAGIC (Ahnen et al., 2016), and *Fermi*-LAT (Malyshev et al., 2015).

is 6.8×10^{-12} TeV/cm^2/s. The total luminosity is found by multiplying the energy density by the surface area of a sphere with radius equal to the GC distance. Using the value from Boehle et al., 2016, the value 8×10^{34} erg/s is consistent with the lower end of the estimate in Genzel et al., 2010. The decorrelation energy, or the energy that minimizes the correlation between flux normalization and spectral index, is about 5 TeV.

7.3.2 Flux Variability

An important result from any analysis is the lightcurve, which plots the source flux in bins of time. In Figure 7.9, I show the lightcurve generated using files from this analysis, with the VHE integral flux binned into time bins that spanned half of each observing season, i.e. about a month and a half in duration. The horizontal bars represent the time frame in which actual data were taken, rather than the bounds of the time bins. Lightcurves are shown for the integral flux above 2 TeV (blue) and 5 TeV (red).

Both lightcurves are well-fit by a constant flux. The reduced χ^2 statistic for the lightcurve
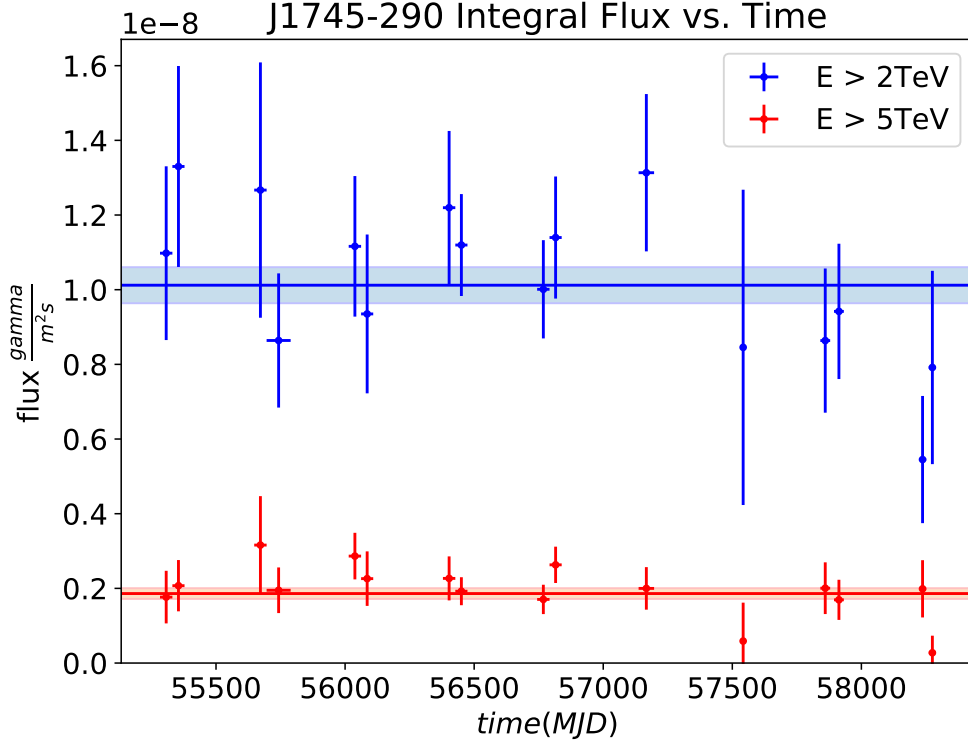
Figure 7.9: Lightcurve of the central source J1745–290, which displays integral flux points (units of $ph/m^2\,s$) binned in time. The time of observation, plotted as MJD, covers 2010 to 2018. The flux above $2\,TeV$ is shown in blue, and the flux above $5\,TeV$ is shown in red. The horizontal bars represent the best-fit mean flux of all observations. The reduced χ^2 values are discussed in the text.

of flux above $2\,TeV$ is 16.64/15 for the best-fit mean of $1.01 \times 10^{-8}\,m^{-2}\,s^{-1}$ and an uncertainty on the mean of $0.05 \times 10^{-8}\,m^{-2}\,s^{-1}$. It is 20.94/15 for the lightcurve of flux above $5\,TeV$, with a best-fit mean of $1.86 \times 10^{-9}\,m^{-2}\,s^{-1}$ and an uncertainty of $0.14 \times 10^{-9}\,m^{-2}\,s^{-1}$. These values are both close to 1.0, showing a reasonable probability that a constant function accurately describes the data. The lightcurve shows no sign of long-term flaring, on month timescales, above $2\,TeV$ or $5\,TeV$.

Models in which emission originates very close to the event horizon of Sgr A* predict variability on much shorter timescales, from minutes to hours. To investigate variability on the timescale of less than one day, I created a lightcurve with daily bins, pictured in Figure 7.10. The figure on the right shows the Δ/σ distribution, which is a histogram

$(F - \bar{F})/\sigma_F$ for each bin, where $\bar{F}$ is the mean flux and σ_F is the error on the mean. The distribution is well-fit by a standard Gaussian, and it does not show an occurrence of strong flaring. There is a slight skewness to the left caused by low-significance bins. This skewness could be reduced if the flux calculation used the correct Poissonian errors; high statistics bins are well-approximated with normal errors by the central limit theorem. In downward fluctuations with low flux, the error on the flux is proportionally low, leading to a low value of Δ/σ.
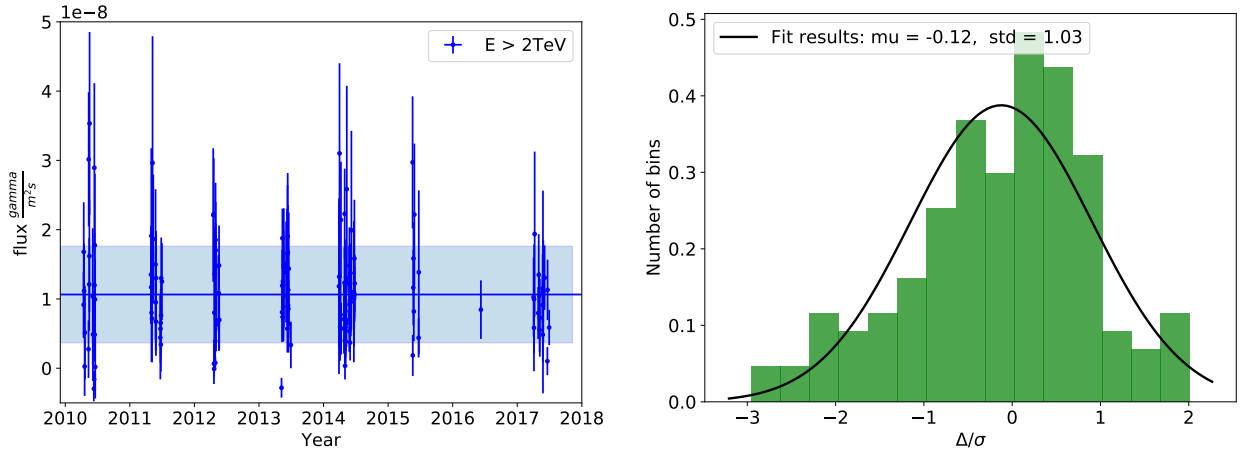
Figure 7.10: Lightcurve of the central source VER J1745–290 integral flux above 2 TeV in daily bins (left). Histogram of Δ/σ values for the lightcurve of J1745–290 with daily time bins (left), where Δ is the difference between the bin flux and the mean flux of all bins, and σ is the error on the flux in that bin.

As mentioned in Section 3.2.2, the lack of flux variability seen in my analysis gives preference to leptonic models of emission that predict no variability, such as the plerion model. This result could also be compatible with models that predict variability over a much longer timescale, on the order of 10^5 years.

The GC is a dynamic system, and so it is possible that strong flaring could occur in future years. If VERITAS continues to monitor the GC for 15 h per year, it could detect, for example, a doubling of the flux from one year to another at a level of 3.4σ (Archer et al., 2014).

170

7.4 Diffuse Analysis

Figure 7.11 shows the CMZ skymap with radio contours overlaid. The radio contours are drawn with data from CS line emission (Tsuboi et al., 1999) and HCCCN emission (Jones et al., 2011) which are effective tracers of dense gas. The HCCCN emission is taken with the Mopra telescope at the *Australia Telescope National Facility* (ATNF). A rough correlation between the gamma-ray emission with the gas density is visible.
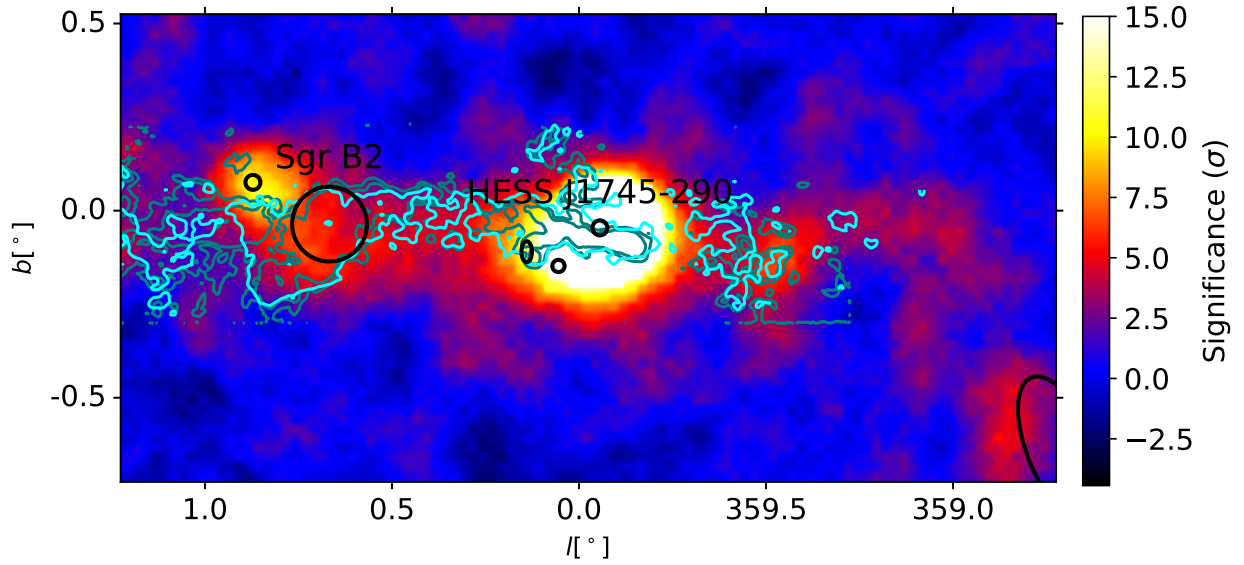
Figure 7.11: Significance skymap of the GC ridge zoomed in on the diffuse emission in the CMZ. Cyan lines are contours of CS(1-0) line emission, which traces dense gas, from Tsuboi et al., 1999. Teal lines are contours of HCCCN emission taken with the *Mopra* telescope (Jones et al., 2011).

In this section, I share the results from my spectral analysis of the diffuse emission, using the program described in Subsection 6.2.1.

7.4.1 Diffuse Spectrum

The spectrum of the diffuse emission was extracted from the regions drawn in Figure 6.7 using the method discussed in Subsection 6.2.1. The cumulative significance of the regions after stacking all of the events is $9.5\,\sigma$, which would be sufficiently high for spectral reconstruction.

The diffuse spectrum is best-fit by a pure power law with an index of -2.22 ± 0.22 and a flux normalization of $(4.72 \pm 0.86) \times 10^{-11}\,\mathrm{m^{-2}\,s^{-1}\,TeV^{-1}}$ at $5.3\,\mathrm{TeV}$. For comparison, the flux normalization is $1.69 \times 10^{-11}\,\mathrm{m^{-2}\,s^{-1}\,TeV^{-1}}$ when fit with a normalization energy of $1\,\mathrm{TeV}$. The spectrum is shown in Chapter 6 with its best-fit power law function.

As explained in Chapter 6, runs for a particular region were excluded if their pointing direction was more than $1.5°$ from that region because of the large relative uncertainty of the effective areas at this offset. For this analysis, all runs with south or west wobble for the $c5$ region were excluded, which reduced the uncertainty in all fit parameters.
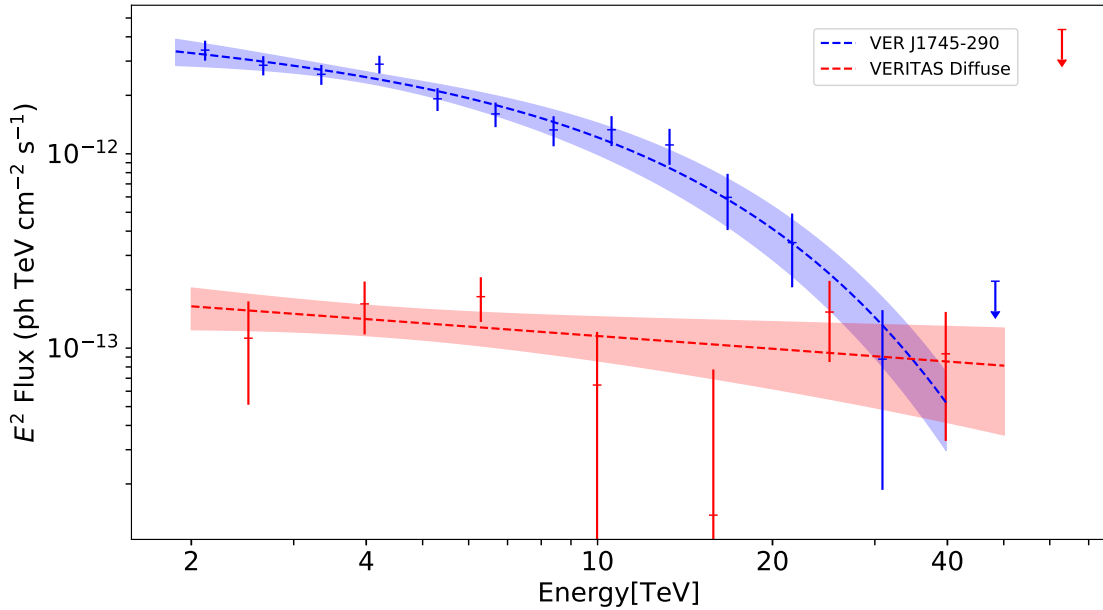
Figure 7.12: Spectrum of the diffuse regions shown in Figure 6.7 (red) overlaid with the spectrum of the central source VER J1745–290 (blue). The best-fit curves are drawn as dashed lines, and the 1σ butterflies are shaded in matching colors. The fit parameters are given in the text.

Recall that the H.E.S.S. Collaboration et al. (2017) found a spectrum of the diffuse emission which included more regions that covered a larger area, so the flux normalization I found cannot be compared directly with theirs. The H.E.S.S. index of $2.28 \pm 0.03_{\mathrm{stat}} \pm 0.2_{\mathrm{syst}}$ is consistent with my VERITAS result, which supports the assumption that the diffuse emission across the ridge all comes from a common mechanism. This is harder than the CR spectrum,

which has an index of about 2.6–2.7 below the knee.

With greater statistics, it would be illuminating to study any dependence of the index on the distance from the center. Because high-energy protons do not lose their energy as fast as electrons during diffusion, a hardening of the spectrum as distance from the center increases would show that protons are at least in part responsible for the diffuse emission. Investigations into any flux variability in the diffuse emission could provide more information about the emission mechanism.

7.4.2 Correlation of the Diffuse Gamma Signal with Molecular Matter

I sought to quantify the visible correlation between VERITAS gamma-ray events and the dense matter tracers to test the hypothesis that the diffuse emission results from the interaction between cosmic rays and interstellar matter. I present my results using the most effective tracer, CS brightness temperature, integrated over velocity (measured in the local standard of rest, LSR) from -200 to $200\,\mathrm{km/s}$ (Tsuboi et al., 1999). The LSR is a point moving at the average velocity of stars in the region of interest.

Figure 7.13 shows the relation between VHE gamma-ray excess and the CS emission signal. To generate Figure 7.13, I used the acceptance-corrected, smoothed VERITAS excess skymap from my analysis as the gamma-ray signal. The tracer signal was reprojected into the bin coordinates of my skymaps. The bins are 0.025° squares in Galactic longitude and latitude, and there are 240 bins covering 6° in each dimension. To factor in the limits of the angular resolution, the tracer signal was then smoothed by convolution with the VERITAS PSF. Every point in the scatter plot represents a spatial bin in which there are values for both the gamma-ray signal and the radio signal. The extent of the radio signal is smaller and only extends from 358.93° to 1.73° in Galactic longitude and from $-0.42°$ to 0.40° in Galactic latitude. Bins within 0.2° of Sgr A* or within 0.15° of G0.9+0.1 are excluded, so presumably only diffuse emission is included.

The line of best fit is shown in orange and its equation is shown in the legend. The correlation coefficient $r = 0.52$, which shows that there is a relationship between dense gas
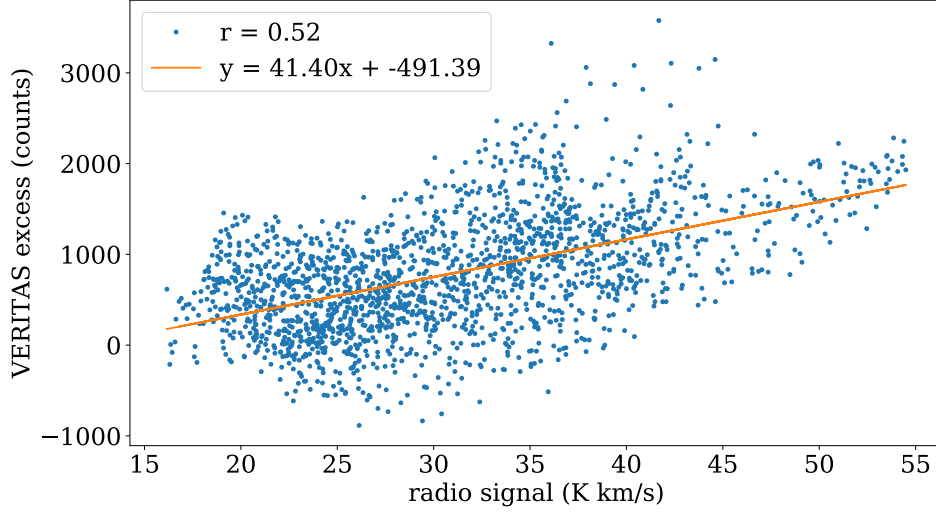
Figure 7.13: Plot of gamma-ray signal from my VERITAS analysis versus velocity-integrated CS(1-0) emission. The line of best fit is shown with the correlation coefficient $r = 0.52$.

and gamma-ray emission. This is consistent with H.E.S.S.'s separation of the dense gas component (DGC) from H.E.S.S. Collaboration et al., 2017, which constitutes about half of the diffuse flux.

The correlation of the diffuse gamma-ray signal with the concentration of cloud matter, along with the lack of a cutoff in the spectrum up to $40\,\mathrm{TeV}$, supports a model of emission in which high-energy cosmic rays diffuse throughout the CMZ and interact with molecular matter. Hadronic models are preferred because protons can be accelerated to much higher energies without experiencing severe radiative losses. Although leptons would only require acceleration up to $100\,\mathrm{TeV}$ rather than $1\,\mathrm{PeV}$ due to their greater efficiency in creating gamma-rays (Abramowski et al., 2016), they would have trouble escaping from the acceleration region unless the magnetic field was unusually small. The total cosmic ray energy above $10\,\mathrm{TeV}$ integrated by Abramowski et al. (2016) is on the scale of $W_p \approx 1.0 \times 10^{49}$ ergs. This amount of energy could be supplied by a single supernova event in the past, which could release up to 10^{51} ergs.

7.5   Other Sources in the CMZ

There are other point and extended sources in the inner region of the GC that can be studied by VERITAS. These include the SNR G0.9+0.1, the emission adjacent to J1745–290, and the unidentified HESS sources J1745–303 and J1741–302. They are not as central to my thesis, but their results are useful to better understand the region.

7.5.1   SNR G0.9+0.1

The second brightest point source that has been identified is VER J1747–281, which is associated with the SNR G0.9+0.1. The skymap zoomed in on the position of G0.9+0.1 is shown in Figure 7.14. My analysis yielded a significance of 8σ at the best-fit position of $(\ell = 0.857°, b = 0.069°)$. The statistical and systematic uncertainty on each coordinate are $0.03°$ and $0.013°$, respectively.
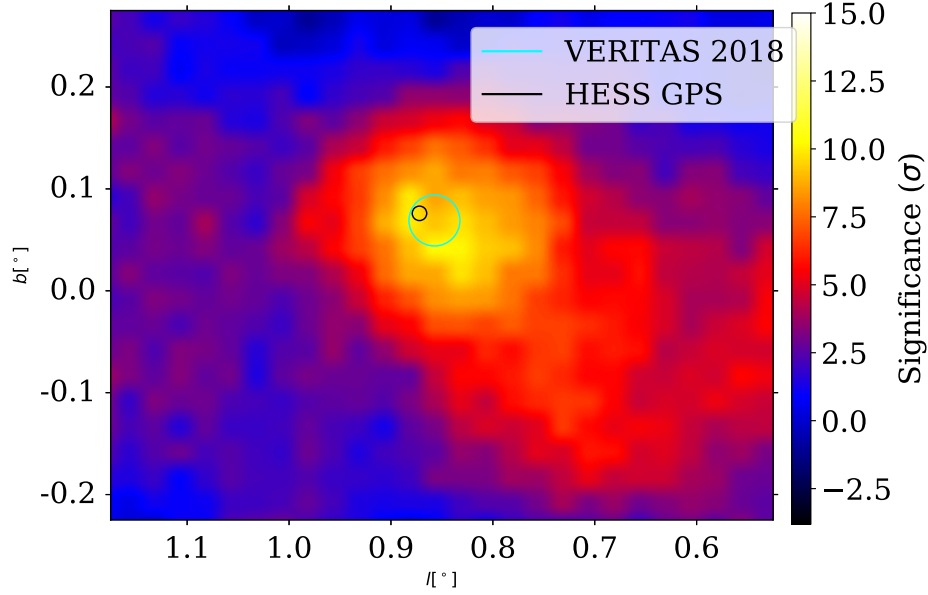
Figure 7.14: VERITAS significance skymap from my analysis zoomed in on G0.9+0.1. The H.E.S.S. position and uncertainty is shown by the black circle (Aharonian et al., 2005). My VERITAS position is shown by the cyan circle.

The joint spectrum of my analysis overlayed with H.E.S.S. points is shown in Figure 7.15.

The blue points are from my analysis, and the red points are the H.E.S.S. points listed in Abdalla et al., 2018 (originally published in Aharonian et al., 2005). The best fit of the joint spectrum is a pure power law which is drawn in purple. The reduced χ^2 value is 8.34/9 for a power law with an index of 2.13 ± 0.19 and a flux normalization of $(1.94 \pm 0.76) \times 10^{-14}\,\mathrm{cm}^{-2}\,\mathrm{s}^{-1}\,\mathrm{TeV}^{-1}$ at $5\,\mathrm{TeV}$. The lack of a cutoff up to approximately $20\,\mathrm{TeV}$ puts constraints on possible models of its emission.
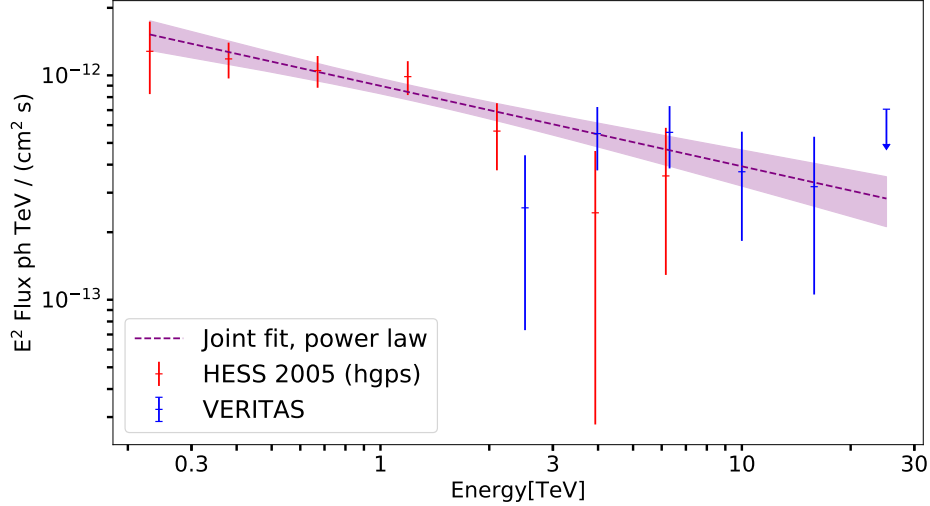
Figure 7.15: Gamma-ray spectrum of the supernova remnant G0.9+0.1. The blue points are from my VERITAS analysis and the red points are from the H.E.S.S. Galactic Plane Survey (Abdalla et al., 2018). The best-fit power laws are shown as dashed lines with matching colors. The shaded regions show the bounds of the 1σ error on the fit.

7.5.2   Unidentified Source VER J1746–289

The bump in the significance skymap near VER J1745–290 (Figure 7.5) is associated with the unidentified source VER J1746–289, which is very near to and possibly associated with the source HESS J1746–285. The emission can be much better seen in the significance skymap produced after the best fit of the J1745–290 excess is subtracted, pictured in Figure 7.16. The significance after subtraction reaches over 13σ. There is a small oversubtraction of the excess that occurs in my analysis. This could be because it is trying to fit VER J1745–290 along with the emission from VER J1746–289 and diffuse emission along the ridge, which is

stronger at higher longitude and lower latitude, causing an oversubtraction in lower longitude and high latitude.

This subtraction reveals the presence of enhanced emission adjacent to VER J1745–290. A spatial fit to the PSF was performed on the subtracted excess map. My best-fit position of VER J1746–289, $(0.097°, -0.135°)$ is still offset from HESS J1746–285 but closer than the previous VERITAS result. Because the fit is less stable to initial conditions, the uncertainty of the position should actually be higher. The centroid of VER J1746–289 is located about $0.2°$ from the centroid of VER J1745–290, close enough for their PSFs to overlap. Proper fits of the central signal would thus require a simultaneous fit of both sources and of the diffuse emission.

I also performed a spectral analysis in the $0.1°$ region around its position. Figure 7.17 shows the spectrum of J1746–289. It is best fit by a pure power law with an index of 2.25 ± 0.15 and a differential flux normalization of $(1.12 \pm 0.29) \times 10^{-12} \, \mathrm{cm}^{-2} \, \mathrm{s}^{-1} \, \mathrm{TeV}^{-1}$ at $1 \, \mathrm{TeV}$. It appears as though the uncertainty is overestimated, as indicated by reduced χ^2 value of 1.12 / 8. This is possibly in part because the effective area is not calculated at a standard offset and must be interpolated which increases its uncertainty. The events counted in this region include some contamination from the central source VER J1745–290 and the diffuse emission.

7.5.3   HESS J1745–303

HESS J1745–303 is a strong source located at Galactic coordinates $(\ell = 358.71°, b = -0.64°)$ with an RMS extension of $\sigma_{\mathrm{source}} = 0.21° \pm 0.06°$, $\sigma'_{\mathrm{source}} = 0.09° \pm 0.04°$, where the orientation angle with respect to Galactic latitude is $\omega = 54° \pm 7°$ (Aharonian et al., 2006b). Because of its proximity to the shell-like SNR G359.1–0.5, emission from J1745−303 is consistent with the model in which the particles accelerated to high energies by SNRs interact with dense matter. Its spectrum was determined by the HESS Collaboration et al. (2008) with an integration radius of $0.4°$ centered on the above position, and was fit to a power law. The index of the whole region was found to be $2.71 \pm 0.11_{\mathrm{stat}} \pm 0.2_{\mathrm{sys}}$ and the integral flux
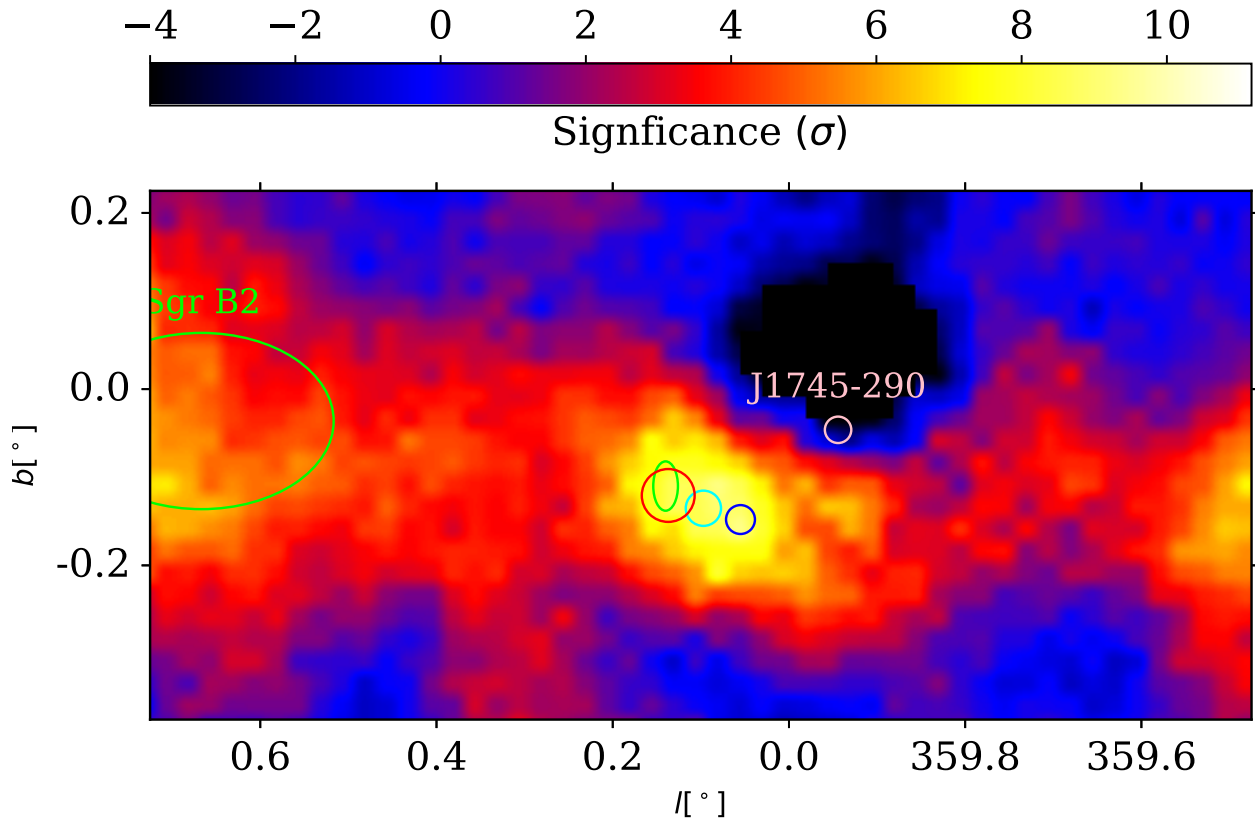
Figure 7.16: Significance skymap of the GC above $2\,\mathrm{TeV}$ after subtraction of the central point source, J1745–290. The position and uncertainty of my best-fit for the adjacent source is shown as the cyan circle. The positions and uncertainties are shown for other sources for comparison: The previous position of VER J1746–289 from Archer et al., 2016 (blue), VER J1745–290 (pink), HESS J1746–285 (green), and MAGIC J1746.4-2853 (red).

$F(1\text{–}10\,\mathrm{TeV}) = (1.63 \pm 0.16) \times 10^{-12}\,\mathrm{cm}^{-2}\,\mathrm{s}^{-1}$.

In my analysis, the location of HESS J1745–303 reached a statistical significance of $4.4\,\sigma$, just shy of a detection. This is insufficient for reconstructing a reliable spectrum.

7.5.4 HESS J1741–302

HESS J1741–302 is another unidentified source whose morphology is consistent with statistical fluctuations (Tibolla et al., 2008). The emission is potentially caused by the interactions of CRs with the molecular material in the region, but an alternate PWN scenario
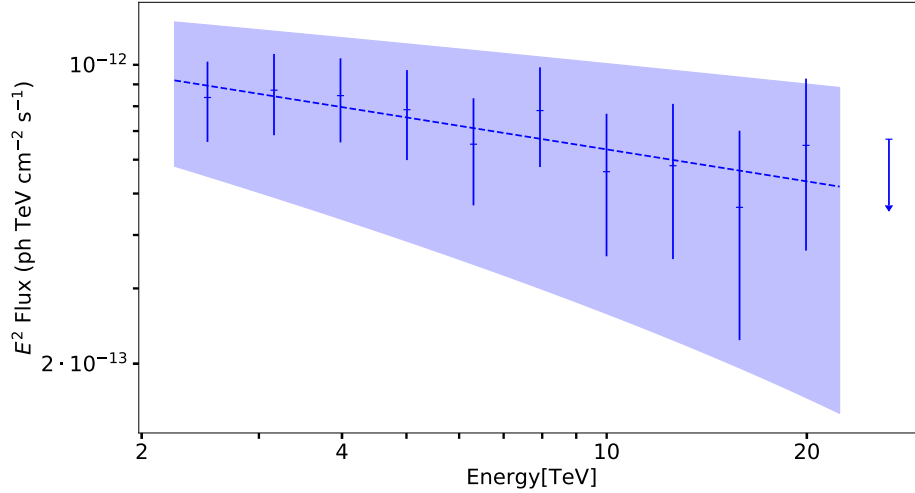
Figure 7.17: Spectrum of J1746–289 from my analysis. The best-fit power law is shown with the 1σ confidence band shaded.

is plausible. However, no strong signal was found at the position of HESS J1741–302, which had a statistical significance of only 0.8 σ in my analysis, insufficient for a detection. HESS J1741–302 and J1745–303 are not very strong sources, and lie toward the outer edges of the VERITAS FoV.

7.6   Summary / Conclusion

The results of my analysis are a major improvement to previous VERITAS results on the Galactic Center due to the use of additional data and advanced techniques. I also produced new results using VERITAS data that strengthen my conclusions. The estimated positions of point sources were consistent with previous results from VERITAS and H.E.S.S. The positional uncertainty of VER J1745–290 was too large to exclude Sgr A East or G359.95–0.04 as counterparts to the source.

Increased statistics on the high end of the energy spectrum of VER J1745–290 shows strong evidence of a cutoff or break energy, both of which are consistent with 10 TeV. A cutoff is predicted by various leptonic models, such as the inverse-Compton model in Aharonian & Neronov, 2005a, or plerion models such as Atoyan & Dermer, 2004 and Kusunose & Takahara,

2012. A cutoff at this energy is also consistent with the emission of SNRs and PWNe, most of which cut off between 10–20 TeV. The low value of the cutoff energy could possibly indicate that the magnetic fields in this source are very strong causing a high rate of electron cooling.

No variability of the flux of VER J1745–290 was observed for timescales of days to years. PWNe are not known to exhibit variable behavior, so a lack of variability gives preference to G359.95–0.04 as a potential central emitter.

I have produced the very first spectrum of the diffuse emission in the GC region as determined by VERITAS. The diffuse emission observed by VERITAS, in contrast to the central source VER J1745–290, does not show any evidence of a cutoff, and it maintains a hard power law up to 40 TeV. The lack of a cutoff in the spectrum supports the case for the presence of an accelerator of PeV cosmic ray particles in the GC. The index parameter of the VER J1745–290 spectrum is consistent with the power law index of the diffuse emission.

There is about a 52 % spatial correlation between gamma-ray emission in the CMZ and dense molecular matter. This provides additional evidence that the diffuse emission results from high-energy cosmic rays interacting with interstellar matter and radiation. Hadronic origins of diffuse emission are preferred; leptonic models are possible but unlikely.

The total energy of the flux in the region could have been supplied by a large supernova event in the past. It is also consistent with a population of 10^4–10^5 millisecond pulsars with luminosities above $10^{34}\,\mathrm{erg\,s^{-1}}$ and modest acceleration efficiencies scattered throughout the CMZ (Guépin et al., 2018). Future studies may help to narrow models of diffuse emission.

7.6.1   Future Prospects

Future observations by an instrument with a better angular resolution, such as with CTA, may be able to give strong evidence for or against steady state hadronic models based on the observed morphology of the TeV emission. CTA will have an improved angular resolution (below 0.05° above 1 TeV), and it is expected to have a systematic pointing uncertainty as small as 5″, which is sufficiently precise to potentially distinguish between Sgr A* and PWN G395.95–0.04 as the source of gamma rays from J1745–290. It will also have improved

Source	Best Spectral fit	Fit Parameters	Conclusions
VER J1745–290	Power law w/ exponential cutoff	$\Gamma = 2.16 \pm 0.18$ $E_{\mathrm{cut}} = 10.82 \pm 2.97\,\mathrm{TeV}$	Consistent with PWN because of cutoff and lack of variability
Diffuse emission	Pure power law	$\Gamma = 2.22 \pm 0.22$	Consistent with a hadronic accelerator to PeV energies
SNR G0.9+0.1	Pure power law	$\Gamma = 2.13 \pm 0.19$	Consistent with SNR
VER J1746–289	Pure power law	$\Gamma = 2.25 \pm 0.15$	unidentified

Table 7.2: Summary table of my results for the VHE sources that were analyzed in this dissertation.

background rejection that will contribute to increased sensitivity (Sitarek et al., 2017).

Pushing the spectral reconstruction to higher energies should give stronger preference to either a smoothly broken power law or power law with exponential cutoff, which steepens more sharply after the cutoff energy. Flares, if they occur, will be more likely to be seen with high-sensitivity experiments such as CTA.

A spatial correlation between TeV neutrinos and diffuse gamma rays could prove the hadronic scenario of diffuse emission in the CMZ. Data from experiments such as *IceCube* could possibly produce such a result in the future.

7.7 VERITAS Acknowledgments

support staff at the Fred Lawrence Whipple Observatory and at the collaborating institutions in the construction and operation of the instrument.

APPENDIX A

Appendix

A.1 Interaction Cross Sections

The cross section σ of an interaction is the area transverse to relative velocity of two particles within which they must pass for that interaction to occur. It is related to the probability p of an incident particle interacting with one of a collection of target particles as it passes,

$$\frac{\sigma N}{A} = p \tag{A.1}$$

where N/A is the number density per unit area of the target collection. In the classical case of light scattering off a charged particle, as in Thomson scattering, the Thomson cross section can be defined as

$$\sigma_T \equiv \frac{\langle P_{\text{scattered}} \rangle}{\langle \Phi_{\text{incident}} \rangle}, \tag{A.2}$$

where $\Phi_{\text{incident}} =$ is the Poynting flux of the incident electromagnetic wave and $P_{\text{scattered}}$ is the total power the accelerated charge re-radiates, and the bracketed quantities represent their time average. While this scattering exhibits azimuthal symmetry around the direction of incident velocity, the scattered photons do not radiate uniformly over different scattering angles. When the cross section depends on the scattering angle or some other variable such as wave number, it is useful to give the differential cross section. For example $\frac{d\sigma}{d\Omega}$ when multiplied by the incident flux will give the power per steradian as a function of scattering angle. The differential cross section can be integrated over the differential variable, e.g. solid angle, to get the total cross section. In the quantum case, the differential cross section $\frac{d\sigma}{d\Omega}$ is the modulus squared of scattering amplitude,

$$\psi(\mathbf{r}) = e^{ikz} + f(\theta)\frac{e^{ikr}}{r} \tag{A.3}$$

which is probability amplitude of a quantum scattering process.

A.2   Gamma Rays from Dark Matter Annihilation

A close examination of the speeds of orbits of stars and other astronomical objects in a galaxy with relation to their distance from the center shows that there is a large amount of mass that we cannot see. To account for this missing mass, physicists have hypothesized the existence of a non-luminous form of matter called dark matter. The universe is thought to contain over five times more DM than ordinary luminous matter, and what constitutes DM is one of the most interesting questions in physics today. If DM is found to be a particle, it would add an extension to the Standard Model of particle physics. The GC of the MW boasts a large concentration of DM thus is a great region in which to search for the DM particle.

There are many paradigms in dark matter theory concerning its structure and distribution in the universe. Though other dark matter models exist, the most compelling is cold dark matter (CDM), a hypothesis that the particles of dark matter move much more slowly than the speed of light, and have moved slowly since as early as the first year of the universe.

There are also diverse proposals for a DM particle, and currently the majority of candidates are weakly interactive massive particles, or WIMPs. These particles interact only through gravity and the weak force, and have high, super-GeV masses. There are many theories about what the DM particle could be, and the most popular one comes from the lightest supersymmetric particle (LSP) predicted by supersymmetry (SUSY). This particle could be either the gravitino, lightest sneutrino, or most favorably the lightest neutralino. Neutralinos are the four eigenstates of the photino, zino, and higgsino, which are all Majorana fermions, or particles that are their own antiparticle.

The lightest neutralino χ will naturally be stable, so they should only decay through self-annihilation. The self-annihilation cross-section of the WIMP is commonly quoted as needing to have a value of $\langle \sigma v \rangle \simeq 3 \times 10^{-26} \, \text{cm}^3/\text{s}$ to explain its current abundance in the universe. This value is mass-independent, but the mass of the particle was expected to

be near the weak-scale mass of $\sim 100\,\mathrm{GeV}$. (Steigman et al., 2012) have made a more specific calculation, relating the cross-section to the WIMP mass. They find a maximum of $\langle \sigma v \rangle \simeq 5.2 \times 10^{-26}\,\mathrm{cm^3/s}$ for $m \approx 0.3\,\mathrm{GeV}$ and $\langle \sigma v \rangle \simeq 2.2 \times 10^{-26}\,\mathrm{cm^3/s}$ with minimal mass-dependence for masses above $10\,\mathrm{GeV}$.

To date, this particle has not been detected by any direct-detection experiment such as *Xenon* or *CDMS* and has not been produced by the *LHC*. This could mean that the mass is actually greater than $100\,\mathrm{GeV}$, and certain models allow masses exceeding $10\,\mathrm{TeV}$. These high mass scenarios can be studied and detected indirectly by observing the decay products of annihilation. Products of $\chi\chi$ annihilation for which VHE experiments commonly search are $b\bar{b}$ (Equation 3.6) and $\tau^+\tau^-$ (Equation 3.7). These products can decay to create gamma rays with energies on the order of the mass of the χ particle.

The DM component of a galaxy organizes into what is called a dark matter halo, which is most dense around the galactic disk but extends beyond the visible limits of the galaxy. Dark matter density profiles describe the density of the halo as a function of radial distance from the center of the galaxy. An early form of DM profiles was found by (Navarro et al., 1996) by fitting simulations to a power law, characterizing the density ρ of dark matter in a halo as a function of distance from the center r:

$$\rho(r) = \frac{\rho_0}{(r/r_s)(1 + r/r_s)^2} \tag{A.4}$$

where ρ_0 and the scale radius r_s are parameters of an individual halo.

There have been simulations of the dark matter distribution in the center of the MW using the orbital properties of thousands of stars, such as Via Lactea (Kuhlen et al., 2008). Many fits of simulations have found profiles that differ from Equation A.4, but follow a similar inverse relationship to r. According to Linden (2013b), nearly all predictions from these simulations expect a high density of DM near the center of the Milky Way.

A way to quantify the amount of signal we expect to see from a region of DM is a dimensionless function called the J-factor, which is proportional to the square of the DM

density integrated along the line of sight: (Bergström et al., 1998)

$$J\left(\psi\right) = \frac{1}{8.5\,\mathrm{kpc}} \cdot \left(\frac{1}{0.3\,\mathrm{GeV/cm^3}}\right)^2 \int_{\mathrm{l.o.s.}} \rho^2(l)dl(\psi) \tag{A.5}$$

The J-factor depends on the square of DM density because in the process of self-annihilation, the DM serves as both the interacting particle and the target. A higher J-factor corresponds to a higher amount of DM signal expected within a specific line of sight. Because the GC is also relatively close to Earth, and the DM annihilation rate is proportional to the square of the density, the GC may give off the highest signal of DM annihilation of any observable source.

A.3 Boosted Decision Tree Training Algorithm

BDTs must be trained before they can be used in an analysis. The model building process proceeds in mostly the same way for classifications and regressions, and I highlight the differences as they arise. For both BDT regressions and classifications, a very large set of events is required to train and test a model. To train a BDT regression for predicting a continuous target variable, the value of the target variable must be known for all events. To train a BDT for classifications, the class of each event must be known, and there should be a large number of each class of event. The dataset is divided randomly into two subsets, one for training and one for testing.

The algorithm for training a single decision tree is as follows: for every training variable, a critical value is found that best separates the training set. A separation index I is chosen to measure the separation quality, with lower values meaning better separation. For classifications, we use the common Gini index,

$$I = 1 - \sum_i \left(\frac{n_i}{N}\right)^2 \tag{A.6}$$

where n_i represent the number of each classification i and N is the total number of events. For regressions of continuous variables, the index is the variance of the target variable x_{target}:

$$I = \left\langle x_{\mathrm{target}}^2 \right\rangle - \left\langle x_{\mathrm{target}} \right\rangle^2 \tag{A.7}$$

186

where the brackets represent the expectation value. The quantity to be maximized is referred to as the separation gain

$$G = N_{\text{parent}}I_{\text{parent}} - N_{\text{left}}I_{\text{left}} - N_{\text{right}}I_{\text{right}} \tag{A.8}$$

where N are the number of events in each node. Essentially, maximizing the separation means grouping the set of events into the two best clusters it can form. The variable and corresponding critical value that yield the best separation are chosen as the head node of the tree.

This node then branches into two new nodes, one with events whose value of the test variable exceed the critical value, and one with the events that do not exceed the critical value. These nodes are said to be at a depth of 2, with depth increasing by one from parent to child with each recursion. Nodes terminate when a predetermined condition is met, such as the node reaching the maximum depth, or the number of events on a new node falling below a minimum value. They are assigned a prediction value that is to be returned if an input event reaches that node. The algorithm iterates recursively over the new nodes created until all nodes have terminated. Terminal nodes in the classification algorithm are written with the purity $p = \frac{s}{s+b}$ where s is the number of signal events and b is the number of background events in the node. In the regression algorithm, they are assigned the mean value of the target variable on that node. An example of a single decision tree can be seen in Figure 5.9.

A single decision tree cannot offer the most accurate predictions for complex data, and is referred to as a "weak learner". An ensemble of trees can be combined to create a much stronger classifier. Boosting is a way to start with a single tree and use the results of that tree to create subsequent trees. There are multiple types of boosting, but only two were used in this analysis: adaptive boosting and gradient boosting. Adaptive boosting modifies the sample distribution at each iteration by weighting more heavily the misclassified or poorly predicted events, training the subsequent tree with a greater focus on difficult-to-solve events. Gradient boosting trains each new tree being added to the ensemble on the error residuals of the current ensemble. Each tree in the forest contributes a weighted amount, where the weights are based on minimization of the error of the forest. Once the chosen number of trees

in the ensemble is trained, the trees and associated weights are written to an xml file.

Test events from the independent set are evaluated by the ensemble to test for overtraining. Given the input variables of an event, a tree is traversed starting at the head node until a terminal node is reached, yielding either a classification score or predicted value of the target variable. For each event, every tree in the ensemble is traversed, and the weighted average of all trees in the ensemble is returned. The same routine is executed when evaluating events for an analysis.

The ROOT TMVA code for the booking options used in my energy regression (Subsection 6.1.2) is provided below:

Listing A.1: TMVA Training Options

```
NTrees=10:nEventsMin=1:BoostType=AdaBoostR2:SeparationType=
    RegressionVariance:nCuts=25:PruneMethod=CostComplexity:
    PruneStrength=30
```

A.4   Physical Constants

· $c = 299\,792\,458\,\text{m/s}$ is the speed of light in a vacuum

· $h = 6.626\,070\,04 \times 10^{-34}\,\text{Js}$ is Planck's constant

· $\alpha = \frac{e^2}{4\pi\epsilon_0 \hbar c}$ - Fine-structure constant

· $\epsilon_0 = 8.854\,187\,817\,\text{F/m}$ is the vacuum permittivity, permittivity of free space, electric constant, or the distributed capacitance of the vacuum.

· $\mu_0 = 4\pi \times 10^{-7}\,\text{H/m}$ is the vacuum permeability, permeability of free space, or magnetic constant.

· $m_e = (9.109\,383\,56 \pm 0.000\,000\,11)\,\text{kg}$ is the rest mass of an electron

· $m_p = 1.672\,621\,9 \times 10^{-27}\,\text{kg}$ is the rest mass of a proton

· $M_\odot = 1.989 \times 10^{30}\,\text{kg}$ is the mass of the Sun (solar mass)

· $e = 1.602\,176\,62 \times 10^{-19}\,\text{coulombs}$ is the electron charge

· $r_\text{e} = \frac{1}{4\pi\varepsilon_0}\frac{e^2}{m_\text{e}c^2} = (2.817\,940\,322\,7 \pm 0.000\,000\,001\,9) \times 10^{-15}\,\text{m}$ is the classical electron radius

A.4.1 Unit Conversions

- A barn is a unit of area, $1\,\text{b} = 10^{-28}\,\text{m}^2$

- $1\,\text{erg} = 10^{-7}\,\text{J}$

- $1\,\text{pc} \approx 3.086 \times 10^{16}\,\text{m}$

A.4.2 Formulas

The expectation value of x is defined as:

$$\langle x \rangle = \sum_i p_i x_i \tag{A.9}$$

$$= \int_{-\infty}^{\infty} p(x)x\,dx \tag{A.10}$$

where p is the weight or probability density of that value of x.

Bibliography

Aartsen, M. G. et al. (Oct. 2013). "Evidence for High-Energy Extraterrestrial Neutrinos at the IceCube Detector". In: *Science* 342.6161, pp. 1242856–1242856. DOI: `10.1126/science.1242856` (72).

Abdalla, H. et al. (2018). "The H.E.S.S. Galactic plane survey". In: *Astronomy \& Astrophysics* 612, A1. DOI: `10.1051/0004-6361/201732098` (163, 176).

Abramowski, A. et al. (2015). "Constraints on an annihilation signal from a core of constant dark matter density around the milky way center with H.E.S.S." In: *Physical Review Letters* 114.8, pp. 1–6. DOI: `10.1103/PhysRevLett.114.081301` (78).

Abramowski, A. et al. (Mar. 2016). "Acceleration of petaelectronvolt protons in the Galactic Centre". In: *Nature* advance on. DOI: `10.1038/nature17147` (29, 30, 54, 56–59, 63, 76, 77, 166, 168, 174).

Acero, F. et al. (Mar. 2010). "Localizing the VHE γ-ray source at the Galactic Centre". In: *Monthly Notices of the Royal Astronomical Society* 402.3, pp. 1877–1882. DOI: `10.1111/j.1365-2966.2009.16014.x` (53, 66, 163).

Aharonian, F. & Neronov, A. (Jan. 2005a). "High-Energy Gamma Rays from the Massive Black Hole in the Galactic Center". en. In: *The Astrophysical Journal* 619.1, pp. 306–313. DOI: `10.1086/426426` (66–69, 73, 179).

Aharonian, F. et al. (Nov. 2004). "Calibration of cameras of the H.E.S.S. detector". In: *Astroparticle Physics* 22.2, pp. 109–125. DOI: `10.1016/j.astropartphys.2004.06.006` (19, 56).

Aharonian, F. et al. (Mar. 2005). "Very high energy gamma rays from the composite SNR G0.9+0.1". en. In: *Astronomy and Astrophysics* 432.2, pp. L25–L29. DOI: `10.1051/0004-6361:200500022` (9, 20, 64, 175, 176).

Aharonian, F. et al. (Feb. 2006a). "Discovery of very-high-energy γ-rays from the Galactic Centre ridge". In: *Nature* 439.7077, pp. 695–698. DOI: `10.1038/nature04467` (20, 21).

Aharonian, F. et al. (Jan. 2006b). "The H.E.S.S. Survey of the Inner Galaxy in Very High Energy Gamma Rays". In: *The Astrophysical Journal* 636.2, pp. 777–797. DOI: `10.1086/498013` (20, 177).

Aharonian, F. et al. (Dec. 2008). "Simultaneous HESS and Chandra observations of Sagitarius A * during an X-ray flare". In: *Astronomy and Astrophysics* 492.1, pp. L25–L28. DOI: `10.1051/0004-6361:200810912` (16).

Aharonian, F. et al. (Sept. 2009). "Spectrum and variability of the Galactic center VHE γ-ray source HESS J1745–290". en. In: *Astronomy and Astrophysics* 503.3, pp. 817–825. DOI: `10.1051/0004-6361/200811569` (53, 55, 57, 166, 167).

Aharonian, F. A. & Atoyan, A. M. (1998). *Nonthermal Radiation of the Crab Nebula.* Tech. rep. (38).

Aharonian, F. & Neronov, A. (Nov. 2005b). "TeV Gamma Rays From the Galactic Center Direct and Indirect Links to the Massive Black Hole in Sgr A". In: *Astrophysics and Space Science* 300.1-3, pp. 255–265. DOI: `10.1007/s10509-005-1209-4` (69).

Ahnen, M. L. et al. (Nov. 2016). "Observations of Sagittarius A* during the pericenter passage of the G2 object with MAGIC". In: DOI: `10.1051/0004-6361/201629355` (54, 56, 65, 66, 167, 168).

Akiyama, K. et al. (Nov. 2013). "Long-term monitoring of Sgr A* at 7 mm with VERA and KaVA". In: DOI: `10.1017/S1743921314000751` (6).

Albert, J. et al. (Feb. 2006). "Observation of Gamma Rays from the Galactic Center with the MAGIC Telescope". In: *The Astrophysical Journal* 638.2, pp. L101–L104. DOI: `10.1086/501164` (20).

Albert, J. et al. (2008). "Implementation of the Random Forest method for the Imaging Atmospheric Cherenkov Telescope MAGIC". In: *Nuclear Instruments and Methods in Physics Research, Section A: Accelerators, Spectrometers, Detectors and Associated Equipment* 588.3, pp. 424–432. DOI: `10.1016/j.nima.2007.11.068` (120, 140).

Archer, A. et al. (Aug. 2014). "Very-High Energy Observations of the Galactic Center Region By Veritas in 2010-2012". In: *The Astrophysical Journal* 790.2, p. 149. DOI: `10.1088/0004-637X/790/2/149` (16, 20, 21, 56, 58, 67, 74, 78, 114, 170).

Archer, A. et al. (Feb. 2016). "TeV Gamma-ray Observations of The Galactic Center Ridge By VERITAS". In: p. 9 (20, 21, 51, 53, 55, 56, 64, 65, 70, 163, 165, 178).

Atoyan, A. M., Aharonian, F. A. & Völk, H. J. (Sept. 1995). "Electrons and positrons in the galactic cosmic rays". In: *Physical Review D* 52.6, pp. 3265–3275. DOI: `10.1103/PhysRevD.52.3265` (29, 30).

Atoyan, A. & Dermer, C. D. (Dec. 2004). "TeV Emission from the Galactic Center Black Hole Plerion". In: *The Astrophysical Journal* 617.2, pp. L123–L126. DOI: `10.1086/427390` (72, 74, 179).

Baganoff, F. K. et al. (Sept. 2001). "Rapid X-ray flaring from the direction of the supermassive black hole at the Galactic Centre". In: *Nature* 413.6851, pp. 45–48. DOI: `10.1038/35092510` (14).

Baganoff, F. K. et al. (July 2003). "Chandra X-Ray Spectroscopic Imaging of Sagittarius A* and the Central Parsec of the Galaxy". In: *The Astrophysical Journal* 591.2, pp. 891–915. DOI: `10.1086/375145` (14, 66).

Bai, Y. et al. (2014). "Neutrino lighthouse at Sagittarius A". In: *Physical Review D - Particles, Fields, Gravitation and Cosmology* 90.6, pp. 1–25. DOI: `10.1103/PhysRevD.90.063012` (72).

Balick, B. & Brown, R. L. (Dec. 1974). "Intense sub-arcsecond structure in the galactic center". In: *The Astrophysical Journal* 194, p. 265. DOI: `10.1086/153242` (3).

Ballantyne, D. R., Schumann, M. & Ford, B. (Sept. 2011). "Modelling the time-dependence of the TeV γ-ray source at the Galactic Centre". en. In: *Monthly Notices of the Royal Astronomical Society* 410.3, no–no. DOI: `10.1111/j.1365-2966.2010.17533.x` (69, 76).

Balogh, A. & Treumann, R. A. (2013). *Physics of Collisionless Shocks: Space Plasma Shock Waves*. ISSI Scientific Report Series. Springer New York (26).

Baring, M. G. (Nov. 1997). "Diffusive Shock Acceleration: the Fermi Mechanism". In: (28).

Barrière, N. M. et al. (May 2014). "NuSTAR DETECTION OF HIGH-ENERGY X-RAY EMISSION AND RAPID VARIABILITY FROM SAGITTARIUS A* FLARES". In: *The Astrophysical Journal* 786.1, p. 46. DOI: `10.1088/0004-637X/786/1/46` (16).

Bartels, R., Krishnamurthy, S. & Weniger, C. (Feb. 2016). "Strong Support for the Millisecond Pulsar Origin of the Galactic Center GeV Excess". In: *Physical Review Letters* 116.5, p. 051102. DOI: `10.1103/PhysRevLett.116.051102` (74).

Bartels, R. et al. (Mar. 2018). "Galactic Binaries Can Explain the Fermi Galactic Center Excess and 511 keV Emission". In: DOI: `10.1093/mnras/sty2135` (74).

Becklin, E. & Neugebauer, G (Jan. 1968). "Infrared Observations of the Galactic Center". In: *APJ* 151, p. 145. DOI: `10.1086/149425` (3).

Bednarek, W. & Sobczak, T. (Aug. 2013). "Gamma-rays from millisecond pulsar population within the central stellar cluster in the Galactic Centre". In: *Monthly Notices of the Royal Astronomical Society: Letters* 435.1, pp. L14–L18. DOI: `10.1093/mnrasl/slt084` (74, 77).

Berezinskii, V. S. et al. (1990). "Astrophysics of cosmic rays". In: *Amsterdam: North-Holland, 1990, edited by Ginzburg, V.L.* (24).

Berge, D., Funk, S. & Hinton, J. A. (2006). "Background Modelling in Very-High-Energy γ-ray Astronomy.pdf". In: 631.November, pp. 1–13 (126, 127).

Bergström, L., Ullio, P. & Buckley, J. H. (Aug. 1998). "Observability of γ rays from dark matter neutralino annihilations in the Milky Way halo". In: *Astroparticle Physics* 9.2, pp. 137–162. DOI: `10.1016/S0927-6505(98)00015-2` (186).

Bertsch, D. L. et al. (1998). "High-energy gamma-ray emission from the Galactic Center". In: *Astronomy and Astrophysics* 172, pp. 161–172 (17).

Bethe, H. & Heitler, W. (Aug. 1934). "On the Stopping of Fast Particles and on the Creation of Positive Electrons". In: *Proceedings of the Royal Society A: Mathematical, Physical and Engineering Sciences* 146.856, pp. 83–112. DOI: `10.1098/rspa.1934.0140` (43).

Bird, D. J. et al. (Nov. 1993). "Evidence for correlated changes in the spectrum and composition of cosmic rays at extremely high energies". In: *Physical Review Letters* 71.21, pp. 3401–3404. DOI: `10.1103/PhysRevLett.71.3401` (31, 32).

Blasi, P. (2013). "Origin of galactic cosmic rays". In: *Nuclear Physics B - Proceedings Supplements* 239-240, pp. 140–147. DOI: `10.1016/j.nuclphysbps.2013.05.023` (33, 34).

Boehle, A. et al. (July 2016). "An Improved Distance and Mass Estimate for Sgr A* from a Multistar Orbit Analysis". In: pp. 1–56. DOI: 10.3847/0004-637X/830/1/17 (4, 168).

Brun, R. & Rademakers, F. (1997). "ROOT - An object oriented data analysis framework". In: *Nuclear Instruments and Methods in Physics Research, Section A: Accelerators, Spectrometers, Detectors and Associated Equipment.* DOI: 10.1016/S0168-9002(97)00048-X (102).

Buckley, J. H. et al. (2003). "The VERITAS Flash ADC Electronics System". In: *Proceedings of the 28th International Cosmic Ray Conference.* Vol. 5, p. 2827 (92).

Bustamante, M et al. (2009). *High-energy cosmic-ray acceleration.* Tech. rep. (34).

Butterfield, N. et al. (Oct. 2017). "M0.20-0.033: An Expanding Molecular Shell in the Galactic Center Radio Arc". In: DOI: 10.3847/1538-4357/aa886e (65).

Carollo, D. et al. (July 2016). "The age structure of the Milky Way's halo". In: DOI: 10.1038/nphys3874 (24).

Cherenkov, P. A. (1934). "Visible emission of clean liquids by action of γ radiation". In: *Doklady Akademii Nauk SSSR* 2, pp. 451+ (87).

Cherenkov, P. A., Frank, I. M. & Tamm, I. E. (1958). *The Nobel Prize in Physics* (87).

Chernyakova, M. et al. (Jan. 2011). "The High-Energy Arcminute-Scale Galactic Center Gamma-Ray Source". In: *The Astrophysical Journal* 726.2, p. 60. DOI: 10.1088/0004-637X/726/2/60 (69, 70, 74).

Chernyshov, D. O. et al. (Jan. 2017). "Origin of X-ray and gamma-ray emission from the Galactic central region". In: DOI: 10.3847/1538-4357/835/2/194 (70, 75).

Clavel, M. et al. (2012). "Chandra observations of the X-ray emission from Molecular Clouds at the Galactic Center related to Sgr A past activity". In: October (16).

Cogan, P. & VERITAS, f. t. C. (2007). "VEGAS, the VERITAS Gamma-ray Analysis Suite". In: pp. 1–4 (102).

Condon, B. et al. (Nov. 2017). "Detection of two TeV shell-type remnants at GeV energies with Fermi-LAT: HESS J1731-347 and SN 1006". In: DOI: 10.3847/1538-4357/aa9be8 (46).

Dahmen, G. et al. (Nov. 1997). "Molecular Gas in the Galactic Center Region II. Gas mass and N(H_2)/I(^12CO) conversion based on a C^18O(J = 1 -> 0) Survey". In: (60).

Daniel, M. K. & VERITAS, C. (Sept. 2007). "The VERITAS standard data analysis". In: *30TH INTERNATIONAL COSMIC RAY CONFERENCE*. Leeds (102).

Davies, J. M. & Cotton, E. S. (Apr. 1957). "Design of the quartermaster solar furnace". In: *Solar Energy* 1.2-3, pp. 16–22. DOI: 10.1016/0038-092X(57)90116-0 (88).

De Angelis, A. & Mallamaci, M. (May 2018). "Gamma-Ray Astrophysics". In: *Eur. Phys. J. Plus* 133, p. 324. DOI: 10.1140/epjp/i2018-12181-0 (76).

Degenaar, N. et al. (June 2013). "THE X-RAY FLARING PROPERTIES OF Sgr A* DURING SIX YEARS OF MONITORING WITH SWIFT". en. In: *The Astrophysical Journal* 769.2, p. 155. DOI: 10.1088/0004-637X/769/2/155 (16, 56).

Devereux, N. A. & Young, J. S. (Feb. 1990). "The origin of the far-infrared luminosity from spiral galaxies". en. In: *The Astrophysical Journal* 350, p. L25. DOI: 10.1086/185659 (13).

Do, T. et al. (Feb. 2009). "A NEAR-INFRARED VARIABILITY STUDY OF THE GALAC- TIC BLACK HOLE: A RED NOISE SOURCE WITH NO DETECTED PERIOD- ICITY". In: *The Astrophysical Journal* 691.2, pp. 1021–1034. DOI: 10.1088/0004-637X/691/2/1021 (13).

Doeleman, S. S. et al. (Sept. 2008). "Event-horizon-scale structure in the supermassive black hole candidate at the Galactic Centre." In: *Nature* 455.7209, pp. 78–80. DOI: 10.1038/nature07245 (5).

Dogiel, V. A., Schönfelder, V. & Strong, A. W. (2002). "The Cosmic-Ray Luminosity of the Galaxy". In: *The Astrophysical Journal*. DOI: 10.1086/341882 (24).

Eisenhauer, F. et al. (2005). "SINFONI in the Galactic Center: Young Stars and Infrared Flares in the Central Light-Month". In: *The Astrophysical Journal* 628.1, pp. 246–259. DOI: 10.1086/430667 (4).

Ekers, R. et al. (June 1983). "The radio structure of SGR A". In: *AAP* 122, 143–150s (7, 10).

Fano, U. (Dec. 1959). "High-Frequency Limit of Bremsstrahlung in the Sauter Approximation". In: *Physical Review* 116.5, pp. 1156–1158. DOI: `10.1103/PhysRev.116.1156` (43).

Fatuzzo, M. & Melia, F. (2012). "Diffusive Cosmic-Ray Acceleration in Sagittarius A*". In: *The Astrophysical Journal Letters* 757.1, p. L16. DOI: `10.1088/2041-8205/757/1/L16` (70, 75).

Fatuzzo, M. & Melia, F. (Feb. 2003). "A Kinship between the EGRET SNR's and Sgr A East". In: DOI: `10.1086/378041` (17).

Fermi, E. (1949). "The origin of cosmic radiation". In: *Physics Today* 2.8, pp. 6–13. DOI: `10.1063/1.3066619` (24, 26).

Fermi-LAT Collaboration et al. (Feb. 2013). "Detection of the Characteristic Pion-Decay Signature in Supernova Remnants". In: DOI: `10.1126/science.1231160` (34, 46).

Fermi-LAT Collaboration et al. (Jan. 2015a). "Fermi Large Area Telescope Third Source Catalog". In: *The Astrophysical Journal Supplement Series, Volume 218, Issue 2, article id. 23, 41 pp. (2015)*. 218. DOI: `10.1088/0067-0049/218/2/23` (18).

Fermi-LAT Collaboration et al. (Nov. 2015b). "Fermi-LAT Observations of High-Energy Gamma-Ray Emission Toward the Galactic Center". In: p. 29 (18).

Frank, I. M. & Tamm, I. E. (1937). "Coherent visible radiation of fast electrons passing through matter". In: *Compt. Rend. Acad. Sci. URSS* 14.3, pp. 109–114. DOI: `10.1007/978-3-642-74626-0_2,10.3367/UFNr.0093.196710o.0388` (87).

Fujita, Y., Kimura, S. S. & Murase, K. (July 2015). "Hadronic origin of multi-TeV gamma rays and neutrinos from low-luminosity active galactic nuclei: Implications of past activities of the Galactic center". In: *Physical Review D* 92.2, p. 023001. DOI: `10.1103/PhysRevD.92.023001` (71).

Gaggero, D. et al. (2017). "Diffuse cosmic rays shining in the Galactic center: A novel interpretation of H.E.S.S. and Fermi-LAT gamma-ray data". In: 031101.July, pp. 1–5. DOI: `10.1103/PhysRevLett.119.031101` (76).

Genzel, R. et al. (Oct. 2003). "Near-infrared flares from accreting gas around the supermassive black hole at the Galactic Centre." In: *Nature* 425.6961, pp. 934–7. DOI: `10.1038/nature02065` (13).

Genzel, R., Eisenhauer, F. & Gillessen, S. (Dec. 2010). "The Galactic Center massive black hole and nuclear star cluster". In: *Reviews of Modern Physics* 82.4, pp. 3121–3195. DOI: `10.1103/RevModPhys.82.3121` (56, 168).

Ghez, A. M. et al. (2003). "Variable Infrared Emission from the Supermassive Black Hole at the Center of the Milky Way". In: *Astrophysical Journal* 601, pp. L159–L162. DOI: `10.1086/382024` (13).

Ghez, A. M. et al. (Feb. 2005). "Stellar Orbits around the Galactic Center Black Hole". In: *The Astrophysical Journal* 620.2, pp. 744–757. DOI: `10.1086/427175` (3, 5).

Ghez, A. M. et al. (Dec. 2008). "Measuring Distance and Properties of the Milky Way's Central Supermassive Black Hole with Stellar Orbits". In: *The Astrophysical Journal* 689.2, pp. 1044–1062. DOI: `10.1086/592738` (4).

Gibbs, K et al. (2003). "The VERITAS Atmospheric Cerenkov Telescopes: Positioner, Optics and Associated Components". In: 5, p. 2823 (90).

Ginzburg, V. L. & Syrovatski, S. I. (1964). *The origin of cosmic rays.* Pergamon Press; [distributed in the Western Hemisphere by Macmillan, New York], p. 426 (29).

Greisen, K. (Apr. 1966). "End to the Cosmic-Ray Spectrum?" In: *Physical Review Letters* 16.17, pp. 748–750. DOI: `10.1103/PhysRevLett.16.748` (32).

Guépin, C. et al. (June 2018). "Pevatron at the Galactic Center: Multi-Wavelength Signatures from Millisecond Pulsars". In: DOI: `10.1088/1475-7516/2018/07/042` (77, 180).

Guo, Y.-Q. et al. (June 2013). "A hybrid model of GeV–TeV gamma ray emission from the Galactic center". In: *Journal of Physics G: Nuclear and Particle Physics* 40.6, p. 065201. DOI: `10.1088/0954-3899/40/6/065201` (75).

Guo, Y.-Q. et al. (Apr. 2016). "The Galactic Center: A PeV Cosmic Ray Acceleration Factory". In: *The Astrophysical Journal, Volume 836, Issue 2, article id. 233, 5 pp. (2017).* 836. DOI: `10.3847/1538-4357/aa5f58` (77).

Hall, J. et al. (2003). "Veritas CFDs". In: *Proceedings of the 28th International Cosmic Ray Conference*, p. 2851 (94).

Halzen, F. et al. (1990). *Cosmology with 100-TeV y-ray telescopes.* Tech. rep., p. 15 (31).

Hanna, D. et al. (Nov. 2009). "An LED-based Flasher System for VERITAS". In: *Nuclear Instruments and Methods in Physics Research Section A, Volume 612, Issue 2, p. 278-287.* 612, pp. 278–287. DOI: `10.1016/j.nima.2009.10.107` (99).

Heck, D et al. (1998). *CORSIKA: A Monte Carlo Code to Simulate Extensive Air Showers.* Tech. rep. (115).

Helder, E. A. et al. (Aug. 2009). "Measuring the cosmic-ray acceleration efficiency of a supernova remnant." In: *Science (New York, N.Y.)* 325.5941, pp. 719–22. DOI: `10.1126/science.1173383` (33).

Herrnstein, R. M. & Ho, P. T. P. (Sept. 2004). "The Nature of the Molecular Environment within 5 pc of the Galactic Center". In: DOI: `10.1086/426047` (6).

HESS Collaboration et al. (Mar. 2008). "Exploring a SNR/Molecular Cloud Association Within HESS J1745-303". In: DOI: `10.1051/0004-6361:20079230` (177).

H.E.S.S. Collaboration et al. (2017). "Characterising the VHE diffuse emission in the central 200 parsecs of our Galaxy with H.E.S.S". In: *Astronomy & Astrophysics* (52, 59–62, 65, 172, 174).

Hillas, A. M. (Sept. 1984). "The Origin of Ultra-High-Energy Cosmic Rays". In: *Annual Review of Astronomy and Astrophysics* 22.1, pp. 425–444. DOI: `10.1146/annurev.aa.22.090184.002233` (32).

— (1985). "Cerenkov light images of EAS produced by primary gamma". In: *Goddard Space Flight Center 19th Intern. Cosmic Ray Conf.* Vol. 3, pp. 445–448 (105).

— (2006). "Cosmic Rays: Recent Progress and some Current Questions". In: (31).

Hinton, J. A. & Aharonian, F. A. (Mar. 2007). "Inverse Compton Scenarios for the TeV Gamma-Ray Emission of the Galactic Center". In: *The Astrophysical Journal* 657.1, pp. 302–307. DOI: `10.1086/510283` (74).

Hoecker, A. et al. (Mar. 2007). "TMVA - Toolkit for Multivariate Data Analysis". In: (120).

Holder, J. et al. (Dec. 2008). "Status of the VERITAS Observatory". In: *AIP Conference Proceedings.* Vol. 1085. 1. AIP, pp. 657–660. DOI: `10.1063/1.3076760` (88).

Holder, J. (Apr. 2012). "TeV Gamma-ray Astronomy: A Summary". In: DOI: `10.1016/j.astropartphys.2012.02.014` (81).

— (Oct. 2015). "Atmospheric Cherenkov Gamma-ray Telescopes". In: (86).

Jackson, J. D. (1999). *Classical electrodynamics*. Third. Wiley (87).

James, F. & Roos, M. (Dec. 1975). "Minuit - a system for function minimization and analysis of the parameter errors and correlations". In: *Computer Physics Communications* 10.6, pp. 343–367. DOI: 10.1016/0010-4655(75)90039-9 (133).

Jansky, K. G. (July 1933). "Radio Waves from Outside the Solar System". en. In: *Nature* 132.3323, pp. 66–66. DOI: 10.1038/132066a0 (9).

Johnson, S. P., Dong, H. & Wang, Q. D. (Nov. 2009). "A large-scale survey of X-ray filaments in the Galactic Centre". en. In: *Monthly Notices of the Royal Astronomical Society* 399.3, pp. 1429–1440. DOI: 10.1111/j.1365-2966.2009.15362.x (14).

Jones, P. A. et al. (Mar. 2011). "Spectral imaging of the Sagittarius B2 region in multiple 7-mm molecular lines". In: *Monthly Notices of the Royal Astronomical Society* 411.4, pp. 2293–2310. DOI: 10.1111/j.1365-2966.2010.17849.x (171).

Klein, O. & Nishina, Y. (Nov. 1929). "Über die Streuung von Strahlung durch freie Elektronen nach der neuen relativistischen Quantendynamik von Dirac". In: *Zeitschrift für Physik* 52.11-12, pp. 853–868. DOI: 10.1007/BF01366453 (45).

Koch, H. W. & Motz, J. W. (1959). *Bremsstrahlung Cross-Section Formulas and Related Data**. Tech. rep. Washington, D. C.: National Bureau of Standards. DOI: 10.1103/RevModPhys.31.920 (43).

Kosack, K. & VERITAS (2004). "TeV Gamma-Ray Observations of the Galactic Center". In: pp. 1–15. DOI: 10.1086/422469 (19).

Koyama, K. et al. (Nov. 1995). "Evidence for shock acceleration of high-energy electrons in the supernova remnant SN1006". In: *Nature* 378.6554, pp. 255–258. DOI: 10.1038/378255a0 (35).

Krause, M., Pueschel, E. & Maier, G. (2017). "Improved γ/hadron separation for the detection of faint γ-ray sources using boosted decision trees". In: *Astroparticle Physics* 89, pp. 1–9. DOI: 10.1016/j.astropartphys.2017.01.004 (123).

Kuhlen, M et al. (July 2008). "The Via Lactea INCITE simulation: galactic dark matter substructure at high resolution". In: *Proceedings of the SciDAC 2008 conference.* Vol. 125. Seattle, WA, p. 012008. DOI: 10.1088/1742-6596/125/1/012008 (185).

Kusunose, M. & Takahara, F. (Mar. 2012). "A LEPTONIC MODEL OF STEADY HIGH-ENERGY GAMMA-RAY EMISSION FROM Sgr A*". In: *The Astrophysical Journal* 748.1, p. 34 (73, 179).

LaRosa, T. N. et al. (Jan. 2000). "A Wide-Field 90 Centimeter VLA Image of the Galactic Center Region". en. In: *The Astronomical Journal* 119.1, pp. 207–240. DOI: 10.1086/301168 (10).

Lau, R. M. et al. (Mar. 2015). "Old supernova dust factory revealed at the Galactic center". In: DOI: 10.1126/science.aaa2208 (7).

Lemiere, a. et al. (Oct. 2015). "Study of the VHE diffuse emission in the central 200 pc of our Galaxy with H.E.S.S". In: *The 34th International Cosmic Ray Conference.* The Hague, The Netherlands (20, 21, 65).

Li, T.-P. & Ma, Y.-Q. (Sept. 1983). "Analysis methods for results in gamma-ray astronomy". In: *The Astrophysical Journal* 272, p. 317. DOI: 10.1086/161295 (128).

Li, Z., Morris, M. R. & Baganoff, F. K. (Dec. 2013). "EVIDENCE FOR A PARSEC-SCALE JET FROM THE GALACTIC CENTER BLACK HOLE: INTERACTION WITH LOCAL GAS". In: *The Astrophysical Journal* 779.2, p. 154. DOI: 10.1088/0004-637X/779/2/154 (3, 17).

Linden, T. (2013a). "Dark Matter Annihilation at the Galactic Center". PhD thesis. UC Santa Cruz (11).

— (Oct. 2013b). "Dark matter in the Galactic center". In: *Proceedings of the International Astronomical Union.* Vol. 9. S303, pp. 403–413. DOI: 10.1017/S1743921314001021 (185).

Linden, T., Lovegrove, E. & Profumo, S. (July 2012). "The Morphology of Hadronic Emission Models for the Gamma-Ray Source at the Galactic Center". In: *The Astrophysical Journal* 753.1, p. 41. DOI: 10.1088/0004-637X/753/1/41 (69).

Lis, D. C. & Goldsmith, P. F. (June 1990). "Modeling of the continuum and molecular line emission from the Sagittarius B2 molecular cloud". In: *The Astrophysical Journal* 356, p. 195. DOI: 10.1086/168830 (7).

Liu, S. et al. (Sept. 2006a). "A Testable Stochastic Acceleration Model for Flares in Sagittarius A*". In: *The Astrophysical Journal* 648.2, pp. 1020–1025. DOI: 10.1086/506194 (13).

Liu, S. et al. (Aug. 2006b). "Stochastic Acceleration in the Galactic Center HESS Source". en. In: *The Astrophysical Journal* 647.2, pp. 1099–1105. DOI: 10.1086/505171 (13, 69).

Liu, T. Z. et al. (June 2017). "Fermi acceleration of electrons inside foreshock transient cores". In: DOI: 10.1002/2017JA024480 (28).

Livio, M. & Silk, J. (2014). "Physics: Broaden the search for dark matter". In: *Nature* 507.7490, pp. 29–31. DOI: 10.1038/507029a (78).

Lo, K. Y. & Claussen, M. J. (Dec. 1983). "High-resolution observations of ionized gas in central 3 parsecs of the Galaxy: possible evidence for infall". In: *Nature* 306.5944, pp. 647–651. DOI: 10.1038/306647a0 (5, 10).

Longair, M. S. (2011). *High Energy Astrophysics, 3rd edn., by Malcolm S. Longair*, p. 880. DOI: 10.1080/00107514.2011.647089 (24, 25, 28, 29, 40, 41, 43, 84).

Lorenzo, R. (2018). *MeerKAT radio telescope inaugurated in South Africa – reveals clearest view yet of centre of the Milky Way* (12).

Lynden-Bell, D. & Rees, M. J. (July 1971). "On Quasars, Dust and the Galactic Centre". en. In: *Monthly Notices of the Royal Astronomical Society* 152.4, pp. 461–475. DOI: 10.1093/mnras/152.4.461 (3).

Maeda, Y. et al. (Feb. 2001). "A Chandra Study of Sgr A East: A Supernova Remnant Regulating The Activity Of Our Galactic Center?" In: DOI: 10.1086/339773 (7).

Maier, G. & Holder, J. (2017). "Eventdisplay: An Analysis and Reconstruction Package for Ground-based Gamma-ray Astronomy". In: pp. 1–8 (102).

Malyshev, D et al. (Oct. 2015). "Leptonic origin of the 100 MeV γ-ray emission from the Galactic centre". In: *Astronomy & Astrophysics* 582.Ic, A11. DOI: 10.1051/0004-6361/201526120 (57, 73, 166, 168).

McKinney, W. (2010). "Data Structures for Statistical Computing in Python". In: *Proceedings of the 9th Python in Science Conference.* Ed. by S. van der Walt & J. Millman, pp. 51–56 (150).

Mori, K. et al. (Oct. 2015). "NuSTAR Hard X-ray Survey of the Galactic Center Region I: Hard X-ray Morphology and Spectroscopy of the Diffuse Emission". In: *Astrophysical Journal* 814.94, p. 27 (14, 15, 75).

Morlino, G. & Caprioli, D. (May 2011). "Strong evidences of hadron acceleration in Tycho's Supernova Remnant". In: DOI: 10.1051/0004-6361/201117855 (34).

Morris, M. & Serabyn, E. (1996). "The Galactic Center Environment". In: *Annual Review of Astronomy and Astrophysics* 34, pp. 645–702. DOI: 10.1146/annurev.astro.34.1.645 (7, 12, 13).

NASA (2013). *Black_hole_artist_conception* (2).

Navarro, J. F., Frenk, C. S. & White, S. D. M. (May 1996). "The Structure of Cold Dark Matter Halos". In: *The Astrophysical Journal* 462, p. 563. DOI: 10.1086/177173 (185).

Neilsen, J. et al. (May 2013). "The 3 Ms Chandra Campaign on Sgr A*: A Census of X-ray Flaring Activity from the Galactic Center". In: *Proceedings of the International Astronomical Union* 9.303, pp. 1–4. DOI: 00.0000/X000000000000000X (16, 56).

Nellen, L., Sánchez, F. A. & Valdés-galicia, J. F. (2008). "Mirror Facets for the VERITAS Telescopes Anodization Aluminizing". In: pp. 1–4 (89).

Nolan, P. L. et al. (July 2003). "Variability of EGRET Gamma-Ray Sources". In: DOI: 10.1086/378353 (17).

Nowak, M. A. et al. (Nov. 2012). "CHANDRA /HETGS OBSERVATIONS OF THE BRIGHT-EST FLARE SEEN FROM Sgr A*". In: *The Astrophysical Journal* 759.2, p. 95. DOI: 10.1088/0004-637X/759/2/95 (16).

Ohm, S., Eldik, C. van & Egberts, K. (2009). "Gamma-Hadron Separation in Very-High-Energy Gamma-Ray Astronomy Using a Multivariate Analysis Method". In: *Astroparticle Physics* 31.5, pp. 383–391. DOI: 10.1016/j.astropartphys.2009.04.001 (120, 123).

Ong, R. A. (2006). *Ultra High Energy Cosmic Ray Research with CASA-MIA.* Tech. rep. PRL (31).

Otte, A. N. & VERITAS, C. (Oct. 2011). "The Upgrade of VERITAS with High Efficiency Photomultipliers". In: *32nd International Cosmic Ray Conference*. Beijing (95).

Parsons, R. D. et al. (Sept. 2015). "Sgr A* Observations with H.E.S.S. II". In: *The 34th International Cosmic Ray Conference*. The Hague, The Netherlands (55, 57).

Pedlar, A. et al. (July 1989). "Radio studies of the Galactic center. I - The Sagittarius A complex". In: *The Astrophysical Journal* 342, p. 769. DOI: `10.1086/167635` (6).

Perkins, J. S., Maier, G. & the VERITAS Collaboration (Dec. 2009). "VERITAS Telescope 1 Relocation: Details and Improvements". In: *Fermi Symposium* (95).

Pierce-Price, D et al. (2000). "A Deep Submillimeter Survey of the Galactic Center". In: *Astrophysical Journal* 545.2, pp. L121–L125. DOI: `10.1086/317884` (12).

Piron, F. et al. (Aug. 2001). "Temporal and spectral gamma-ray properties of Mkn 421 above 250 GeV from CAT observations between 1996 and 2000". In: *Astronomy & Astrophysics* 374.3, pp. 895–906. DOI: `10.1051/0004-6361:20010798` (54, 58).

Pohl, M. (Dec. 2004). "A variability and localization study of 3EG J1746-2851". In: (17).

Ponti, G et al. (2015). "Fifteen years of XMM-Newton and Chandra monitoring of Sgr A* : Evidence for a recent increase in the bright flaring rate". In: *Monthly Notices of the Royal Astronomical Society* 454, pp. 1525–1544. DOI: `10.1093/mnras/stv1537` (15, 16).

Porter, T. A. et al. (Aug. 2018). "Galactic PeVatrons and helping to find them: Effects of Galactic absorption on the observed spectra of very high energy gamma-ray sources". In: DOI: `10.1103/PhysRevD.98.041302` (77).

Ptitsyna, K. & Troitsky, S. (2008). "Physical conditions in potential sources of ultra-high-energy cosmic rays: Updated Hillas plot and radiation-loss constraints". In: DOI: `10.3367/UFNe.0180.201007c.0723` (32).

Reid, M. J. & Brunthaler, A. (Aug. 2004). "The Proper Motion of Sgr A*: II. The Mass of Sgr A*". In: DOI: `10.1086/424960` (3).

Rho, J. et al. (July 2002). "X-Ray Synchrotron Emitting Fe-Rich Ejecta in SNR RCW 86". In: DOI: `10.1086/344248` (35).

Rodriguez-Fernandez, N. J., Martin-Pintado, J. & Vicente, P. de (July 2001). "Large scale ionization of the Radio Arc region by the Quintuplet and the Arches cluster". In: DOI: `10.1051/0004-6361:20010981` (65).

Rolke, W. A. (2005). "Limits and Confidence Intervals in the Presence of Nuisance Parameters arXiv : physics / 0403059 v4 7 Jul 2005". In: *Statistics* July. DOI: `10.1016/j.nima.2005.05.068` (148).

Rossi, B. B. (1952). *High Energy Particles*. Englewood Cliffs, NJ: Prentice-Hall, Inc. (84).

Roy, S. & Rao, A. P. (Feb. 2004). "Sgr A* at low radio frequencies: GMRT observations". In: DOI: `10.1111/j.1365-2966.2004.07693.x` (6).

Rybicki, G. B. & Lightman, A. P. (1979). "Radiative processes in astrophysics". In: *New York, Wiley-Interscience, 1979. 393 p.* (41).

Ryu, S. G. et al. (Apr. 2013). "X-Ray Echo from the Sagittarius C Complex and 500-year Activity History of Sagittarius A*". en. In: *Publications of the Astronomical Society of Japan* 65.2, p. 33. DOI: `10.1093/pasj/65.2.33` (71).

Sasano, M. (1999). "Limits on the Isotropic gamma-ray / Cosmic ray Ratio in the Ultra High Energy region from the EAS Experiment at Ooty". In: *Proceedings of the 26th International Cosmic Ray Conference*. Ed. by D. Kieda, M. Salamon & B. Dingus. Vol. 4. Salt Lake City, Utah: International Union of Pure and Applied Physics (IUPAP)., p. 85 (31).

Schödel, R., Merritt, D. & Eckart, A. (July 2009). "The nuclear star cluster of the Milky Way: proper motions and mass". In: *Astronomy and Astrophysics* 502.1, pp. 91–111. DOI: `10.1051/0004-6361/200810922` (4).

Sentürk, D. G. (2013). "Observational Properties of Gigaelectronvolt-Teraelectronvolt Blazars and the Study of the Teraelectronvolt Blazar RBS 0413 with VERITAS". PhD thesis (108).

Sentürk, G. D. & the VERITAS Collaboration (2011). "The Disp Method for Analysing Large Zenith Angle Gamma-Ray Data". In: *ArXiv e-prints*, pp. 1–3. DOI: `10.7529/ICRC2011/V09/0925` (113).

Sitarek, J. et al. (Oct. 2017). "Nature of the low-energy, {\gamma}-like background for the Cherenkov Telescope Array". In: DOI: 10.1016/j.astropartphys.2017.10.005 (181).

Smith, A. W. (2015). "VERITAS Observations of The Galactic Center Ridge". In: *arXiv.org.* Vol. astro-ph.H, pp. 1–4 (20).

Steigman, G., Dasgupta, B. & Beacom, J. F. (July 2012). "Precise relic WIMP abundance and its impact on searches for dark matter annihilation". In: *Physical Review D* 86.2, p. 023506. DOI: 10.1103/PhysRevD.86.023506 (185).

Strong, A. W. & Moskalenko, I. V. (July 1998). "Propagation of cosmic-ray nucleons in the Galaxy". In: DOI: 10.1086/306470 (31).

Strong, A. W., Moskalenko, I. V. & Reimer, O. (2000). "Diffuse Continuum Gamma Rays from the Galaxy". In: *The Astrophysical Journal.* DOI: 10.1086/309038 (43).

Strong, A. W., Moskalenko, I. V. & Ptuskin, V. S. (Jan. 2007). "Cosmic-ray propagation and interactions in the Galaxy". In: DOI: 10.1146/annurev.nucl.57.090506.123011 (31).

Su, M., Slatyer, T. R. & Finkbeiner, D. P. (Dec. 2010). "GIANT GAMMA-RAY BUBBLES FROM FERMI -LAT: ACTIVE GALACTIC NUCLEUS ACTIVITY OR BIPOLAR GALACTIC WIND?" In: *The Astrophysical Journal* 724.2, pp. 1044–1082. DOI: 10.1088/0004-637X/724/2/1044 (18).

Supanitsky, A. D. (Jan. 2014). "Gamma rays and neutrinos from a cosmic ray source in the Galactic Center region". In: *Physical Review D* 89.2, p. 023501. DOI: 10.1103/PhysRevD.89.023501 (71).

Tanabashi, M et al. (Aug. 2018). "Review of Particle Physics". In: *Phys. Rev. D* 98.3, p. 30001. DOI: 10.1103/PhysRevD.98.030001 (32, 33, 48, 83, 85).

Terrier, R et al. (2010). "Fading hard X-ray emission from the Galactic center molecular cloud Sgr B2". In: *The Astrophysical Journal* 719, pp. 143–150. DOI: 10.1088/0004-637X/719/1/143 (16).

Tibolla, O. et al. (Dec. 2008). "A new source discovered close to the Galactic Center: HESS J1741-302". en. In: *AIP Conference Proceedings.* Vol. 1085. AIP, pp. 249–252. DOI: 10.1063/1.3076652 (20, 178).

Tsuboi, M. et al. (Oct. 1986). "Prominent polarized plumes in the galactic center region and their magnetic field". In: *The Astronomical Journal* 92, p. 818. DOI: 10.1086/114215 (11).

Tsuboi, M., Handa, T. & Ukita, N. (1999). "Dense Molecular Clouds in the Galactic Center Region. I. Observations and Data". In: *The Astrophysical Journal Supplement Series* 120.1, p. 1 (7, 51, 52, 59, 171, 173).

Tsuchiya, K. et al. (May 2004). "Detection of Sub-TeV Gamma Rays from the Galactic Center Direction by CANGAROO-II". In: *The Astrophysical Journal* 606.2, pp. L115–L118. DOI: 10.1086/421292 (18).

Tsujimoto, T. et al. (Dec. 1995). "Relative frequencies of Type Ia and Type II supernovae in the chemical evolution of the Galaxy, LMC and SMC". In: *Monthly Notices of the Royal Astronomical Society* 277.3, pp. 945–958. DOI: 10.1093/mnras/277.3.945 (34).

van Eldik, C. (Dec. 2015). "Gamma rays from the Galactic Centre region: A review". In: *Astroparticle Physics* 71, pp. 45–70. DOI: 10.1016/j.astropartphys.2015.05.002 (12, 56, 57, 67, 69, 78).

Vanhollebeke, E., Groenewegen, M & Girardi, L (2009). "Astronomy & Astrophysics Stellar populations in the Galactic bulge Modelling the Galactic bulge with TRILEGAL". In: *Astronomy & Astrophysics* 498, pp. 95–107. DOI: 10.1051/0004-6361/20078472 (4).

Wang, Q. D., Lu, F. J. & Gotthelf, E. V. (Apr. 2006). "G359.95-0.04: an energetic pulsar candidate near Sgr A". In: *Monthly Notices of the Royal Astronomical Society* 367.3, pp. 937–944. DOI: 10.1111/j.1365-2966.2006.09998.x (66, 73, 164).

Wang, Q. D., Lu, F. & Lang, C. C. (2002). "X-Ray Thread G0.13-0.11: A Pulsar Wind Nebula?" In: *Astrophysical Journal* 581, pp. 1148–1153. DOI: 10.1086/344401 (65).

Wang, Y.-P., Lu, Y. & Chen, L. (July 2009). "Injected spectrum for TeV γ-ray emission from the galactic center". en. In: *Research in Astronomy and Astrophysics* 9.7, pp. 761–769. DOI: 10.1088/1674-4527/9/7/004 (69).

Ward, J. E. et al. (2015). *MAGIC and the Galactic Center Region: Variability Searches During the G2 Pericenter Passage and Morphological Studies* (56).

Weekes, T. C. (Dec. 2003). "TeV Gamma-ray Observations and the Origin of Cosmic Rays: I". In: *28th International Cosmic Ray Conference* (33).

Weinstein, A. (Sept. 2007). "The VERITAS trigger system". In: *arXiv:0709.4438 [astro-ph]*, pp. 2–6 (92).

Winston, R. (Feb. 1970). "Light Collection within the Framework of Geometrical Optics*". In: *Journal of the Optical Society of America* 60.2, p. 245. DOI: `10.1364/JOSA.60.000245` (90).

Witzel, G. et al. (June 2018). "Variability Timescale and Spectral Index of Sgr A* in the Near Infrared: Approximate Bayesian Computation Analysis of the Variability of the Closest Supermassive Black Hole". In: DOI: `10.3847/1538-4357/aace62` (13).

Yamamoto, T. & for the Pierre Auger Collaboration (July 2007). "The UHECR spectrum measured at the Pierre Auger Observatory and its astrophysical implications". In: (32).

Yang, H.-Y. K. et al. (Dec. 2012). "THE FERMI BUBBLES: SUPERSONIC ACTIVE GALACTIC NUCLEUS JETS WITH ANISOTROPIC COSMIC-RAY DIFFUSION". In: *The Astrophysical Journal* 761.2, p. 185. DOI: `10.1088/0004-637X/761/2/185` (18).

Yusef-Zadeh, F (2003). "The origins of the galactice center nonthermal radio filaments: young stellar clusters". In: *The Astrophysical Journal* 598, pp. 325–333. DOI: `10.1086/378715` (11).

Yusef-Zadeh, F, Morris, M. & Chance, D (Aug. 1984). "Large, highly organized radio structures near the galactic centre". In: *Nature* 310.5978, pp. 557–561. DOI: `10.1038/310557a0` (10, 11, 51, 163).

Yusef-Zadeh, F., Hewitt, J. W. & Cotton, W. (Dec. 2004). "A 20 Centimeter Survey of the Galactic Center Region. I. Detection of Numerous Linear Filaments". en. In: *The Astrophysical Journal Supplement Series* 155.2, pp. 421–550. DOI: `10.1086/425257` (11).

Zatsepin, G. T. & Kuz'min, V. A. (1966). *Upper Limit of the Spectrum of Cosmic Rays* (32).

Zhao, J.-H. et al. (July 2009). "DYNAMICS OF IONIZED GAS AT THE GALACTIC CENTER: VERY LARGE ARRAY OBSERVATIONS OF THE THREE-DIMENSIONAL VELOCITY FIELD AND LOCATION OF THE IONIZED STREAMS IN SAGITTARIUS

A WEST". In: *The Astrophysical Journal* 699.1, pp. 186–214. DOI: 10.1088/0004-637X/699/1/186 (8).

Zhu, Z. et al. (Nov. 2018). "A Deep Chandra View of A Candidate Parsec-Scale Jet from the Galactic Center Super-massive Black Hole". In: DOI: 10.3847/1538-4357/ab0e05 (3).